Department of Chemical and Process Engineering
University of Strathclyde

Real-time rheological investigation of complex behaviour in cornstarch suspensions

Christopher Boyle

201782993

Thesis submitted in fulfillment of the requirements of the degree of Doctor of Philosophy

2021

Declarations

This thesis is the result of the author's original research. It has been composed by the author and has not been previously submitted for examination which has led to the award of a degree.

The copyright of this thesis belongs to the author under the terms of the United Kingdom Copyright Acts as qualified by University of Strathclyde Regulation 3.50. Due acknowledgement must always be made of the use of any material contained in, or derived from, this thesis.

Signed: **Date:**

Acknowledgements

> *"Coffee is a way of stealing time that should by rights belong to your older self."*
>
> Terry Pratchett, "Thud!"

I would like to thank Aditi Mukhopadhyay for interesting conversations and support in the lab, as well as Jose Ruiz-Lopez for help with experiments and discussion of results. Finally, many thanks to my supervisors Mark Haw and Leo Lue who have supported me throughout the last four years.

Abstract

Cornstarch suspensions are well known for their surprising property of being able to support a person running across the surface of a pool of the suspension — a phenomenon called shear jamming. This phenomenon has far reaching importance across industries involving granular and colloidal solids transport. In this thesis, the design of a novel custom rheometer for the investigation of these suspensions is described. The results of applying the custom rheometer are shown and analysed in the context of the popular Wyart-Cates model of jamming suspensions. The work confirms the presence of unsteady behaviour in these suspensions, but only for a narrow range of particle concentrations; and of lower density than previously reported. This highlights some of the weaknesses of the WC model, especially as applied to suspensions of polydisperse anisometric particles such as cornstarch (deviating from monodisperse hard spheres).

Contents

Nomenclature

Symbol	Description	Unit
$\dot{\gamma}$	Shear rate	s^{-1}
μ	Viscosity	$\mathrm{Pa\,s}$
ω	Frequency or rotation rate	Hz or $\mathrm{rot\,s}^{-1}$
ω_r	Angular velocity	$\mathrm{rad\,s}^{-1}$
ϕ	Volume fraction	–
ϕ_B	Volume fraction of high rate shear band $\equiv \phi_{hr}$	–
ϕ_{hr}	Volume fraction of high rate shear band $\equiv \phi_B$	–
ϕ_{lr}	Volume fraction of low rate shear band	–
ψ	Porosity of cornstarch particles	$^{ml}/_{\mathrm{ml}}$
ρ	Density	$\mathrm{g\,cm}^{-3}$
$\mathrm{c_p}$	Specific heat capacity	$\mathrm{J\,kg}^{-1}\,\mathrm{K}^{-1}$
Ta	Taylor number	–
σ	Shear stress	Pa
$\Sigma_x^{\%}$	Uncertainty in measurement x, expressed as a percentage	%
Σ_x^{abs}	Uncertainty in measurement x, expressed as an absolute value	as x
τ	Process time constant	s
$\boldsymbol{\sigma}$	Stress	Pa

$\boldsymbol{\varepsilon}$	Dielectric constant	F/m
$\boldsymbol{D}$	Electric displacement	$\mathrm{C/m^2}$
$\boldsymbol{d}$	Direct piezoelectric effect coefficients	C/N
$\boldsymbol{E}$	Applied electric field	V/m
θ	Angular position	rot
ξ	Moisture content of cornstarch particle	$^{g}/_{\mathrm{g}}$
C	Electrical capacitance	F
ca	PI control action.	V
H	Couette cell fill height	mm
h_{fw}	Fluid – Couette cylinder wall heat transfer coefficient	$\mathrm{W\,m^{-2}\,K^{-1}}$
h_{wa}	Couette cylinder wall – air heat transfer coefficient	$\mathrm{W\,m^{-2}\,K^{-1}}$
K	Process gain	varies
k	Spatial frequency	$\mathrm{rad^{-1}}$
K_I	Integral control coefficient.	$V\,Pa^{-1}\,s^{-1}$ or V
K_P	Proportional control coefficient.	$V\,Pa^{-1}$ or $V\,s$
k_w	Thermal conductivity of Couette cylinder glass	$\mathrm{W\,m^{-1}\,K^{-1}}$
$k_{\omega_r \to M}$	Coefficient converting angular velocity to torque due to friction	$\mathrm{N\,m\,s\,rad^{-1}}$
$k_{LC \to M}$	Coefficient converting loadcell reading to torque	N m
LC_z	Loadcell measurement offset	–
$M_{friction}$	Measured torque due to friction	N m
M_{load}	Measured torque due to fluid	N m
M_{total}	Total torque recorded by sensor	N m
M_{visc}	Torque evolved by fluid	W
Q	Electrical charge	C
r	Gap position	mm

r'	Reduced inner cylinder radius	–
r_B	Radial position of shear band	m
r_{in}	Couette cell inner cylinder radius	mm
r_{out}	Couette cell outer cylinder inner radius	mm
T	Temperature	°C
t	time	s
t_D	Process dead-time	s
t_w	Thickness of Couette cylinder glass	m
t_{period}	Period of rotation	s
u	Process input, controller output	varies
V	Electrical potential difference	V
V_t	Total volume of Couette cell	m^3
V_{hr}	Volume of low rate shear band	m^3
V_{lr}	Volume of high rate shear band	m^3
W_{heat}	Rate of heat transfer	W
W_{mech}	Mechanical power	W
W_{visc}	Mechanical power input to fluid	W
y	Process output, controller input	varies

1. Introduction

> *“In the beginning there was nothing, which exploded.”*
>
> Terry Pratchett, “Lords and Ladies”

Cornstarch suspensions are well known for their peculiar ability to support the weight of a person — as long as that person is moving quickly across the surface. This is due to the phenomenon of shear jamming: an extreme transition of a fluid to a solid-like state found prominently in dense colloidal and granular suspensions. Investigation of jamming fluids is industrially important; many processes use fluids as a means of solids transport (or otherwise involve suspensions at some part of the process) such as in the production of paints [1] and cements [2], [3]. Jamming fluids are also of interest to the development of smart materials which utilise the stress-dependent properties to their advantage such as in the development of smart body armour which is flexible, but hard when necessary [4].

Alongside jamming, particle suspensions have shown a propensity for unstable flow — a constant input rate (or stress) can result in oscillatory stress (or rate). This effect has been dubbed “rheochaos” [5].

The link between these fluctuations — which are local in origin — and the global, system-spanning, shear jamming is not completely understood. The prevailing theory behind shear jamming tells of the formation of frictional contacts and networks between particles through the mean-field Wyart-Cates theory [6]. Rheochaos has been typically explained through the use of shear banding [7] — whereby the fluid organises and partitions itself into areas of high and low shear.

Typical laboratory rheometers provide means to measure global rheology. They are typically modular, allowing the study of fluid under different flow patterns (shear or extensional flow) or geometry (Couette cell or parallel plate). Accessing local rheology requires bespoke sensors for this purpose, as well as a rheometer flexible enough to admit the sensor without impacting the global measurements.

In this thesis, the rheological phenomena of cornstarch suspensions are investigated. The goals of this project follow two main streams: the design, construction, and verification of a new, flexible, open-source, 3D-printed laboratory rheometer, and the investigation of dynamic rheology of dense cornstarch suspensions. he rheometer designed is flexible enough to admit a bespoke local stress sensor — the so called Piezoelectric Needle Device (PND) — and thus facilitate the rheological investigation.

The custom open-source rheometer is to be designed for use in this investigation and such that it can be recreated (using the design described here) as part of undergraduate or high school laboratory projects. Rheology is a field prime for investigation in these situations due to the complexity of the research output (so there are many fruitful investigations to pursue) which can be obtained from simple systems such as cornstarch and water.

The prime goal of the project is to investigate the flow instability of shear jamming fluids through the application of dynamic rheometry in tandem to the use of a novel local stress sensor (PND), first introduced in a previous work [8].

This thesis opens with an overview of the main theoretical concepts in Chapter 2. This chapter reviews some of the literature investigating the phenomenon of shear jamming. The main theoretical framework for explaining shear jamming is introduced, as well as the theories for explaining flow instability.

The custom rheometer is described in Chapter 3. The design is presented as a breakdown of the rheometer into its constituent components. Enough detail is given for the rheometer to be re-created independently. The limitations of the components are given, and uncertainty analysis on measurements is performed.

In Chapter 4, the materials used in this thesis are described: any relevant chemistry, the relevant preparation methods, and the expected rheologies. Experimental methodology for rheological testing is described in this chapter, as well as some data analytical methods.

Newtonian baseline rheology is investigated in Chapter 5. This chapter presents both mean rheometry and dynamic rheometry for a variety of Newtonian mixtures. This is used to provide a base picture of the measurements available from the custom rheometer.

Shear thickening behaviour is investigated in Chapter 6. As for the previous chapter, mean and dynamic rheometry is reported. This provides further base measurements for the custom rheometry and shows the rheological features of cornstarch suspensions.

In the final results chapter, Chapter 7, the dynamic rheometry of dense suspensions in the unstable discontinuous shear thickening regime are investigated in detail.

Finally, the key findings are summarised in Chapter 8 along with a summary of directions in which the work should be continued.

Work Outputs

- Open-source design for a desktop concentric cylinder rheometer.

  Hosted online, on `github`:

  Hardware: `https://github.com/cbosoft/rheometer_designs`

  Software: `https://github.com/cbosoft/rheometer`

- Open-source design for a desktop syringe-pump (pipe flow) rheometer.

  Hosted online, on `github`:

  Software: `https://github.com/cbosoft/syringepump`

  Further information in Appendix F. Used in two MEng projects [9], [10] and another PhD project [11].

- Paper detailing the design and use of the custom rheometer, with a focus to use of the project as a demonstration or project piece for higher education.

  C. Boyle, M. D. Haw, and L. Lue, “3D printed rheometer for investigation of dense suspension flow instability,” *American Journal of Physics*, 2021, In preparation.

  Paper text is included in Appendix I.

References

[1] R. R. Eley, “Applied rheology and architectural coating performance,” *Journal of Coatings Technology and Research*, vol. 16, no. 2, pp. 263–305, 2019.

[2] P. F. G. Banfill, “The rheology of fresh cement and concrete — a review,” in *Proceedings of the 11th International Cement Chemistry Congress*, vol. 1, 2003, pp. 50–62.

[3] O. Boukendakdji, S. Kenai, E. Kadri, and F. Rouis, “Effect of slag on the rheology of fresh self-compacted concrete,” *Construction and Building Materials*, vol. 23, no. 7, pp. 2593–2598, 2009.

[4] N. Asija, H. Chouhan, S. A. Gebremeskel, and N. Bhatnagar, “Impact response of shear thickening fluid (stf) treated high strength polymer composites — effect of stf intercalation method,” *Procedia engineering*, vol. 173, pp. 655–662, 2017.

[5] M. Hermes, B. M. Guy, G. Poy, M. E. Cates, M. Wyart, and W. C. K. Poon, “Unsteady flow and particle migration in dense non-brownian suspensions,” *Journal of Rheology*, vol. 60, p. 905, 2016.

[6] M. Wyart and M. E. Cates, “Discontinuous shear thickening without inertia in dense non-Brownian suspensions,” *Physical Review Letters*, vol. 112, no. 9, pp. 1–5, 2014.

[7] P. D. Olmsted, “Perspectives on shear banding in complex fluids,” *Rheologica Acta*, vol. 47, no. 3, pp. 283–300, 2008.

[8] C. Forsyth, “Complex flow of concentrated suspensions,” Ph.D. dissertation, University of Strathclyde, 2015.

[9] I. Panesar, “Automation and controller of laboratory experiments using a raspberry pi — for use in analysing phenomena in non-Newtonian fluids by creating a time dependant rheometer,” M.S. thesis, University of Strathclyde, 2019.

[10] C. Laing, “Controlling the flow of shear-thickening non-Newtonian fluid in a pipe using PI control,” M.S. thesis, University of Strathclyde, 2020.

[11] A. Mukhopadhyay, “Jamming and flow in dense suspensions,” In preparation., Ph.D. dissertation, University of Strathclyde, 2021.

[12] C. Boyle, M. D. Haw, and L. Lue, “3D printed rheometer for investigation of dense suspension flow instability,” *American Journal of Physics*, 2021, In preparation.

2. Background

"παντα ρει" — *Everything flows.*

Heraclitus

2.1 Overview

Detailed in this chapter is the background information behind this thesis. Relevant literature will investigated and reviewed, and important concepts described and explained.

The chapter is structured such that each section builds on the previous, starting from 'Rheology'. Rheology, the study of flow, is a field of widespread importance. Rheology is applied in industrial fluid and particle transport [1], food science [2], cement [3], [4], cosmetics [5], and paint [6] production, medical research — especially with regards to blood-related disorders [7], [8], and even civil engineering [9].

Section 2.2 begins the chapter describing an overview of the field of rheology which is built upon in Section 2.3 which describes the rheology specific to suspensions of solids in liquids and the phenomena typically observed in such systems. Once such phenomenon is of particular significance in this work: shear thickening which is described in Section 2.3.3. A dramatic form of thickening is of particular interest, shear jamming, and is discussed in Section 2.3.4. The prevailing phenomenological model for shear jamming is described in Section 2.4: the Wyart and Cates (WC) frictional transition model [10]. An interesting feature of shear jamming fluids is the existence of an unstable region in which flow fluctuations appear — a phenomenon described in Section 2.3.6.

2.2 Rheology

Rheology is the study of flow of both fluids and soft solids (solids which exhibit plastic deformation) — a field important to many industries and research areas. Some industrial applications of rheology are obvious, such as the processing of fluids like oils [1] and cosmetics [5], and suspensions like cements [3], [4] and paints [6]. Rheology also has applications in city planning and civil engineering [9] (what is the ground if not a suspension of soil and rocks in air and water?) and also in food production [2].

The core parameter in rheology is **viscosity** — a parameter describing the ease of flow. This was first described by Sir Isaac Newton in his viscosity law:

> “ The resistance which arises from the lack of slipperiness originating in a fluid — other things being equal — is proportional to the velocity by which the parts of the fluid are being separated from each other. ” [11]

In other words, the stress response of a fluid is directly proportionally to the rate of strain, stated mathematically in Equation 2.1. The constant of proportionality is called the viscosity.Stated mathematically:

$$\sigma = \mu \dot{\gamma} \tag{2.1}$$

where $\dot{\gamma}$ is the rate at which the fluid is strained (strain rate, units s^{-1}), σ is the stress used in shearing the fluid (units Pα), and μ is the viscosity: the factor converting between stress and strain rate (units Pα s).

Newton’s law (Equation 2.1) introduces viscosity as a coefficient relating a strain rate to a stress. When a fluid can be described using this scalar viscosity, it is said to be **Newtonian**. These fluids have a linear relationship between stress and strain rate. Examples of fluids which follow this law closely are water and glycerol.

However, only a few fluids follow this rule, many break it. For these fluids the relationship between the stress and the strain rate may actually be function of the stress itself or of the strain rate or some other flow parameter. In this case the fluid is said to be **non-Newtonian** or **complex**.

These fluid behaviours are compared on the **flow curve** — plot of stress against strain rate. An example plot show casing the different behaviours of fluids is shown on Figure 2.1.

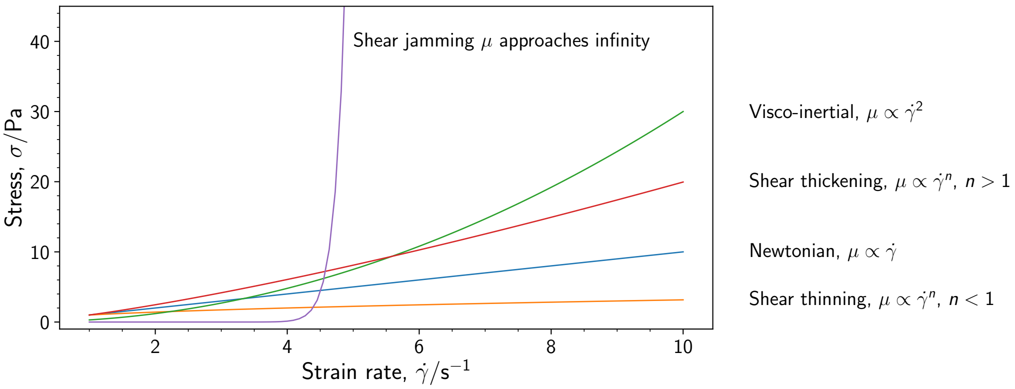

Figure 2.1: *Flow curve: plot of shear stress against shear rate, showing different material behaviours. Newtonian is a straight line, thinning has a power law constant less than one, and thickening has a constant over one. Visco-inertial, a specific type of thickening, has a constant of 2. Shear jamming has a dramatic increase in stress above a critical stress, going to infinity. Adapted from [12].*

2.3 Suspension Rheology

Particles suspended in fluid will impede flow, increasing the effective viscosity. Even dilute hard spheres have an effect on viscosity. “How much of an effect?”, is a question as yet not comprehensively answered. Models and estimates have been proposed for over a century [13], but some details are left out of the models. In this section the effect of particles in suspension on rheology will be discussed.

2.3.1 Concentration

Suspension rheology is dependent on the amount of particles in suspension, normally through the volume fraction ϕ, the ratio of volume of particles in suspension to the total volume of suspension:

$$\phi = \frac{v_{particles}}{v_{suspension}} = \frac{v_{particles}}{v_{solvent} + v_{particles}}$$

At the low end of volume fraction, $\phi = 0$, the suspension is not actually a suspension; being entirely solvent. In this case, the rheology is just that of the solvent (likely a Newtonian fluid — nice and simple). As ϕ increases, the more of an impact the particles will have on the viscosity. ϕ cannot increase to 1; the suspension cannot be all particle and no solvent. It cannot increase to a point close to 1 for monodisperse particles (all of one diameter) due to the void left between closely packed spheres.

For *carefully ordered* monodisperse spheres the maximum packing (face-centred cubic arrangement) is $\phi_{max}^{fcc} = 0.74$ [14]. However, in physical suspensions this limit will not be achieved. Instead, a lower maximum packing will be achieved depending on the stability of the random positioning of the particles. This lower limit is called Random Close Packing (RCP) and is $\phi_{RCP} = 0.64$ for monodisperse spheres [15]. For polydisperse systems, the smaller particles can fit in-between the larger ones and thus a larger volume fraction can be obtained.

Another important packing value is Random Loose Packing (RLP, ϕ_{RLP}). This value is the minimum packing fraction for forming mechanically stable structures [16]. Many values of ϕ_{RLP} have been reported, and it seems that it is very dependent on the method of packing as well as the roughness of the spheres [17]. $\phi_{RLP} = 0.555$ for monodisperse quasi-frictionless spheres [18] and describes the limiting fraction where the spheres can support themselves against external forces, *i.e.* the particles have formed a contact network. As particles friction increases, they are better able to form supporting structures and so ϕ_{RLP} decreases (e.g. $\phi_{RLP} = 0.550$ for roughened glass spheres [18]).

As volume fraction approaches the maximum value for the system, we expect the viscosity to rapidly increase and diverge as the system becomes a solid.

The above discusses RLP in the context of monodisperse suspensions — but the distribution of particle sizes has an important effect on RLP value. An increase in polydispersity — a bigger mixture of sizes — can result in a higher RLP value as smaller particles can fit in-between the larger particles [15].

2.3.2 Viscosity

In 1906 [13] (corrected in 1911 [19]) Einstein calculated the viscosity rise for a very dilute (low volume fraction ϕ) suspension of hard spheres as:

$$\frac{\mu}{\mu_f} = 1 + B\phi \tag{2.2}$$

where B is the Einstein coefficient and was given the value 2.5. This equation relied on the particles being sufficiently far apart that they do not interact hydrodynamically or otherwise. The equation becomes less representative of real suspensions with increasing volume fraction ϕ, a rough threshold below which having acceptable error has been given as $\phi = 0.1$ [20] and more complete solutions are required, due to the hydrodynamic interaction which cannot be ignored.

Particles interact in suspension in many different ways. A particle may push fluid which then pushes into subsequent particles (hydrodynamic interaction [21], [22]), charged particles may interact electrostatically [23], [24]. Particles close together can impede flow or even halt it entirely. Particle ordering can change as flow increases, resulting perhaps in lower viscosity (as particles become ordered perhaps forming streamlines and reducing interaction) or higher viscosity (as order drops and particle interaction becomes more prevalent) [12].

Small suspended particles may be affected by Brownian motion (thermal noise). Larger particles are negligibly affected by Brownian motion. Particles suspended in fluid not density matched will either fall to the bottom and sediment (for negatively buoyant particles) or rise to the top and “cream” (for buoyant particles).

On top of all this, there is the interaction between the particle and the solvent. The particles may be broken down in (or absorb into) the solvent, or be otherwise unstable resulting in a suspension which changes over time.

Empirical models have been established, extending Einstein’s equation out of the very dilute limit [25], [26]. Expanding the polynomial past the first degree gives:

$$\frac{\mu}{\mu_f} = 1 + \sum_{n=1} B_n \phi^n \tag{2.3}$$

where B_n are coefficients depending on the particle size and interaction. This model goes further than Einstein’s, seeming to be valid for suspensions below $\phi = 0.25$ however it fails to capture the jammed state as $\phi \to \phi_{\mathrm{max}}$.

Another, related, empirical fitting model is [26]:

$$\frac{\mu}{\mu_f} = \left(1 - \frac{\phi}{\phi_{\mathrm{max}}}\right)^{-2} \tag{2.4}$$

where ϕ_{max} is the maximum possible packing fraction (e.g. RCP = 0.64 for randomly packed monodisperse spheres). This model captures the diverging viscosity as $\phi \to \phi_{\mathrm{max}}$. The resulting viscosity, being a function of ϕ only, is still Newtonian.

2.3.3 Shear Thickening

A Non-Newtonian fluid may require a diminishing stress driving force per shear rate at increasing rates, in which case it is called shear-thinning. The opposite is also possible: a fluid which requires increasing amounts of stress to drive shear at ever higher rates is said to be shear thickening. Shear thickening is a common property of suspensions of granular or colloidal particles [12], [27]–[29]. Thickening occurs via a number of mechanisms, which present in different ways. Weak thickening is a relatively small increase in viscosity, without sudden increase or jumps. This type of thickening is called Continuous Shear Thickening (CST). Thickening is often described as beginning when a system is sheared above a critical rate, implying a rate driven process [12], [30]. More recently, and more commonly, thickening is attributed to a stress driven process [10], [12], [31] whereby thickening begins above an critical **onset stress**.

A stronger form of thickening is also possible wherein the viscosity of a fluid under shear may increase to such an extent that it appears solid. This type of thickening is called Discontinous Shear Thickening (DST) or Shear Jamming (SJ). DST is a global phenomenon alone, arising from an interaction between the fluid and its container [12].

Rheology tends to be described on a local basis. Shear jamming fluids can, on a local basis, exhibit non-thickening behaviour (even shear thinning) [30]. The bold form **dst** is used to describe these globally thickening (locally thinning) materials, distinct from the generic "DST"*.

At low Reynolds' number, inertia has negligible impact on the fluid, and solvent viscosity dominates. For flow in a specified geometry, as shear rate (Reynolds' number) increases, inertia begins to gain importance creating a regime of intermediate visco-inertial flow [32] and with further increases to rate there exists a transition to a regime where inertia fully shadows viscous effects [12]. The regimes can be identified on a log-log plot of stress against rate of strain (the *flow curve*: Figure 2.1). The stress in the viscous regime scales with the strain rate linearly, and so on the log-log flow curve has a gradient of 1. In the inertial regime, the stress varies with the square of the rate, and so has a gradient of 2 on the flow curve. Intermediary regimes will have a mixture of the two and gradients between 1 and 2.

Particles moving in suspension near one another experience a hydrodynamic lubrication force inversely proportional to their surface-surface separation [33]. For many particles, this will keep the particles separate. However, if particles are pushed close enough together by flow stresses, they can enter into an "orbit" around one another: the hydrodynamic force keeps the particles in close proximity to one another [34]. This is the basis for a phenomenon called Hydroclustering. Particles forced together stay together and act as a larger particle: increasing viscous drag and thus viscosity. Hydroclustering describes continuous shear thickening well [12], but does not describe

---

*This is in contrast to the terminology discussed in Brown and Jaeger [12], which uses capitalised form DST to distinguish from plain "discontinuous shear thickening". Bold form is used here to enhance distinction.

strong thickening on its own.

Particles at rest in a dense ($\phi > \phi_{RLP}$ [17]) suspension are in a tight initial configuration. As the suspension is sheared, particles will have to move away from each other to facilitate flow (Figure 2.2), resulting in a decrease of the suspension volume fraction and therefore a volume increase. If confined, this results in particles unable to flow past one another. This phenomenon is called **dilatancy** [35].

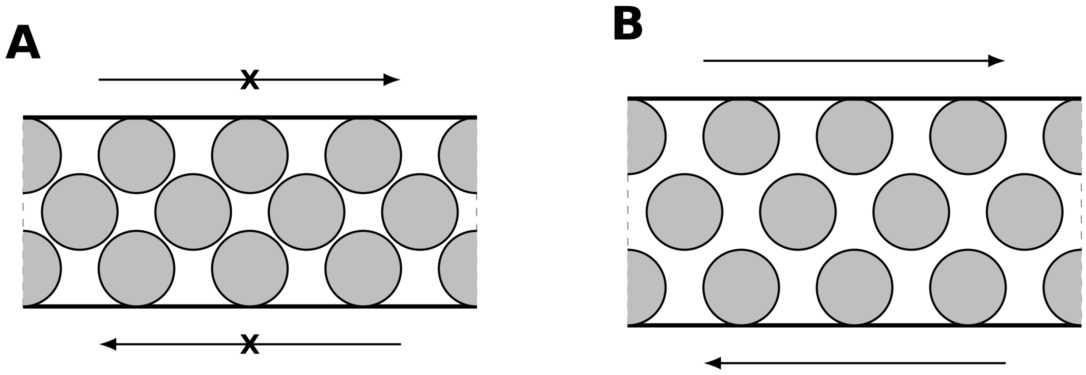

Figure 2.2: *Sketch of particles in suspension dilating. Particles between two planes, initially at (close to) RCP (***A***). As fluid is sheared, particles must move apart to allow flow: the planes are pushed apart (***B***).*

Dilatancy requires an expansion in order to facilitate flow. If the volume is fixed (confined) then the flow will not be possible. This is an example of **dst**. The confinement and expansion results in an apparent overall thickening behaviour, but dilatancy requires a decrease in concentration locally in the fluid — resulting in local thinning.

Shear jamming is closely linked to dilatancy, so much so that fluids which shear jam were known as “Dilatant” fluids [36]. However, it has been shown that dilatancy can occur without **dst** and so dilatancy is required for **dst**, but not without confinement [37]. As the fluid dilates, it is pushed into the boundaries and the friction forces cause the increase in stress known as **dst**.

As suspended particles move apart from one another near the surface, a change in texture can be seen. Particles “poke” out of the fluid resulting in a transition from a glassy to a rough surface [12].

2.3.4 Shear Jamming

A jammed suspension is no longer able to flow. This can occur when the density of solids is too high — above the close packing threshold for the material. Jamming can also be sparked by shearing a dense suspension. A transition from a fluid state to a solid-like state by application of shear — shear jamming. This phenomena is an extension of **dst** whereby flow incites a dramatic increase in viscosity creating the solid-like state.

As with normal **dst**, shear jamming (SJ) requires confinement. This sparked theories explaining SJ comes about due to the formation of solid networks of particles, so-called force chains [38]. Dilation and confinement play a role too, with the dilation causing a “roughness” to appear on the surface

SJ is seen in suspensions of hard particles at high concentration: poly-methyl-methacrylate (PMMA) particles in decalin [39], and glass rods in water [40] are examples of systems which exhibit SJ. SJ is the effect which gives cornstarch-in-water suspensions the remarkable ability to act solid enough for a person to run on, but not walk [12].

A model of a shear jamming system has been sought after in rheology for some time. Hydrodynamic models of particle suspensions gained popularity with Accelerated Stokesian Dynamics (ASD) in the late 80s [22], but lacked the ability to describe shear jamming — used to investigate regular shear thickening [41], [42].

In the new millennium, investigation into dilatancy and shear jamming made some head way with the addition of contact friction modelling [43]. It was found that inter-particle friction is essential to the existence of shear jamming [44]. Tribology (friction science) is a complex field in itself, with many facets not understood — such as the origin and exact nature of static friction [45]. Adding a friction to the hydrodynamic model is part of the answer; but more information on the nature of the friction (static vs dynamic? sliding?) is perhaps needed to encompass the phenomena observed in SJ suspensions.

2.3.5 Shear Banding

A phenomenon seen in a variety of suspensions is that of shear banding: separating of the fluid into distinct areas of low- and high-rate (gradient banding) or of low- and high-stress (vorticity banding) [46]. Banding has been thoroughly investigated with regard to suspensions of worm-like micelles, a shear thinning system composed of polymer strings and other fluids which have strong interaction such as gels [47]. Interestingly, banding has been observed in systems without such strong interlinking/interaction such as PMMA spheres [48] or other colloidal hard-sphere systems [46], the latter system tending to vorticity banding as opposed to gradient banding.

Banding in polymer systems is owed to the ability of the polymers in melt or suspension to form networks or structures together, but also to break apart and reform elsewhere. This forms moving areas of high viscosity and density polymer, which consumes more stress to shear at the same rate as an area of the fluid without structure in the case of vorticity banding or shears at a lower rate than a non-networked area in gradient banding. The formation and destruction of bands causes a fluctuation in flow properties: **rheochaos** [49].

2.3.6 Unsteady Flow

Rheochaos, or flow instability, seen in fluids alongside shear banding, is a result of a competition within the sheared fluid between flow and structure [46], [50], [51].

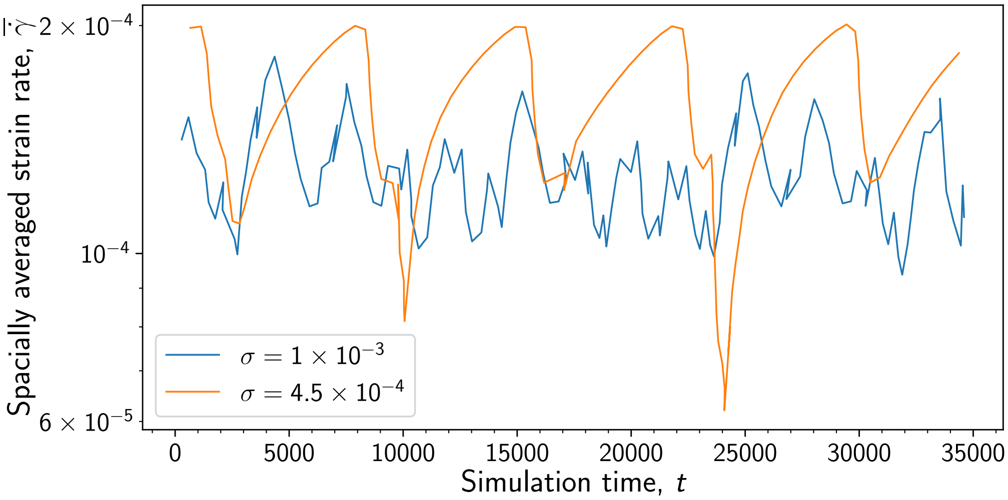

Figure 2.3: *Simulation results (adapted from [52], Figure 2) showing rheo-chaotic and oscillatory fluctuation. Values are non-dimensionalised. At low stress (orange line) the fluctuation is a stable oscillation. At a higher stress the fluctuation has become chaotic.*

Flow instability is seen in thickening suspensions at high density [37], [49], [52], [53]. For a constant applied shear stress, a constant shear rate might be expected from a shear thickening fluid. However, fluctuations in the form of steady or chaotic oscillations appear near the minimum jamming fraction. An example of such fluctuations are shown on Figure 2.3.

"Rheochaos" — unstable flow — has been posed to originate from a competition between the imposed flow (stress) on a system, and force-chains or network formation [46], [50]. Aradian and Cates model these chaotic flows in as a prey-predator system [50], [54]: stress σ competes with memory m (a parameter describing structural relaxation of the fluid stress). The system attempts to form steady bands, but the stress diffuses out from the bands; creating unstable bands moving in space and in time as the system tries to maintain a selected stress.

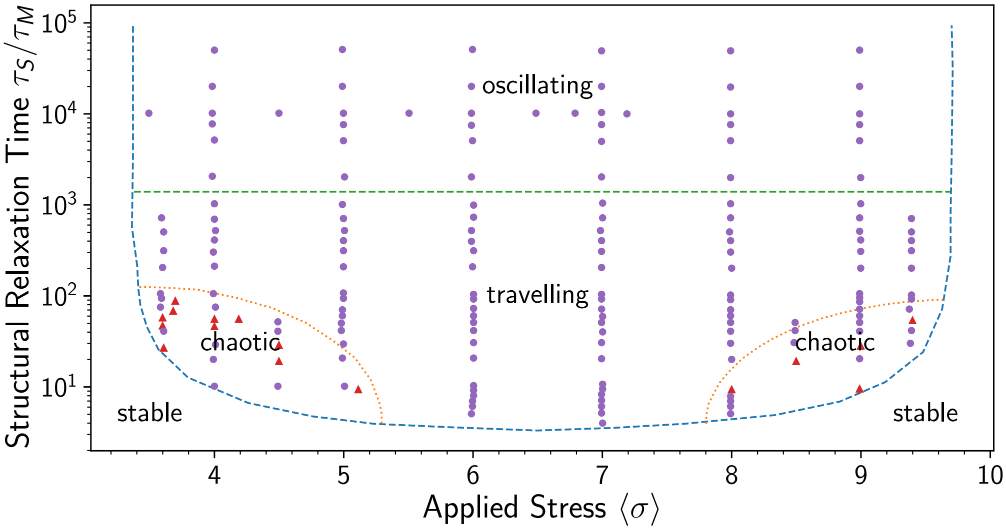

Figure 2.4: *Phase diagram for fluctuation in terms of structural relaxation time (τ_S, non-dimensionalised by the Maxwell time τ_M) and applied (average, non-dimensionalised) stress $\langle\sigma\rangle$. Blue dashed line is linear stability limit. Green dashed line indicates transition between steady temporal-oscillatory bands and spatio-temporal-oscillatory (travelling) bands. Orange dotted lines circle the chaotic regimes. Purple circles are periodic, red triangles are chaotic flows. Adapted from [50] (Figure 4).*

Presented by Aradian and Cates for the model is a phase diagram (Figure 2.4): describing areas of stability depending on the ratio of structural relaxation time τ_s to stress relaxation time (Maxwell time) τ_M and the applied stress. Instability presents for fast structural relaxation $\tau_s/\tau_M > 4$ (this value for the model parameters as presented in [50]). Very fast structural relaxation results in oscillatory bands ($\tau_s/\tau_M \gtrsim 1000$). There is an upper-middle section with travelling bands ($\tau_s/\tau_M \gtrsim 100 \lesssim 1000$), and a lower middle with chaotic banding ($\tau_s/\tau_M \gtrsim 5 \lesssim 100$). Below this, the bands are stable.

Structural relaxation time is a material property; it will change with concentration. As density increases, the structural relaxation time *increases* [55]: the system becomes more sluggish as it is concentrated. This implies that there is a minimum concentration required for unsteady flow.

2.4 Wyart-Cates theory

A phenomenological, mean-field, model was proposed by Wyart and Cates (WC) in 2014 [10]. This framework was built upon the phenomenon of DST in dense suspensions: that shear jamming seems to be driven by a transition from frictionless flow to frictional flow [28], [56], [57].

In the WC model, particles at rest in suspension are separated by the solvent — lubricated. As the shear rate increases, the stress increases. There is then a competition between the lubrication and the stress. When the stress overcomes lubrication, the particles move from lubricated and frictionless (Figure 2.5 **A**), to frictional (Figure 2.5 **C**). This can be sudden, and results in the **dst** phenomenon seen in these suspensions.

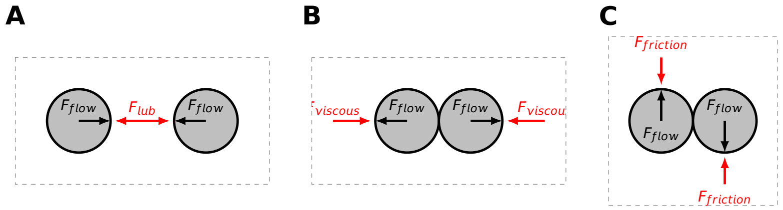

Figure 2.5: *Sketch of interparticle forces before (**A**) and after (**B**, **C**) lubrication is overcome.*

The fraction of particles in frictional contact is described by f: the fraction of particles that have overcome lubrication force F_{lub}. Lubrication force depends on particle relative velocities, solvent viscosity, and particle sizes. If we consider two particles interacting, they may be pushed together by a force related to the fluid stress, depending on the direction and magnitude of the stress at their location [58].

Jamming is described in terms of a “jamming volume fraction” — the volume fraction above which the suspension is solid-like, ϕ_j . Thickening is modelled by changing ϕ_j linearly with f between a minimum ϕ_m, and maximum (the volume fraction for jamming at rest) ϕ_0:

$$\begin{aligned}\phi_j(\sigma) &= \phi_m + (\phi_0 - \phi_m) f(\sigma) \\ &= \phi_m f(\sigma) + \phi_0 \left(1 - f(\sigma)\right)\end{aligned} \tag{2.5}$$

where ϕ_j is the modified jamming point, ϕ_m is the minimum volume fraction required for particles to jam, and ϕ_o is the zero-stress jamming fraction (random close packing for monodisperse spheres). For monodisperse spheres, $\phi_o = \phi_{RCP}$. For polydisperse systems, ϕ_o is lower, often reported to have values in the range of ϕ_{RLP} [31], [59]. f is a function of stress, σ, increasing from 0–1 as stress increases.

The theory (Equation 2.1 and Equation 2.5, in combination with Equation 2.4 and some form of $f(\sigma)$, e.g. Equation 2.7) generates a sigmoidal flow curve for even monotonic $f(\sigma)$, *i.e.* even if the function f is simply linear, the resulting flow curve will be sigmoidal. This s-shaped flow curve is characteristic of the model, and has been demonstrated in experiment [31], [59], [60]. Due to the backwards bend on the flow curve, the gradient of the line (viscosity) is negative — an unstable state. It is due to this bend that discontinuous thickening emerges. Flowcurves for WC systems of different packings is shown on Figure 2.6.

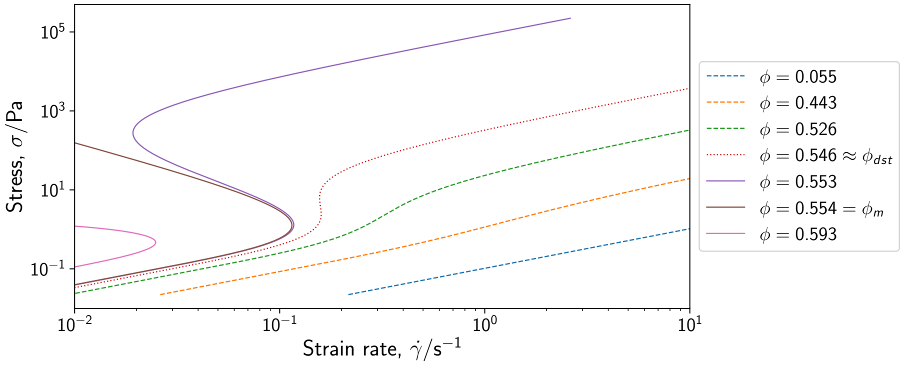

Figure 2.6: *Plot of stress against strain rate for different packing fractions emphasising the sigmoidal shape and possibility for DST above a critical fraction* ϕ_m*.*

Wyart and Cates give an example functional form for how f is related to σ, (CDF for an exponential distribution):

$$f(\sigma) = 1 - e^{-(\sigma/\sigma^{\star})} \tag{2.6}$$

An alternative form is used by Guy *et al*:

$$f(\sigma) = e^{-\left(\frac{\sigma^{\star}}{\sigma}\right)^{\beta}} \tag{2.7}$$

where β is a tunable parameter related to the polydispersity [31]. This functional form for f has found good agreement with fit to experimental results [31], [59].

These forms of f do not take concentration into account, as there is only a weak relation between onset stress ($\sigma^\star$) — the stress at which thickening begins — and volume fraction (ϕ) [10].

The viscosity of the suspension below the threshold volume fraction ϕ_j is governed by proximity of the current volume fraction to the jamming fraction. Shear in suspensions well below ϕ_j results in continuous or no thickening, $\phi < \phi_{dst}$ on Figure 2.6. At the point where the flowcurve becomes vertical, the suspension viscosity (gradient of the line) becomes infinite and we get discontinuity in rheology: $\phi = \phi_{dst}$. Above this volume fraction, discontinuity is present in all flowcurves. For volume fractions $\phi_{dst} \leq \phi < \phi_m$ there is no jamming. Above ϕ_m, there is the possibility of shear jamming. Finally, for $\phi > \phi_0$, the system is classically jammed.

A phase diagram (Figure 2.7) can be drawn for WC suspensions, based on whether they will thicken, shear jam, or already be jammed.

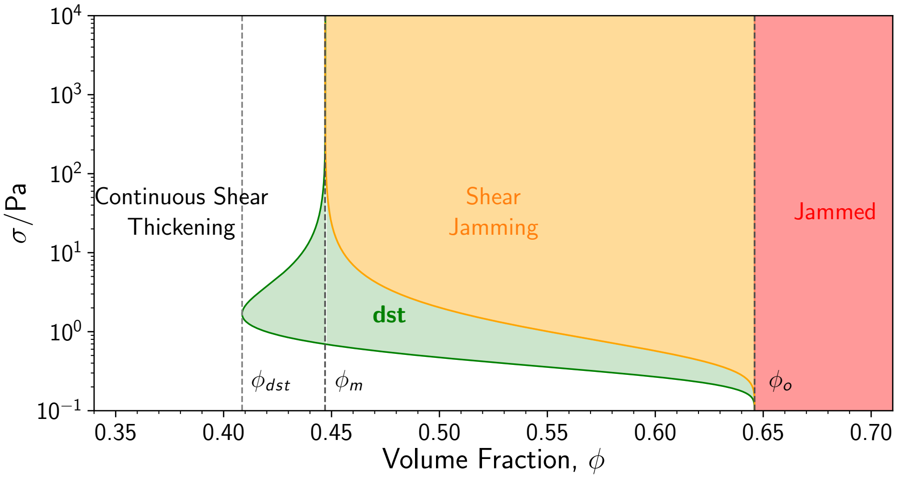

Figure 2.7: *Phase diagram: regions where a suspension is non-jamming (continuous thickening), already jammed, and shear jamming are shown. The latter is where fluctuations are expected.*

The red region on Figure 2.7 is simply where the volume fraction exceeds the volume fraction for jamming at rest ϕ_0. Above the orange line is the region where the fluid is shear jammed. This line is obtained by rearrangement of Equations (2.5) and (2.7) where $\phi = \phi_j$ and therefore $\sigma = \sigma_j$:

$$\sigma_j = \sigma^\star \left(-\ln \frac{\phi - \phi_0}{\phi_m - \phi_0} \right)^{\frac{-1}{\beta}} \tag{2.8}$$

Between the orange and green lines (green shaded area) flow is unstable ($\frac{d\sigma}{d\dot{\gamma}} \leq 0.0$) and thus the fluid will respond discontinuously. For the part of the shaded region to the right of the ϕ_m line, this results in shear jamming. The left represents non-jamming **dst**.

The green line is found by finding the rate of change of the WC stress with respect to strain rate. The WC stress is given by combination of Equation 2.4 with Equation 2.5. The rate of change with respect to strain rate is given by

$$\frac{d\dot{\gamma}}{d\sigma} = \frac{2\beta\phi\left(\frac{\sigma^\star}{\sigma}\right)^{\beta}(\phi_m - \phi_o)\left(-\frac{\phi}{\phi_o+(\phi_m-\phi_o)e^{-\left(\frac{\sigma^\star}{\sigma}\right)^{\beta}}} + 1\right)e^{-\left(\frac{\sigma^\star}{\sigma}\right)^{\beta}}}{\mu_f\left(\phi_o + (\phi_m - \phi_o)\,e^{-\left(\frac{\sigma^\star}{\sigma}\right)^{\beta}}\right)^2} + \frac{\left(-\frac{\phi}{\phi_o+(\phi_m-\phi_o)e^{-\left(\frac{\sigma^\star}{\sigma}\right)^{\beta}}} + 1\right)^2}{\mu_f} \tag{2.9}$$

Solving for stationary points $\frac{d\dot{\gamma}}{d\sigma} = 0.0$ by numerical method yields the green **dst** line on the phase diagram.

Qualitatively comparing the WC jamming phase diagram (Figure 2.7) with the Aradian-Cates fluctuation phase diagram (Figure 2.4) shows agreement of expected behaviours between the two. Structural relaxation time increases with concentration, therefore moving *right* on the WC phase diagram (increasing concentration) is the same as moving *up* on the Aradian-Cates banding phase diagram (increasing structural relaxation time). Picking out the horizontal line at 1 Pa on Figure 2.7 and moving from left to right, the regime is initially of continuous or no thickening. Entering into the green **dst** regime implies a discontinuity of the flow curve and here instability in flow may be expected, tallying with the diagram of Aradian and Cates. Travelling further right on WC, **dst** gives way to a shear-jammed state (orange) — at which point the Aradian model no longer captures the phenomena.

The Wyart-Cates model is a mean-field description of phenomena that have been seen in dense suspensions of colloidal and granular particles, like cornstarch. However the model takes the particles as monodisperse (while some investigation has gone in to expanding to bi-disperse systems [31]). The model cannot capture fully the phenomenon of unsteady flow — only hinting at its location. This is an active research question. Some recent work points out that the particles are not uniformly in frictional contact and this may lead to instability [61].

2.5 Summary

In this chapter the foundation has been laid for the work presented in this thesis: from rheology basics [12], [46] through to complex fluid modelling [10], [31]. Complex fluids, such as hard sphere suspensions, have been seen to have an array of interesting phenomena from plain shear thickening [12], to dramatic shear jamming [12], and flow instability [53].

Suspension rheology has been of mainstream interest in both the industrial community (for processing of materials such as cements [3], [4], paints [6], and even food [2]) and in the research community for over a century [13], [19]. This has lead to theories and discoveries about the nature of the thickening phenomenon seen in these fluids. A recent model — the WC model [10] — captures fairly well [31] the shear jamming phenomena for which fluids like cornstarch-water suspensions are known.

Prevailing theory tells of the formation of bands of high- and low-stress (vorticity banding) or high- and low-strain rate (gradient banding) [46]. These bands move around and grow and shrink. Models, such as Aradian and Cates' [54], attempt to capture the instability of flow as a result of these moving bands. The model predicts oscillatory fluctuation for suspensions of high density, and chaotic flows possible for low density suspensions at particular stresses.

References

[1] S. W. Hasan, M. T. Ghannam, and N. Esmail, “Heavy crude oil viscosity reduction and rheology for pipeline transportation,” *Fuel*, vol. 89, no. 5, pp. 1095–1100, 2010.

[2] X.-Q. Gao, W.-G. Zhang, and G.-H. Zhou, “Emulsion stability, thermo-rheology and quality characteristics of ground pork patties prepared with soy protein isolate and carrageenan,” *Journal of the Science of Food and Agriculture*, vol. 95, no. 14, pp. 2832–2837, 2015.

[3] P. F. G. Banfill, “The rheology of fresh cement and concrete — a review,” in *Proceedings of the 11th International Cement Chemistry Congress*, vol. 1, 2003, pp. 50–62.

[4] O. Boukendakdji, S. Kenai, E. Kadri, and F. Rouis, “Effect of slag on the rheology of fresh self-compacted concrete,” *Construction and Building Materials*, vol. 23, no. 7, pp. 2593–2598, 2009.

[5] C. Gallegos and J. M. Franco, “Rheology of food, cosmetics and pharmaceuticals,” *Current Opinion in Colloid & Interface Science*, vol. 4, pp. 288–293, 1999.

[6] R. R. Eley, “Applied rheology and architectural coating performance,” *Journal of Coatings Technology and Research*, vol. 16, no. 2, pp. 263–305, 2019.

[7] G. Lowe, “Blood rheology in arterial disease,” *Clinical Science*, vol. 71, no. 2, pp. 137–146, 1986.

[8] F. Yilmaz and M. Y. Gundogdu, “A critical review on blood flow in large arteries; relevance to blood rheology, viscosity models, and physiologic conditions,” *Korea-Australia Rheology Journal*, vol. 20, no. 4, pp. 197–211, 2008.

[9] L. Viens, M. A. Denolle, N. Hirata, and S. Nakagawa, “Complex near-surface rheology inferred from the response of greater tokyo to strong ground motions,” *Journal of Geophysical Research: Solid Earth*, vol. 123, no. 7, pp. 5710–5729, 2018.

[10] M. Wyart and M. E. Cates, “Discontinuous shear thickening without inertia in dense non-Brownian suspensions,” *Physical Review Letters*, vol. 112, no. 9, pp. 1–5, 2014.

[11] I. S. Newton, *Philosophiae naturalis principia mathematica*. 1687, vol. 2.

[12] E. Brown and H. M. Jaeger, “Shear thickening in concentrated suspensions: Phenomenology, mechanisms and relations to jamming,” *Reports on Progress in Physics*, vol. 77, 2014.

[13] A. Einstein, “Eine neue bestimmung der moleküldimensionen,” *Annalen der Physik*, vol. 324, no. 2, pp. 289–306, 1906.

[14] A. Baule, F. Morone, H. J. Herrmann, and H. A. Makse, “Edwards statistical mechanics for jammed granular matter,” *Reviews of Modern Physics*, vol. 90, no. 1, p. 015 006, 2018.

[15] V. Baranau and U. Tallarek, “Random-close packing limits for monodisperse and polydisperse hard spheres,” *Soft Matter*, vol. 10, no. 21, pp. 3826–3841, 2014.

[16] G. W. Delaney, J. E. Hilton, and P. W. Cleary, “Defining random loose packing for nonspherical grains,” *Physical Review E*, vol. 83, no. 5, p. 051 305, 2011.

[17] G. Y. Onoda and E. G. Liniger, “Random loose packings of uniform spheres and the dilatancy onset,” *Physical Review Letters*, vol. 64, no. 22, p. 2727, 1990.

[18] M. Jerkins, M. Schröter, H. L. Swinney, T. J. Senden, M. Saadatfar, and T. Aste, “Onset of mechanical stability in random packings of frictional spheres,” *Physical Review Letters*, vol. 101, no. 1, p. 018 301, 2008.

[19] A. Einstein, “Berichtigung zu meiner arbeit: Eine neue bestimmung der moleküldimensionen,” *Annalen der Physik*, vol. 339, no. 3, pp. 591–592, 1911.

[20] G. Kynch, “The effective viscosity of suspensions of spherical particles,” *Proceedings of the Royal Society of London. Series A. Mathematical and Physical Sciences*, vol. 237, no. 1208, pp. 90–116, 1956.

[21] R. P. Mohanty and R. N. Zia, “The impact of hydrodynamics on viscosity evolution in colloidal dispersions: Transient, nonlinear microrheology,” *AIChE Journal*, vol. 64, no. 8, pp. 3198–3214, 2018.

[22] J. F. Brady and G. Bossis, “Stokesian dynamics,” *Annual Review of Fluid Mechanics*, vol. 20, no. 1, pp. 111–157, 1988.

[23] M. F. Hsu, E. R. Dufresne, and D. A. Weitz, “Charge stabilization in nonpolar solvents,” *Langmuir*, vol. 21, no. 11, pp. 4881–4887, 2005.

[24] J. F. Morris, “Shear thickening of concentrated suspensions: Recent developments and relation to other phenomena,” *Annual Review of Fluid Mechanics*, vol. 52, pp. 121–144, 2020.

[25] I. R. Rutgers, “Relative viscosity and concentration,” *Rheologica Acta*, vol. 2, no. 4, pp. 305–348, 1962.

[26] S. Mueller, E. Llewellin, and H. Mader, “The rheology of suspensions of solid particles,” *Proceedings of the Royal Society A: Mathematical, Physical and Engineering Sciences*, vol. 466, no. 2116, pp. 1201–1228, 2010.

[27] J. Bender and N. J. Wagner, “Reversible shear thickening in monodisperse and bidisperse colloidal dispersions,” *Journal of Rheology*, vol. 40, no. 5, pp. 899–916, 1996.

[28] N. Fernandez, R. Mani, D. Rinaldi, D. Kadau, M. Mosquet, H. Lombois-Burger, J. Cayer-Barrioz, H. J. Herrman, N. D. Spencer, and L. Isa, “Microscopic mechanism for shear thickening of non-Brownian suspensions,” *Physical Review Letters*, vol. 111, p. 108 301, 2013.

[29] E. Han, M. Wyart, I. R. Peters, and H. M. Jaeger, "Shear fronts in shear-thickening suspensions," *Physical Review Fluids*, vol. 3, no. 7, p. 073 301, 2018.

[30] A. Fall, F. Bertrand, D. Hautemayou, C. Méziere, P. Moucheront, A. Lemaitre, and G. Ovarlez, "Macroscopic discontinuous shear thickening versus local shear jamming in cornstarch," *Physical Review Letters*, vol. 114, no. 9, p. 098 301, 2015.

[31] B. M. Guy, C. Ness, M. Hermes, L. J. Sawiak, J. Sun, and W. C. K. Poon, "Testing the Wyart-Cates model for non-Brownian shear thickening using bidisperse suspensions," *Soft Matter*, vol. 16, no. 1, pp. 229–237, 2020.

[32] M. Trulsson, B. Andreotti, and P. Claudin, "Transition from the viscous to inertial regime in dense suspensions," *Physical Review Letters*, vol. 109, no. 11, p. 118 305, 2012.

[33] J. F. Brady and G. Bossis, "The rheology of concentrated suspensions of spheres in simple shear flow by numerical simulation," *Journal of Fluid Mechanics*, vol. 155, pp. 105–129, 1985.

[34] N. J. Wagner and J. F. Brady, "Shear thickening in colloidal dispersions," *Physics Today*, vol. 62, no. 10, pp. 27–32, 2009.

[35] O. Reynolds, "On the dilatancy of media composed of rigid particles in contact," *Philosophical Magazine*, vol. 20, 1885.

[36] A. Metzner and M. Whitlock, "Flow behavior of concentrated (dilatant) suspensions," *Transactions of the Society of Rheology*, vol. 2, no. 1, pp. 239–254, 1958.

[37] E. Brown and H. M. Jaeger, "The role of dilation and confining stresses in shear thickening of dense suspensions," *Journal of Rheology*, vol. 56, no. 4, pp. 875–923, 2012.

[38] M. Cates, J. Wittmer, J.-P. Bouchaud, and P. Claudin, "Jamming, force chains, and fragile matter," *Physical Review Letters*, vol. 81, no. 9, p. 1841, 1998.

[39] C. Forsyth, "Complex flow of concentrated suspensions," Ph.D. dissertation, University of Strathclyde, 2015.

[40] V. Rathee, S. Arora, D. L. Blair, J. S. Urbach, A. K. Sood, and R. Ganapathy, "Role of particle orientational order during shear thickening in suspensions of colloidal rods," *Physical Review E*, vol. 101, p. 040 601, 2020.

[41] D. Dratler, W. Schowalter, and R. Hoffman, "Dynamic simulation of shear thickening in concentrated colloidal suspensions," *Journal of Fluid Mechanics*, vol. 353, pp. 1–30, 1997.

[42] J. W. Swan and J. F. Brady, “The hydrodynamics of conned dispersions,” *Journal of Fluid Mechanics*, vol. 687, pp. 254–299, 2011.

[43] M. M. Denn and J. F. Morris, “Rheology of non-brownian suspensions,” *Annual Review of Chemical and Biomolecular Engineering*, vol. 5, pp. 203–228, 2014.

[44] R. Mari, R. Seto, J. F. Morris, and M. M. Denn, “Shear thickening, frictionless and frictional rheologies in non-brownian suspensions,” *Journal of Rheology*, vol. 58, no. 6, pp. 1693–1724, 2014.

[45] F. Lacombe, S. Zapperi, and H. J. Herrmann, “Dilatancy and friction in sheared granular media,” *The European Physical Journal E*, vol. 2, no. 2, pp. 181–189, 2000.

[46] P. D. Olmsted, “Perspectives on shear banding in complex fluids,” *Rheologica Acta*, vol. 47, no. 3, pp. 283–300, 2008.

[47] T. Divoux, M. A. Fardin, S. Manneville, and S. Lerouge, “Shear banding of complex fluids,” *Annual Review of Fluid Mechanics*, vol. 48, pp. 81–103, 2016.

[48] R. Besseling, L. Isa, P. Ballesta, G. Petekidis, M. Cates, and W. Poon, “Shear banding and flow-concentration coupling in colloidal glasses,” *Physical Review Letters*, vol. 105, no. 26, p. 268 301, 2010.

[49] S. M. Fielding and P. D. Olmstead, “Spatiotemporal oscillations and rheochaos in a simple model of shear banding,” *Physical Review Letters*, vol. 92, no. 8, 2004.

[50] A. Aradian and M. E. Cates, “Minimal model for chaotic shear banding in shear thickening fluids,” *Physical Review E*, vol. 73, 2006.

[51] P. T. Callaghan, “Rheo NMR and shear banding,” *Rheologica Acta*, vol. 47, no. 3, pp. 243–255, 2008.

[52] M. Grob, A. Zippelius, and C. Heussinger, “Rheological chaos of frictional grains,” *Physical Review E*, vol. 93, p. 030 901, 2016.

[53] M. Hermes, B. M. Guy, G. Poy, M. E. Cates, M. Wyart, and W. C. K. Poon, “Unsteady flow and particle migration in dense non-brownian suspensions,” *Journal of Rheology*, vol. 60, p. 905, 2016.

[54] A. Aradian and M. E. Cates, “Instability and spatiotemporal rheochaos in a shear-thickening model,” *Europhysics Letters*, vol. 70, no. 3, pp. 397–403, 2005.

[55] W. C. Poon, S. Meeker, P. Pusey, and P. Segre, “Viscosity and structural relaxation in concentrated hard-sphere colloids,” *Journal of Non-Newtonian Fluid Mechanics*, vol. 67, pp. 179–189, 1996.

[56] R. Seto, R. Mari, J. F. Morris, and M. M. Denn, “Discontinuous shear thickening of frictional hard-sphere suspensions,” *Physical Review Letters*, vol. 111, no. 21, p. 218 301, 2013.

[57] C. Clavaud, A. Bérut, B. Metzger, and Y. Forterre, “Revealing the frictional transition in shear-thickening suspensions,” *Proceedings of the National Academy of Sciences*, vol. 114, no. 20, pp. 5147–5152, 2017.

[58] R. Radhakrishnan, J. R. Royer, W. C. Poon, and J. Sun, “Force chains and networks: Wet suspensions through dry granular eyes,” *Granular Matter*, vol. 22, no. 1, p. 29, 2020.

[59] R. E. ONeill, J. R. Royer, and W. C. Poon, “Liquid migration in shear thickening suspensions flowing through constrictions,” *Physical Review Letters*, vol. 123, no. 12, p. 128 002, 2019.

[60] J. F. Morris, “Lubricated-to-frictional shear thickening scenario in dense suspensions,” *Physical Review Fluids*, vol. 3, no. 11, p. 110 508, 2018.

[61] J.-C. J. Tsai, G.-H. Huang, and C.-E. Tsai, “Signature of transition between granular solid and fluid: Rate-dependent stick slips in steady shearing,” *Physical Review Letters*, vol. 126, no. 12, p. 128 001, 2021.

3. Rheometer Design

> *"Cheops' Law: Nothing ever gets built on schedule or within budget."*
>
> Robert A. Heinlein, "Time Enough for Love"

3.1 Overview

A rheometer is a device that measures rheological properties of a fluid [1]: typically flow properties, such as stress and strain rate. This is achieved by developing a controlled and well-known flow in a fluid such that the flow properties can be measured, or at least calculated from measurements. Rheometers differ on the flow pattern employed (*e.g.* shear or extensional flow) and thus record different properties. Commercial rheometers typically record or report extra information like the normal stress difference (measurement of the visco-elasticity of the material) [2], [3] or relaxation time (measurement of fluidity) [4] for extensional rheometry.

Part of the main objectives of this work is to design and build a cost-effective rheometer, leveraging the newly available technology of domestic 3D printing, which can be employed for small scale rheological testing, or as a learning tool for electronics, programming, and physics.

To the best of the author's knowledge, a 3D printed rheometer has not been presented before. 3D printed flow cells have been used [5], but not a rheometer device in full. This novel device provides a flexible framework for the testing of fluids with bespoke sensors (the piezoelectric needle device used here) and enables rapid development of new hardware for different applications — an extreme flexibility not seen in commercial devices where additional accessories provide a limited means to expand functionality.

The main use of the custom Couette rheometer (CCR) is to investigate unsteady flows in dense cornstarch suspensions under shear. This is done by measuring stress and strain rate while a sample of suspension is sheared. In addition, the rheometer is to feature *no time averaging*, thereby being suitable to investigation of dynamic effects. In addition the design is completely open source (both open hardware and open software) [6], [7].

The rheometer is specified as follows; the rheometer should:

- report stress and strain rate for a test fluid,
- report instantaneous (non-averaged) measurements with acceptable accuracy to allow the investigation of dynamic properties in jamming fluids under shear,
- be able to interface with other sensors for further insight into the material, and
- be extensible and customisable to suit alternative purposes (measure alternative flow patterns, different sizes of cylinder).

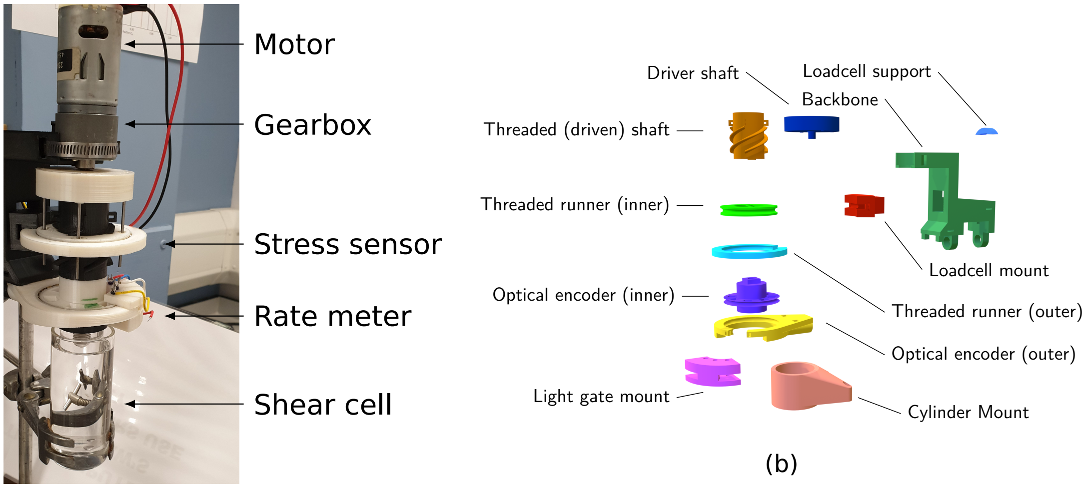

(a)

(b)

Figure 3.1: *(a) Annotated photograph of the completed rheometer and (b) annotated render of the 3D printed components.*

The rheometer consists of a Couette shear cell (Section 3.3) in which flow is driven through the inner cylinder by a DC motor (Section 3.6). In this rotating shaft is the stress sensing mechanism (Section 3.5), and the structure is held by a bearing providing stability, and housing the shear rate measurement (Section 3.4): an optical encoder built into the bearing.

Bearing, encoder disk, and sensor mount were designed in OpenSCAD and FreeCAD software and 3D printed on a Prusa i3 MK3 FDM 3D printer.

The sensors are controlled by a Raspberry Pi Single Board Computer (SBC, Section 3.2), and supporting electronics were soldered onto a single perfboard and includes an analogue to digital converter (ADC) for reading data from the Piezoelectric Needle Device (PND — a novel sensor design for investigating local flow — Section 3.8). A pair of temperature sensors are included to monitor shear cell and ambient temperatures (Section 3.7). The hardware were primarily 3D printed, with some standard laboratory clamp stands to aid stability.

After a brief description of the Raspberry Pi backbone, the other component systems (shear cell, rate sensor, stress sensor, motor, PND) of the custom rheometer are detailed in turn in the following sections. Each of these sections is structured as follows:

- **Purpose** introduces the reasoning for the component, how it relates to the greater work, and the specifications of the component.
- **Implementation** describes the physical nature of the component: how it is built, where it physically fits in the work, and any electrical or mechanical requirements it has. Electronic circuit diagrams are given for the component, when required. Details of the electronics used are given in Appendix D.
- **Data Processing** describes the process of obtaining data from the component, where applicable.
- **Limitations** discusses the conditions under which the component works, where it fails, and the implications with respect to the overall objective of the design.

3.2 Raspberry Pi

A Raspberry Pi (RPi) Single Board Computer (SBC) [8] is used as the main board powering the custom rheometer. Measurements are logged by software written for the RPi. The RPi is a credit-card sized computer used widely in education and for hobbyist projects. The power of the Raspberry Pi lies it its ability to interface with hardware, like a microcontroller, while also providing a full desktop computer experience. A labelled diagram of the RPi is shown on Figure 3.2

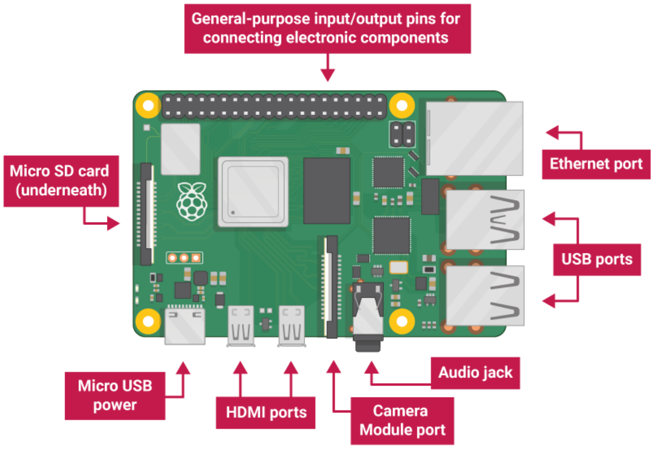

Figure 3.2: *Raspberry Pi labelled diagram. From [9].*

The RPi has general purpose input/output (GPIO) hardware interface pins. These are a set of pins made available to interface with any hardware the user may desire. These pins can be in either input or output mode. As an input, they measure the voltage difference between themselves and ground. If the measurement is above a threshold (seen to be roughly a volt) then the pin regards itself as on or “high”. If the voltage is below this threshold, then the pin is off or “low”. In output mode, the pins can be set “high” or “low” by software, and their voltage levels will be set accordingly.

In addition to the GPIO, there are hardware interface protocols I2C and SPI available; used to facilitate communication between the RPi and peripheral devices. Both SPI and I2C are serial interfaces (information sent down one wire one bit at a time). These are used in this design to interface with analogue to digital converters (ADCs) for the loadcell, PND, and thermocouple.

The RPi’s low cost (£30 for the model 3 used here, £4 for the model Zero also available) make it especially suitable for hobbyists and in education environments. However, the board is low-power: having four processing cores at a limited processor frequency of around $1GHz$ (compare with a typical consumer PCs desktop processor frequency which may be 3–5× this). For this application, the processing power is a slight limitation but the other advantages (many interface options available, low cost, high availability) make up for it.

3.3 Shear cell

3.3.1 Purpose

Different rheometry methods have different geometries and flow patterns. For this work, a simple shear flow is desired. Shear flow is an aspect of a few different flow schemes: pipe flow includes shear near the walls, fluid is sheared between plates in a parallel plate geometry, nozzle flow includes some shear flow (along with extensional), and the flow in a concentric cylinder arrangement also involves shear flow.

A further constraint is in the use of external sensors to measure rheological aspects of the fluid. The chosen rheometry design needs to allow for a large enough gap, in which the fluid is sheared, to admit these sensors. Concentric cylinder rheometers can have gaps large enough to admit additional sensors into the fluid. In contrast, parallel plate and cone-and-plate rheometers' gaps are limited by the capillary forces required to keep the test fluid in place [10]. In addition, capillary rheometers are closed, so it would make it very difficult to fit in an additional sensor into the fluid.

3.3.2 Implementation

The Couette cell [11] (Figure 3.3) is a combination of a glass outer cylinder and a perspex inner cylinder. The outer cylinder is mounted in a 3D printed stand attached onto an XY table (from a microscope), which is in turn attached to a clamp stand. The XY table allows for the careful positioning and alignment of the cylinders to ensure they are indeed coaxial. The clamp attachment of the table allows the XY table to be raised and lowered to allow cylinders be filled and emptied.

A Couette cell can have the property of a linear velocity profile, provided the gap is small enough with respect to the cylinder radii — narrow gap approximation (discussed further in Section 3.4). Where the gap is too large for this, a non-linear velocity profile is developed as shown on Figure 3.3. An equation for strain rate $\dot{\gamma}$ is also shown on the figure.

The inner cylinder, a solid cylinder of perspex, has a thread drilled in from top that allows it to attach/detach from the drive shaft. The outer cylinder, a cup-shaped hollow cylinder of glass, is held by by friction only within its mount allowing easy removal from the XY table and facilitating cleaning. Both cylinders are transparent, which allows viewing of the fluid within; useful for filling (checking fill level), and allowing camera to film the fluid.

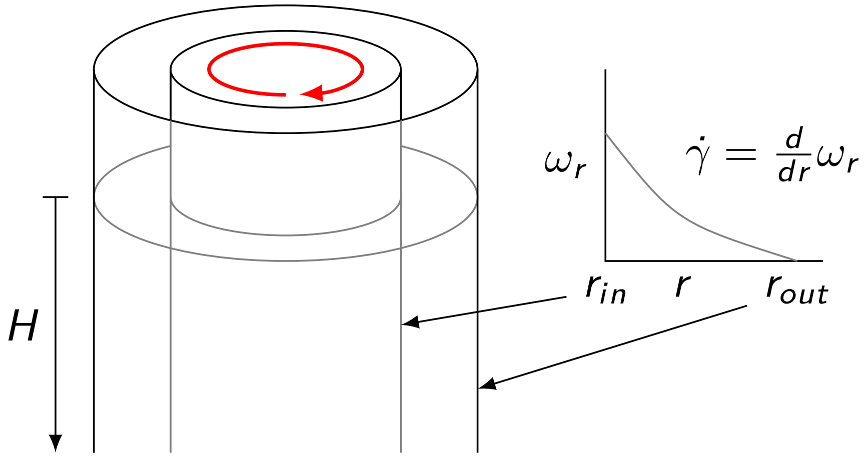

Figure 3.3: *Diagram of a Taylor-Couette shear cell*

Table 3.1: *Table of shear cell key measurements.*

Parameter	**Symbol**	**Value**
Fill depth	H_{fill}	Variable; 50–75 mm ± 2%
Inner cylinder radius	r_{in}	15.05 mm ± 0.017%
Outer cylinder radius	r_{out}	19.75 mm ± 0.013%
Gap width	l_{gap}	4.7 mm ± 0.11%

Key measurements of the shear cell are summarised on Table 3.1. These measurements are used to calculate properties (shear stress, strain rate). “Fill depth” is the depth to which the inner cylinder is immersed in the fluid: it is the height the cylinder is in contact with fluid.

3.3.3 Limitations

Fill volume

The inner cylinder is held above the bottom of the outer cylinder, so there is fluid in this gap. There is then a mixture of flow patterns here, a Couette shear flow in the most of the apparatus, and a parallel-plate-like flow pattern between the bottom of the inner cylinder and the inside bottom of the outer cylinder. This bottom component of the flow can be considered negligible if a majority of the flow is Couette, and if the vertical spacing between the inner and outer cylinders is large (meaning the shear rate in the parallel section is small).

The large gap at the bottom therefore requires a large volume of fluid to fill. For a 2 cm gap at the bottom, this results in approximately 14 ml of fluid required which will not take part in the measured shear. On top of this is up to 70 mm of fill which takes up approximately another 35 ml. Counter-intuitively, a lower fill depth may require more fluid (assuming constant total fluid height), as more fluid is in the space below the inner cylinder.

This is the first limitation of the design; the cell requires a large volume of fluid making it uneconomic for many additives which may improve rheology: such as density matching solvent, or alternative rheological test materials.

In the same vein, the fill depth must be measured after the fluid is loaded in the cylinder, and done so by hand. Due to the method of positioning the cylinders, it is almost impossible to get the same outer cylinder position between runs. This means that a depth measurement must be made for every run. Each depth measurement is made by measuring the distance from the fluid surface up the inner cylinder to the bottom of the thread (seen as the cylinder is transparent). The fill depth can be found by subtracting the measurement from the distance from the cylinder bottom to the same point. This measurement introduces reading error into the equation, which is reflected as an error in the fill depth as reported in Table 3.1.

Taylor Number

Couette flow at high Reynolds number can bring about turbulent flow in the form of Taylor vortices [12] if the inner cylinder is rotated. These are unstable fluxes of fluid moving from the rotating cylinder towards the stationary cylinder. These vortices form as the inner cylinder provides a centrifugal effect driving fluid towards the outer cylinder. A centripetal pressure gradient forms, pushing fluid back towards the inner cylinder. If the fluid has too much angular momentum however, the centripetal pressure gradient is insufficient to push it back. This results in vortices of flow not in the direction of cylinder rotation. This effect results in higher-than-expected viscosity measurements due to the cross flow dissipating energy and enhancing momentum transfer and so can disrupt any rheological measurements [13]. Care must be taken to ensure the Taylor-Couette flow regime is not entered.

The Taylor number (Tα) is used to test for the possibility of Taylor vortices in flow, given by [12]

$$\mathrm{Ta} = \frac{\omega_r^2 r_{in}(r_{out} - r_{in})^3 \rho^2}{\mu^2} \tag{3.1}$$

where r_{out} and r_{in} are the radii of the outer and inner cylinders respectively, and ω_r is the angular velocity of the Couette cell inner cylinder in $\mathrm{rad\,s^{-1}}$.

Above a critical limit (1700 [12], [14]) Taylor vortices form. The largest possible Taylor number is calculated from the highest rotation rates and lowest viscosities that can be used in the rheometer.

A conservative worst case scenario for fluids run in the custom rheometer used in this work would be a 85wt% aqueous glycerol solution ($\mu_{25} = 0.0802\,\mathrm{Pa\,s}$) run at 500RPM. This results in a Taylor number of 994. This is far below the limit of 1700 and highly unlikely that Taylor vortices are formed in the Couette cell.

Uncertainty Analysis

Uncertainties introduced in this component are all measurement uncertainties. Measurements summarised in Table 3.1 were made with a set of digital calipers. The calipers gave measurements in mm to two decimal places. Uncertainty in the measurement is estimated as half of the smallest measurement:

$$\Sigma_x^{\mathrm{abs}} = 0.005\,\mathrm{mm}$$

the percentage error is therefore found from

$$\begin{aligned}\Sigma_x^{\%} &= \frac{\Sigma_x^{\mathrm{abs}}}{x} \times 100\% \\ &= \frac{0.5}{x}\,\%\end{aligned}$$

The uncertainties for radii and gap width shown in Table 3.1 were calculated in this manner.

3.4 Strain rate Measurement

3.4.1 Purpose

The shear rate, in a Couette cell, is the rate of change of the velocity with position in the gap (the spatial derivative of the velocity profile). The strain rate can be calculated knowing the boundary velocities and the geometry of the gap. The outer cylinder is held stationary and so has zero velocity. The inner cylinder is rotated at some angular velocity $\omega_r\,\mathrm{rad\,s^{-1}}$. These are the two velocity boundaries. The geometry bounds are the outer and inner cylinder and so the outer and inner radius. The strain rate at a position in the gap r of a Couette cell is given by [15]:

$$\dot{\gamma}(r) = -\frac{2\omega_r}{r^2} \cdot \frac{{r_{in}}^2 {r_{out}}^2}{{r_{out}}^2 - {r_{in}}^2} \tag{3.2}$$

where ω_r is the angular velocity of the inner cylinder. This non-linear equation can be approximated, in the narrow gap limit, by the mean value across the gap:

$$\bar{\dot{\gamma}} = r' \omega_r \tag{3.3}$$

where $r' = {}^{r_{in}}/_{(r_{out} - r_{in})}$.

The narrow gap approximation results, approximately, in a 19% variation in strain rate across the gap for the cylinder radii and resulting gap size used here. The narrow gap-mean strain rate will be reported throughout the rest of this thesis, and unless otherwise stated, this is what is meant by "strain rate". The strain rate measurement system should be quick to report measurements to provide accurate recovery of dynamic behaviour. In addition, it should be accurate without requiring time-averaging, to further improve recording of dynamics. To this end, an optical encoder was employed as a simple but effective rate measurement device.

3.4.2 Implementation

Angular velocity is measured using an optical encoder: a device consisting of a pair of LEDs with corresponding light sensors (phototransistors). Between the LEDs and sensors is a slotted disk. As the disc rotates, the beam of light between LED and sensor is broken and repaired. This encodes the rotation into a square wave signal which can be processed to obtain the rate of rotation. A diagram of the encoder is shown on Figure 3.4.

The light gates circuit is shown on Figure 3.5. The signal from the light gate is read digitally from the GPIO pins on the Raspberry Pi (Section 3.2). If the light gate is blocked, the phototransistor is closed and the GPIO pin (pulled up with an internal 10kΩ resistor) has a “high” value (3.3v). If the gate is unblocked, the GPIO will have a “low” value as it is pulled to ground. The GPIO is monitored; the time when its value changes is recorded. When a gate becomes blocked, we can call this a “break” event. When a gate becomes unblocked, we can call this a “repair” event. In this way, the rotation of the disk as it varies in time is encoded as a square wave.

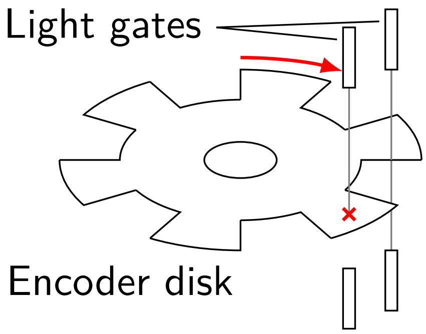

Figure 3.4: *Diagram of optical encoder, showing encoder disk and the two light gates. At any time one light gate is closed while another is open. On this diagram, the left gate is open (light does not reach sensor) while the right gate is closed (light reaches sensor).*

The encoder disk has 6 evenly spaced, equally sized slots between 6 evenly spaced, equally sized spokes. One full rotation of $2\pi\,\mathrm{rad}$ is encoded as a square wave with 6 full waves (peak and trough). Therefore each peak and trough ($^1/_{12}$ rotation) in the square wave correspond to $^{\pi}/_{6}\,\mathrm{rad}$ of rotation.

Two light gates are used in tandem to provide some redundancy: averaging between the results of the two signals gives a more accurate result. The two gates are each one encoded-wavelength out of step, meaning the speed at each point in the resulting timeseries results from a different kind of encoder event — a “break” event is averaged with a “repair” event — reducing possible variation between the event types.

To improve stability, the disk was built into a bearing. This prevents wobbling between the disc and the gate array, removing a source of noise in the output signal. This has the added benefit of providing an anchor point for the rheometer, a stable base where the rheometer can be held by the mounting clamp stand.

3.4.3 Data Processing

Logged data are processed to find the period of the wave, which is used in turn to find the frequency and thus the angular velocity. Data are logged in the form of a list of event times; the time at which light is blocked from a sensor (a break event) or the time at which light is un-blocked (a repair event). Time between these events gives the period (T in seconds), the reciprocal of which gives the frequency of rotation ω in

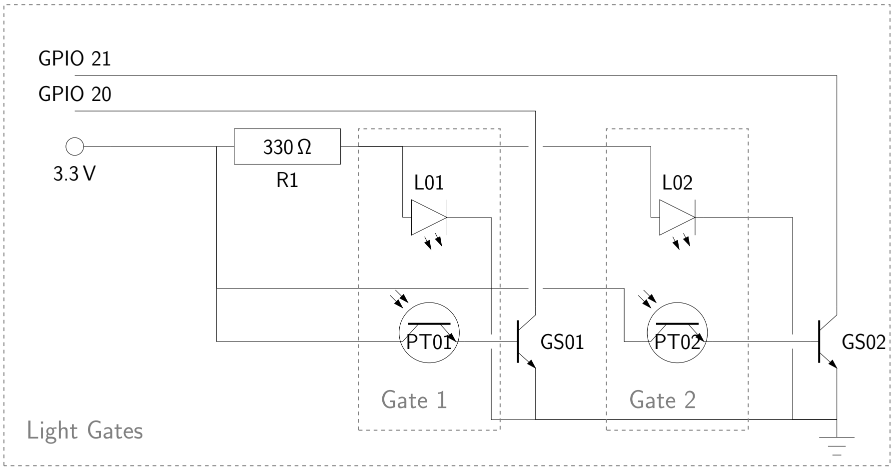

Figure 3.5: *Circuit diagram of light gate circuitry.*

rot s^{-1} or Hz:

$$\omega = \frac{1}{t_{period}} \tag{3.4}$$

This gives an indication of the rotation rate, which is converted to angular velocity by multiplying by $2\pi\, {}^{rad}/_{\text{rot}}$. There is noise in the measured data which must be cleaned up before continuing; there are practical limitations of the measurement method which must be taken into account, and finally the different logs for each sensor must be taken into account.

Error rejection

There are sometimes misfires of the light-gates: reflections, wobble, mechanical faults, or variations in the power supply can cause the GPIO to mis-register a different value, and as such be logged improperly as a switch. This is dealt with in post-processing. Three sensors working together allows transient noise to be rejected by performing a simple sanity check over the resulting data.

Due to the sensitivity of the GPIO, the transition of the light-gate from blocked to un-blocked, may trigger several value-change events. The GPIO has a threshold above which it sees as “high”, below this is “low”. However if a voltage is held near this threshold, then natural fluctuations in supply voltage may move this threshold and the reading will flicker between “high” and “low”. Therefore, there may be multiple readings of an event, for every actual event. The timing of these events can be used to check the veracity of the recording. The flicker events will occur at nearly the same time, however real events will have some time delay between them, by check for events occurring at the same time, and discarding them, the data can be tidied. This effect of this error rejection algorithm is shown on Figure 3.6.

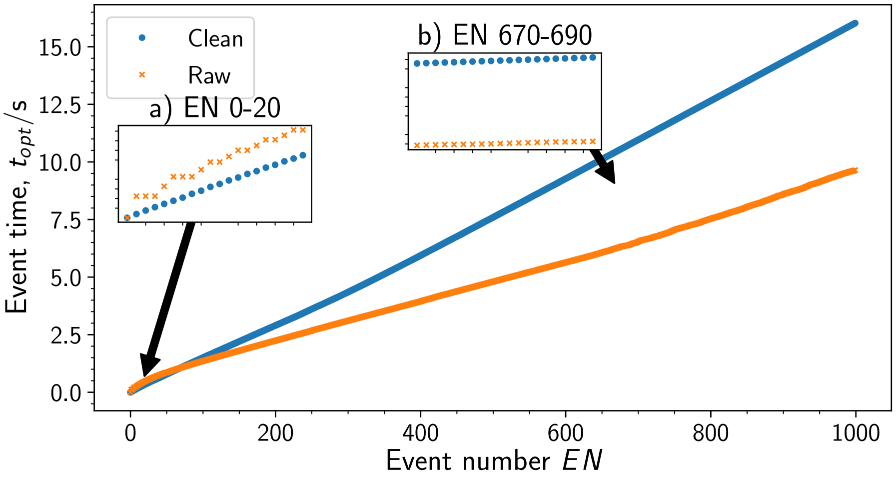

Figure 3.6: *Comparison of raw optical encoder event data (orange) with a sanitised version (blue). Event time is plotted against event number to highlight, qualitatively, the erroneous multiple readings. For a particular time, there should be only one event. However as can be seen on the orange plot, there are multiple dots for a single time. This corresponds to the multiple measurement of a single event. For a constant velocity, a straight line is expected. The blue dots are still not in a line, but have no multiples. This curving shows the acceleration in the apparatus, especially noticeable near the start.*

Period calculation

After unreliable data has been dealt with, speed reported by each sensor can be calculated. The period of the square wave is the difference between every other time point, Equation 3.5.

$$t_{period,i} = t_{i+2} - t_i \tag{3.5}$$

If the difference between a time point and the immediate next time point was used, this would return the half-period of the wave. This could still be used to calculate the rotational rate, indeed it would provide a 2× increase in time-granularity of the measurement. However, the light from the LED is not laser light (it is not uni-directional) and it shines out from the side of the slot. This causes the square wave to not be uniform, the trough time (the time the gate is closed) to differ significantly from the peak time (time the gate is open). This effect is illustrated on Figure 3.7.

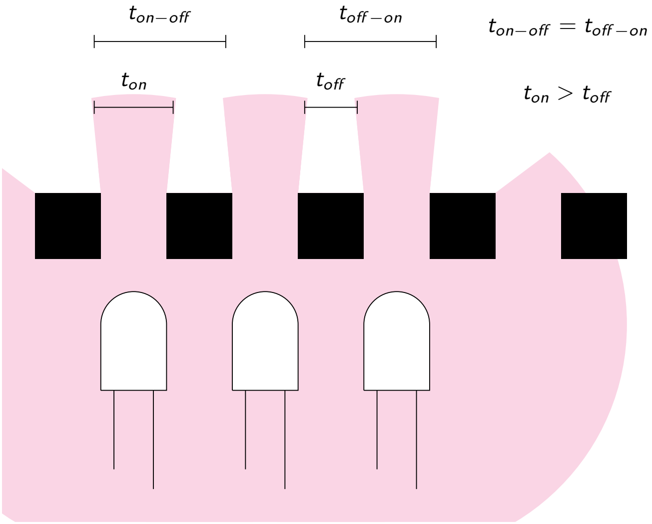

Figure 3.7: *Schematic of variation in time between events, highlighting the difference between measuring intervals between every event, and every other event.*

Due to this effect, the full period is used to calculate angular velocity rather than the half period, as shown on Equation (3.5).

Rationalising timeseries

The optical encoder data at this stage is as error free as possible, and converted to a timeseries of rotation period. There is a timeseries for each sensor and these need to be rationalised together into a single timeseries of angular velocity that is coherent with the other measured timeseries: stress.

This could be achieved by merging the separate timeseries' together, and interpolating from the result with the stress timeseries. If the two encoder series' differ then this will create a noisy result. This can be mitigated by interpolating first, to obtain two timeseries coherent to the stress series, then creating the final single timeseries as an average of the two other signals:

$$\hat{\omega}_{r,i} = \frac{1}{2}\left(\omega_{r,i}^{1\star} + \omega_{r,i}^{2\star}\right) \tag{3.6}$$

where subscript i refers to a sample number i, $\hat{\omega}_r$ is the averaged resulting angular velocity series, and $\omega_r^{1\star}$ and $\omega_r^{2\star}$ are the measured angular velocities of each sensor after interpolation. This method allows a noise reduction in the measured signal without resorting to time averaging. This algorithm is shown by example on Figure 3.8.

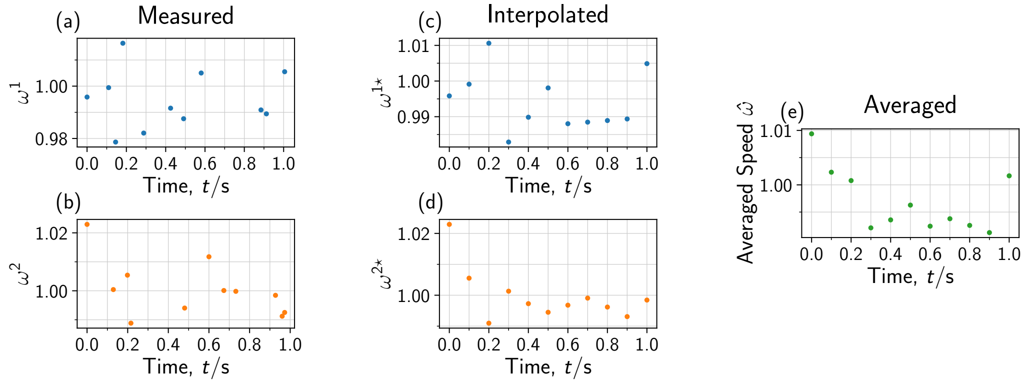

Figure 3.8: *Schematic plots exemplifying the procedure for rationalising the two optical encoder data sets. Plots (a) and (b) show the measured angular velocity signals for the two sensors. Note the signals do not align with the axis grid. Plots (c) and (d) show the same angular velocity signals, after interpolating to align them with the stress timeseries. Note the signals are now aligned with the grid. Finally, plot (e) shows the average between the two signals obtained using Equation* (3.6).

3.4.4 Limitations

Uncertainties Analysis

Uncertainty in speed measurement is difficult to estimate. Angular velocity is calculated by differentiation of angular position. The position “signal” is cleaned in software by removing unreliable data points (as outlined in Section 3.4.3). The uncertainty in the resulting angular velocity can be estimated roughly by making measurements of the percentage relative standard deviation (PRSD) of the speed data of empty rheometer runs, see Figure 3.9. Empty runs are used to preclude fluid interaction from impacting the uncertainty estimate.

The speed is then used to estimate the strain rate by multiplying by radius and dividing by the gap. These two measurements introduce uncertainty (discussed in Section 3.3.3):

$$\begin{aligned}\Sigma^{\%}_{\dot{\gamma}} &= \Sigma^{\%}_{\omega_r} + \Sigma^{\%}_{l_{gap}} + \Sigma^{\%}_{r_{in}} \\ &= 3.9\% + 0.11\% + 0.017\% = 4.03\%\end{aligned}$$

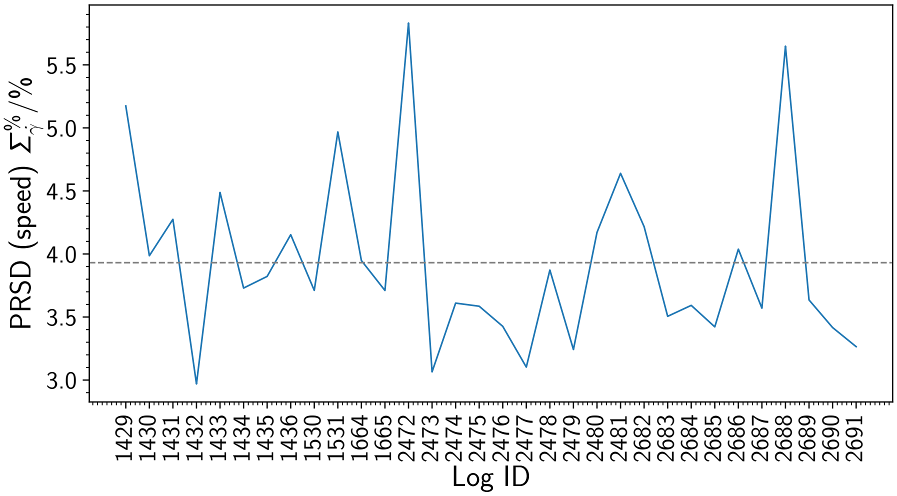

Figure 3.9: *Percentage Relative Standard Deviation (PRSD) measured in the speed signal across 32 logs. Dashed line shows the average PRSD of* 3.9%*.*

The measurement error of 4.03% is significantly less than the variation of strain rate through the gap (see Section 3.4.1). In addition to the measurement error, there is random uncertainty. To estimate this, the standard deviation of strain rate measurements were calculated across repeated runs of the same material at the same motor duty cycle setpoint (see Section 3.6 for description of duty cycle and motor control). This analysis yielded a percentage random error in strain rate of 3.6% across runs of cornstarch suspension (avoiding the **dst** region — the data presented in Chapter 5). As this estimate of random error encompasses the variation due to the equipment (calculated above), but results in a similar value, it can be concluded that random error in strain rate measurement is negligible at least when the **dst** region is avoided.

3.5 Stress Measurement

3.5.1 Purpose

The stress measurement component of the rheometer records the stress developed in the fluid during the induced flow, one of the two main rheological measurements.

3.5.2 Implementation

Stress driving flow comes from the motor via the inner shaft, and depends on the fluid fill depth and the radius of the inner cylinder. Torque from the driving shaft is transmitted to the contact area of fluid, providing stress and shearing the fluid. Equation (3.7) shows this relationship between stress, torque and geometry.

$$\sigma = \frac{M}{2\pi r_{in}^2 H_{fill}} \tag{3.7}$$

where σ is stress at the inner cylinder (Pa), M is torque (N m), r_{in} is inner Couette cylinder radius (m), and H_{fill} is the height of fluid in contact with the rheometer (m).

Torque is measured by first converting the from rotational torque into a vertical force, which can then be measured by a loadcell in a design taking inspiration from in-line torque measurement devices used in bicycles [16], [17] and cars [18]. In addition, the stress sensor design draws from other designs in published work: the designs of F. Dalton *et al.* [19].

A schematic of the sensor is shown on Figure 3.10. The main shaft is split into two: a driving shaft, and a driven shaft. The driving shaft supplies the torque and it connected directly to the motor. The driven shaft connects to the inner cylinder in the Couette where the load torque is developed. The driven shaft is threaded and an annular runner is similarly threaded such that as the driven shaft rotates, the runner moves along the shaft axis. The runner is connected to the driven shaft by steel rods that allow axial movement but not rotation between runner and driving shaft. The result is that any difference in rotation between the driving and driven shaft is expressed as an axial movement of the runner.

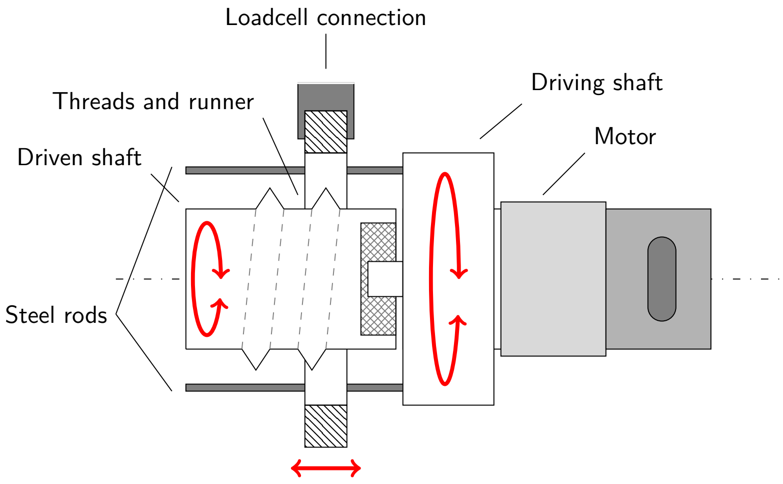

Figure 3.10: *Schematic of torque sensor design. Design takes inspiration from in-line torque measures used in cars [18] and bicycles [16], [17]. Red arrows indicate movement directions.*

The axially-moving runner is attached to a loadcell so that and difference in torque of the driver and driven shafts (*i. e.* the torque load) is translated to a force on the loadcell which can be measured as a voltage by an analogue-to-digital converter (ADC). The connection between (rotating) runner and (stationary) loadcell is facilitated by a bearing into which the runner is built. The driver and driven shafts are connected by an 8mm bearing (Bones China "Reds" skateboard bearings [20]) to reduce friction.

The loadcell is of the type easily available to hobbyists consisting of an aluminium block with a strain gauge attached. The particular loadcell in use is rated to 5 kg (or 49 N), obtained from ebay*. This gives an upper stress limit of $\mathcal{O}\left(10^4\right)$ Pa, calculated using the shear cell geometry in Table 3.1 and Equation (3.7). This stress far outreaches the required stress for the intended investigation into shear thickening of cornstarch (for which the onset stress is $\mathcal{O}(1)$ Pa — see Chapter 4). For this reason, a second loadcell rated to 100 g was obtained†, corresponding to an approximate upper stress limit of $\mathcal{O}\left(10^2\right)$ Pa. This smaller loadcell was better placed to measure stresses around the fluid's onset stress. The loadcell is read from by a loadcell-specific 24 bit ADC (HX711, Avia Semiconductor‡). Figure 3.11 shows the circuit diagram for the loadcell connection to the SBC.

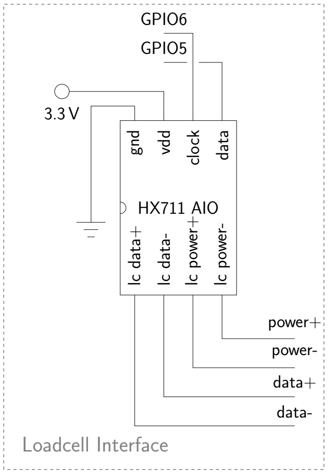

Figure 3.11: *Circuit diagram of loadcell. Loadcell connection is via the HX711 all-in-one (AIO) chip, which includes noise filters and provides an easy interface to the chip.*

---

[*] The exact loadcell used is no longer listed. The same loadcell is available from other sellers but may be from different manufacturers. An example is [21].

[†] Again, the exact loadcell used is no longer listed. The same loadcell is available from other sellers but may be from different manufacturers. An example is [22].

[‡] Similar to the loadcell, the ebay listing is no longer available. A similar product is [23].

The driver shaft, threaded shaft, runner, and runner bearing were designed in FreeCAD software and 3D printed.

3.5.3 Calibration

The calibration's purpose is to fit a model for the mechanical load on the loadcell to measurements of loadcell value and known torque data so that torque measurements can be made. This is done by shearing a fluid of known viscosity in the rheometer, while measuring strain rate and loadcell value. The stress evolved is therefore found using Equation (2.1):

$$\sigma = \mu \dot{\gamma} \tag{2.1 again}$$

The connection between the loadcell value and stress is modelled below. Using the model, the loadcell value can be converted to a torque, and then a stress, by fitting the model parameters to the system.

The data from the stress sensor are recorded as a 24 bit number, indicative of the voltage level measured by the HX711 which, represents the force on the loadcell. The force measurement originates as a torque on the inner cylinder, transferred by threaded cylinder ($F \propto M$). The function transferring torque to loadcell is linear, so torque on the cylinder can be expressed as a simple linear function of the loadcell measurement

$$M_{total} = k_{LC \to M} \left(LC - LC_z \right) \tag{3.8}$$

where M_{total} is the total torque loaded on the driven shaft in N m, $k_{LC \to M}$ (unit N m) is a calibration coefficient converting loadcell number to a torque, and LC_Z is calibration offset in loadcell measurement and is a 24-bit number.

Since torque is conserved, a torque balance over the system can be performed. In the driving direction, torque is provided by the motor only. It is this torque that is measured. Counter to that there is a torque imposed by the fluid by action on the cylinder with which it is in contact as well as any friction in the apparatus:

$$M_{total} = M_{friction} + M_{load} \tag{3.9}$$

where $M_{friction}$ is the component of the torque on the shaft due to friction in the coupling, and M_{load} is the torque on the shaft due to the fluid in the Couette. Both have units of N m.

The torque due to dynamic friction scales with angular velocity:

$$M_{friction} = k_{\omega_r \to M} \omega_r \tag{3.10}$$

where $k_{\omega_r \to M}$ is a coefficient converting angular velocity to dynamic friction torque, with units of $\mathrm{N\,m\,s\,rad^{-1}}$, the quantification of which will be discussed shortly.

Protocol

Several mixtures of glycerol and water were prepared as a set of Newtonian fluids with different viscosities. Solution names, compositions, and expected viscosity are shown on Table 3.2. Expected viscosity for the glycerol solutions were found using the expression (fit to tabulated data) of Cheng [24]. These fluids were sheared in the rheometer at varying strain rates while loadcell measurement LC and strain rate $\dot{\gamma}$ were recorded.

Table 3.2: *Mixture compositions and expected viscosity used in the calibration. Materials are discussed further in Chapter 4.*

Material	**Percentage Glycerol**	**Expected Viscosity** Pa s, at 20°C
G0999	99.99 wt%	1.314 Pa s
G95:W05	95 wt%, rest water	0.485 Pa s
G85:W15	85 wt%, rest water	0.105 Pa s

Motor supply voltage is altered to change the rate of rotation, with no actual control in place. This is discussed in Section 3.6. For a particular supply voltage, the fluid is sheared at a single rate as it is Newtonian. By changing the supply voltage, different angular velocities (strain rates) are obtained. In this manner a strain rate sweep can be achieved.

The materials were sheared at each strain rate (each voltage) for 3 minutes before stopping, and restarting at the next strain rate (voltage). During a run, temperature, strain rate, angular velocity, and raw loadcell (24-bit) are measured. After the sweep of voltages, the shear cell was emptied and refilled with fresh fluid and the set of runs repeated.

The shear data is used to find the fitting parameters $k_{LC \to M}$, $k_{\omega_r \to M}$, and LC_Z. By using tabulated data [24] and measured temperature, the viscosity of the fluids are known. Measured strain rate was used to obtain a value for the expected stress by multiplying with viscosity, $\sigma = \mu\dot{\gamma}$. Guess values are provided for the fitting parameters. A guess stress is calculated using Equations (3.8) to (3.10). Error in the guess is calculated as the sum of the square differences between the guess stress and the expected stress. Optimising for least error yields a set of calibration parameters.

Results

Resulting parameters for the fit for each loadcell are summarised on Table 3.3. The values of parameter $k_{\omega\to M}$, the dynamic friction factor converting angular velocity to a torque, should be the same for each loadcell as this depends on the linkage between loadcell and motor only. The parameter is similar between the two loadcells, being approximately twice the value for the 100 g loadcell as for the 5 kg loadcell. The errors presented on Table 3.3 are not exhaustive and are only resulting from the fit: complete measurement uncertainty is discussed later in Section 3.5.5 The calibration results are assessed by plotting measured (calibrated) stress and viscosity and comparing to expectation from literature. These plots are shown on Figure 3.12.

Table 3.3: *Summary of calibration results.*

Parameter	Value	Unit	Percentage Error
Loadcell 1, rated to 5 kg			
LC_z	$2,147,401,064$	—	$3.58 \times 10^{-5}\%$
$k_{LC\to M}$	1.320×10^{-7}	Nm	2.41%
$k_{\omega_r\to M}$	9.63×10^{-5}	$\mathrm{N\,m\,s\,rad^{-1}}$	23.15%
Loadcell 2, rated to 100 g			
LC_z	$2,148,329,623$	—	$1.88 \times 10^{-3}\%$
$k_{LC\to M}$	2.63×10^{-9}	Nm	3.17%
$k_{\omega_r\to M}$	1.90×10^{-4}	$\mathrm{N\,m\,s\,rad^{-1}}$	14.27%

The calibration results shown on Figure 3.12 are plots of measured viscosity (filled circles) against strain rate, in comparison to expectation (dashed lines). Also plotted are stresses on the same x-axis. In general the fit is good. The viscosity measurements are around that expected, the stress lines are increasing with rate at a constant gradient. However, there is a not insignificant scatter, especially for the higher viscosity

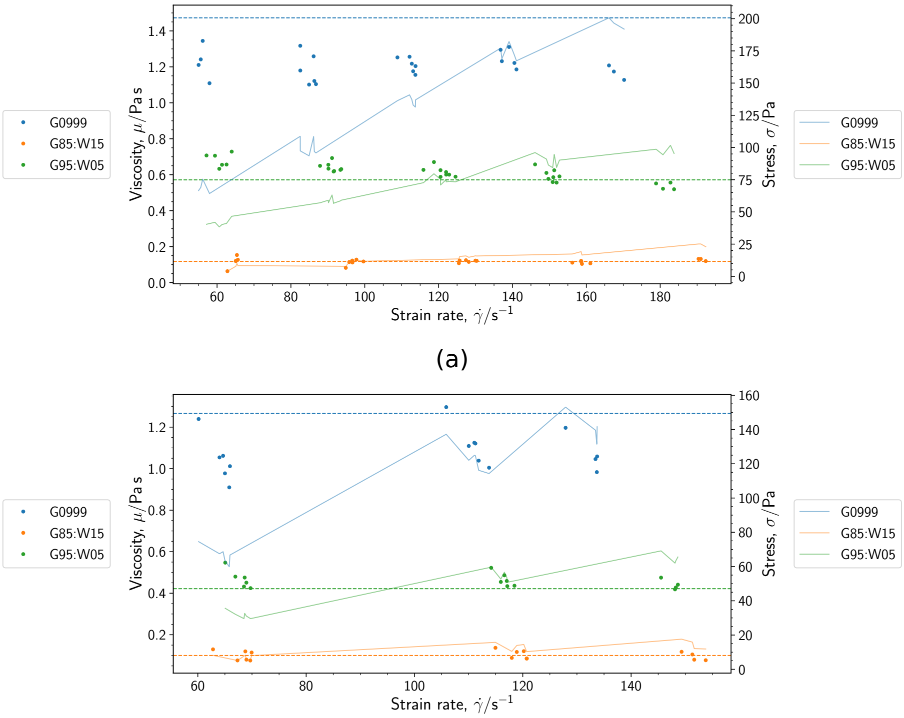

(a)

(b)

Figure 3.12: *Calibration results for **(a)** Loadcell 1 and **(b)** Loadcell 2. Plot showing expected viscosities (dashed lines) and the measured viscosities obtained using the optimization (coloured circles). Faint solid lines show the stresses. Colours indicate material as in legend (notation described in Section 4.2.1). The expected viscosity is obtained using correlation of Cheng [24] as outlined in Chapter 4. The stress lines show an apparent drop in viscosity — this is only due to scatter in the results, accounted for in Section 3.5.5*

glycerol runs (in blue).

Part of the spread could be attributed to possible water ingress. Glycerol's viscosity is highly sensitive to the presence of water. Care was taken to ensure the glycerol is kept dry, but even atmospheric water can be taken into the glycerol due to its hygroscopic nature. However this is unlikely the cause due to the amounts of water required to alter the rheology (discussed in Section 4.2.1). A more likely cause is due to differences in initial loading can create an erroneously high stress measurement — due to increased friction in the force transmission. The lower two compositions tend to have lower scatter than the pure glycerol run. In addition, the scatter increases when the rate is lower — indicating perhaps the scatter is due to the increase in stress measurement scatter with decreasing rate.

3.5.4 Data Processing

Data are recorded from the ADC as a 24-bit number. This number is converted to a torque using the calibration coefficients Table 3.3, and Equations (3.8) to (3.10). Torque is them converted to stress using Equation (3.7) and the geometry (Table 3.1) with the specific fill depth H_{fill} used in the run.

3.5.5 Limitations

Sensitivity and Range

The relationship between loadcell force measurement and stress can be estimated by tracing its route from the loadcell to the cylinder. The loadcell is connected to the cylinder by an arm connected to the screw: the torque on the screw (radius $r_s = r_{in}$) is converted to a force on the arm.

$$F_{arm} = \frac{M_{screw}}{r_{in}} \tag{3.11}$$

The stress on the cylinder is converted to a torque by action on the wetted area A of the cylinder.

$$M_{cyl} = A\sigma \tag{3.12}$$

$$= 2\pi r_{in}^2 H_{fill}\sigma \tag{3.13}$$

Bringing Equations (3.11) and (3.12) together gives the approximate relationship between force and stress:

$$F \approx 2\pi\sigma H_{fill} r_{in}$$

$$\sigma \approx \frac{F - F_{friction}}{2\pi H_{fill} r_{in}} \tag{3.14}$$

where $F_{friction}$ is force due to connection between cylinder and loadcell.

Two loadcells were used over the course of the project with different operating ranges. The first (misc loadcell, eBay) had an upper sensing limit of $5kg$. The maximum measurement is obtained at minimum fill $H_{fill,\mathrm{min}} = 0.05\,\mathrm{m}$ giving a maximum measurable stress of:

$$\sigma_{\mathrm{max}}^{5\,\mathrm{kg}} = \frac{5 \times 9.81}{2 \times \pi \times 0.05 \times 0.01505} = 15\,\mathrm{kPa}$$

This loadcell's high upper limit gave it the ability to withstand any force any suspension threw at it; however with such a range range came poor sensitivity: low end of the scale is marked by an increase in measurement scatter below $\sim 20\,\mathrm{Pa}$ — taken as an estimate for the lower limit of this loadcell. The lower limit of a loadcell can be expressed as a percentage of the upper limit:

$$\sigma_{\mathrm{min}}^{5\,\mathrm{kg}} = \frac{20}{15000}\Sigma_{\mathrm{max}}^{5\,\mathrm{kg}} = 0.\overline{33}\%\Sigma_{\mathrm{max}}^{5\,\mathrm{kg}}$$

The latter loadcell (misc loadcell, eBay) used in this project has a much lower 100 g maximum loading which corresponds to a lower maximum stress measurement:

$$\sigma_{\mathrm{max}}^{100\,\mathrm{g}} = \frac{0.1 \times 9.81}{2 \times \pi \times 0.05 \times 0.01505} = 300\,\mathrm{Pa}$$

The low sensing range gave much higher sensitivity at low stress. The percentage estimate for sensing range lower bound of this loadcell is assumed to be the same as for the first: $0.\overline{33}\%$. Using this assumption, the lower sensing limit for this loadcell is calculated by:

$$\sigma_{\mathrm{min}}^{100\,\mathrm{g}} = 0.\overline{33}\%\Sigma_{\mathrm{max}}^{100\,\mathrm{g}} = 1\,\mathrm{Pa}$$

Sample rate

Unfortunately the interfacing hardware (specifically the HX711 ADC) is limited to a sample rate of at most $80\,\mathrm{s}^{-1}$ [25]: less than the optical encoder's sample rate of $\sim 1000\,\mathrm{s}^{-1}$. In order to plot use data from each sensor together it is required to either interpolate the stress signal, or reduce the sample rate of the encoder (possibly by time averaging). In order to preserve the higher time-resolution data from the optical encoder the former was done: first in first interpolation between stress measurements was done and subsequently the interpolated stress values were divided by the strain rate to give a viscosity.

Friction pre-loading

The torque transmission section of the stress measurement relies on there being little friction in the transmission. Some losses are included in the calculation — mainly dynamic friction in the bearing. Static friction is included in the linear fit (hidden inside the constant LC_z). However, static friction depends on how tightly the components are held together and how well lubricated they are. Unfortunately, the static friction can change between runs, noticed especially between changes in motor. This was mitigated by cleaning and lubricating the components frequently, however there were still runs taken with the erroneous stress measurement. These aberrant measurements are in the minority. The effect can be seen in results shown in Chapter 5.

Uncertainty Analysis

The calibration process fits parameters to a linear function transforming loadcell to load torque. Then stress is calculated from torque using geometric measurements. The uncertainty in the calibrated function is three-fold: there is the fitting uncertainty (totals 25.56% and 17.44% for the 5 kg and 100 g loadcells respectively, Table 3.3), and the uncertainty in both the empirical data (2.3% [24]) and speed measurement (3.9%, Section 3.4.4), to which the fit is performed:

$$\begin{aligned}\Sigma^{\%}_{M_l} &= \Sigma^{\%}_{fit} + \Sigma^{\%}_{\omega_r} + \Sigma^{\%}_{\mu,empirical}\\ 5\,\mathrm{kg\ loadcell}: &\\ \Sigma^{\%}_{M_l,5\,\mathrm{kg}} &= 25.56\% + 3.9\% + 2.3\% = 31.76\%\\ 100\,\mathrm{g\ loadcell}: &\\ \Sigma^{\%}_{M_l,100\,\mathrm{g}} &= 17.44\% + 3.9\% + 2.3\% = 23.64\%\end{aligned}$$

Then the uncertainty (measurement error) in stress has the addition of uncertainty in the geometric measurements (Section 3.3.3):

$$\begin{aligned}\Sigma^{\%}_{\sigma} &= \Sigma^{\%}_{M_l} + 2\Sigma^{\%}_{r_{in}} + \Sigma^{\%}_{H}\\ 5\,\mathrm{kg\ loadcell}: &\\ \Sigma^{\%}_{\sigma,5\,\mathrm{kg}} &= 31.76\% + 2\times 0.0166\% + 2\% = 33.79\%\\ 100\,\mathrm{g\ loadcell}: &\\ \Sigma^{\%}_{\sigma,100\,\mathrm{g}} &= 23.64\% + 2\times 0.0166\% + 2\% = 25.67\%\end{aligned}$$

To check how well this estimate is, the average PRSD can be found from measurements of stress in Newtonian fluids — a similar procedure to that performed in Section 3.4.4 to estimate uncertainty in speed measurement. The resulting PRSDs are plotted for each log on Figure 3.13 which shows the average PRSD is around one-third of the estimated error. The larger estimate of uncertainty will be reported throughout.

In addition to the measurement error calculated above, uncertainty in the reported stress will include some random error (due to unaccounted for or unexpected changes in materials,). To estimate this, the standard deviation of stress measurements were

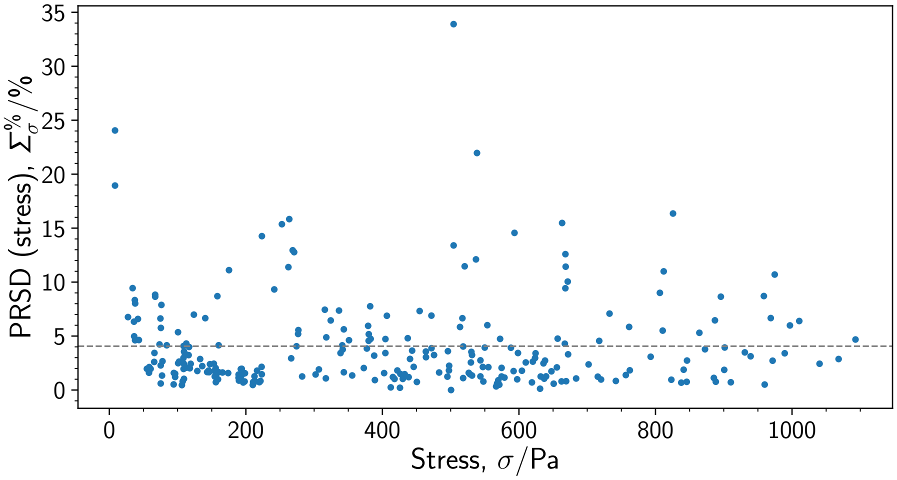

Figure 3.13: *Percentage Relative Standard Deviation (PRSD) plotted for logged runs of Newtonian fluids (glycerol, glycerol* 95wt% *and water, and glycerol* 85wt% *and water). Dashed grey line denotes the average value of approx.* 4%*, however there are large swings up to above* 100%*. This is likely an impact of the fluid on the measurement.*

calculated across repeated runs of the same material at the same motor duty cycle setpoint (see next section, Section 3.6, for description of duty cycle and motor control). This analysis yielded a percentage random error in stress of 36.2% across runs of cornstarch suspension (avoiding the **dst** region — the data presented in Chapter 5). As this estimate of random error encompasses the variation due to the equipment (calculated above), but results in a similar value, it can be concluded that random error in stress measurement is negligible.

3.6 Motor Control

3.6.1 Purpose

The shear flow in the cell is driven by rotating the inner cylinder with an electric motor. The rate and torque with which the shaft is rotated is directly related to the efficacy of the rheometer. Stress or strain rate should be controlled throughout a rheometer run, this is achieved by controlling the rate or torque output of the motor.

3.6.2 Implementation

A DC motor [26] consists of coils of wire and some permanent magnets so that a current through the coils creates a magnetic field pushing against the permanent magnets and rotation as a result. The rate of rotation depends on the size of the induced magnetic field and the load (torque) of the motor. For a specified power, there is an inverse relationship between angular velocity ω_r and torque output M for a DC motor, stemming from an energy balance over the motor:

$$M = \frac{1}{\omega_r}\eta(I_{ms}, V_{ms})I_{ms}V_{ms} \tag{3.15}$$

where I_{ms} is the current drawn by the motor in A, V_{ms} is the voltage supplied to the motor in V, and $\eta(I_{ms}, V_{ms})$ is the motor efficiency at the supply voltage and current.

A motor can be characterised by two numbers [27]: the angular velocity with which it rotates with when unloaded, the “no-load speed” [28], [29] ($\omega_{r,NL}$), and the torque at which the motor stalls, the “stall torque” (M_{stall}), both at design-nominal supply voltage. These define the motor characteristic curve and describe the relationship between angular velocity and torque. For a particular voltage, a straight line approximately joins the two parameters on the plot of rotation rate against torque. As voltage increases the line moves up, and as it decreases, the line moves down. A schematic motor characteristic curve is plotted on Figure 3.14.

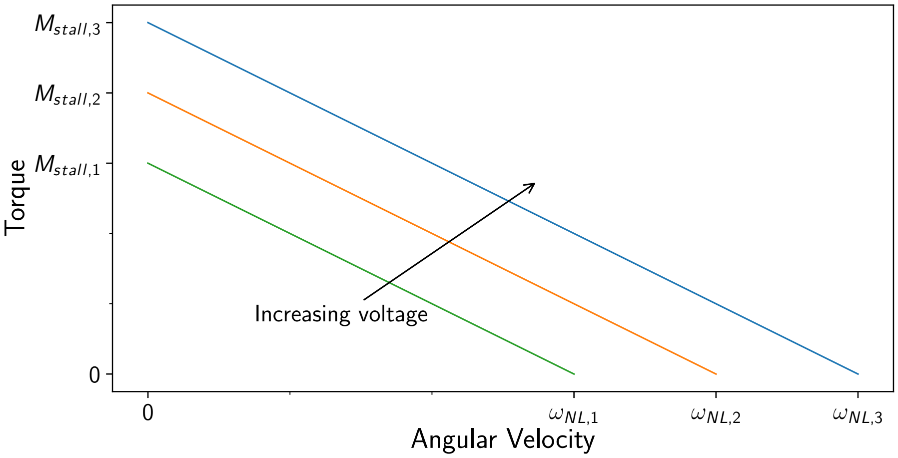

Figure 3.14: *Sketch of a typical motor characteristic curve.*

DC motors operate better when rotated quickly; tending to stall or stutter at low rotation rate due to the amount and position of the permanent magnets used to drive motion. To obtain a low frequency rotation, a gear system is used. A gear ratio G_{12}

is the ratio of number of teeth on connected gears $\left(\frac{n_2}{n_1}\right)$ in a gear train. Gear ratios decide the resulting rate and torque of the system according to:

$$\frac{\omega_{r,1}}{\omega_{r,2}} = \frac{M_2}{M_1} = \frac{n_2}{n_1} = G_{12} \tag{3.16}$$

A gear box, in combination with electronic control (see Figure 3.15), allows a DC motor to cover a wide range of rotation rates and output torques.

Motor rotation speed is affected by two factors:

- the load upon the motor, and
- the voltage supplied to the motor.

Load on the motor depends on amount and composition of the fluid, and for non-Newtonian fluids, the strain rate as well. At steady state (where possible — barring fluctuations in rate or stress in time), the rotation rate of the motor is set only by supply voltage. Motor supply voltage is set per-run, using Pulse Width Modulation (PWM) [30]. The motor is supplied with a voltage as high-frequency square wave, the rate of rotation is decided by the ratio of peaks to troughs in the wave; a ratio called the Duty Cycle (DC; typically a unitless fraction, or expressed as a percentage), with rate directly proportional to DC. PWM has several advantages over pure voltage control: the voltage supplied to the motor is always high so motor stall is mitigated, motor efficiency is not constant over the range of voltages it can operate under and so very low or very high voltages may cause unexpected variation in resulting speed or torque output.

Over the course of the development of the hardware, three motors were trialled to obtain the best possible range of strain rates and stresses for the rheological investigation.

The last motor was used for the vast majority of measurements, however some glycerol-water (Newtonian) measurements were made with the first motor (“ORIG”). The main difference between the motors are in fact the attached gear boxes, which change up the available speed ranges. The third trialled motor was used with several different gearboxes. Each motor and gearbox combination was named chronologically from “FIRST” up to “SEVENTH” [§]. A summary of the motors is included in Table 3.4.

[§] There is a gap in the naming scheme; the second motor was used in several runs but runs obtained with it do not reach adequate strain rates — the naming scheme is preserved to maintain parity with the underlying database of results.

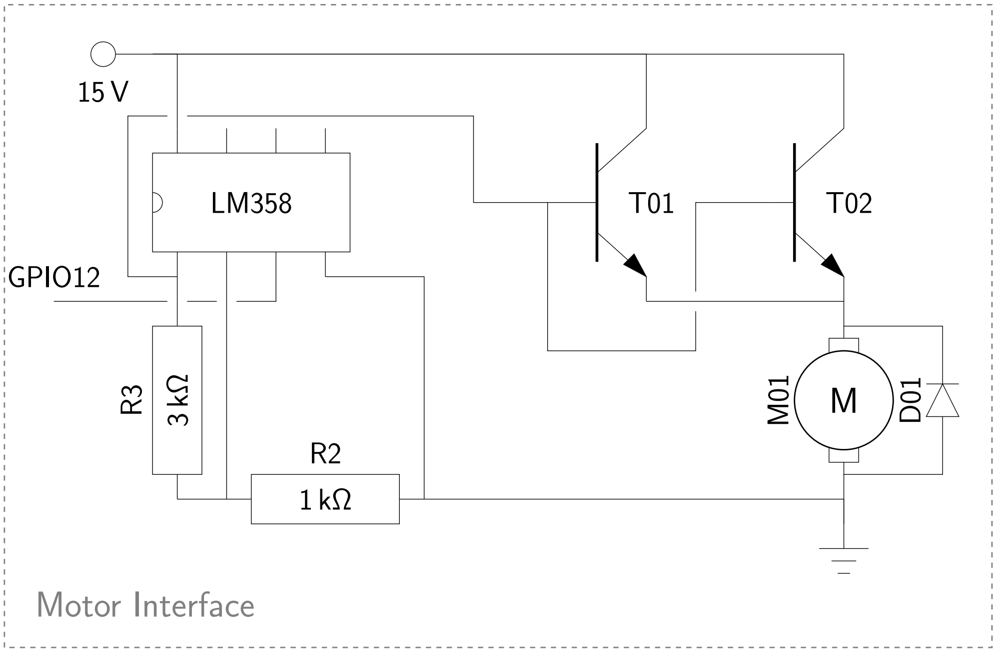

Figure 3.15: *Circuit diagrams for the motor supply voltage control system.*

There are some important advantages to the voltage supply methodology shown in Figure 3.15; if there is no actual control mechanical happening, there can be no interference by the control system with the response of the fluid. This is especially important for investigation of unstable or time dependent flows. Secondly, this simple control scheme is much less error prone: there is no input variable, there is no measured noise (to affect the control method), there is no time delay and competing time constants. This “control” method results in a measured signal that results mostly due to the fluid’s action on the apparatus, without controller action to confuse matters. The addition of an explicit control system is discussed in Appendix C.

3.6.3 Limitations

A motor have maximum speeds and torques as per their characteristic curves. The reasonable limits for a motor’s operation are slightly below the maximum values (a motor running under no load is doing no work; a motor running under maximum load is not moving). A motor is also limited by the voltage and current it draws. The circuit which powers the motor is limited to 15V and 6A, and so the motors are too. The limiting speeds and torques of the motors are affected by loading and supply voltage, so while limits could be calculated from the characteristic curve, they are more usefully

Table 3.4: *Table of Motors showing characteristics and gear ratios*

Name	**Model and Manufacturer**	**Gear Ratio**
FIRST	238–9759, RS Components	Unkn.
THIRD	942D, RS Components	27:1,
FOURTH	942D, RS Components	264:1
FIFTH	942D, RS Components	51:1
SIXTH	942D, RS Components	100:1
SEVENTH	942D, RS Components	516:1

measured.

3.7 Temperature sensor

3.7.1 Purpose

Viscosity is often dependent on temperature. This parameter is controlled in most commercial rheometers, but for this design it was deemed sufficient to measure temperature. This is to take into account any shear-heating, rather than erroneously identifying shear-thinning as a result.

3.7.2 Implementation

Temperature is measured by a thermocouple attached to the outside of the outer cylinder. The thermocouple is “type K” (NiCr) and has a measurement range of $-40\,°C$ to $1000\,°C$ and accuracy $\pm 1.5\,°C$ or 0.4% of the measurement (whichever is greater) [31], [32]. The thermocouple is taped as tightly as possible to the glass cylinder to facilitate heat transfer to the probe and correct temperature readings. The heat transfer from the fluid inside the cylinder through the glass to the thermocouple is assumed to be fast in comparison to the length of the experiment, and the steady state temperature difference between the fluid and outside wall is assumed to be negligible — see calculation in Appendix G for details. Thermocouple is measured with the aid of an interface board (MikroE-2501, RS Components) which uses an MCP9600 chip, containing the ADC which converts the thermocouple voltage to 16-bit signal transferable to the SBC by serial (I^2C) interface, where it is converted to temperature in °C. Despite having 16 bits available to store information down to a sensitivity of ± 0.0624°C, the MCP only has conversion accuracy to $\pm 0.25°C$ [33], therefore this is the minimum increment for temperature measurement available using this hardware.

Two further temperature probes are used to monitor the ambient temperature, to allow the shear heating effect to be measured. These ambient temperature probes are both DS18B20 (Maxim integrated) and are slow to measure ($\sim$ 750ms) making them better suited to ambient measurement, which is not expected to change rapidly. The ambient sensors are interfaced using a 1-wire interface, a high level interface which reports temperature in °C. The logged ambient temperature data is the average of the two ambient sensors.

Circuit diagram

The temperature system requires only a small supporting circuit (Figure 3.16) to interface with the SBC due to the use of all-in-one (AIO) components containing noise reduction and conversion circuitry.

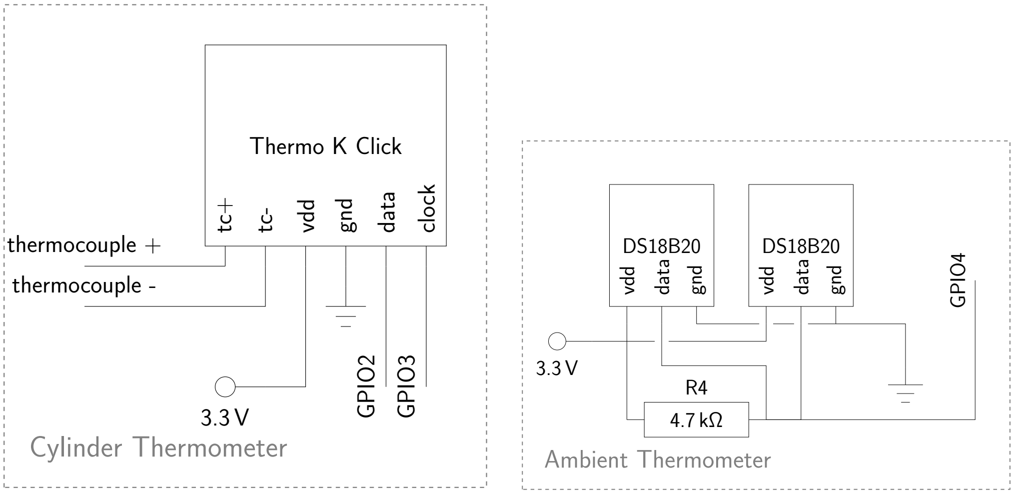

(a) (b)

Figure 3.16: *Circuit diagrams for the cylinder thermometer (a) and ambient thermometer (b).*

3.7.3 Limitations

The main limitation of the temperature measurement system is the low sample rate of the ambient sensor, which records once a second. This is not a huge problem for the system as the ambient temperature is not expected to change at all over the course of a run, and if it did it would change slow enough to be captured sufficiently.

3.8 Piezoelectric Needle Device (PND)

3.8.1 Purpose

The Piezoelectric Needle Device (PND) was conceived by Forsyth [34] to gain further insight into jamming fluids. It is used to get a picture of instantaneous, local, flow conditions in a sheared sample of jamming suspension.

This sensor should:

- indicate flow properties (rheology: stress and/or strain rate) within the cell,
- in a localised manner, and
- not affect the flow within the cell **or** affect it in a way that can be accounted for.

3.8.2 Implementation

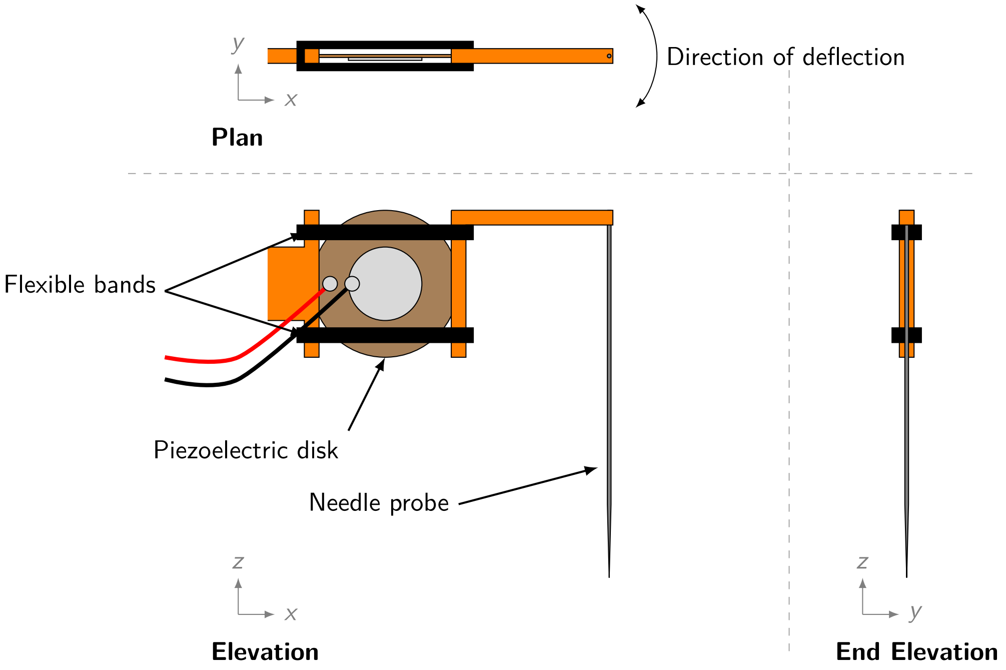

Figure 3.17: *Schematic of PND construction.*

The PND consists of a sewing needle attached to an arm, in turn attached to a piezoelectric disk. This set up is mounted on an articulated arm on the custom Couette rheometer (mounted on to the clamp stand forming the base of the rheometer). The articulation is achieved by 3D printed beams screwed together — the screws can be relaxed to allow movement and tightened to fix the PND position. The needle can then be set so the tip sits below the surface of a fluid and stress can be transmitted by the fluid to the needle, which moves and in-turn strains the sensor and registers a voltage on the disk. Thus recording local stresses within the fluid.

This contrasts with Forsyth's original design where a needle probe is attached separate from the piezoelectric disk such that fluid viscosity perturbation would cause the probe to hit the disk. The design used in this work was used to simplify the process and to be able to better quantify the PND signal. A schematic of the design used is shown on Figure 3.17.

The piezoelectric effect transforms a strain into a voltage [35]. The relationship between the magnitudes of strain and voltage is given by[¶]:

$$V = \frac{d_{y,yx} A_c}{C} \varepsilon_{yx} \tag{3.17}$$

where $d_{y,yx}$ is a coefficient describing the piezoelectric effect, A_c is the area of the crystal, C is the capacitance, and ε_{yx} is the strain.

To observe the characteristic peak-and-overshoot response of the piezoelectric disk, it was tapped manually at a steady rate while the voltage across the piezoelectric disk is measured and recorded. The result is shown on Figure 3.18.

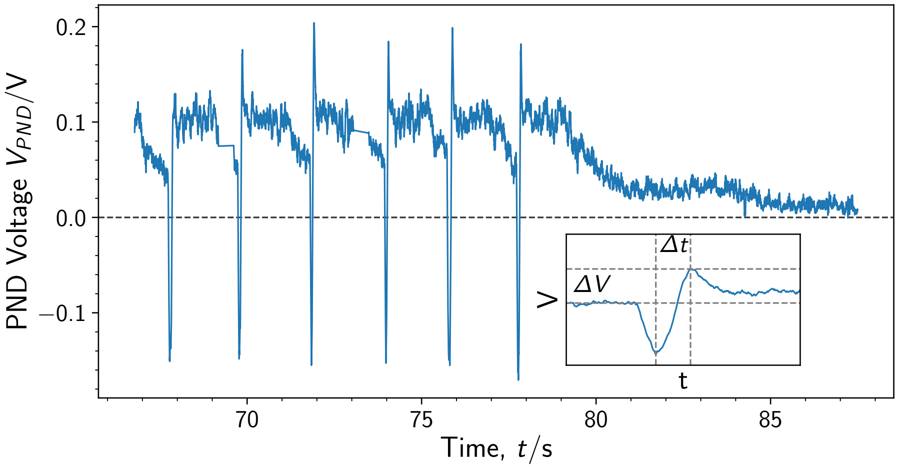

Figure 3.18: *Plot of voltage across a piezoelectric crystal against time during tapping (up to* 78 s*) and after tapping subsides. This shows the characteristic response of the PND. Inset shows detail of the peak-overshoot event.* Δt *is the loading time of the event, and* ΔV *the change in output voltage due to charge leakage.*

This voltage is recorded by ADC (MCP3208, RS Components). Due to the overshoot in response, there is significant information in both positive and negative parts of the signal, which cannot be picked up by a single ADC channel alone. The signal is split into positive and negative channels using two half-wave rectifier diode arrangements (Figure 3.19). The resulting two channels are fed to channels 1 and 2 of the ADC, where the voltage can be measured by the SBC. Large measurement resistance (in

---

[¶] See Appendix A for more discussion of piezoelectricity.

the ADC) and shielded cabling is used to reduce the charge leak and thus overshoot, but it persists.

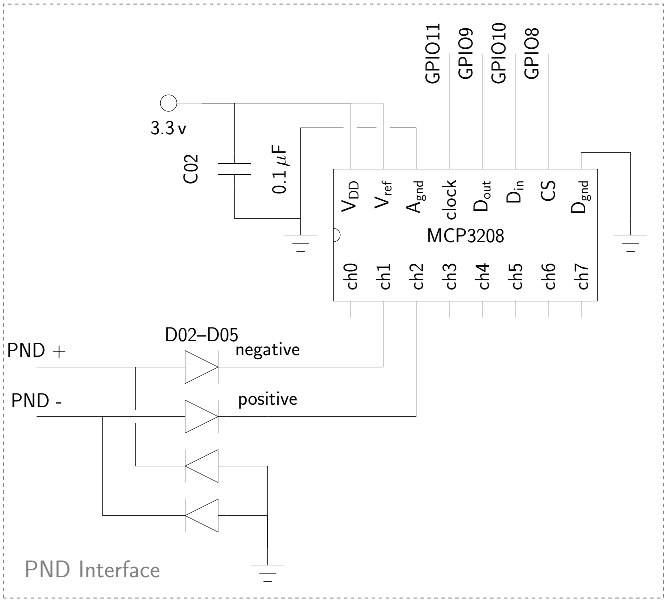

Figure 3.19: *Circuit diagram of PND interface.*

3.8.3 Data Processing

Recombination of the channels is simple:

$$V_{PND} = V_{PND}^{+ve} - V_{PND}^{-ve} \tag{3.18}$$

where V_{PND} is the signed (positive and negative) voltage measured by the ADC from the PND, and V_{PND}^{+ve} and V_{PND}^{-ve} are, respectively, the individual positive and negative channels.

3.8.4 Limitations

Noise Interference

As the piezoelectric disk is essentially a microphone, there is the possibility of picking up unrelated data — noise — from the sounds in the lab. A large source of sonic noise is the motor which makes a loud, high-pitched whirring sound. In addition, vibration produced by the motor could similarly be picked up as it moves through the clamp stand which holds both the shear cell and the PND apparatus.

To estimate the latter source of noise, the PND was suspended from the ceiling during a logging run in the rheometer and compared to a run with the PND in its usual place, but with no fluid thus isolating the effect of noise, and of noise in combination with vibration transferred through the supporting structure. The resulting timeseries of PND voltage, and Fourier transform of same, are shown on Figure 3.20.

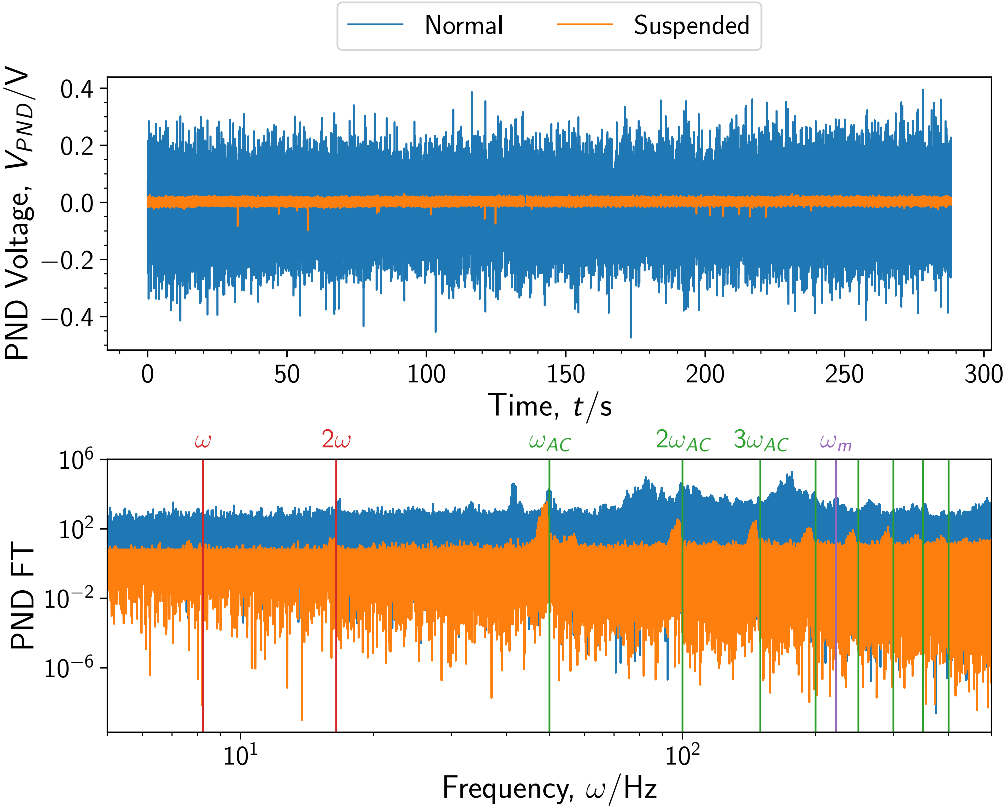

Figure 3.20: *Timeseries and Fourier transform plots of PND voltage, comparing unattached PND suspended in air to attached PND..*

The PND suspension results show a dramatic increase in noise magnitude on the timeseries plots between the suspended (orange) and non-suspended (i.e. normally attached, blue) runs. The Fourier transform plots give an indication of what noise sources are creating the remaining noise in the suspended run. There is a peak at 50 Hz and its integer multiples suggesting that the noise comes from AC interference. In the non-suspended runs the noise is of much higher power, dwarfing the timeseries and even the Fourier plots. This suggests that little to no sound (travelling through the air) is picked up by the PND, but vibration (travelling through the metal frame) is picked up.

In the non-suspended Fourier plot, it is difficult to pick out many known peaks. There is a slight peak at AC frequency (marked in green), but not any reflections at integer multiples. There is a hint of another peak at the motor rotation frequency ($\omega_m = \omega \times N_{gear}$, picked out in purple).

There is a wide spectrum of peaks from 70 Hz up to just under 200 Hz. These are plausibly vibrations from the motor and gearing. The gearing in the motor has unknown intermediate stages, which could lead to peaks at other multiples of the rotation rate. One frequency we can guess is the rotation rate of the motor (ω_m), not the gearbox output (ω), by dividing by the gear ratio. The intermediate frequencies, between motor and shaft rates, may come from intermediate stages in the gearing and could be spread out by mechanical interference as it travels through the structure to the sensor.

Dynamic response v Static response

The response from a piezoelectric device to an step of strain (from rest to a value and held) is shown on Figure 3.18. Note the sharp spike down as the sensor is impulsed, then the overshoot back up and slow decay. The magnitude of the initial spike is related to the magnitude of the strain. The decay means the piezo is not suited to slow-moving signal measurement; it is best suited to high frequency measurement [35].

The overshoot is due to charge leaking from the crystal [36]. If a strain on the crystal charges it to 10 coulomb, while strained 2 C leaks (leaving a charge of 8 coulombs), the removal of the strain will result in a -10 coulomb change in charge. This takes the charge on the crystal to $8-10=-2$ C and is seen as an overshoot.

This makes the PND most suitable for very high frequency measurement. Piezoelectric disks are typically used as microphones as the relatively high-frequency signal (sound) is easy for it to pick up. However, slow-moving signals will present with much noise.

For this use, as a probe within a sheared suspension, the rotation rate of the cylinder in the shear cell will impact the noise in the PND measurement. Slow rotation rates will result in more decay-overshoot in the measurement. This is not noise, however, but potentially useful information. The time between a loading peak and its overshoot informs how long the strain was placed on the crystal. If the decay time constant of the crystal is known, then the duration of the response can be estimated knowing the peak and overshoot magnitudes. If an overshoot appears in an otherwise Gaussian-noisy signal then it is an indicator that a long-duration strain was placed and removed from the needle.

Needle size

The needle takes up a significant portion of the shear cell gap (1 mm in a gap of 4 mm), limiting the number of possible positions. If the needle is placed near the wall as opposed to a central position, then the needle tends to “hug” the wall and not move with the fluid as desired. This effect is seen especially for tests of high concentration suspensions ($\phi > 30\%$).

3.9 Summary

In this chapter the design of the custom rheometer is detailed, including the construction and limitations of each design component. The custom rheometer will be assessed further in Chapter 5. Usage of the custom rheometer is described in Chapter 4. Further detail on related topics are included in the Appendices: piezoelectricity (Appendix A), 3D printing (Appendix B), PI control (Appendix C), and a summary of electronics (Appendix D). Using similar design principles a syringe pump rheometer was design along the course of this project (more information in Appendix F), used in a related PhD project [37].

References

[1] J. Harris, *Rheology and non-Newtonian flow*. Longman, 1977.

[2] “Discovery hr 10,” TA Instruments. (2021), [Online]. Available: `https://www.tainstruments.com/hr-10/` (visited on 07/26/2021).

[3] “Haake mars iq rotational viscometer,” Thermo Fischer. (2021), [Online]. Available: `https://www.thermofisher.com/order/catalog/product/379-0700?icid=MSD_SPEC_MP_379-0700_rheometers-viscometers_0619#/379-0700?icid=MSD_SPEC_MP_379-0700_rheometers-viscometers_0619` (visited on 07/26/2021).

[4] "Haake caber 1," Thermo Fischer. (2021), [Online]. Available: https://www.thermofisher.com/document-connect/document-connect.html?url=https%3A%2F%2Fassets.thermofisher.com%2FTFS-Assets%2FCAD%2FSpecification-Sheets%2FD11476~.pdf&title=U3BlY2lmaWNhdGlvbiBTaGVldDogSEFBS0UgQ2FCRVIgMQ== (visited on 07/26/2021).

[5] C. E. Owens, A. J. Hart, and G. H. McKinley, "Improved rheometry of yield stress fluids using bespoke fractal 3d printed vanes," *Journal of Rheology*, vol. 64, no. 3, pp. 643–662, 2020.

[6] "Rheometer designs." (2021), [Online]. Available: https://www.github.com/cbosoft/rheometer_designs (visited on 04/01/2021).

[7] "Rheometer." (2021), [Online]. Available: https://www.github.com/cbosoft/rheometer (visited on 04/01/2021).

[8] "Raspberry Pi 3 Model B+," Raspberry Pi Foundation. (2021), [Online]. Available: https://www.raspberrypi.org/products/raspberry-pi-3-model-b-plus/ (visited on 06/13/2021).

[9] "Getting started with raspberry pi." (2021), [Online]. Available: https://projects.raspberrypi.org/en/projects/raspberry-pi-getting-started/2 (visited on 04/01/2021).

[10] C. F. Ferraris and N. S. Martys, "Concrete rheometers," in *Understanding the Rheology of Concrete*, Woodhead Publishing, 2012, pp. 63–82.

[11] R. J. Donnelly, "Taylor–couette flow: The early days," *Phys. Today*, vol. 44, no. 11, pp. 32–39, 1991.

[12] F. M. White, "Fluid mechanics," 2009.

[13] G. I. Taylor, "Stability of a viscous liquid contained between two rotating cylinders," *Philosophical Transactions of the Royal Society of London. Series A. Containing Papers of a Mathematical or Physical Character.*, vol. 223, pp. 289–343, 1923.

[14] D. Ting, *Basics of engineering turbulence*. Academic Press, 2016.

[15] M. C. Wendl, "General solution for the couette flow profile," *Physical Review E*, vol. 60, no. 5, p. 6192, 1999.

[16] S. Li, "Torque detection device," US6263992B1, 1999.

[17] T. Boudet, "Torque meter device for a cycle," US9354129B2, 2012.

[18] J. R. Sobel, J. Jeremiasson, and C. Wallin, “Instantaneous crankshaft torque measurement in cars,” *SAE transactions*, pp. 147–155, 1996.

[19] F. Dalton and D. Corcoran, “Self-organized criticality in a sheared granular stick-slip system,” *Physical Review E*, vol. 63, p. 061 312, 2001.

[20] “Bones china reds bearings.” (2021), [Online]. Available: https://www.amazon.co.uk/Bones-Reds-Precision-Skate-Bearings/dp/B000FDRQ1S/ref=sr_1_1?crid=2C3AAX2WONVWK&dchild=1&keywords=bones+reds+bearings&qid=1617299252&sprefix=bones%5C%2Caps%5C%2C194&sr=8-1 (visited on 04/01/2021).

[21] “5 kg load cell.” (2021), [Online]. Available: https://www.robotshop.com/uk/micro-load-cell-5-kg.html (visited on 04/01/2021).

[22] “0–100g electronic scale aluminium alloy weighing sensor load cell weight.” (2021), [Online]. Available: https://www.ebay.co.uk/itm/172293613951 (visited on 12/20/2021).

[23] “HX711 load cell weighing pressure sensor module for Arduino UNO.” (2021), [Online]. Available: https://www.zaelahmar.com/index.php?main_page=product_info&products_id=355557 (visited on 04/01/2021).

[24] N.-S. Cheng, “Formula for the viscosity of a glycerol-water mixture,” *Industrial & Engineering Chemistry Research*, vol. 47, 2008.

[25] *HX711: 24-bit analog-toDigital Converter (ADC) for weigh scales*, [Online]. Available: https://www.digikey.com/htmldatasheets/production/1836471/0/0/1/hx711.html (visited on 16/01/2022), AVIA Semiconductor, 2009.

[26] A. Hughes and B. Drury, *Electric motors and drives: fundamentals, types and applications*. Newnes, 2019.

[27] S.-K. Sul, *Control of electric machine drive systems*. John Wiley & Sons, 2011, vol. 88.

[28] K. Nakamura, M. Kurosawa, and S. Ueha, “Design of a hybrid transducer type ultrasonic motor,” *IEEE transactions on ultrasonics, ferroelectrics, and frequency control*, vol. 40, no. 4, pp. 395–401, 1993.

[29] E. Grant, “No-load speed characteristics of the 2-phase servomotor,” *IEEE Transactions on Applications and Industry*, vol. 83, no. 75, pp. 393–397, 1964.

[30] M. Barr, “Pulse width modulation,” *Embedded Systems Programming*, vol. 14, no. 10, pp. 103–104, 2001.

[31] *Product 363-0250 thermocouple RS Pro datasheet*, [Online]. Available: https://docs.rs-online.com/a01a/0900766b815bb509.pdf (visited on 21/07/2020)., RS Components, Oct. 2016.

[32] *Rs Pro thermocouple selection guide*, [Online]. Available: https://docs.rs-online.com/96d5/0900766b815e5302.pdf (visited on 21/07/2020)., RS Components, Sep. 2017.

[33] *MCP960X*, [Online]. Available: http://ww1.microchip.com/downloads/en/DeviceDoc/MCP960X-L0X-RL0X-Data-Sheet-20005426F.pdf (visited on 21/07/2020)., Microchip, 2019.

[34] C. Forsyth, "Complex flow of concentrated suspensions," Ph.D. dissertation, University of Strathclyde, 2015.

[35] J. Tichý, J. Erhart, E. Kittinger, and J. Prívratská, *Fundamentals of piezoelectric sensorics: mechanical, dielectric, and thermodynamical properties of piezoelectric materials*. Springer Science & Business Media, 2010.

[36] "Introduction to piezoelectric force sensors." (2020), [Online]. Available: https://www.pcb.com/resources/technical-information/introduction-to-force-sensors (visited on 01/10/2020).

[37] A. Mukhopadhyay, "Jamming and flow in dense suspensions," In preparation., Ph.D. dissertation, University of Strathclyde, 2021.

4. Materials and Methods

4.1 Overview

In this chapter, materials and methods used in this work are discussed. Experimental materials — fluids used in rheological experiments — are discussed first; beginning with a description of the fluid properties (including rheology). This is to give background on potential issues and idiosyncrasies of working with the fluid before detailing the preparation of the fluid. Cornstarch is suspended in a mixture of glycerol and water. Cornstarch is the solute of choice due to its ease of suspension in solvents like water, its low-cost, low reactivity, and wide availability. However, it has its downsides such as its polydispersity and porosity. Glycerol is added to water for use as a solvent as the increased viscosity makes measurement of stresses easier and makes the rheology more prominent [1]. In addition, glycerol-water mixtures are a useful Newtonian standard that can be tuned to different viscosities by altering the water content. Experimental methods follow, detailing the procedures used in experimental testing, finally followed by a description of data analyses.

4.2 Materials

4.2.1 Glycerol

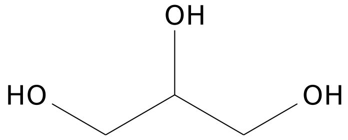

Figure 4.1: *Molecular structure of glycerol showing the three hydroxyl groups giving glycerol its characteristic hygroscopy.*

Glycerol (Figure 4.1) is a highly polar, viscous, hygroscopic, Newtonian fluid [2]. Glycerol's high viscosity, Newtonian nature, and low cost make it a useful rheological test fluid. However, its viscosity is highly sensitive to water content (see Figure 4.2). This is problematic for a fluid which is hygroscopic. Any change in viscosity must be prevented by careful handling and storage of the glycerol: beakers and other containers sealed with parafilm or other plastic to prevent atmospheric water ingress.

Temperature also has an effect on the viscosity [3], albeit not as pronounced as composition. Mixtures of glycerol and water have a less steep temperature dependence as the glycerol is mediated by the water. The composition (water content) sensitivity of pure glycerol is very high at low water content. As water is added, this sensitivity drops dramatically.

Viscosity and density data were compiled by [3] and used to obtain empirical formulae for the rheological properties of a glycerol water mixture for different compositions and temperatures. The viscosity for water (μ_w in $\mathrm{Pa\,s}$) and glycerol (μ_g in $\mathrm{Pa\,s}$) are given by:

$$\mu_w = 1.79 \times 10^3 \exp\left(\frac{-1230T - T^2}{36100 + 360T}\right) \tag{4.1}$$

$$\mu_g = 1.21 \times 10^7 \exp\left(\frac{-1233T + T^2}{9900 + 70T}\right) \tag{4.2}$$

where temperature T is in °C. Component viscosities are combined to give the mixture viscosity:

$$\mu_m = \mu_w^{\alpha} \mu_g^{1-\alpha} \tag{4.3}$$

where

$$\begin{aligned}
\alpha &= 1 - C_m + \frac{abC_m(1 - C_m)}{aC_m + b(1 - C_m)} \\
b &= (4.9 + 0.036T)a^{2.5} \\
a &= 0.705 - 0.0017T
\end{aligned}$$

and C_m is mass fraction of glycerol in the suspension.

Effect of composition on glycerol-water mixture rheology

The viscosity of glycerol-water mixtures is shown on Figure 4.2. The viscosity grows near-exponentially from the viscosity of pure water (at $Cm = 0$) up to the viscosity of pure glycerol (at $Cm = 1$). The sensitivity of the viscosity to composition (*i.e.* the

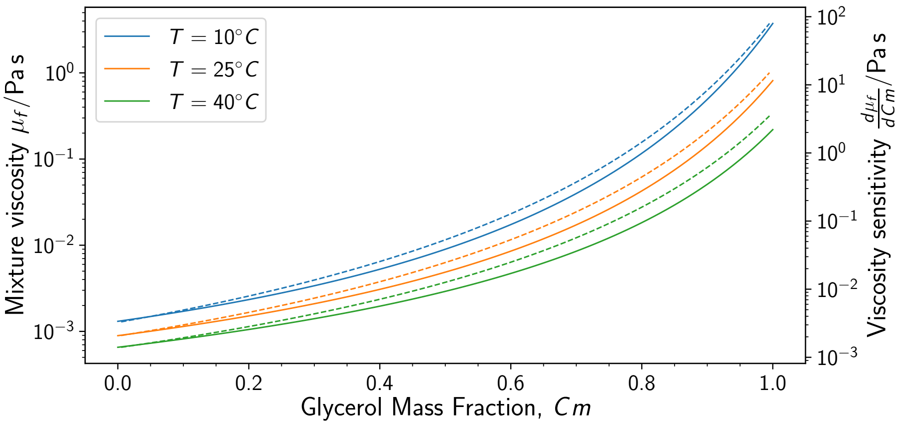

Figure 4.2: *Plot of viscosity of glycerol-water mixtures against glycerol mass fraction (solid line; left y-axis) and plot of viscosity sensitivity (gradient of previous; dashed line; right y-axis). Plotted using Equation* (4.3)*. Colour indicates temperature as in legend. Note rapid increase in viscosity and sensitivity for* $C_m \gtrsim 0.8$.

gradient of the curve) is also near-exponential. It can be seen that as glycerol concentration increases, there is a large increase in sensitivity — the rate of change of viscosity decreases from $\mathcal{O}(10^{-4})$ Pa s[*] to $\mathcal{O}(10^{-1})$ Pa s exponentially with composition.

The hygroscopic nature of glycerol means a pure glycerol sample left open to the atmosphere for any length of time will leach water from the air and reduce in viscosity. For making suspensions, a rheologically stable solvent is required. A threshold for stability of $Cm = 0.85$ was chosen as this is a good balance of high viscosity $\mu_{0.85} \approx 0.1$ Pa s and not too-high sensitivity $\left.\frac{d\mu}{dCm}\right|_{\mu 0.85} \approx 1$ Pa s (viscosity values correspond to a temperature of 25°C). In addition a composition of $C_m = 0.85$ was used by previous researchers in the author's lab. By using the same composition comparison between current and previous runs are enabled.

The glycerol is stored in glass bottles inside a cupboard within our lab. The bottles, once opened, are sealed with parafilm to prevent water/humid air ingress. The average laboratory humidity is a little over 50% (discussed more later, see Figure 4.10) and an average temperature of 14°C — corresponding to an absolute humidity of $0.007\,\mathrm{kg\,m^{-1}}$. Assuming the seal is perfect, then no more than 40 mg of water will enter into any volume of 850 g of glycerol — a negligible water content increase of 4×10^{-4} wt%.

---

[*] where $\mathcal{O}(\ldots)$ may be read as "on the order of . . . ".

Effect of temperature on glycerol-water mixture rheology

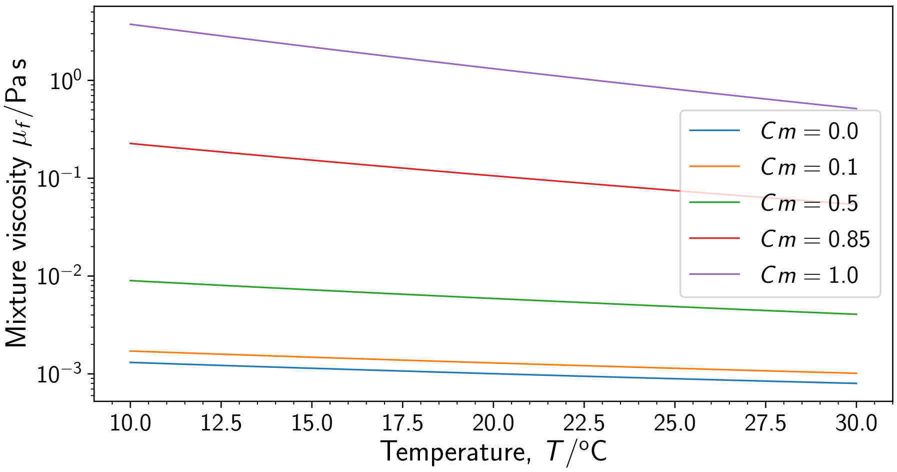

Figure 4.3: *Plot of viscosity of glycerol-water mixtures against temperature, for different glycerol mass fractions. Plotted using Equation* (4.3)*.*

The effect of temperature on the viscosity of glycerol-water mixtures is summarised on Figure 4.3: a plot of viscosity of glycerol-water mixtures as temperature increases. The previously selected, relatively rheologically stable[†], mass fraction of 0.85 has a relatively low temperature dependence ($\mathcal{O}\left(10^{-3}\right)$ Pa s °C^{-1}), in addition to the previously mentioned qualities. This makes this and lower concentrations well suited to use as a solvent for making suspensions.

Preparation

Glycerol (Sigma Aldrich, 99.99%) solutions in water (deionised; prepared using Millipore “Milli-DI” membrane purifier) are prepared on a mass ratio basis. This is in part due to the extreme difficulty in measuring out small quantities of glycerol necessary to obtain accurate compositions. Syringes are the best way to dispense glycerol, even at small volumes as they provide the necessary plunging pressure to move the high viscosity fluid. Other methods, such as air-displacement micro-pipettes suffer from a lack of accuracy due to the required suction-power to accurately move volumes of high-viscosity fluids like glycerol: the fluid resists the piston and less-than the desired amount will be dispensed. There are techniques which can be used to mitigate this (reverse pipetting [4]) but for the large volumes of glycerol required here measuring

---

[†] rheologically stable in that the rheology is not very sensitive to composition changes.

by weight was deemed more suitable.

Preparation involves weighing out glycerol and deionised (DI) water into a beaker on a balance. The solution is then thoroughly mixed and allowed to settle for at least two hours before use which allows any trapped gas bubbles to escape.

The resulting mixture is stored in a 1l glass bottle, with cap sealed by parafilm to ensure no exchange of moisture between the atmosphere and the solution. Each solution is made up and used within two weeks.

Notation

“Pure” stock glycerol is referred to by the letter “G” followed by the concentration on the bottle of the glycerol. Glycerol-water mixtures are denoted by the mass ratio of the two components with the letter “G” on the glycerol side of the ratio and the letter “W” on the water side. A list of glycerol stock and glycerol water mixtures and the relevant notation is given on Table 4.1.

Table 4.1: *Table of glycerol and glycerol-water mixture compositions and their reference symbols.*

Symbol	**Composition**	**Source**	**Viscosity** at 20°C/Pa s
G0999	Stock glycerol, 99.99wt%.	Sigma Aldrich.	1.6
G95:W05	Glycerol 95wt% and DI water 5wt%.	Millipore	0.5
G85:W15	Glycerol 85wt% and DI water 15wt%.	Millipore	0.1

4.2.2 Cornstarch Suspension

Cornstarch is a common tool used in rheological study of shear thickening suspensions [6], [7]. It is also has importance in the food and drink industry as a thickening agent due to its ability to form a paste-like gel after cooking in water, and as an alternative to wheat based starch thickeners. Starch is composed of polymers of glucose: amylose (Figure 4.4a), a long chain, and amylopectin (Figure 4.4b), a highly branched chain. The two components appear in different quantities depending on the source, normally around 25wt% amylose, the rest amylopectin [8]. On heating with water, these chains cross-link and create a network of chains, forming the basis of the gel. Without heating, the particles in suspension in water will physically change over time

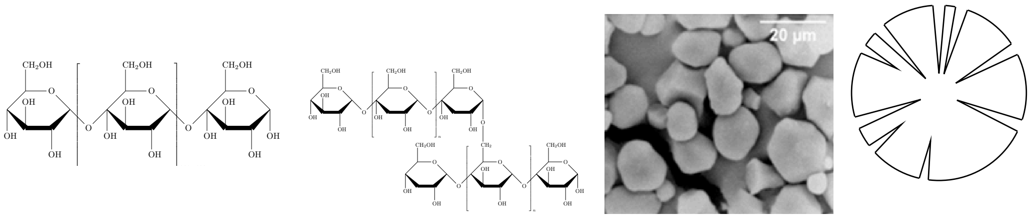

(a) (b) (c) (d)

Figure 4.4: *Molecular structure of (a) amylose and (b) amylopectin, (c) SEM image of cornstarch particles from [5] and (d) rough schematic of cornstarch particle showing the pores.*

resulting in a changing rheology (shown on Figure 4.5). It is possible this effect is due to the particle absorbing water: this “wicking” effect decreases the available solvent and thus increases the packing fraction.

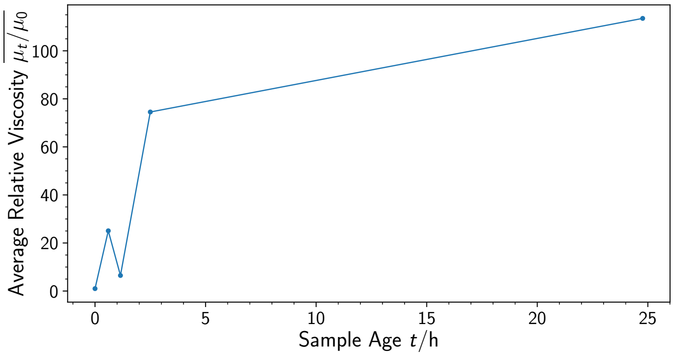

Figure 4.5: *Plot of average relative viscosity (viscosity at time t, μ_t relative to initial viscosity μ_0) against age for Cornstarch suspensions allowed to swell in solvent. Up to 36 minutes, there is little change. After an hour, there is an apparent change (low viscosity at low stress, high viscosity at high stress: an increase in shear thickening effect). This effect is relatively stable after a few hours. Experimental data from Dr. Jose Ruiz-Lopez (Basque Center for Applied Mathematics).*

Figure 4.5 shows the change in measured rheology of a suspension of cornstarch as it is aged. Viscosity of cornstarch suspensions is measured at different suspension ages resulting in different viscosities measured. This is shown on the Figure as a sharp increase in viscosity up to four hours, which slows down after this point. Therefore, suspensions are allowed to age for a full day before use, to allow the rheology to stabilise. If suspensions are used straight away, the suspension rheology (high gradient on Figure 4.5) is likely to be sensitive to even small delays of under an hour, while leaving the suspension to age for longer results in lower sensitivity and more consistent rheology.

Cornstarch granules are porous, roughly spherical particles (Figure 4.4d) composed of starch chains. Some of the pores are open to the outside and allow solvent in, resulting in the wicking effect [9]. The extent of wicking may be estimated using a measure of the porosity and moisture content of the particle prior to making up the suspension. Han *et.al.* have estimated the porosity for a sample of cornstarch using ultrasound [7]. The volume fraction ϕ_{cs} of an aged (*i.e.* fully wetted) suspension of cornstarch can be estimated from its mass fraction w_{cs} using:

$$\phi_{cs} = \frac{1}{1-\psi} \frac{(1-\xi)\, w_{cs}/\rho_{cs}}{(1-\xi)\, w_{cs}/\rho_{cs} + w_{solvent}/\rho_{solvent} + \xi w_{cs}/\rho_{water}} \tag{4.4}$$

where ψ is the particle porosity or void fraction in $^{ml}\!/_{ml}$, ξ is the particle mass basis moisture content (of "dry" particles before suspension) in $^{g}\!/_{g}$, and ρ is density in $\mathrm{g\,cm^{-3}}$. ρ_{cs} is the material density of the cornstarch particles themselves, not bulk density. The value obtained by density matching in organic solvents [7]. w_{cs} and $w_{solvent}$ are the mass fractions of cornstarch and solvent in suspension. A comparison of the estimated volume fraction with mass fraction for cornstarch (cs.) suspensions is presented on Figure 4.6.

Moisture in the air adsorbs onto the pore surface to equilibrium described by the relative humidity. Water sorption into starch was a topic of interest in the mid 20th century. The moisture content of a cornstarch powder can be estimated from the relative humidity in which it is stored using Figure 4.7 from [10]. Note on the Figure that at zero relative humidity, there is a minimum moisture content for the starch. Laboratory humidity is discussed in Section 4.2.2

Sedimentation

To prevent sedimentation, the solvent density may be matched to the particle density. This is usually accomplished by the addition of salt to the solvent, increasing mass while not affecting volume [9], [11]–[13].

The density of a solution increases as salt is dissolved, however not in a simple linear fashion. The amount of solute required to achieve the density increase required may be calculated from tabulated solubility data. However, solubility data for the solvent in use is difficult to find, and experimental trial-and-error may be employed.

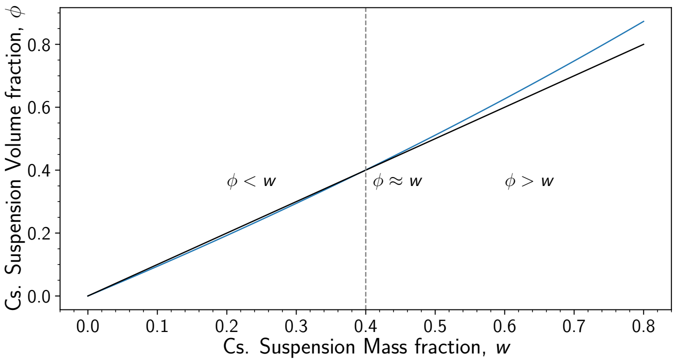

Figure 4.6: *Plot of estimated cornstarch (Cs.) suspension volume fraction against mass fraction. Volume fraction estimated using Equation 4.4 and values* $\psi = 0.31$ *[7],* $\xi = 0.14$ *[10],* $\rho_{solvent} = 1.25\,\mathrm{g\,cm^{-3}}$ *[3] and* $\rho_{cs} = 1.65\,\mathrm{g\,cm^{-3}}$ *[3]. This results in volume fractions less than the mass fraction, for mass fraction less than* 0.4 *and volume fractions greater than mass fraction for mass fractions greater than* 0.4*. Around a value of* 0.4*, the mass and volume fractions are the same. For the mass fractions in this work* $w \leq 0.44$*, the volume fraction is never deviates more than* 0.8% *from the mass fraction.*

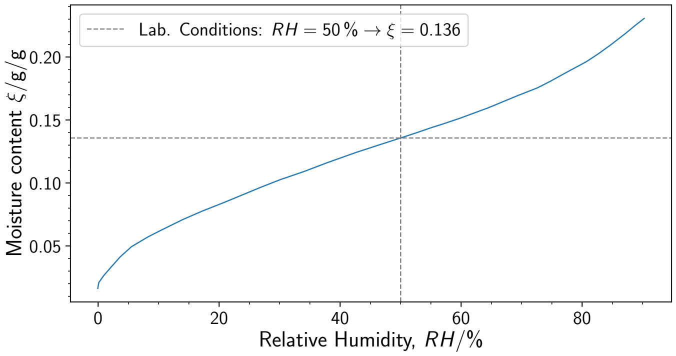

Figure 4.7: *Graph of cornstarch moisture content by mass against relative humidity. Adapted from [10]. Lab humidity discussed later on in Section 4.2.2.*

Salt choice is made on a basis of solubility (it must dissolve readily enough to be able to affect the desired change in density) and reactivity (it should not react with the components of the suspension: water, glycerol, amylose, and amylopectin). Starch hydrolyses in acidic or basic solutions. Starch forms a complex with tri-iodide ions [14]. Salts which would enable these reactions are to be avoided.

A possible choice of salt is Caesium Chloride [7] however this material is fairly expensive and would therefore not be feasible to use in the amounts needed for this work. Alternative salts were sought, however could not be found to be sufficiently soluble and non-reactive, while also being economically feasible.

Experiments were therefore conducted under the assumption that suspensions could be re-suspended following ageing, and that they would not re-sediment appreciably in the short time frame of an experimental run.

In any case, Derjaguin-Landau-Verwey-Overbeek (DLVO) [15] theory describes a screening effect between charged particles in the presence of ions. The cornstarch particles in suspension are charged, allowing the suspension to remain relatively stable. By introducing salts to the suspension, ions would screen the particle charges and cause agglomerates to form. This has been investigated in the context of shear thickening [16], [17], showing that addition of salt reduces and eventually removes the inter-particle repulsion and thus the frictionless state necessary for **dst**. By not adding salt to match density, the stability of the suspension is preserved (no agglomeration) as well as its rheology (frictionless to frictional transition maintained).

Rheology

The WC phase diagram (Figure 4.8) gives an indication of the expected behaviour for a suspension of cornstarch in Newtonian solvent.

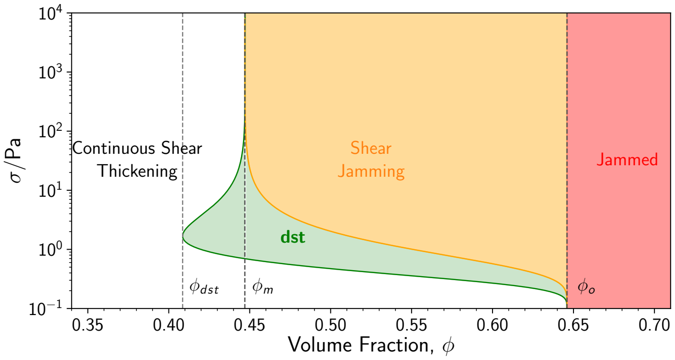

Figure 4.8: *Phase diagram for cornstarch suspensions in terms of composition (volume fraction of cornstarch) and applied stress.*

The phase diagram is given in terms of volume fractions, but suspensions are prepared on a mass basis. The volume fraction can be obtain from the mass fraction by use of Equation (4.4), knowing the humidity the cornstarch is stored in and the cornstarch porosity (using the estimate of 0.31 of Han *et al* [7]).

Prepared suspensions are shear thickening, and exhibit shear jamming [6]. These suspensions show a middling onset stress of $\sigma^{\star} = \mathcal{O}(10\,\mathrm{Pa})$ [18]. (Compare with PMMA in decalin systems which have an onset stress which varies with particle size between $\mathcal{O}(100\,\mathrm{Pa})$ and $\mathcal{O}(0.1\,\mathrm{Pa})$ [19].)

The Wyart Cates model (Equations 2.1, 2.4, 2.5, and 2.7 — repeated below) is fit to experimental data.

$$\sigma = \mu\dot{\gamma} \tag{2.1 again}$$

$$\frac{\mu}{\mu_f} = \left(1 - \frac{\phi}{\phi_j}\right)^{-2} \tag{2.4 again}$$

$$\phi_j(\sigma) = \phi_m f(\sigma) + \phi_0\left(1 - f(\sigma)\right) \tag{2.5 again}$$

$$f(\sigma) = e^{-\left(\frac{\sigma^{\star}}{\sigma}\right)^{\beta}} \tag{2.7 again}$$

The model equations together are used to predict the strain rate $\dot{\gamma}$ which which a fluid (of volume fraction ϕ) is sheared with stress σ (*i.e.* $\dot{\gamma} = f_{WC}(\sigma, \phi)$). Equation 2.7 is used to first get the fraction of frictional contacts f, followed by Equation 2.5 yielding the jamming volume fraction required to calculate the effective suspension viscosity using Equation 2.4. Finally, the strain rate is calculated using Newton's viscosity law, Equation 2.1. In addition, it is necessary to estimate volume fraction using Han's method (Equation 4.4). The model has five parameters (not including the inputs ϕ and σ): solvent viscosity μ_f, minimum jamming volume fraction ϕ_m, jamming volume fraction ϕ_0, friction function exponent β, and onset stress $\sigma^{\star}$. There are a further five parameters required when estimating volume fraction from mass fraction: ξ, ψ, ρ_{water}, ρ_{cs}, and $\rho_{solvent}$, making for a total of ten parameters to be fit, but a number of these are already known: the viscosity of the solvent can be calculated using Equation 4.3, the densities of water and glycerol are known for the temperatures involved, and the density of the solvent (**G85:W15**) can be approximated using the following equation[3]:

$$\rho_{solvent} = \rho_{glycerol} C_m + \rho_{water}\left(1 - C_m\right) \tag{4.5}$$

where $\rho_{solvent}$, $\rho_{glycerol}$, ρ_{water} are the densities of the glycerol-water mixture, pure glycerol, and pure water respectively all in $\mathrm{g\,cm^{-3}}$, and C_m is the mass fraction of glycerol in the solvent. The porosity ψ of cornstarch particles has been calculated to be 0.31 [7]. The moisture content ξ at the relative humidity of storage is given by Figure 4.7 ($\xi = 0.14$ for the average relative humidity in which the cornstarch was stored).

Table 4.2: *Wyart-Cates model parameters summary.*

Parameter	**Fixed?**	**Value or range**	**Sources**
μ_f	Used in fit.	$0.03\,\mathrm{Pa\,s} \leq \mu_f \leq 0.3\,\mathrm{Pa\,s}$	Equation 4.3
ϕ_m	Used in fit.	$0.3 \leq \phi_m \leq 0.5$	[18]
$\phi_0 - \phi_m$	Used in fit.	$0.01 \leq (\phi_0 - \phi_m) \leq 0.3$	[18]
$\sigma^\star$	Used in fit.	$1\,\mathrm{Pa} \leq \sigma^\star \leq 10\,\mathrm{Pa}$	[18]
β	Used in fit.	$0.1 \leq \beta \leq 10$	[18], [21], [22]
ψ	Fixed value.	$\psi = 0.31$	[7]
ξ	Fixed value.	$\xi = 0.14$	Figure 4.7, [10]
ρ_{cs}	Fixed value.	$\rho_{cs} = 1.65\,\mathrm{g\,cm^{-3}}$	[7], [20]
$\rho_{solvent}$	Fixed value.	$1.25\,\mathrm{g\,cm^{-3}}$	Equation 4.5
ρ_w	Fixed value.	$1\,\mathrm{g\,cm^{-3}}$	[3]

The density of cornstarch particles (not bulk density) is reported as $1.65\,\mathrm{g\,cm^{-3}}$[7], [20]. This reduces the number of fit-able parameters to five. Bounds can be estimated for the search region for most of the remaining parameters. Solvent viscosity is estimable using Equation 4.3, but is allowed to vary in the fit between $0.03\,\mathrm{Pa\,s}$ and $0.3\,\mathrm{Pa\,s}$ — found to be required to achieve a good fit. Onset stress for cornstarch suspended in glycerol-water is $\mathcal{O}(5\,\mathrm{Pa})$ [18]. ϕ_0 is larger than ϕ_m and is around the value of ϕ_{RLP} [18]. ϕ_m is ~ 0.4 [18]. To enforce $\phi_0 > \phi_m$, the difference $\phi_0 - \phi_m$ is used in the fit. β has a value $\mathcal{O}(1)$ [18], [21], [22].

Experimental data from this work are fit (least-squares) to the model, as well as to data collected[‡] on a commercial rheometer in our lab (TI Discovery Hybrid Rheometer 3 or DHR-3). These fits are compared to a fit from literature [18] on Table 4.3.

The WC fit parameters are used to draw phase diagrams for all three fits, as per the phase diagram construction method outlined in Section 2.4. These diagrams are shown on Figure 4.9. The systems forming the basis for the fits are similar — two have the same composition (this work's system and the DHR-3 system) and the other differs by having a lower glycerol concentration in the solvent: 50 wt% as opposed to 85 wt%. All three, however, use different geometries (and hence, flow patterns): the DHR-3 system is a parallel plate, O'Neill *et al.* [18] used an extruder (resulting in a combination of shear and extensional flow), and this work uses a concentric cylinder geometry. The resulting fits are quite distinct, despite their similarities.

[‡] Data from Dr. Jose Ruiz-Lopez, now at Basque Center for Applied Mathematics

Table 4.3: *Results of fitting Wyart-Cates model to experimental data recorded by the custom Couette rheometer (CCR), a Discovery HR-3 (DHR-3) parallel plate rheometer, and data reported for another cornstarch system in the literature [18]. Standard errors are reported alongside fit values.*

Parameter	**O'Neill *et al.* [18]**	**DHR-3**	**CCR**
ϕ_m	0.439 ± 0.002	$0.444 \pm 0.05\%$	$0.509 \pm 0.15\%$
ϕ_o	0.538 ± 0.003	$0.517 \pm 1.95\%$	$0.678 \pm 3.44\%$
μ_f	not given	$0.0557\,\mathrm{Pa\,s} \pm 1.96\%$	$0.113\,\mathrm{Pa\,s} \pm 1.37\%$
$\sigma^\star$	$4.7 \pm 0.2\,\mathrm{Pa}$	$0.991\,\mathrm{Pa} \pm 2.35\%$	$2.25\,\mathrm{Pa} \pm 0.46\%$
β	0.62 ± 0.03	$2.16 \pm 0.9\%$	$1.85 \pm 0.46\%$

The shape of the jamming line (solid line on Figure 4.9) is sensitive to the value of parameter β, and especially affects the protrusion of the **dst** line (dashed line on Figure 4.9) — even when controlling for other fit parameters. The lower β; the less protrusion. This can be seen on the figure as the **dst** line for O'Neill *et al.*'s fit shows a very small protrusion (minimum volume fraction for **dst** $\phi_{dst} = 0.429$ down from $\phi_m = 0.430$), compared to the DHR-3 data fit with a much larger β value which has an extreme protrusion of the **dst** region into the low volume fractions (as low as $\phi_{dst} = 0.392$ down from $\phi_m = 0.444$), or to the CCR fit which shows a protrusion down to $\phi_{dst} = 0.433$ from $\phi_m = 0.509$. This is shown to emphasise the sensitivity of the WC model to this system of cornstarch; a semi-hard aspherical, porous, and polydisperse colloid.

Preparation

The cornstarch used in this work was obtained from Sigma Aldrich (product code S4126, approx. 73% amylopectin and 27% amylose). The starch is an insoluble white powder. The starch is stored in a cool, dry laboratory cupboard with temperature and humidity monitored but not controlled. Temperature varies over the course of a year between 11°C and 16°C, with an average temperature of around 14°C. Relative humidity varies between 42% and 54%, and has mean value of 51%. The measurements are plotted on Figure 4.10 to show the distribution of points.

The solvent, a mixture of glycerol (85% by weight) and water, is prepared first, as described in Section 4.2.1. Once mixed, the solvent is allowed to stand for at least an

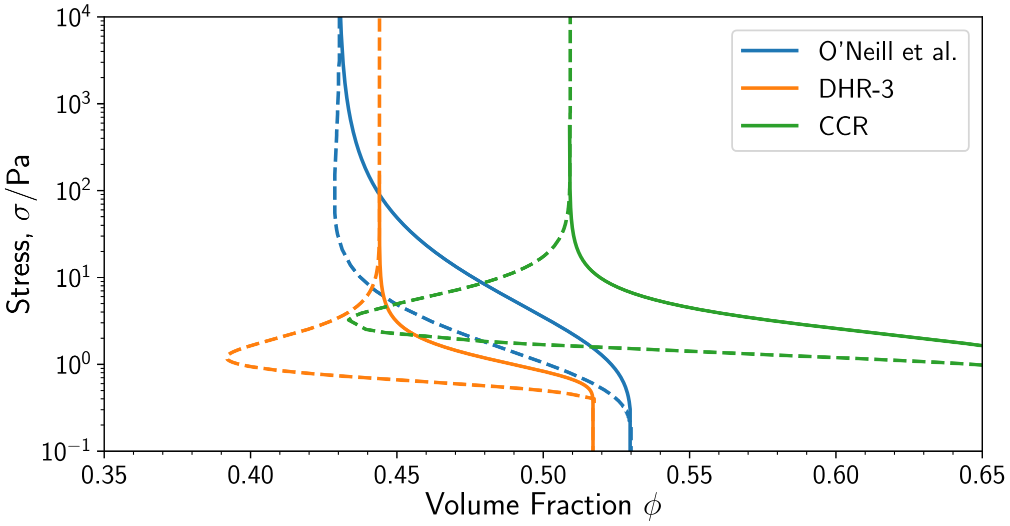

Figure 4.9: *Comparison of WC phase diagram for three sets of fit parameters (see Table 4.3), including data from O'Neill et al. [18]. Solid line delineates transition to a jammed or solid-like state as stress or volume fraction is increased. The dashed line encompasses the unstable **dst** regime.*

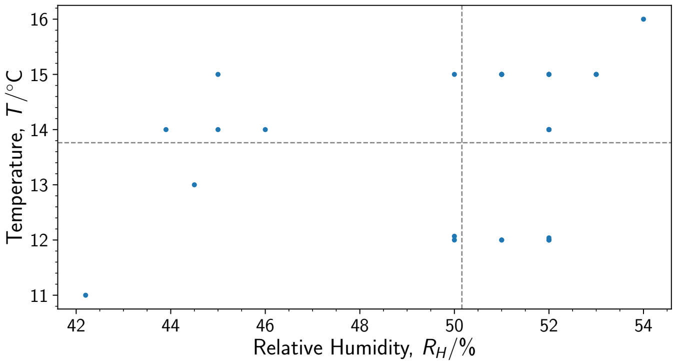

Figure 4.10: *Humidity and temperature of corn starch storage area. Measurements span the course of nearly one year (from January 2020 to December 2020). Average values of humidity and temperature are shown on the vertical and horizontal dashed lines respectively.*

hour.

Cornstarch is weighed into a beaker on a balance to the required amount, then a standard mass (200 g) of the solvent is added. The composition of the suspension is altered by changing the mass of cornstarch. This mixture is gently stirred to get the cornstarch off the bottom of the beaker, then vigorously stirred to wet all the cornstarch, ensuring no lumps persist. After mixture, the beaker is labelled and covered with parafilm or other plastic wrap to prevent the suspension composition from altering either by evaporation or by taking in water from the atmosphere.

Due to the swelling/wicking effect (Section 4.2.2), cornstarch suspensions are left to rest for 24 hours. After rest, suspensions are re-suspended by (vigorous) stirring with a spatula until no lumps remain and the suspension is, once again, homogenous.

Notation

Similar to glycerol-water mixtures, cornstarch suspensions are denoted by the mass ratio of components involved, with letters indicating the component in the ratio. Suspensions involving a composite solvent, i.e. involving a solvent of multiple components like glycerol and water do not have their composition explicitly stated, but are implied to be the make up. The two digits give mass of cornstarch in ratio to the solvent mass which is given by $N_{solvent} = 100 - N_{CS}$. Example cornstarch suspension compositions and symbols are shown on Table 4.4.

Table 4.4: *Table of cornstarch suspension compositions and their reference symbols.*

Symbol	**Composition**
CS10:(G85:W15)	Corn starch suspension, 10 wt% cornstarch, 90 wt% glycerol-water mixture of which 85 wt% is glycerol and 15 wt% is water.
CSX:(G85:W15)	Corn starch suspension, $X\,wt\%$ cornstarch, $100 - X$ wt% glycerol-water mixture of which 85 wt% is glycerol and 15 wt% is water.

4.3 Methods

In this section a description of the use of the custom rheometer is given: starting with loading procedure, then fixing the position of the cylinder (to ensure it is not off-centre), and then a description of the test schedule (how experiments are run).

4.3.1 Loading procedure

Before fluid is loaded into the rheometer, the device is empty with the outer cylinder lowered and moved off to the side. The goal for the filling procedure is to provide a consistent starting point for running materials in the rheometer. The stress measurement is sensitive to variations in contact area between the inner cylinder and fluid. This is managed by fixing the contact area (≡ fill height) to the same value for each run.

The shear cell in the rheometer is loaded to a constant volume of 50 ml. The viscous nature of the test fluids makes measurement by volume very difficult by normal means: pipettes fail to suck up the fluid, and syringes can cause filtration of a suspension [18] resulting in a less dense test fluid than would be expected. The density of some of the test fluids is hard to establish also as the suspended material swells and has a non-quantifiable effect on the suspension volume. Filling is accomplished by pouring fluid into the cylinder up to a volume indicated by graduations on the side of the shear cell.

With fluid loaded, the outer cylinder is moved to the loading position: it lies beneath the inner cylinder. It is then raised slowly. Fluid height is monitored and the cylinder is considered in position once the fluid meets the graduation mark on the inner cylinder (where the anchor bolt ends). Alternatively, the cylinder is raised until enough fluid is in contact with the column > 50% and then fill depth can be measured from the surface of the fluid to the inner cylinder graduation.

50 ml is used as this is enough fluid to fill the gap between cylinders sufficiently to allow the fluid level to rise to the inner graduation level while also allowing a sufficient gap between outer cylinder rim and optical encoder for peripheral sensors (like the Piezoelectric Needle Device, Section 3.8).

By ensuring a consistent loading procedure, shear stress can be measured given the geometry and the fill height (≡ fluid contact area).

4.3.2 Positioning

With the fluid loaded and cylinder raised, the next step is to ensure the two cylinders are concentric. First, orientation is ensured to be consistent by way of a spirit level. Orientation is adjusted by rotating the components around the clamps which hold them up.

Next, position is checked. A middling voltage (ranges from $3-5V$) is applied to the motor to shear the fluid. When the fluid is sheared, any eccentricity in the position of the cylinder can be seen as an increase in height of the fluid. This allows the eccentricity to be corrected by adjusting the XY table.

4.3.3 Test schedule

In a typical testing scenario of a fluid with the custom rheometer, a fluid is run at different motor duty cycles — producing different stresses and strain rates (duty cycles and motor control are discussed further in Section 3.6). Once loaded, the fluid is run at a constant duty cycle for a set amount of time: from 90 s up to 5 min. The majority of runs were done at 3 min. At the beginning of the run, the motor is ramped up sharply to a high duty cycle before falling back to the set point: this is to prevent stalling on very thick suspensions, and is done to all fluids for sake of consistency. This step is called “pre-shear”. After the pre-shearing, the fluid is run at the desired DC for its time limit, while the loadcell, rotation, temperature and, optionally, the PND are recorded (PND insertion is described in Section 4.3.4 below). Once the run is complete the shearing is halted and the fluid comes to rest for a second or so while the logged data is saved. Then the next run begins at the next run in the schedule.

A schedule of runs is set up to see any possible hysteresis, if it is present. Hysteresis — a change in rheological behaviour after repeated shearing during measurement — is not normally seen in these suspensions. However any hysteresis that the equipment introduces should be highlighted and that is the purpose of the run schedule here. Runs are conducted from low DC up to high, then back down. This is typically done in steps of five (DC varying from 20% to 100% in steps of 16%): so one fluid may be tested ten times before being swapped out and the schedule is repeated with fresh fluid. Fluid schedules are repeated at least once. Further details of the experimental data is given in the relevant results chapters in the “Experimental Details” section (Section 5.2, Section 6.2, and Section 7.2).

4.3.4 PND Insertion and Positioning

The Couette cell gap is quite narrow (less than half a centimetre, Table 3.1) and so there is little leeway when positioning the PND probe. If the needle is too close to either cylinder then the needle and cylinder wall interact as described in Section 3.8.4. The only option is to aim for the centre of the gap. This is done by moving the articulated arm until the needle can be seen to be approximately centred in the gap. The arm is maintained at a consistent height so that the needle depth is also consistent in the fluid.

4.4 Analyses

In this section the main types of plots shown in this work are described: how the plots are produced, as well as what kind of information is expected to be learned from the plot.

4.4.1 Flow curve

The flow curve, introduced in Section 2.2, is a plot of stress against strain rate. These plots are used to examine the rheological behaviour of a system. Flow curves of cornstarch suspensions typically have an ‘s’ shape owing to an unstable region (see Section 2.4).

These plots are used to compare between the WC model and measured data. Any point where a line on the flow curve bends backwards indicates an unstable region — a jump in viscosity.

4.4.2 Timeseries

A timeseries is a plot of a measurement against time. This is used to qualitatively analyse the measurement. These plots can be stacked, one above the other, for different measurements with the same x-axis thereby allowing multiple measurements to be compared.

4.4.3 Fourier transform

The Fourier transform [23] (FT) decomposes a measured signal into a spectrum of sine waves and returns the power of each wave frequency. This is useful for analysis of a dynamic wave for highlighting sources of the dynamics. For example, in electronic signals a frequency peak at 50 Hz is likely to be due to AC interference as this is the frequency of AC power (in the UK).

The Fourier analyses in this work take two forms: with respect to time, and with respect to position.

Temporal Fourier Transform

A signal varying in time passed into the Fourier transform will return the power of the time-frequencies (in units of reciprocal time) of waves which, added together, recreate the original signal. As mentioned, this is useful for identifying sources of dynamics in the signal. This time-based Fourier Transform can be referred to as time-FT or tFT to differentiate it from the spatial FT.

Spatial Fourier Transform

A Fourier transformed signal does not need to vary in time; it can vary in any dimension. A spatial Fourier transformed signal unveils the component spatial frequencies (k, in units of reciprocal length or angle e.g. m^{-1} or rad^{-1} or rot^{-1}). A peak at $2\,\mathrm{m}^{-1}$ indicates a sine wave component of the signal with period of $0.5\,\mathrm{m}$ — there is a recurring peak in the original signal every half-meter. Where time-frequency gives number of occurrences per unit time, spatial frequency gives number per unit length. This spatial Fourier Transform can be referred to as spatial-FT or sFT to differentiate it from the time-based FT.

In this work, position refers to the angular position of the inner cylinder of the Couette cell. This is obtained by integrating the rotational speed with time, the result being the cumulative angular position of the cylinder (the total radians rotated — not reduced to between $0\,\mathrm{rad}$ and $2\pi\,\mathrm{rad}$). On the Fourier transform of a measurement (stress, for example) with respect to angular position, there might be expected a peak at a position-frequency of $1\,\mathrm{rot}^{-1}$ due to imperfections in the bearing, or some regular flow phenomena occurring once every rotation.

This spatial FT removes distinction between rotation rates (one rotation at $5\,\mathrm{rot\,s}^{-1}$ is the same as one rotation at $15\,\mathrm{rot\,s}^{-1}$) and allows easier comparison between measurements taken at different rates. For example, a peak that appears to grow with rotation rate is more difficult to confirm on a tFT, whereas on a sFT the peak is positioned relative to one rotation. If the peak is at a multiple of a rotation rate, then it will be in the same place on the sFT. This effect can be seen on the comparison plot Figure 4.11, discussed in the next section.

Comparing Fourier Transforms

It is useful to compare FTs, but there is a lot of information to encode. A common technique is to offset the power of Fourier transformed measurements and plot them on the same graph (*e.g.* [12, Figure 2]). However this can become cluttered when comparing many measurements together. To increase information density while not cluttering the information, a heatmap can be constructed with every horizontal line encoding the FT of a single measurement, the colour at each point indicating the power of the FT at a frequency indicated by the x-position of the point. An example of this is shown on Figure 4.11.

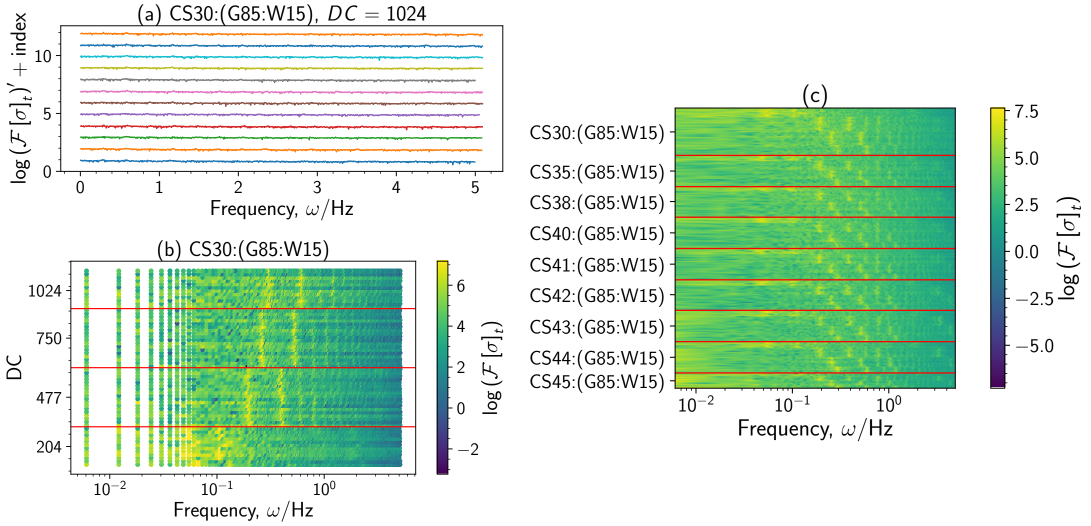

Figure 4.11: *(a) tFT of stress for CS30, only showing top Duty Cycle (DC) values (more information in Section 3.6.2). (b) tFT for CS30 at all DC values, as a scatter. (c) Example heatmap plot of tFT of stress measurements. Calligraphic capital 'F' ($\mathcal{F}$) represents Fourier transform power. Measurements are grouped by composition. Each group is sorted by DC. Composition and DC increase going from top to bottom. The plot shows how comparison of many FT measurements is made more clear. Plot (c) is taken from Chapter 7.*

Figure 4.11 shows time-FT of measurements of stress. Brighter colours indicates a higher power of the indicated frequencies. The bright spots moving right for each composition as rate increases is a multiple of the rotation frequency — an effect more clearly seen on the corresponding pFT plot (discussed later on, in Chapter 7). The heatmap is formed by first taking the Fourier transform of the desired measurement. Comparison between FT of comparatively few measures can be made by normalising the FT and adding a factor to split the lines apart for clarity, see Figure 4.11 (a). This is not very information dense, and becomes unwieldy when trying to compare large amounts of data. A scatter plot is then formed on (b), showing the magnitude of the tFT as colour, and the y-axis now represents the DC (Duty Cycle) of the measurement (roughly indicates rotation rate). This gives a good manner of viewing the FT of many different measures. Then, comparisons can be made across materials by decreasing the size of the scatter points and thus forming the heatmap in (c).

4.4.4 Correlation

By performing a two-dimensional histogram of a pair of signals, their correlation (or lack thereof) is seen. This plot makes use of a heatmap to encode 2D information in a clear, dense manner. An alternative is to simply scatter one measurement against another, then fit a line. The goodness-of-fit gives the strength of the correlation — the less spread the data is, the better the linear fit, and the better the correlation. The advantage to the heatmap plot is increased clarity for noisy data like the PND measurements.

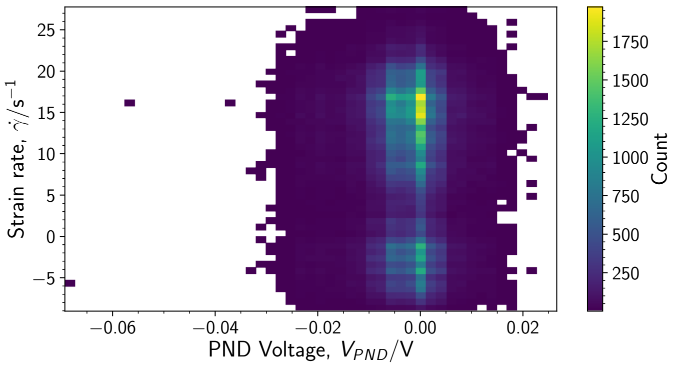

Figure 4.12: *Example Piezoelectric Needle Device (PND) voltage to strain rate histogram. Brighter colours indicate higher co-incidence of the two measurements. The plot shows no correlation between the two measurements — as shown by the vertical line of bright colour at* 0 V*.*

An example of a 2D histogram is shown on Figure 4.12. This plot shows no correlation between the measurements as the main backbone of the plot is a vertical yellow line near the origin. There is no increased coincidence of PND and strain rate along any of the diagonals. This type plot has the advantage over scatter plots in that it shows the density of the measurements. There are many measurements of the PND which drop below −0.02 V, however these pale in comparison to the amount of PND measurements much closer to 0 V. This type of information would be difficult to encode in a scatter plot although it would be possible by using opacity to encode density.

4.5 Summary

In this chapter the materials used in this Thesis were described, including rheological properties.

Glycerol (and aqueous solutions of glycerol) make a decent Newtonian standard, despite the potential sensitivity of the solution's viscosity to water concentration. The sensitivity drops off rapidly. 85% solutions of glycerol by weight are deemed to be a good balance between viscosity and rheological stability.

Cornstarch suspensions are an example of a shear jamming fluid; shearing a corn starch suspension results in a large increase in viscosity. These suspensions are a great test system for rheological investigation of jamming suspensions due to the ease of procurement of cornstarch, its safe and inert nature, low cost, and the ease of suspension (pure water is a valid solvent for this system). However, it has some draw backs: it swells in water (volume fraction inaccessible), it is very polydisperse, and is non-spherical.

References

[1] S. K. Pattanayek, A. K. Ghosh, *et al.*, "Role of hydrogen bond interactions in water–polyol medium in the thickening behavior of cornstarch suspensions," *Colloid and Polymer Science*, vol. 295, no. 7, pp. 1117–1129, 2017.

[2] R. Christoph, B. Schmidt, U. Steinberner, W. Dilla, and R. Karinen, "Glycerol," in *Ullmann's Encyclopedia of Industrial Chemistry*. American Cancer Society, 2006, isbn: 9783527306732.

[3] N.-S. Cheng, "Formula for the viscosity of a glycerol-water mixture," *Industrial & Engineering Chemistry Research*, vol. 47, 2008.

[4] S. Koivisto, "Effect of liquid properties in pipetting: Liquid handling note — No. 1," *Thermo Fisher Scientific Technical Note*, 2009.

[5] R. Karmakar, D. Ban, and U. Ghosh, "Comparative study of native and modified starches isolated from conventional and nonconventional sources," *International Food Research Journal*, vol. 21, no. 2, p. 597, 2014.

[6] E. Brown and H. M. Jaeger, “Shear thickening in concentrated suspensions: Phenomenology, mechanisms and relations to jamming,” *Reports on Progress in Physics*, vol. 77, 2014.

[7] E. Han, N. Van Ha, and H. M. Jaeger, “Measuring the porosity and compressibility of liquid-suspended porous particles using ultrasound,” *Soft Matter*, vol. 13, no. 19, pp. 3506–3513, 2017.

[8] H. A. Fonseca-Florido, J. Hernández-Ávilab, A. I. Rodrguez-Hernández, J. Castro-Rosas, O. A. Acevedo-Sandoval, N. Chavarria-Hernández, and C. A. Gómez-Aldapa, “Thermal, rheological, and mechanical properties of normal corn and potato starch blends,” *International Journal of Food Properties*, vol. 20, no. 3, pp. 611–622, 2017.

[9] E. Han, M. Wyart, I. R. Peters, and H. M. Jaeger, “Shear fronts in shear-thickening suspensions,” *Physical Review Fluids*, vol. 3, no. 7, p. 073 301, 2018.

[10] L. Sair and W. Fetzer, “Water sorption by starches,” *Industrial & Engineering Chemistry*, vol. 36, no. 3, pp. 205–208, 1944.

[11] S. Majumdar, I. R. Peters, E. Han, and H. M. Jaeger, “Dynamic shear jamming in dense granular suspensions under extension,” *Physical Review E*, vol. 95, no. 1, p. 012 603, 2017.

[12] B. Saint-Michel, T. Gibaud, and S. Manneville, “Uncovering instabilities in the spatiotemporal dynamics of a shear-thickening cornstarch suspension,” *Physical Review X*, vol. 8, no. 3, p. 031 006, 2018.

[13] G. Ovarlez, A. V. N. Le, W. J. Smit, A. Fall, R. Mari, G. Chatté, and A. Colin, “Density waves in shear-thickening suspensions,” *Science Advances*, vol. 6, no. 16, eaay5589, 2020.

[14] S. Madhu, H. A. Evans, V. V. Doan-Nguyen, J. G. Labram, G. Wu, M. L. Chabinyc, R. Seshadri, and F. Wudl, “Infinite polyiodide chains in the pyrroloperylene–iodine complex: Insights into the starch–iodine and perylene–iodine complexes,” *Angewandte Chemie International Edition*, vol. 55, no. 28, pp. 8032–8035, 2016.

[15] J. N. Israelachvili, *Intermolecular and surface forces*. Academic press, 2011.

[16] C. Clavaud, A. Bérut, B. Metzger, and Y. Forterre, “Revealing the frictional transition in shear-thickening suspensions,” *Proceedings of the National Academy of Sciences*, vol. 114, no. 20, pp. 5147–5152, 2017.

[17] N. C. Crawford, B. Yohe, S. Kim, R. Williams, D. Boldridge, and M. W. Liberatore, “Shear thickening and shear-induced agglomeration of chemical mechanical polishing slurries using electrolytes,” *Rheologica Acta*, vol. 52, no. 5, pp. 499–513, 2013.

[18] R. E. ONeill, J. R. Royer, and W. C. Poon, “Liquid migration in shear thickening suspensions flowing through constrictions,” *Physical Review Letters*, vol. 123, no. 12, p. 128 002, 2019.

[19] B. Guy, M. Hermes, and W. C. Poon, “Towards a unified description of the rheology of hard-particle suspensions,” *Physical Review Letters*, vol. 115, no. 8, p. 088 304, 2015.

[20] R. L. Whistler, J. N. BeMiller, and E. F. Paschall, *Starch: chemistry and technology*. Academic Press, 2012.

[21] R. Mari, R. Seto, J. F. Morris, and M. M. Denn, “Shear thickening, frictionless and frictional rheologies in non-brownian suspensions,” *Journal of Rheology*, vol. 58, no. 6, pp. 1693–1724, 2014.

[22] B. M. Guy, C. Ness, M. Hermes, L. J. Sawiak, J. Sun, and W. C. K. Poon, “Testing the Wyart-Cates model for non-Brownian shear thickening using bidisperse suspensions,” *Soft Matter*, vol. 16, no. 1, pp. 229–237, 2020.

[23] R. N. Bracewell and R. N. Bracewell, *The Fourier transform and its applications*. McGraw-Hill New York, 1986, vol. 31999.

5. Simple Rheometry

> *“Making the simple complicated is commonplace;*
> *making the complicated simple, awesomely simple,*
> *that’s creativity.”*
>
> Charles Mingus

5.1 Overview

A simple fluid is one that follows Newton’s law of viscosity: the viscosity of these fluids is constant with respect to stress and rate of strain.

In this chapter, a series of shear experiments on simple Newtonian fluids (glycerol and aqueous glycerol solutions, Chapter 4) are performed using the custom rheometer (designed in Chapter 3). The results are compared to tabulated viscosity data. In this way, the capabilities of the custom rheometer can be assessed. In addition the dynamic features of the rheological properties measured by the custom rheometer are investigated; further assessing the ability of the device.

The objective of this chapter is to use the custom rheometer to investigate the rheology of various Newtonian mixtures of glycerol and water (**G0999**, **G95:W05**, **G85:W15**, in the notation system described in Chapter 4). The results of the investigation are compared with tabulated data from literature, and so critically appraising the ability of the custom rheometer to measure viscosity of a sample. In addition, limitations of the custom rheometer as highlighted in Chapter 3 will be investigated, discovering their practical impact. The primary limiting factor of measurement noise will be investigated and characterised to provide a baseline for the experiments on complex systems discussed in the following chapter. Noise uncovered here would not be expected to originate from any interesting behaviour of the fluid, but from the device itself.

This chapter begins with a description of the experimental methods used (Section 5.2), followed by mean rheology results for shear experiments displayed on a flow curve (Section 5.3). The custom rheometer is qualitatively benchmarked against a commercial rheometer in Section 5.3.1. Dynamic results are then analysed through the use of timeseries and Fourier transform plots. Timeseries plots of strain rate, stress, and viscosity are analysed in Section 5.4, Fourier analysis in Section 5.6. Trends in noise in the rheological measurements are investigated in Section 5.5. The novel sensor, the Piezoelectric Needle Device (PND) is investigated in Section 5.7.

5.2 Experimental Details

The dataset for this chapter encompasses 164 individual runs on the custom rheometer totalling approximately 6.5 hours of total run time, and 102,000 rotations of the shear cell. The dataset includes three compositions of glycerol-water solution (from pure glycerol to 85 wt%) which were run for a range of motor duty cycles, resulting in a decade of range for strain rate summarised on Table 5.1.

Glycerol-water mixtures were used as the Newtonian fluid due to its easily tunable rheology (Chapter 4). Three compositions were used: pure glycerol (**G0999**), low-water content (5wt%, **G95:W05**) and medium water content (15wt%, **G85:W15**). This provided a viscosity range of $\sim 1.5\,\mathrm{Pa\,s}$ down to $\sim 0.15\,\mathrm{Pa\,s}$.

Strain rates used were dependent on both the duty cycle set by the control program and the motor used (discussed in Chapter 3). By varying the motor and duty cycle, a range of strain rates between $1\,\mathrm{s}^{-1}$ and $300\,\mathrm{s}^{-1}$ were achieved. For the Newtonian materials used, a constant viscosity is expected despite the change in rate.

Each run was conducted following the procedure described in detail in in Section 4.3.1: the cylinder is loaded with approximately 50ml of material; the outer cylinder then raised to meet the inner cylinder such that the inner cylinder is ap-

Table 5.1: *Summary of simple rheometry dataset*

Material Sub-set	Contents	Strain rate Range
G0999	55 logs	From $17.1\,\mathrm{s}^{-1}$ to $170\,\mathrm{s}^{-1}$
G95:W05	54 logs	From $18.9\,\mathrm{s}^{-1}$ to $184\,\mathrm{s}^{-1}$
G85:W15	55 logs	From $1.9\,\mathrm{s}^{-1}$ to $192\,\mathrm{s}^{-1}$

prox 73 mm deep in the test fluid (the actual *fill depth* is measured and recorded); the fluid is pre-sheared to highlight eccentricity in position which can be corrected using the XY table; finally the fluid in the Couette is sheared for 1—5 min with the duty cycle at the desired level.

During each run, a core set of measurements are always taken: loadcell (→ stress), optical encoder (→ strain rate). In addition, some measurements were added to the schedule over time which were not initially available. Ambient temperature was available early on, but more direct temperature measurement of the fluid in the cylinder came later.

The raw measurements are processed as described in Chapter 3 to obtain the rheological measurements.

5.3 Flow curve

Mean rheology is investigated and compared to literature by plotting a flow curve, Figure 5.1: a plot of stress against strain rate. For each run in the dataset, the average stress is plotted against the average strain rate. Error bars are used to indicate the uncertainty Sections 3.4.4 and 3.5.5 in both. For a Newtonian material the flow curve should show a straight line through the origin with the gradient being the viscosity. Deviation from this shows eccentricity in the measurements due to machine error.

Table 5.2: *Expected viscosities of materials used in this chapter. Calculated using Equation* (4.3)*: empirical correlations of Cheng [1]. Temperatures used in the calculation are average temperatures measured during shear runs of each material.*

Material	**Temperature** T/°C	**Viscosity** μ/Pa s
G0999	19.3	1.41
G95:W05	17.55	0.60
G85:W15	18.43	0.12

The viscosity of glycerol-water mixtures is dependent on the temperature. Temperature is not controlled throughout the runs, but measured. Average temperatures and viscosities (from tabulated data) are shown on Table 5.2.

On the flow curve, Figure 5.1, the expected viscosity (calculated using the method set out in Section 4.2.1) is plotted alongside the gathered data. This is to provide a

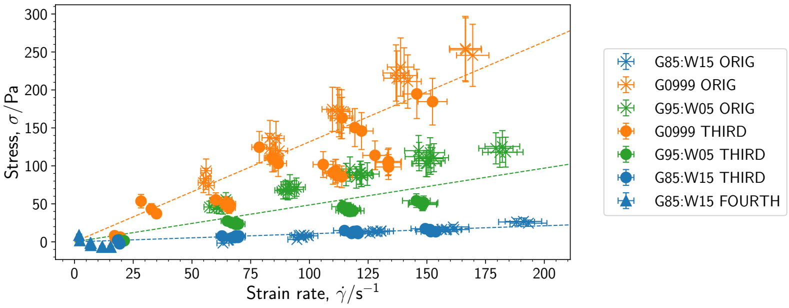

Figure 5.1: *Plot of stress against strain rate for Newtonian test fluids. Faint dashed lines show the expected viscosities from Table 5.2. Each point is a over a* 3 min *run of the material in the rheometer at a specific supply voltage. The legend names both the material, and the combination of gearbox and motor used ("ORIG", "THIRD", or "FOURTH", see Table 3.4). Error bars indicate measurement error, see Sections 3.4.4 and 3.5.5.*

reference to which the data can be compared. Looking at the plot, it can be seen that there is good agreement of the measured data with the expectation for **G0999** (for the most part) and **G85:W15** fluids: the expected viscosity lines are generally within the uncertainty bars on the plot.

This is not the case for the middling fluid, **G95:W05**, and for some measures of **G0999**. **G95:W05** is, on average, in line with expectation. However it has split into two sub-lines: one above and one below. This suggests not a fault with the fitting or calibration procedure, but perhaps a mis-step in the preparation of the fluids. It is discussed in Section 4.2.1 that these solutions' viscosity have a high sensitivity to water concentration. While every care was taken to ensure the solutions were kept away from possible sources of water intrusion, even a decigram of water would noticeably affect the viscosity of 1 kg of **G95:W05**: a 0.1 g increase in water content of a 1 kg mixture of glycerol and water results in a viscosity drop of 5.13×10^{-4} Pa s — a 16% drop in viscosity for only a 1% change in composition (calculated using Equation 4.3 [1]). **G0999** is presenting in some runs to have the same viscosity as that of **G95:W05**, suggesting a drop in concentration to 95 wt% from 99.99 wt% — an increase of $\sim$ 50 g in a $\sim$ 1 kg sample of glycerol. While some water may intrude from the atmosphere, it is unlikely to be on the order of 50 g. A more likely cause of this is due to friction in the torque transmission — causing an artificial increase in stress — or a decrease in this case given that the aberrant measurements are lower. This is discussed in Section 3.5.5.

5.3.1 Qualitative benchmark

A qualitative benchmark of the custom Couette rheometer's ability to measure simple rheology is performed by comparison with a commercial rheometer. A suspension of cornstarch of very low concentration (10wt% approximately Newtonian fluid) is used in both rheometers. The suspension used in both machines was prepared in the same manner. The commercial rheometer data was recorded by another member of the author's lab (Aditi Mukhopadhyay [2]) and is reproduced with permission here. The DHR data is a result of five repeated runs of **CS10:(G85:W15)**, both sweeping up in stress and back down. The CCR (custom Couette rheometer) data are collected as described in Section 4.3. The data from both CCR and DHR are plotted as a flow curve on Figure 5.2.

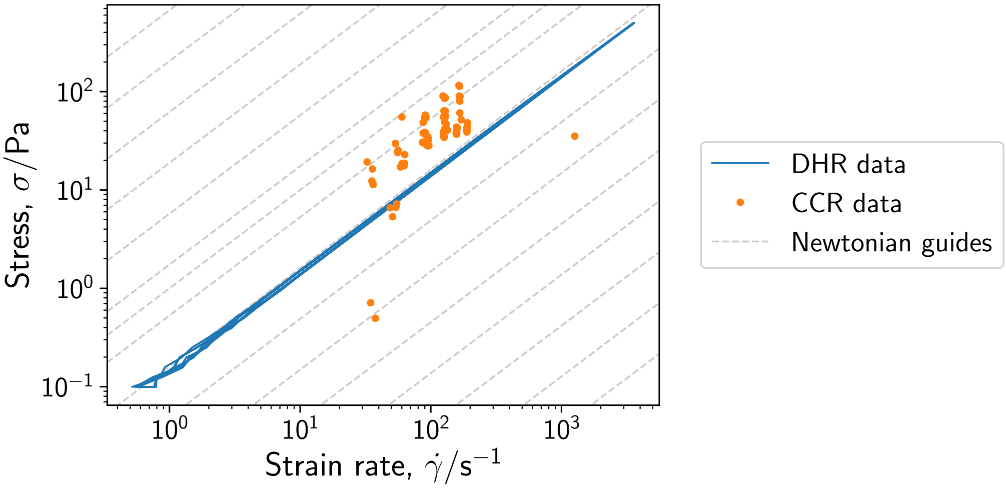

Figure 5.2: 10wt% *Cornstarch in glycerol and water suspension (**CS10:(G85:W15)**) flow curve recorded using the custom rheometer (orange circles) and for a commercial rheometer (TA Discovery HR-2, solid blue lines). Data courtesy of another researcher in the author's lab, Aditi Mukhopadhyay [2]. Newtonian guide lines are provided to guide the eye.*

The flow curve on Figure 5.2, compares the custom rheometer and a commercial rheometer — a TA DHR-3. The measurements taken with the custom rheometer are close to the DHR measurements, but are slightly off. This is likely due to differences in temperature — the DHR experiments were run at 20°C while the CCR data were collected at 16°C. The amount of scatter varies between the two rheometers starkly. The CCR shows a fair amount of scatter, while the DHR shows little scatter. However this is to be expected in a commercial machine as compared to a custom (hand-made) machine. As will be shown, however, the advantages of the custom machine are its ability to take dynamic measurements (Section 5.4 and Section 5.6) and to inter-operate with custom sensors (the Piezoelectric Needle Device — Section 5.7).

5.4 Timeseries

The behaviour of the custom rheometer through time is assessed by looking at how it reports the rheology of a Newtonian fluid in a timeseries. A Newtonian fluid has a viscosity that is constant with respect to strain rate, and this should be seen on the timeseries: each measurement should have a constant value, ideally. However, this is not practicable. Each signal will have noise, so a more realistic expectation is for each of stress and strain rate to fluctuate around a mean value.

Possible sources of noise are discussed in detail in Chapter 3. Briefly, noise enters into into the measurement due mainly to electrical fluctuation, but also due to temperature fluctuation and construction eccentricity. Uncertainty analysis performed in Chapter 3 gives an idea of what range of fluctuation should be expected. The strain rate measurement can be expected to fluctuate $\pm 12\%$ (Section 3.4.4), stress $\pm 42\%$ (Section 3.5.5), and viscosity $\pm 54\%$ (combination of stress and strain rate uncertainties).

Runs of **G0999** are plotted on Figure 5.3, showing how each of the main measurements (strain rate, stress, and viscosity) vary over time. Looking at the leftmost strain rate timeseries first, we notice an expected fluctuation of approximately 15%. Both the absolute and relative magnitude of the fluctuation decreases as the magnitude of the strain rate increases: to approximately 11% in the second strain rate timeseries and 10% in the third. The highest rate series has the lowest fluctuation range of around 8%. This reduction in fluctuation as strain rate (and also rotation rate) is due to the increase in number of optical encoder events: the more events happen the more precise (less fluctuating) the dynamic speed measurement is. This effect is discussed for all measurements in more detail in Section 5.5. Other features of the strain rate series can be seen are the sudden peaks — a form of noise due to electrical interference and too many encoder events happening in a short span of time. There are also “fatter” patches of the strain rate series (somewhat resembling the saddle of an earthworm) which is also potentially a artefact of electrical interference. It is possible that the signals are being affected by another device in use in the lab on the same power circuit causing periodic interference. In general, the strain rate series is flat, with a constant mean value as expected.

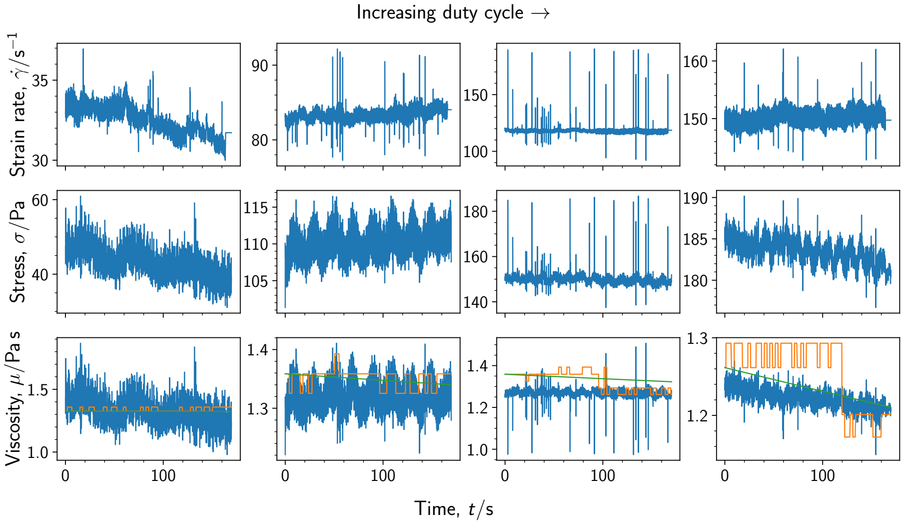

Figure 5.3: *Timeseries for runs of* ***G0999*** *in the custom rheometer at four motor duty cycles, setting four different strain rates. Viscosity timeseries have alongside the measured value (blue solid lines), the expected viscosity (orange dashed lines) for the material using the measured temperature and the relation of [1]. Note the slight downward trend which is expected to be due to a small increase in temperature. Green line shows viscosity drop due to viscous heating effect — described in Appendix E.*

Next, looking at the four stress series, a common feature of the stress runs can be seen: the relatively low-frequency oscillation. This is a by-product of mechanical imperfections, especially in construction of the bearing and con-centring of the cylinders in the shear-cell. The same large peaks are seen in the stress series as in the strain rate series, further evidence that the origin of the peaks are electrical and not a mechanical sensor fault. Also mirrored are the earthworm saddle-like bumps — again seeming to support the hypothesis that the origin of this interference is electrical as the electrical circuit is common ground for both sensors; if a spike in electrical signal affects one sensor, it is likely to affect the other. The precise mirroring of the spikes and saddles between the two sensors indicate an origin common to both, with an electrical source being most likely.

Finally, the viscosity series contain the same features of its constituents. Generally, there is a downward lilt to the viscosity over time (in the first and last series). In the latter, there is a similar decrease in the expected viscosity indicating there may have been an increase in temperature – possibly due to the effect of shear-heating (described in Appendix E). The estimated viscosity drop due to this heating effect is shown on Figure 5.3 in green. The estimated viscosity drop mirrors the observed drop, albeit with an offset in value.

5.5 Signal and Noise

To analyse the consistency of measurement — to see if there is a change in measurement "quality" over a number of logs — estimates of noise can be plotted against measurement (stress, strain rate) magnitude. This will show any trends in measurement noise. For both stress and strain rate measurements, there is an expected relative increase in fluctuation magnitude with decrease in signal magnitude. For the stress measurement, this is due to the decrease in signal to noise ratio in reading measurements from the loadcell — the signal becomes lost in the electrical noise. For strain rate measurement, the increase in noise with lower magnitude is expected as there are fewer rotations per unit of time at low rate which means there are fewer "ticks" of the optical encoder and therefore an increase in measurement scatter

Scatter plots of Percentage Relative Standard Deviation (PRSD) against strain rate and stress are shown on Figure 5.4. In line with expectation the stress noise shows a noise increase as magnitude decreases. The loadcell used in this dataset is the larger of the two used in this Thesis (rated up to 5 kg load — minimum of $\sim 20\,\mathrm{Pa}$). (Measurement span and minimum possible measurements are discussed in Section 3.5.) The PRSD is acceptably low above the minimum of 20 Pa: PRSD below 10%. The strain rate shows an unexpectedly stable PRSD — almost constant at $\sim 4\%$.

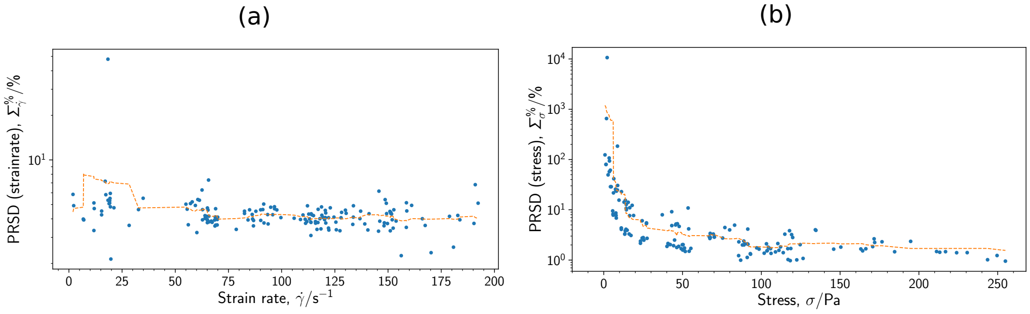

Figure 5.4: *Scatter of Percentage Relative Standard Deviation (PRSD) against* ***(a)*** *strain rate and* ***(b)*** *stress for the dataset of Newtonian runs.*

5.6 Fourier Analysis

5.6.1 Fourier Transform

By applying the Fourier transform to the time-domain signal, constituent frequencies and their power are shown. This is useful for finding more information about which frequencies are more impactful on the signal. For example, an electrical signal with large interference from a poorly shielded AC transformer will have a peak at 50 Hz on the Fourier transform.

Mechanical error due to construction or off-centre cylinder placement should show up as having a frequency with the rate of rotation. Integer multiples of this value may also show up in the FT.

As mentioned, electrical noise due to interference from the AC power supply will show a peak at around 50 Hz. Other electrical noise due to thermal fluctuation will show low-power across all frequencies. This would be most likely to prevail in the stress signal, however the sampling rate of the stress, limited by the ADC (analogue-to-digital converter), is not sufficient, topping out at frequencies of ~ 10 Hz (discussed in Section 3.5).

The time-FT of the strain rate and stress measurements for runs of **G0999**, **G95:W05**, and **G85:W15** are shown on Figure 5.5. It is difficult to pick out any obvious features of the spectra; there are no consistently active frequencies — this is expected for measures of a simple Newtonian fluid.

It is useful to perform the Fourier transform on a measurement with respect to spatial position, instead of time. This is advantageous as it makes rationalising logs

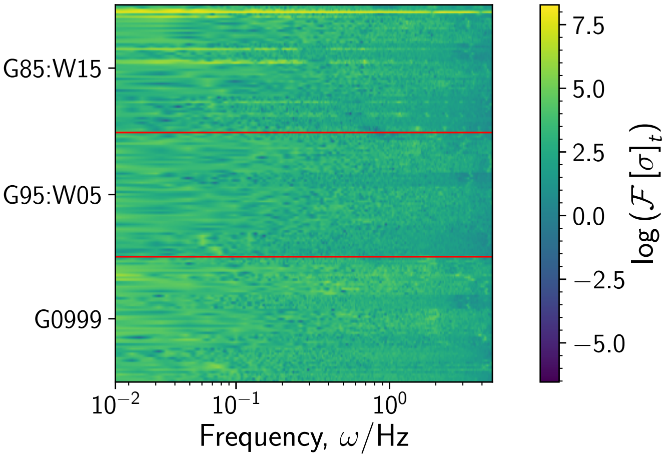

Figure 5.5: *Time-FT of stress for runs of* ***G0999****,* ***G95:W05****, and* ***G85:W15****. FT heatmap is constructed as outlined in Section 4.4.3. No pattern is noticeable in the FT spectra.*

from runs at different rates easier to compare — a single rotation is at the same point for all runs. This spatial-FT is plotted for the same stress measurements as Figure 5.5 on Figure 5.6.

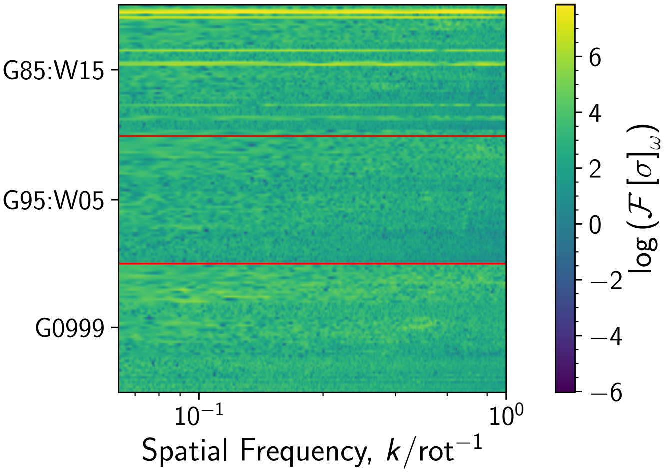

Figure 5.6: *Spatial-FT of stress for runs of* ***G0999****,* ***G95:W05****, and* ***G85:W15****. FT heatmap is constructed as outlined in Section 4.4.3. No pattern is obvious in the sFT spectra.*

With respect to angular position, the Fourier analysis is easier to compare. With the rotation peak fixed at $1\,\mathrm{rot}^{-1}$, there is a fixed reference frame. Going from left to right, increasing rate, if any peaks were increasing or decreasing in frequency we could see it as they move towards or away from the unity line. This doesn't provide more information than the ordinary time-frequency Fourier transform, but frames the information nicely, aiding in the recognition of underlying patterns. As in the tFT, the spatial-FT shows no obvious active frequencies.

5.7 PND Measurements

5.7.1 Timeseries

The measurements made by the novel sensor, the Piezoelectric Needle Device or PND, need a baseline before being used in complex fluid rheometry. Timeseries of the PND voltage over time can be looked at it to get a feel for the dynamics revealed by the sensor. For this dataset, Newtonian fluids, the expectation is that the PND will not show anything interesting. The voltage should fluctuate around a mean of zero, but no peaks should be seen which would indicate something interesting, rheologically speaking, is happening.

The PND voltage from the four **G0999** logs investigated throughout this chapter are shown on Figure 5.7. This shows the voltage hovering around zero, as expected for all four runs. Further, this shows an increase in noise magnitude as the rotation rate (duty cycle) increases.

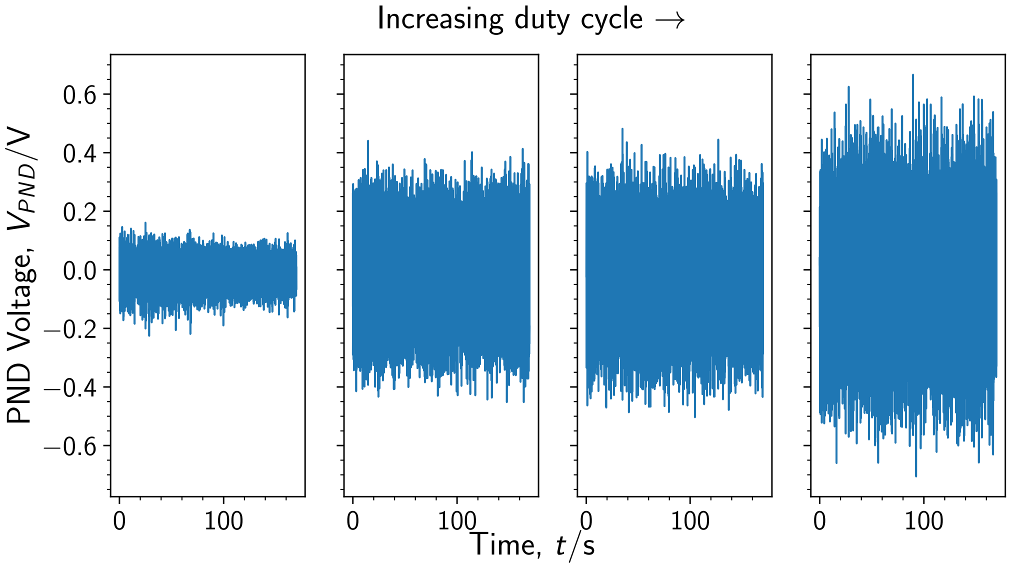

Figure 5.7: *Timeseries of PND value.*

5.7.2 Fourier Transform

The Fourier transform of PND measurements highlights frequencies and therefore possible sources of noise and shows how these are affected by duty cycle, and stress. As with any electrical measurement involving analogue to digital conversion, a peak at 50 Hz due to interference from AC mains supply [3], [4]. Also expected is a possible peak at the rotation frequency, due to mechanical eccentricity resulting in surface waves hitting the needle.

The Fourier transform of the four runs of glycerol presented previously are plotted on Figure 5.8. The FT shows none of the expected features. There is a consistent peak at around 70–80 Hz. This peak increases in magnitude going from low to high duty cycle and is likely the cause of the bulk of noise in the timeseries. Interestingly, this frequency does not shift right as rate increases — it only increases in magnitude. Due to the nature of the piezoelectric disk as, essentially, a microphone, it is possible this noise is in fact the sound of the motor being picked up. However, the low frequency makes this unlikely to be sound, and most likely to be vibration transmitted through the structure of the rheometer. The frequency does not change with motor DC (or rotation rate) making vibration (occurring due to the rotation of the motor) less likely, unless attenuated by the structural materials themselves (clamp stands) to a characteristic frequency (the material's "natural frequency"). The clamp stand forming the basis of the custom rheometer's structure can be approximated as a cantilever with load on one end; for which the natural frequency is estimable from [5]

$$f_n \approx \frac{1.732}{2\pi}\sqrt{\frac{EI}{ml^3}} \tag{5.1}$$

where $E \approx 200\,\text{GPa}$ is the Young's modulus of steel, $I = 490\,\text{mm}^4$ is the area moment of inertia for a 10 mm diameter rod, $m = 0.5\,\text{kg}$ is the mass of the motor and other structure suspended on the end of the bar, and $l = 150\,\text{mm}$ is the length of the rod. These numbers describe an approximation of the structure only. The resulting natural frequency is $\sim 150\,\text{Hz}$ — on the order of that seen in the measurements. More in depth analysis into the features of the PND measurement are given in Chapter 7.

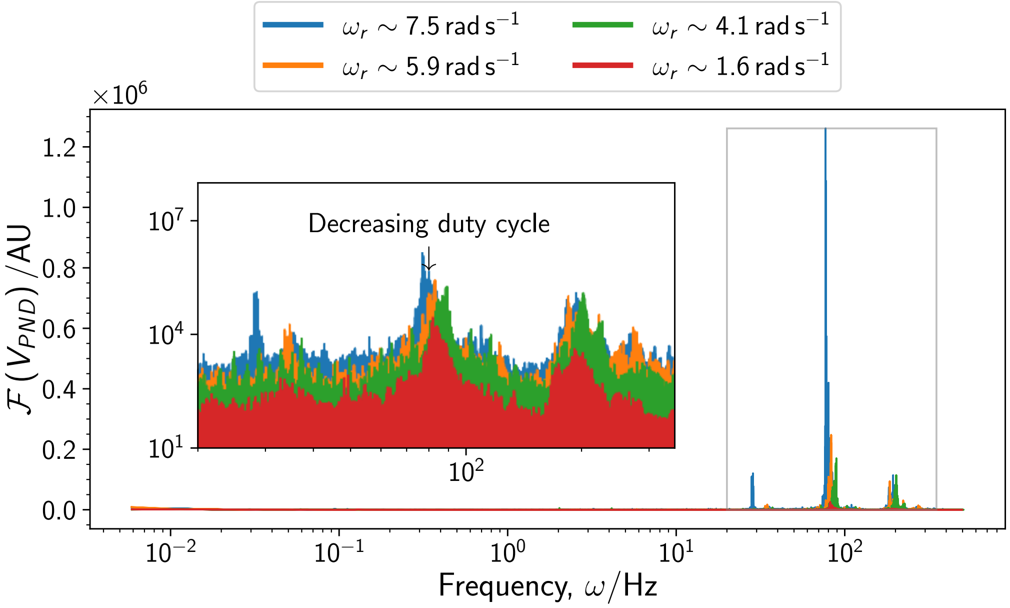

Figure 5.8: *Time-frequency Fourier transform of PND value.*

5.8 Conclusions

In this chapter the ability of the rheometer to report mean-rheological data for Newtonian fluids has been investigated through a flow curve plot constructed of many data points each the mean-average of a 3-5 minute run of the relevant fluid. This curve is compared to tabulated data from literature. Low-water-content solutions of glycerol and water (**G95:W05**) were shown to be poorly fit to expectation — likely due to error in preparing the sample, very easy due to the high sensitivity of the viscosity to water content.

Dynamic, real-time, reporting of rheological properties is important for a rheometer used in the investigation of fluctuations in dense suspensions and is assessed for Newtonian fluids first by reporting typical timeseries plots of the main rheological properties (strain rate, stress, and viscosity) for a sample of glycerol (**G0999**) and latterly by reporting the Fourier transform of the same timeseries plots. Through these analyses it was seen that the rheometer works as expected for Newtonian fluids yielding flat viscosity curves — with a downward trend due to shear heating which is measured and within expectation.

Further dynamic analyses is provided by investigation of the measurements of the novel sensor, the PND. PND output is plotted as a timeseries and as a Fourier transform of same. This showed a characteristic 70–80 Hz noise, seemingly due to the vibration of the motor, present in both plots. This seeks to provide a baseline characteristic for PND measurements to which future analyses can be compared.

References

[1] N.-S. Cheng, “Formula for the viscosity of a glycerol-water mixture,” *Industrial & Engineering Chemistry Research*, vol. 47, 2008.

[2] A. Mukhopadhyay, “Jamming and flow in dense suspensions,” In preparation., Ph.D. dissertation, University of Strathclyde, 2021.

[3] Y. Weiting and Z. Runjing, “An improved self-adaptive filter based on LMS algorithm for filtering 50 Hz interference in ECG signals,” in *2007 8th International Conference on Electronic Measurement and Instruments*, IEEE, 2007, pp. 3–874.

[4] M. Zhi, G. Zhang, X. Zhang, and H. Xue, “A new seismic data processing method for suppressing 50 Hz interference wave,” *Coal Geology & Exploration*, vol. 6, 2010.

[5] W. C. Young, R. G. Budynas, and A. M. Sadegh, *Roark’s formulas for stress and strain*. McGraw-Hill Education, 2012.

6. Complex Rheometry

6.1 Overview

Rheometry is used in complex fluid analysis to observe behaviours such as shear thinning and shear thickening. The latter effect is most characteristic of suspensions such as cornstarch and (glycerol and) water. In this chapter, the custom rheometer will be used to study shear thickening fluids. These measurements will be fit to the popular Wyart-Cates model [1], [2]. From which, a phase diagram for the system will be drawn and will be used to inform investigation of flow instability in Chapter 7.

The chapter will begin with a description, in Section 6.2, of the dataset used in this chapter; the fluids used and their place within the WC framework. This is followed by mean rheology investigation by flow curve in Section 6.3. This is followed by some initial dynamic analysis in Section 6.3 and qualitative benchmarking of the custom Couette rheometer as compared to a commercially available rheometer in Section 6.3.1. Noise trends are unveiled in Section 6.6, followed by more in-depth dynamic analysis in Section 6.7.

6.2 Experimental Details

The data collected for this chapter are summarised briefly in Table 6.1. Runs of cornstarch suspension, following the generic loading procedure laid out in Section 4.3.1, at low to high rate — encompassing thickening behaviour and probable rheological instability. Discussion of the latter is saved for Chapter 7. Rate is set by motor duty cycle (DC), from 20% up to 100% in steps of 16%. The collected data forms a dataset comprised of 417 runs of cornstarch suspended in glycerol-water with 8 compositions ranging from 10wt% up to 44wt%. These runs total 13.3 hours and 96,564 rotations of the shear cell — over the course of 3–5 minute individual runs. The WC phase diagram (Figure 6.1) shows the expected behaviour for the runs of each material at different

Table 6.1: *Summary of dataset including indication of behaviour as predicted by Wyart-Cates model (see Figure 6.1): CST — continuous shear thickening,* ***dst*** *— discontinuous shear thickening including potential unstable flow, whereas (shear) jamming is the phenomenon in which the suspension becomes solid-like under shear. This predicted behaviour is very approximate and relies on accuracy of WC fit to experimental data: see Section 6.3 for WC fit appraisal.*

Material	**Run Count**	**Strain Rate Range**	**WC Behaviour**
CS30:(G85:W15)	38	1s^{-1} to 180.1s^{-1}	CST only
CS35:(G85:W15)	19	1s^{-1} to 168.2s^{-1}	CST only
CS38:(G85:W15)	19	0.9s^{-1} to 5.9s^{-1}	CST only
CS40:(G85:W15)	119	1s^{-1} to 149.8s^{-1}	CST only
CS41:(G85:W15)	20	0.9s^{-1} to 5.9s^{-1}	CST only
CS42:(G85:W15)	97	0.9s^{-1} to 130.5s^{-1}	CST only
CS43:(G85:W15)	20	1s^{-1} to 6s^{-1}	**dst**, no jamming
CS44:(G85:W15)	31	1s^{-1} to 99.2s^{-1}	**dst**, no jamming

measured stress. According to the phase diagram, the majority of the runs performed are in the continuous shear thickening regime (unshaded area on diagram). The two highest concentrations (**CS43:(G85:W15)** and **CS44:(G85:W15)**) encroach upon the discontinuous regions. It is in this region that unstable flow is expected to be seen.

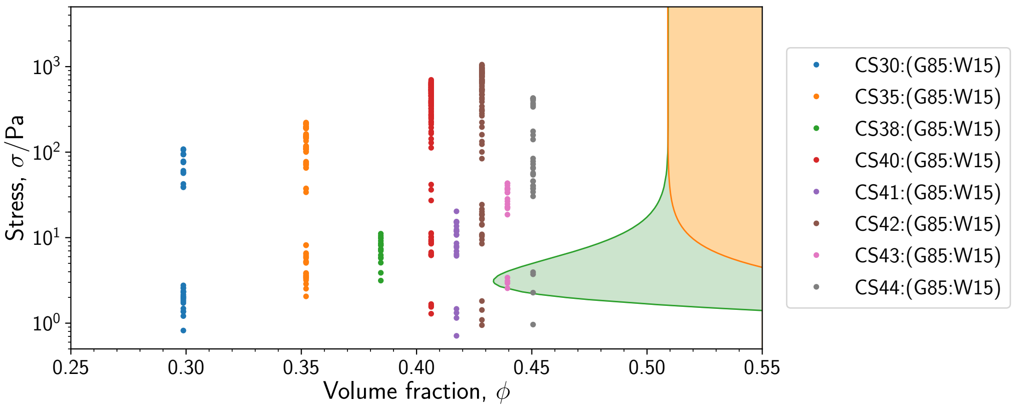

Figure 6.1: *Phase diagram: plot of stress against composition for runs of cornstarch suspension. Shaded areas indicate expected rheological behaviour: green for discontinuous shear thickening and orange for shear jammed. Phase diagram construction and equations described in detail in Section 2.4; fitting of experimental parameters is described in Section 4.2.2. Note difficulty in performing fit (discussed in Section 4.2.2): actual suspension behaviour may not match prediction. WC parameter values used in this plot are the values obtained for the CCR, shown on Table 4.3.*

6.3 Flow curve

The flow curve shown on Figure 6.2 shows the mean behaviour for this dataset. The expected behaviour for a suspension of cornstarch when sheared depends on its concentration. A dilute suspension when sheared will have a Newtonian viscosity slightly higher than the solvent viscosity (Estimable using Einstein's viscosity law Equation (2.2)). As concentration increases, the relationship between stress and strain becomes muddied. Applying the Wyart-Cates framework, reveals a link between stress and strain rate mediated by a probability of frictional contacts. By fitting this framework to this dataset, we can infer rheological properties such as the onset stress and compare to other works. This will further assess the effectiveness of the custom rheometer. Fitting procedure was described in Section 4.2.2.

The data plotted on Figure 6.2 are mean points of stress plotted against mean strain rate for all runs of cornstarch suspension. These show shear thickening behaviour — characterised by the steepening gradient which returns to linear after the suspension is fully thickened (fully frictional flow, $f = 1$ in WC theory). Additionally, the WC model gives context for the behaviour which might be expected for these suspensions.

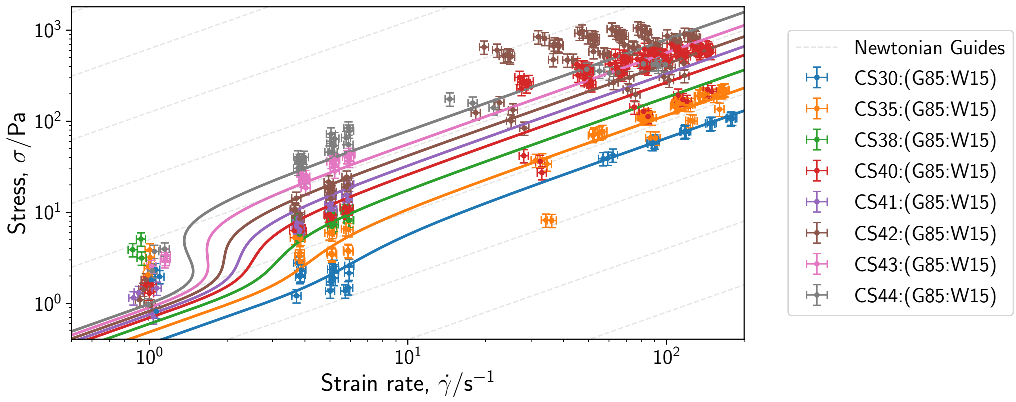

Figure 6.2: *Flow curve plot. Scatter plot of mean stress and strain rate for runs of cornstarch suspensions. Error bars indicate measurement error, see Sections 3.4.4 and 3.5.5. Faint dashed lines indicate gradient of unity (Newtonian behaviour). Coloured lines indicate WC model fit to the data points: Equations 2.1, 2.4, 2.5, and 2.7 combined to give stress as a function of strain rate and the WC fit parameters (WC fitting procedure described in Section 4.2.2). For a comparison of the CCR measurements with a commercial rheometer see Figure 6.3.*

The shallow steepening of **CS30:(G85:W15)**, and **CS35:(G85:W15)** shows a weaker increase in viscosity with strain rate. The higher gradients of **CS38:(G85:W15)**, **CS40:(G85:W15)**, and **CS41:(G85:W15)**, show a stronger thickening effect. Then, from **CS42:(G85:W15)** and above, the flow-curve starts to become s-shaped, and **dst** could be observed. It is important to note the difficulties in the fitting procedure discussed in Section 4.2.2; these predicted behaviours may not be accurate for real cornstarch suspensions.

6.3.1 Rheometer benchmark

In order to gauge, qualitatively, how well the custom Couette rheometer works in comparison to a commercial rheometer, data from both are presented on Figure 6.3.

In the experiments in the commercial rheometer, the suspensions were prepared according to the procedure as laid out in Section 4.2.2. The suspensions were then loaded 500 μl at a time onto the DHR, between the 40 mm Peltier plates (temperature controlled to 20 °C). The top plate is spun to shear the suspension, in two runs. The rheometer is run in stress-controlled mode. One run ‘up’ (increasing stress) and another ‘down’ (decreasing stress). The stress set points are geometrically spaced from

0.1 Pa up to 1000 Pa. These runs can be seen as coloured lines on Figure 6.3.

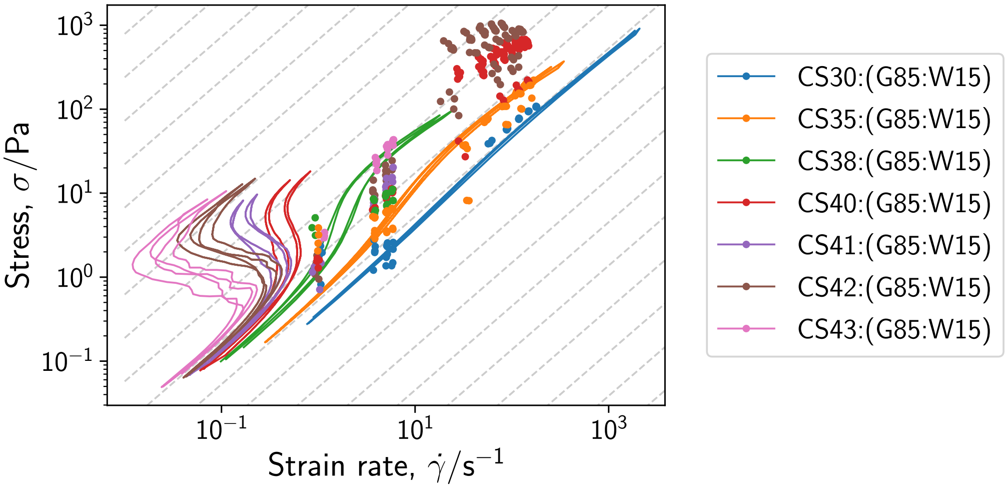

Figure 6.3: *Cornstarch in glycerol and water suspension flow curves for a variety of materials (see legend) recorded using the custom rheometer (circles) and for a commercial rheometer (TA Discovery HR-2, solid lines). Data courtesy of Dr. Jose Ruiz-Lopez (formerly of the author's lab, now at the Basque Center for Applied Mathematics). Newtonian guide lines are provided to guide the eye. For a comparison of the CCR measurements with Wyart-Cates theory see Figure 6.2.*

At high strain rate ($\dot{\gamma} > 10\text{s}^{-1}$), the commercial data presented on Figure 6.3 seem to align with the custom rheometer's measurements. For the higher compositions, extrapolation along the Newtonian guide lines is necessary, but the alignment between measurements can still be seen. There is a discrepancy between the methods in the complex regime at lower rates. This could be explained by the difference in geometries — the DHR being a parallel plate rheometer in contrast to the Couette cell in the custom rheometer.

6.4 Viscosity plot

Mean behaviour of the thickening fluids investigated in this chapter is further analysed by plotted mean viscosity measurements against strain rate. The viscosity of the fluids should increase with strain rate, *to a point*, after which (in the WC framework) the fraction of frictional contacts is saturated and the fluid cannot thicken further resulting in a second Newtonian regime. At very high concentration ($w > 0.4$) the suspension may jam which should present as a very large viscosity but in reality may result in a yielded or broken jam. Other possibilities are a lower viscosity due to dilation and shear (gradient) banding causing the formation of a low-density band within the Couette cell [3].

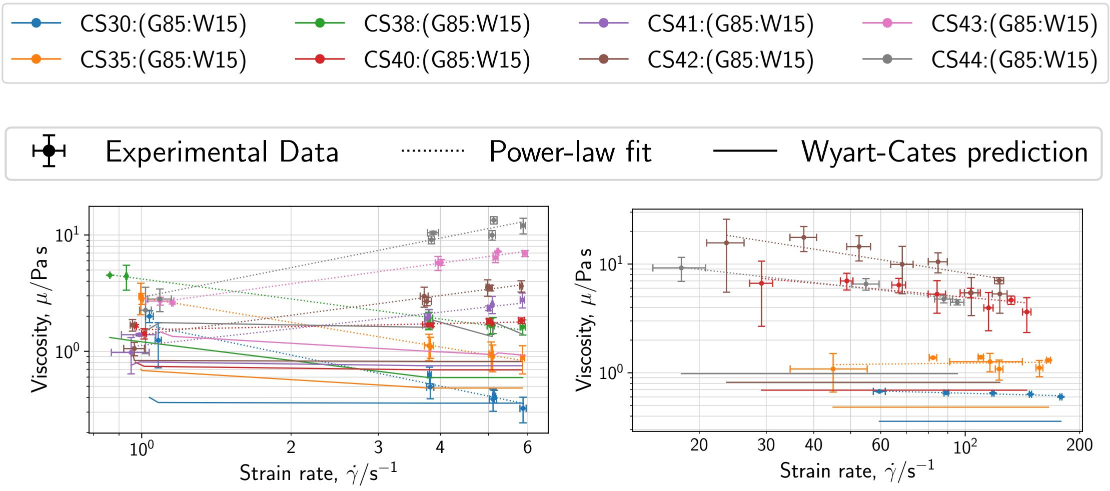

(a) (b)

Figure 6.4: *Mean viscosity measurements plotted against strain rate, split for clarity into two plots:* ***(a)*** *low and* ***(b)*** *high strain rate. Dotted lines are power law fits to the measurements — included to emphasise the general trends in the measurements. Power law fits chosen to better fit the data. Wyart-Cates predictions of viscosity are shown on the solid lines. Each point is a result of averaging across many measurements at that strain rate. Error bars indicate standard deviation between these measurements.*

Mean viscosity is plotted against mean measurements of strain rate on Figure 6.4. This plot is split into two parts: a low-rate part on Figure 6.4a and a high-rate part on Figure 6.4b. This is to show the detail in both parts, otherwise the range of viscosities involved in the high-rate part overshadows the low-rate part.

The low-rate plot (Figure 6.4a) shows the simple shear thickening expected for thickening suspensions for the higher concentration experiments (**CS40:(G85:W15)**, **CS41:(G85:W15)**, **CS42:(G85:W15)**, **CS43:(G85:W15)**, and **CS44:(G85:W15)**). For the lower concentration lines however no thickening is seen: in fact, it seems the fluid is thinning.

The high-rate plot (Figure 6.4b) has a much less clear-cut description. The lowest concentrations, **CS30:(G85:W15)** and **CS35:(G85:W15)**, are maintaining a nearly-

Newtonian behaviour. The higher three concentrations (**CS40:(G85:W15)**, **CS42:(G85:W15)**, and **CS44:(G85:W15)**) all show large variability in measurements. The average trend of this data indicates a thinning regime coming down from a high viscosity ($\mu > 30\,\mathrm{Pa\,s}$).

For both the high- and low-rate plots on Figure 6.4 a Wyart-Cates viscosity prediction is included. The viscosity prediction at low rate is closer to measured viscosity than at high rate, likely arising from the difficulty in performing the fit, discussed in Section 4.2.2.

Thinning in dense suspensions at higher stresses has been seen as a side effect of migration: liquid migration [3], [4] describes the movement of fluid towards a highly sheared region of the suspension as it dilates. In a Couette cell, this could create a high density (and high viscosity) jammed area by the fixed outer cylinder wall. The fluid from this section would then have migrated into the area close to the moving cylinder; this region has dilated and lowered its particle concentration[*]. Calculation of the size of the low- and high-rate bands is conducted in Appendix H. Band position r_B was calculated for a few selected runs in the CCR — runs chosen were within the green **dst** region on Figure 6.1 and so are expected to have dilated.

The calculation was performed once with the set of Wyart Cates parameters found after fitting to data recorded by the CCR, and to data recorded by the commercial DHR (TA Discovery HR-3) — parameters presented on Table 4.2. The four exemplified runs are of two concentrations (**CS44:(G85:W15)** and **CS45:(G85:W15)**, with approximate volume fractions ϕ of 0.44 and 0.45 — see Figure 4.6) with stresses between 2.9 Pa–3.8 Pa. The results are summarised on Table 6.2 for CCR WC parameters, and on Table 6.3 for DHR WC parameters. Both sets of parameters are presented on Table 4.2. The percentages are jammed region size with respect to the Couette gap size. There are two strain rates that can be defined: the nominal strain rate is where the velocity difference is realised across the entire gap, and estimated actual strain rate where the velocity difference is realised across the dilated region (no velocity in the shear jammed region). A “measured viscosity” can then be defined as the ratio between the shear stress (assumed uniform in a narrow gap approximation) and the nominal strain rate. An estimate of the dilated region viscosity can be defined as the

---

[*] This is not the only scenario that can be envisaged. As well as the inner cylinder region ordinarily being highly sheared, it also has higher shear stress, moving it closer to the jammed region in the phase diagram. Thus jamming might occur instead near the inner cylinder, and dilation might occur near the outer cylinder. At which cylinder jamming or dilation occurs therefore remains an open question

Table 6.2: *Shear band sizes r_B for several runs in the CCR. Calculation described in Appendix H and performed using CCR WC fit parameters (see Table 4.2). For comparison, the inner cylinder radius is* 0.01505 m *and the outer cylinder radius is* 0.01975 m*. Numbers in parentheses are size of the low-rate and thickened band expressed as a percentage of gap.*

Volume Fraction ϕ	**Stress** σ	**Measured Viscosity** μ	**Shear Band Location (CCR)** r_B	**Band Viscosity** μ_B	**Band Volume Fraction** ϕ_B
0.44	2.981 Pa	2.561 Pa s	0.01962 m (3%)	2.524 Pa s	0.433
0.44	3.501 Pa	2.969 Pa s	0.01965 m (2%)	2.949 Pa s	0.434
0.45	3.567 Pa	3.386 Pa s	0.01930 m (10%)	3.062 Pa s	0.434
0.45	3.751 Pa	3.225 Pa s	0.01927 m (10%)	2.959 Pa s	0.436

ratio between the shear stress and the aforementioned estimate of the actual strain rate. The latter viscosity value is always smaller than the former, because (for specified stress) the latter is based on a smaller thickness and hence on a larger estimate of the strain rate.

The different sets of estimated parameters result in very different estimates of how much of the gap is jammed. The CCR WC parameters result in jammed region sizes up to 10% of the gap while the DHR results in jammed region sizes up to 100% of the gap (meaning the suspension is fully jammed). (WC parameter sets are given in Table 4.3 and corresponding phase diagrams are shown on Figure 4.9.) Correspondingly, there are very different viscosities predicted for the dilated band. The CCR parameters (Table 6.2) result in shear thinning in the dilated band for the correspondingly small jammed band.

The DHR (Table 6.3) parameters predict in shear jamming with a jammed band nearly completely encompassing the gap. Despite this predicted complete jamming, the system still shears and so the (dilated band viscosity is estimated to be very low. The parameters used for this calculation were fit to data from the DHR, a parallel plate rheometer: the differing geometry may go some way to explain the differences in behaviour. Moreover, there were the issues faced in fitting the parameters: discussed in Section 4.2.2.

Table 6.3: *Shear band sizes r_B for several runs in the CCR. Calculation described in Appendix H and performed using commercial DHR (TA Discovery HR 3) WC fit parameters (see Table 4.2). For comparison, the inner cylinder radius is* 0.01505 m *and the outer cylinder radius is* 0.01975 m. *Numbers in parentheses are size of the low-rate and thickened band expressed as a percentage of gap.*

Volume Fraction ϕ	**Stress** σ	**Measured Viscosity** μ	**Shear Band Location (DHR)** r_B	**Band Viscosity** μ_B	**Band Volume Fraction** ϕ_B
0.44	2.981 Pa	2.561 Pa s	0.01756 m (47%)	1.388 Pa s	0.425
0.44	3.501 Pa	2.969 Pa s	0.01799 m (37%)	1.889 Pa s	0.430
0.45	3.567 Pa	3.386 Pa s	0.01515 m (98%)	0.074 Pa s	0.431
0.45	3.751 Pa	3.225 Pa s	0.01503 m (100%)	Jammed	0.432

6.5 Timeseries

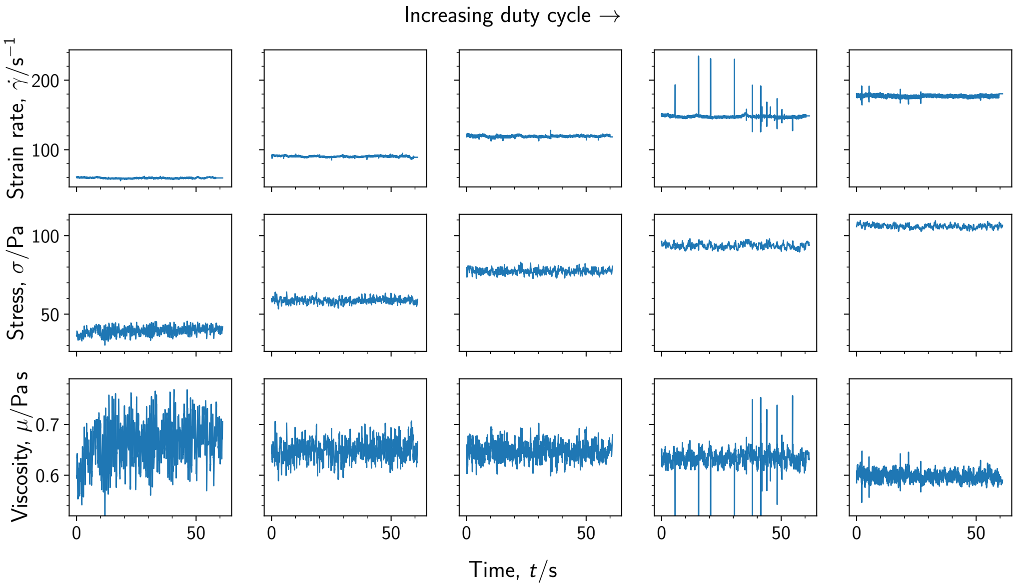

Figure 6.5: *Typical timeseries plots of strain rate, stress, and viscosity for* ***CS30:(G85:W15)***.

Timeseries plots for rheological properties are shown on Figure 6.5 for a typical subset of the dataset for **CS30:(G85:W15)**. These plots increase in duty cycle from left to right and thus also strain rate. This particular cross section of the runs of **CS30:(G85:W15)** has a lowest stress of $\sim 30\,\mathrm{Pa}$, far above the system's onset stress of $\sigma^\star \approx 1$–$10\,\mathrm{Pa}$. Due to this, the system should in fact be seen to have a constant viscosity — an expectation which is indeed shown on the plot, and consistent with that seem on Figure 6.4b. Similar features are seen on these timeseries as previously seen in Section 5.4: fluctuation about a mean, sudden peaks, and “saddling” (earthworm-like bulging) — taken to be an effect of electrical interference.

6.6 Signal and Noise

The noise present in a measurement is estimated by calculating the PRSD (percentage relative standard deviation). Comparing the PRSD in a measurement with the magnitude shows trends in fluctuation. In the Newtonian system discussed in Section 5.5, PRSD for stress measurements should increase for lower value measurements. Strain rate measurements were initially thought to follow a similar path, but found instead in Section 5.5 to be consistent across all values of rate.

PRSD plots are shown on Figure 6.6. Figure 6.6b shows the same increased PRSD for low stress values as expected, and as seen previously for Newtonian measurements. However, the strain rate PRSD shows a deviation from that seen in Section 5.5: there is a slight increase in PRSD at lower rate — in-line with the original expectation due to low rotation rate (see Section 3.4).

Due to the Newtonian result, it is presumable that the increase in PRSD is not a property of the sensor itself but an effect of the fluid — indicating perhaps the presence of the unstable flows described in Section 2.3.6. Looking at the phase diagram, Figure 6.1, flow instabilities are expected for runs which impinge on the green “dst” region. Fluctuation should therefore be seen at the low-middle stresses producible by the custom rheometer, shown on Figure 6.6 as pink and grey circles. It should be noted that higher stresses could be developed by the rheometer here. These fluctuations are investigated in detail in Chapter 7.

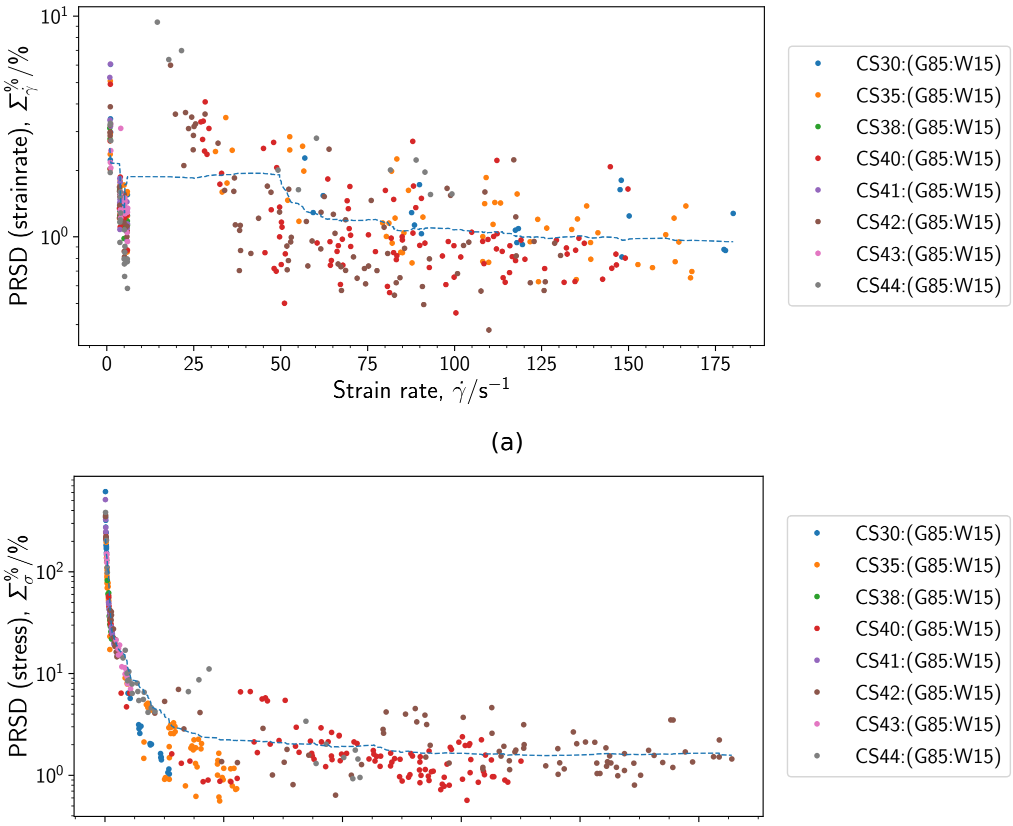

(a)

(b)

Figure 6.6: *Plots of PRSD against* ***(a)*** *strain rate, and* ***(b)*** *stress.*

6.7 Fourier Analysis

Fourier transforms (time-FTs) are shown on Figure 6.7. The FTs have only a few active modes in which a pattern can be seen. At low frequency, $\omega < 0.1\,\mathrm{Hz}$, there is a wide mode increasing with rate for **CS40:(G85:W15)** and **CS42:(G85:W15)** — but not noticeable in other materials. In the middle frequencies, $0.3\,\mathrm{Hz} < \omega < 1\,\mathrm{Hz}$ there are several different peaks. It is difficult to discern if these peaks vary with rotation rate from this plot. Finally, there is a set of active modes/peaks at the high end of the frequency range, $\omega > 3\,\mathrm{Hz}$, increasing in rotation rate.

As the first and last set of modes increases with rotation rate (bright colour moving right as rate increases moving downward on Figure 6.7), these are both likely related to a mechanical noise introduced to the system, the higher frequency is likely due to the

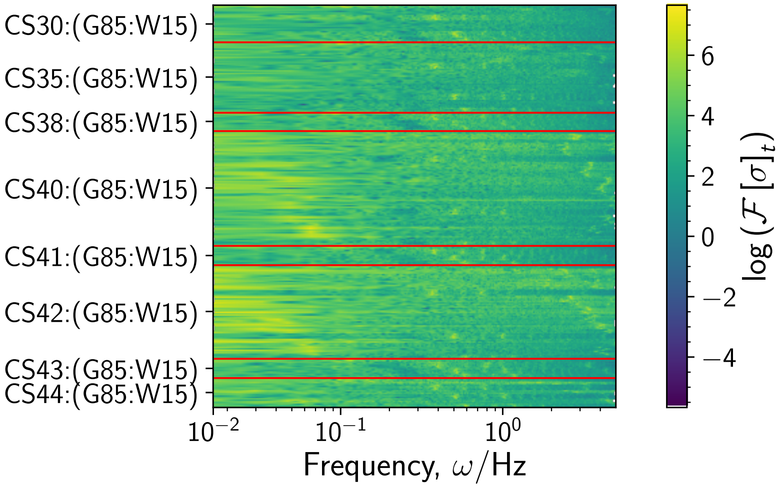

Figure 6.7: *Time-FT of stress measurements of cornstarch suspensions. Plots are constructed as outlined in Section 4.4.3. Within each band of a material, delineated by the red lines, each horizontal line of pixels represents a run of the material at a motor duty cycle setpoint (see Section 6.2), which increases within the band from top to bottom.*

small bumps or grooves in the 3D printed bearing. The low frequency noise however is only present in a few runs but is consistently in those runs (**CS40:(G85:W15)** and **CS42:(G85:W15)**). This suggests it is related to the fluid — perhaps an interaction of a slightly off-centre cylinder (see Section 4.3.2).

Fourier transforming instead with respect to angular position and not to time yields the spatial-FT plotted on Figure 6.8. On this plot, the rotation rate effects seen on the previous tFT plot can be confirmed: a vertical line on the sFT shows that the oscillations occur the same number of times in a given rotation (i.e. at some multiple of the rate of rotation). The low frequency modes seen for **CS40:(G85:W15)** and **CS42:(G85:W15)** prior are seen again here. The scatter of active modes in the mid frequencies presents as a set of lines at spatial frequencies of integer values — at multiples of the (temporal) rotation rate. This further supports the theory that it is due to mechanical fault in the bearing, although it could also be explained by an off-centre inner cylinder. A strong oscillation at a frequency will present, on a Fourier transform, as a set of peaks at integer multiples — the effect seen here.

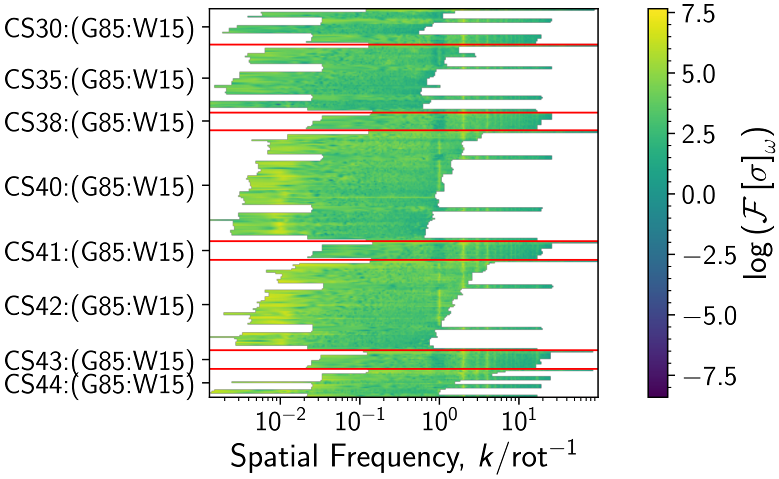

Figure 6.8: *Spatial-FT of stress measurements of cornstarch suspensions. Plots are constructed as outlined in Section 4.4.3. Within each band of a material, delineated by the red lines, each horizontal line of pixels represents a run of the material at a motor DC setpoint (see Section 6.2), which increases within the band from top to bottom. Due to the poor overlap of the frequencies (in turn due to the wide range of rotation rates) the ends of the runs are included resulting in the blank spaces on the ends of the heatmap.*

6.8 Conclusions

In this chapter, shear thickening behaviour of suspensions of cornstarch in glycerol-water are investigated. The WC phase diagram presented in Section 6.2 sets the tone for the dataset: showing what behaviours are expected for each run. Mean-rheometry in Section 6.3 showed the thickening behaviour expected for these suspensions. The WC model was fit to this flow curve, which was used in plotting the phase diagram.

Features observed in the data are then described in the context of the WC phase diagram (where fluid is in one of the continuous, discontinuous, or jammed regimes). Typical data were exemplified in timeseries form to gain a feel for the features and phenomena measured by the custom rheometer for these fluids.

Fourier analysis was used to aid in identifying sources of noise/fluctuation in measurements. These plots also set a baseline to which results in the following chapter are compared.

References

[1] M. Wyart and M. E. Cates, “Discontinuous shear thickening without inertia in dense non-Brownian suspensions,” *Physical Review Letters*, vol. 112, no. 9, pp. 1–5, 2014.

[2] B. M. Guy, C. Ness, M. Hermes, L. J. Sawiak, J. Sun, and W. C. K. Poon, “Testing the Wyart-Cates model for non-Brownian shear thickening using bidisperse suspensions,” *Soft Matter*, vol. 16, no. 1, pp. 229–237, 2020.

[3] A. Fall, F. Bertrand, D. Hautemayou, C. Méziere, P. Moucheront, A. Lemaitre, and G. Ovarlez, “Macroscopic discontinuous shear thickening versus local shear jamming in cornstarch,” *Physical Review Letters*, vol. 114, no. 9, p. 098 301, 2015.

[4] R. E. ONeill, J. R. Royer, and W. C. Poon, “Liquid migration in shear thickening suspensions flowing through constrictions,” *Physical Review Letters*, vol. 123, no. 12, p. 128 002, 2019.

7. Local Rheometry

> *"Nothing happens until something moves."*
>
> Albert Einstein

7.1 Overview

In this chapter the dynamic rheology of cornstarch suspensions will be assessed both using global rheometry and using local measurements from the Piezoelectric Needle Device (PND) — the bespoke local stress sensor based around a needle inserted into the surface of the fluid (Section 3.8).

This chapter begins with a description of the dataset in focus in Section 7.2, describing expected behaviour by fit to WC theory shown on the phase diagram. Then the timeseries (Section 7.3) will be shown for typical runs of materials in different points on the phase diagram to provide a qualitative idea of the differences in dynamics. These differing dynamics are more quantitatively investigated in Section 7.4 in which the time and space frequency spectra are displayed. PND voltage measurements are investigated in Section 7.5. Analysis of the peaks in PND measurements is given in Section 7.6. A description of some anomalous measurements is given in Section 7.7. Finally, a summary of the findings are then given in Section 7.8.

7.2 Experimental Details

The dataset for this chapter encompasses 358 individual runs of cornstarch suspensions, totalling approximately 16.3 hours of total run time and 11,924 rotations of the shear cell, summarised on Table 7.1. The dataset includes 9 compositions from **CS30:(G85:W15)** up to **CS45:(G85:W15)**. The range of strain rates (approximately

Table 7.1: *Summary of dataset*

Material Sub-set	Contents	Strain rate Range
CS30:(G85:W15)	60 logs	From $1\,\mathrm{s}^{-1}$ to $6\,\mathrm{s}^{-1}$
CS35:(G85:W15)	40 logs	From $1\,\mathrm{s}^{-1}$ to $5.9\,\mathrm{s}^{-1}$
CS38:(G85:W15)	39 logs	From $0.9\,\mathrm{s}^{-1}$ to $6\,\mathrm{s}^{-1}$
CS40:(G85:W15)	40 logs	From $0.9\,\mathrm{s}^{-1}$ to $5.9\,\mathrm{s}^{-1}$
CS41:(G85:W15)	40 logs	From $0.9\,\mathrm{s}^{-1}$ to $5.9\,\mathrm{s}^{-1}$
CS42:(G85:W15)	39 logs	From $0.9\,\mathrm{s}^{-1}$ to $5.9\,\mathrm{s}^{-1}$
CS43:(G85:W15)	40 logs	From $1\,\mathrm{s}^{-1}$ to $6\,\mathrm{s}^{-1}$
CS44:(G85:W15)	40 logs	From $1\,\mathrm{s}^{-1}$ to $5.9\,\mathrm{s}^{-1}$
CS45:(G85:W15)	20 logs	From $1.1\,\mathrm{s}^{-1}$ to $5.9\,\mathrm{s}^{-1}$

between $1\,\mathrm{s}^{-1}$ and $10\,\mathrm{s}^{-1}$) were chosen to cover a range of stresses around the onset stress, around 5–10 Pα, see Sections 2.3.3 and 4.2.2. Note the difficulties in estimating onset stress by fitting data to the Wyart Cates model hence the decade-wide strain rate range).

The entire dataset is plotted in the form of a phase diagram on Figure 7.1: measured stresses in each run of suspension are plotted against volume fraction (estimated from mass fraction using the method of Han et al [1] (Equation 4.4), described in Section 4.2.2). Picked out on the figure in solid black circles are three example runs which will be shown in more detail in Section 7.3. Flow curves for the materials in the example runs (**CS35:(G85:W15)**, **CS40:(G85:W15)**, and **CS43:(G85:W15)**) are given in Section 6.3. This is plotted on the backdrop of the WC phase diagram, providing context for the measurements. From the plot, it could be expected that runs of cornstarch above **CS42:(G85:W15)** would experience unstable flow at stresses approximately between between 2 Pα and 5 Pα. This is not the case — likely due to difficulties in fitting the WC framework to a polydisperse porous material like cornstarch (discussed previously in Section 4.2.2 — see Figure 4.9 and Table 4.3). Instead here the interesting flow phenomena are seem at a lower volume fraction around 40 % — perhaps explained by the effect polydispersity has been seen to have on packings. As described in Section 2.3.1: an increase in polydispersity changes ϕ_{RLP} (the volume fraction of Random Loose Packing or RLP) therefore could be expected to change the volume fraction at which frictional contact affects flow, although an increase in poly-

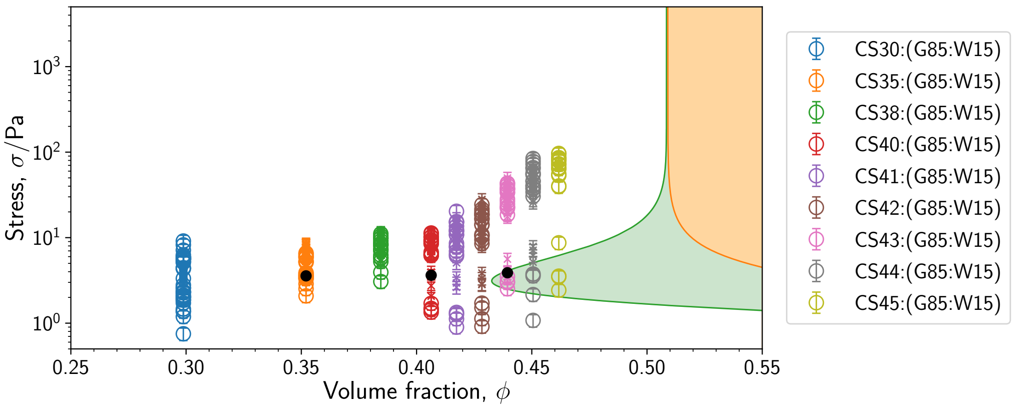

Figure 7.1: *Phase diagram: plot of stress against composition for runs of cornstarch suspension. Shaded areas indicate expected rheological behaviour (according to the WC model): green for discontinuous shear thickening and orange for shear jammed. Note difficulty in fitting the WC model — see Figure 4.9 and Table 4.3 in Section 4.2.2. Colour of points indicates material as in legend; symbol type indicates use or otherwise of novel sensor Piezoelectric Needle Device (PND): cross for lack of PND and empty circle for presence of PND. Phase diagram construction described in detail in Section 2.4. Solid black circles indicate location of three exemplified points showing Newtonian (**G0999** at $\sigma = 143.2$Pa, off to the left of the plot), CST (**CS30:(G85:W15)** at $\sigma = 3.70$Pa), and **dst** (**CS43:(G85:W15)** at $\sigma = 40.9$Pa). Faint dashed horizontal lines show WC parameters; horizontal for onset stress, left vertical for ϕ_{dst} (minimum volume fraction for **dst**) and right vertical for ϕ_m (minimum volume fraction for jamming). These particular plots are made example of as they show a cross section of features observed in runs using the device discussed in Section 7.3.*

dispersity has been linked to an increase in ϕ_{RLP}, not a decrease [2]. The aspherical shape of the cornstarch particles may also have an effect on the concentration at which particles interact [3]. Figure 4.4(c) shows an SEM image of the cornstarch particles where their shape can be seen to range from polyhedral/approximately spherical to more elongated shapes.

7.3 Timeseries

Runs of cornstarch were performed, measuring strain rate, stress, and voltage from the PND. Timeseries of these measurements (and viscosity) a typical set of three runs for a dense ($w = 42\,$wt%) suspension of cornstarch are shown on Figure 7.2.

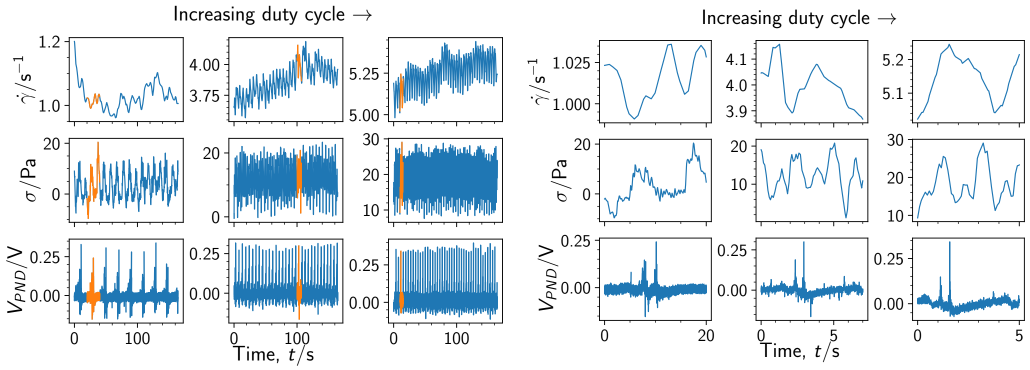

(a) (b)

Figure 7.2: *Timeseries of strain rate, stress, and PND for a typical set of runs of cornstarch (**CS42:(G85:W15)** shown). Orange sections in **(a)** are magnified in **(b)**. Sections were chosen to encompass a single PND "event".*

The timeseries show both a long time plot and a magnified segment. The long-time plots are 3-minute runs in the custom rheometer and show the slow-moving dynamics of the measurements. All three of the full typical runs (Figure 7.2a) show no appreciable change in the course of the runs for stress, and viscosity. These two measurements have a consistent mean. The strain rate shows a more dynamic behaviour: falling in the first run, rising in the middle two, and jumping slightly in the last one. However, this change is not significant and is only visible due to the low measurement noise.

The magnified typical runs on Figure 7.2b were chosen to capture a single PND "event" — a peak. These peaks are regularly spaced, at a frequency increasing with rotation rate — the peaks occur once per rotation (discussed further in Section 7.6). Looking at the strain rate timeseries, there are small variations in the measured rate. Stress has a larger magnitude variation, which then carries through to the viscosity series. The PND peaks tend to coincide with a high stress value (an effect explored further in Section 7.5).

The PND measurements have different "quality", depending on the suspension concentration. Lower concentrations ($w < 0.4$) have a "plain" response, with a lack of peaks or obvious features other than noise. Higher concentrations ($w > 0.4$) can have a wavy response, or a completely flat response like the low concentrations. As mentioned earlier, there is an interesting response seen around **CS40:(G85:W15)** (approximately $\phi = 0.4$). There are large peaks seen in these measurements, typically once per rotation.

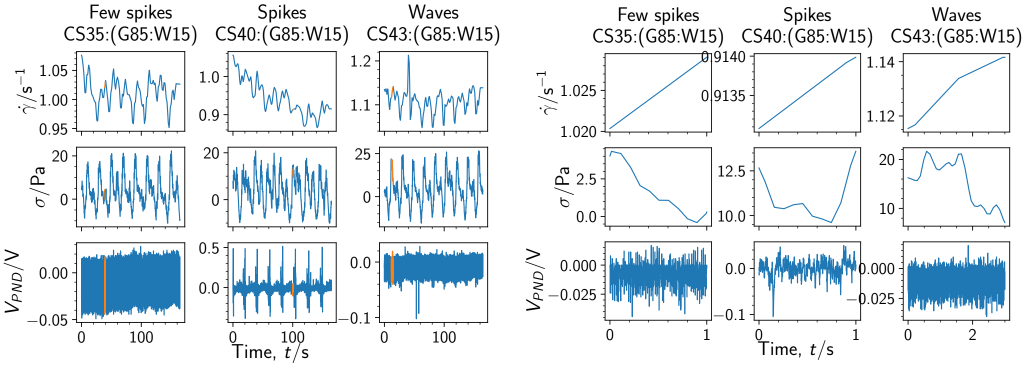

(a) (b)

Figure 7.3: *Timeseries of strain rate, stress, and PND voltage for a set of three runs exemplifying three possible states: few spikes (**CS35:(G85:W15)** at $\sigma = 3.57\,\mathrm{Pa}$), spiky (**CS40:(G85:W15)** at $\sigma = 3.63\,\mathrm{Pa}$) and wavy (**CS43:(G85:W15)** at $\sigma = 3.89\,\mathrm{Pa}$). Orange sections in **(a)** are magnified in **(b)**.*

In the same manner as Figure 7.2, the timeseries picked out on Figure 7.3 have magnified sections intended to show the different qualities in the measurements. The **CS35:(G85:W15)** plots shown have a characteristically noisy PND response — sitting generally around $0\,\mathrm{V}$ but dropping as low as $-0.2\,\mathrm{V}$ very occasionally. In contrast, **CS40:(G85:W15)** shows a surprising defined peak at about one peak-per-rotation ($\omega_r \sim 0.289\mathrm{rad\,s^{-1}}$). These defined peaks disappear going up in concentration further, turning into waves for **CS43:(G85:W15)** and disappearing altogether into noise above this (not shown on the figure).

This transition from noise (not spiky) to peaks (spiky) to waves (not spiky) could be explained by WC theory. The particles in suspension are closer together as concentration increases and therefore more likely to be in frictional contact. This could result in the formation of clusters (Section 2.3.3) travelling around the suspension at the rotation rate. As concentration increases and the unstable region is entered, the fluid could organise itself into low-density and high-density areas — the low density area allowing flow to continue — an effect seen in the literature [4], [5]. The waves seen for **CS43:(G85:W15)** could be these areas of high density travelling around the cylinder. Alternatively, it could be a dense (shear banded) region growing and shrinking and thus moving in and out of contact with the needle.

7.4 Fourier Analysis

Fourier transformation (FT) of stress measurements shows the dynamic components of the measurement. The Fourier transforms of the stress signal for every run is plotted as a pair of heat maps on Figure 7.4 with respect to time (time-FT, or tFT), and to angular position (spatial-FT or sFT). The former shows dynamics which change in time, and the latter highlights oscillations which occur as the cylinders rotate (changing angular position). More information on the FT procedure is given in Section 4.4.3. These stress plots are a **dst**-focussed subset of the plots previously presented in the previous chapter (Figures 6.7 and 6.8) — they are **dst** focussed in that the runs chosen for these plots have stresses commensurate with the **dst** region on the WC phase diagram. These plots are presented here to give context for and to facilitate comparison with PND voltage Fourier transform plots (Figure 7.5).

The lack of consistent vertical lines on the tFT of stress (Figure 7.4a) shows there are no significant oscillations present in the stress signal at least none which are present irrespective of rotation rate. However, due to the low sampling rate of stress (see Section 3.5.5), this Fourier transformed signal is truncated at a fairly low frequency of 5 Hz and would not show electrical interference around 50 Hz or possible higher frequency noise. From top to bottom the rotation rate of the runs within each composition bracket (delineated by the red line). Within a 1D horizontal strip for any composition, any rate, we see short bright lines — indicating peaks on the stress tFT. These peaks move from left to right as rate increases which indicates they are linked to rotation rate. These peaks seem to have reflections with diminishing power at integer multiples — indicating an irregularity in the shape of the oscillation (not able to be approximated nicely by a sine wave). At low rotation rate, there are fewer peaks at higher frequency. There is a brighter (higher power) region at low frequency.

The stress sFT shows a strong vertical line at $1\,\mathrm{rot}^{-1}$ — indicating a recurring signal occurring once every rotation. As seen in the time-based FT are other lines of diminishing power at integer multiples. As the needle was inserted while these measurements were taken, it is possible that this resulted in the once-per-rotation signal.

The Fourier transform of PND voltage measurements is shown as a pair of heatmaps on Figure 7.5 with respect to time and angular position. On the time-based FT plot, Figure 7.5a, there are non-aligned vertical lines indicative of some oscillation related to the rotation rate, similar to those on the stress FT. However there is also a solid line at 50 Hz — indicating some interference from AC power. There is another set of

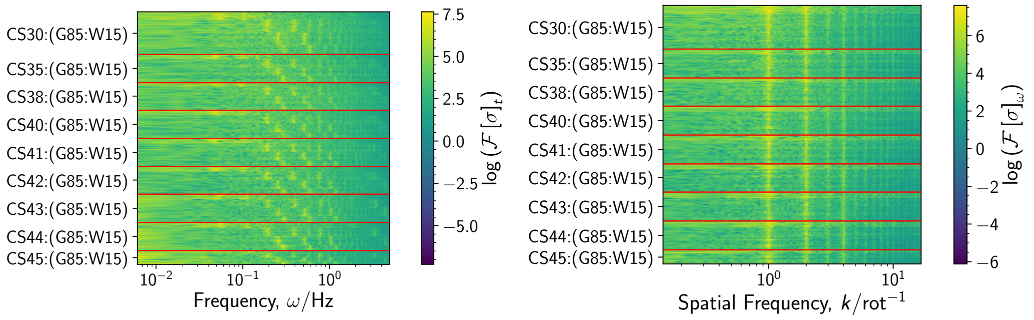

(a) (b)

Figure 7.4: *Heat map showing Fourier transform of stress for different compositions of suspension* ***(a)*** *with respect to time, and* ***(b)*** *with respect to angular position. Plots are constructed as outlined in Section 4.4.3. Within each band of a material, delineated by the red lines, each horizontal line of pixels represents a run of the material at a motor DC setpoint, which increases within the band from top to bottom. The data plotted here are a subset of that shown on Figure 6.7 and Figure 6.8.*

un-aligned lines around 200 Hz.

On the spatial-FT for PND voltage, there is a strong peak at 1 rot^{-1}, present only for concentrations above 38 wt%. There are a group on unaligned lines around 200 rot^{-1} corresponding to the single line at 50 Hz on the time-based FT. The last feature is a line at 700 rot^{-1}. This line is present for all compositions, but only appears for higher duty cycle runs. This is likely motor mechanical interference (vibration) which increases in magnitude as duty cycle is increased. While there is no single frequency mode appearing for **CS40:(G85:W15)**, there is an increase in activity for this material — shown by the bright lines stretching horizontally on both FT plots. These features at **CS40:(G85:W15)** are discussed in Section 7.5.

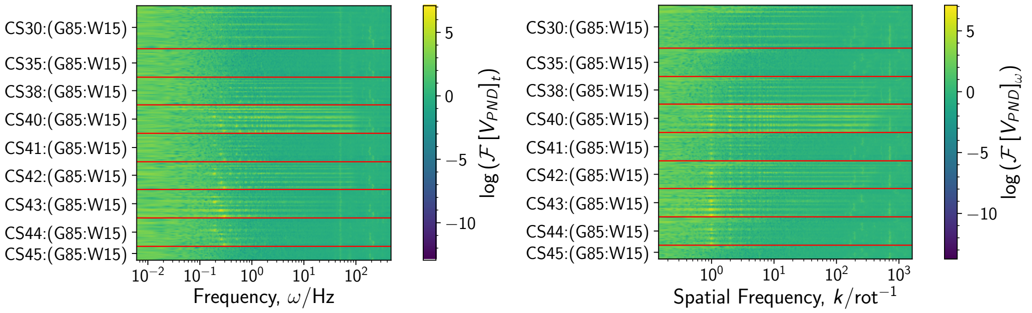

(a) (b)

Figure 7.5: *Heat map showing Fourier transform of PND voltage for different compositions of suspension (indicated along y axis)* ***(a)*** *with respect to time, and* ***(b)*** *with respect to angular position. Plots are constructed as outlined in Section 4.4.3. Within each band of a material, delineated by the red lines, each horizontal line of pixels represents a run of the material at a motor DC setpoint, which increases within the band from top to bottom.*

7.5 PND Voltage

To understand the PND measurement better, the distribution of voltages is first investigated. Subsequently any correlation of PND voltage with rheological measures is investigated.

7.5.1 Rank Plot

To investigate the distribution of PND measurements, the voltage magnitude is plotted in rank order on Figure 7.6. This is a plot of the PND voltage measurement, sorted by magnitude in reverse order so that the highest recorded voltage is rank 1, and the lowest voltage is rank *N* out of *N* measurements. In this manner, common values can be seen together as horizontal lines.

On Figure 7.6, compositions above and below 40 wt% and tend to have lower magnitude measurements than those recorded at 40 wt%. This effect is especially noticeable on the negative channel, where the voltage magnitudes are generally lower for compositions apart from **CS40:(G85:W15)** (this the only difference that can be seen between the channels). This shows an increase in flow unsteadiness for **CS40:(G85:W15)**.

The rank plots for all compositions show a shoulder or “hump” — increasing with

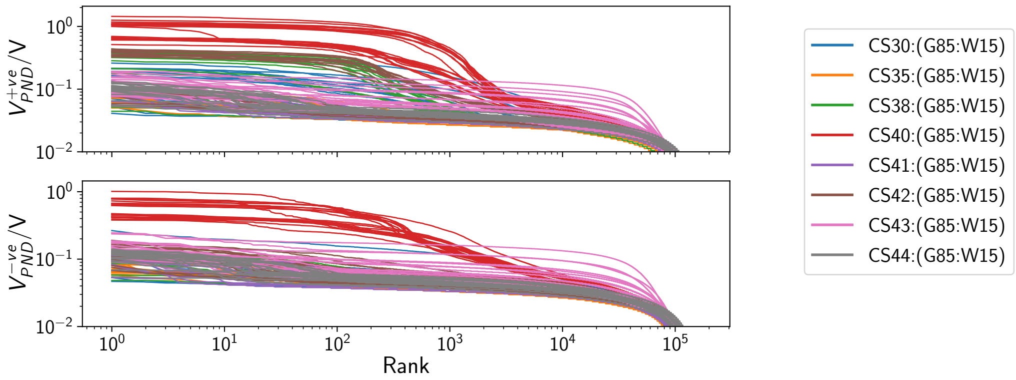

Figure 7.6: *Plot of PND voltage, sorted and ranked by magnitude. Colours indicate the mass fraction. Long horizontal lines indicate frequent voltages. Each line is rank plot for a single run of a composition of suspension; lines differing in applied motor duty cycle, strain rate, and stress. PND Voltage is split into positive (above) and negative (below) channels — there is no qualitative difference between the two save for a reduction in the highest magnitude (negative) voltage for all compositions bar* ***CS40:(G85:W15)****.*

composition up to the 40 % mark and then falling, suddenly. This tallies with what can be expected from a shear thickening fluid approaching the **dst** region: as the system moves into the dst region the suspension forms a band of jammed material *e.g.* at the outer cylinder and a dilated band *e.g.* near the inner cylinder. As the suspension shears, the size of these bands varies as the system organises itself to try to maintain the applied shear. This could result in a thickened/jammed band moving into contact with the needle, or the dilated band varying in viscosity which is picked up by the needle (see Section 6.4). As the stress increases, the size of the jammed/thickened band increases until it almost covers the gap: resulting in steady flow and not dynamics to be picked up by the inserted PND.

7.5.2 Correlation with Stress

2D histograms of stress (y axis) and PND voltage (x axis) are shown for different compositions of cornstarch suspension on Figure 7.7, increasing left-to-right, top-to-bottom. Colour indicates count on the histogram, with white indicating no value.

The stress correlation plots differ for each composition. For the lowest density suspension (**CS35:(G85:W15)**, Figure 7.7 (a)), the stress-PND plot consists of a straight yellow backbone, with a slight bulge of green/blue (indicating lower counts). The ver-

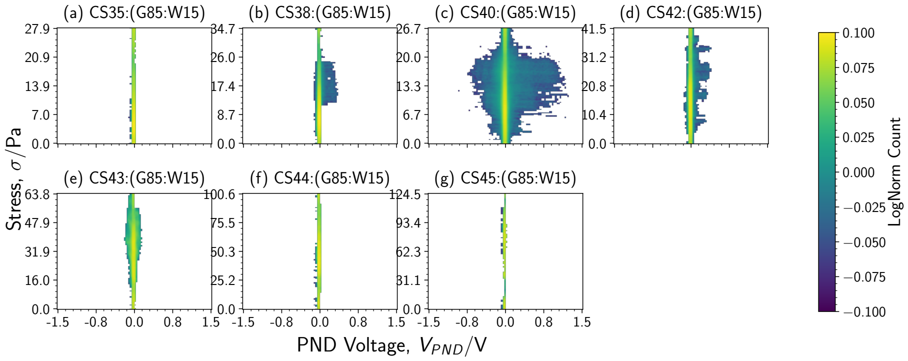

Figure 7.7: *2D Histogram of stress and PND voltage by composition. Colour indicates normalised histogram count as noted by the colour bar. White indicates no value.*

tical high density (yellow) backbone is a feature present throughout, indicative of a component of the stress that is not correlated to the PND measurement. The higher densities of **CS44:(G85:W15)** and **CS45:(G85:W15)** ((f) and (g) respectively) also consist almost entirely of this backbone. However **CS38:(G85:W15)** shows a blue area in addition to the backbone, at high stress coinciding with high values of PND voltage. This effect is amplified in the next material (**CS40:(G85:W15)**, Figure 7.7 (c)), where there is a large “blob” of blue/green points reaching out to the top right of its plot, and stretching slightly out left too. This indicates high PND activity at middling-to-high stresses. Lowest and highest stresses resulting meanwhile in low measured PND voltage. This is consistent with with predictions from the WC phase diagram (Figure 7.1): stresses below the green **dst** region and above it do not result in unsteady flow; those within the green region do.

7.6 PND Peaks

The PND measurement is of the form of a series of peaks, which tend to occur once per rotation. This is shown by plotting the PND voltage modulo one rotation, with reduced opacity (5%, is used on Figure 7.8) — faint lines de-emphasise irregular parts of the signal while making clear the repeated parts. Voltages are standardised,

$$V'_{PND} = \frac{V_{PND}}{V_{PND,\max}}$$

where $V_{PND,\max} = 1.44\,\mathrm{V}$ is the maximum PND voltage measured across all runs and all concentrations, to ease plotting and still ensure a comparable measurement. In this way, the voltage for each composition and duty cycle can be superimposed on itself; any regular patterns are shown as distinct, solid lines. Occasional, inconsistent measurement (noise) would present faintly as compared to regular measurement. This is plotted on Figure 7.8 and shows several interesting features.

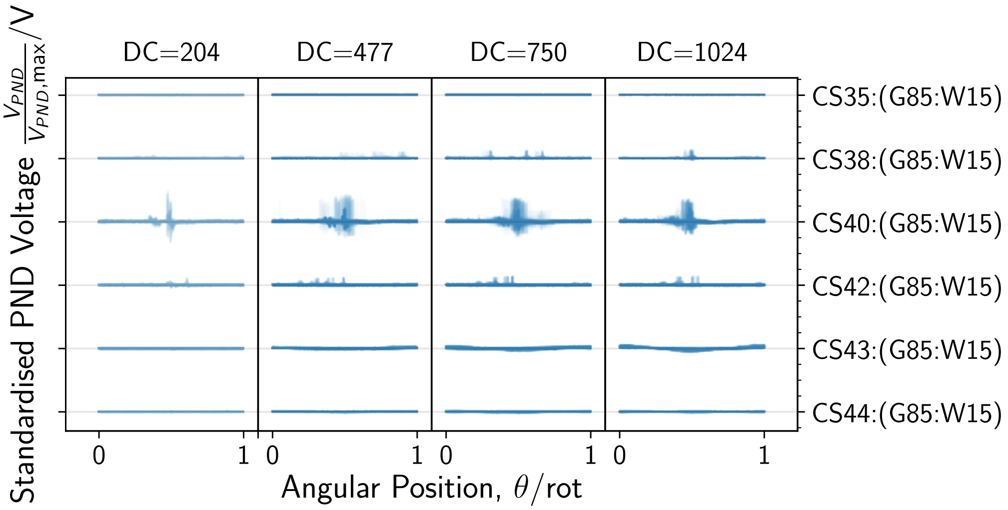

Figure 7.8: *Measurements of PND voltage for different compositions plotted against angular position (θ, in rotations) of the inner cylinder, modulo one rotation. Plot segments are split according to duty cycle (DC) and composition. Duty cycle increasing from left to right, and composition increasing from bottom to top. The voltage is standardised by the maximum in the dataset. Voltage is plotted with faint lines; repeated parts of the signal where many lines overlay each other are therefore shown more clearly while non-repeated parts remain faint and are de-emphasised.*

First, the highest composition and lowest compositions (**CS44:(G85:W15)** and **CS35:(G85:W15)**) have negligible measured PND voltage. This indicates there were no sudden changes in rheological characteristics over the course of the run: the PND being adept at picking up dynamic loading (*changes* in stress), but not static loading (see Section 3.8).

Then, the next-highest composition (**CS43:(G85:W15)**) develops an increasing "wave" shaped measurement with increasing DC (rotation rate, strain rate, and, by extension, stress).

Some middling runs, **CS42:(G85:W15)** and **CS38:(G85:W15)** show an increase in PND activity as duty cycle increases: with intermittent peaks forming and increasing in magnitude with DC. This indicates there are small, irregular changes in rheology which are deflecting the needle probe.

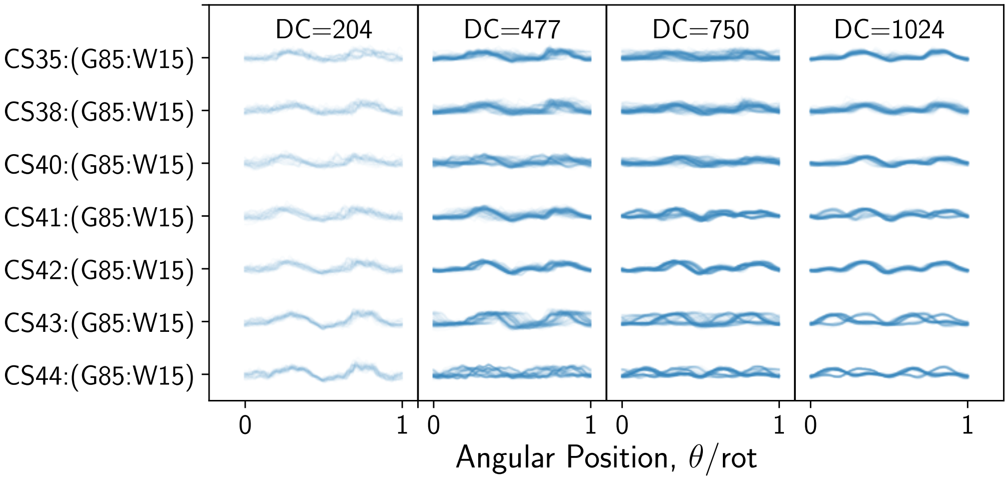

Figure 7.9: *Standardised stress measurements for different compositions plotted against angular position (θ, in rotations) of the inner cylinder, modulo one rotation. Plot segments are split according to duty cycle (DC) and composition. Duty cycle increasing from left to right, and composition increasing from bottom to top. Voltage is plotted with low opacity (5%); repeated parts of the signal are therefore shown more clearly while non-repeated parts are de-emphasised.*

Finally, there is a stark difference between the measurements of **CS40:(G85:W15)** and the others. There are large magnitude peaks, of very short duration with respect to rotation period, occurring with inconsistent frequencies close to the rotation frequency. This indicates the presence of a sudden change in deflection of the PND needle approximately at least once per rotation, with some waves seeming to repeat twice per rotation at higher concentrations (**CS43:(G85:W15)**, **CS44:(G85:W15)**) or low DC (204).

It is useful to compare the behaviour of the average PND event to a similar plot for stress: shown on Figure 7.9 — the stresses on the figure are standardised in the same way as PND voltage was on Figure 7.8: subtract the mean and divide by the maximum. The stresses for all the runs of each composition at each duty cycle are superimposed on themselves, as for PND voltage, and the result is a distinct wave indicative of a regular disturbance being measured.

The repeating wave in stress measurement is of a relatively consistent shape: almost “m” or “w” shaped. There are two peaks and two troughs in a rotation of the cylinder, however when superimposed (as on Figure 7.9, but for a period of half of a rotation) the peaks and troughs do not align. This wave could be thought of, therefore, as a composite of two out-of-phase waves (approximately sinusoidal in shape). This wave occurs mostly once per rotation. The magnitude is not consistent however: increasing with composition. The wave phase is not always consistent with rotation rate: especially for higher DCs and higher compositions, there are areas where the wave becomes out of phase.

Comparing the stress average event plot with that for the PND, there is expected to be something interesting occurring around the middle DCs for **CS40:(G85:W15)**. There are more out-of-phase measurements in the **CS40:(G85:W15)**, but not more than there are for **CS43:(G85:W15)** and **CS44:(G85:W15)** at the same duty cycle — however, for **CS40:(G85:W15)** these occur at comparatively lower stress and disappear at the highest duty cycle: this aligns with the out-of-phase PND events on Figure 7.8.

The PND measurements have little noise in a run — if a large voltage is measured then it is measured consistently. Therefore the PND measurements can be plotted as a phase diagram, where areas of high PND activity can be related to run average stress and mass fraction. This is plotted on Figure 7.10.

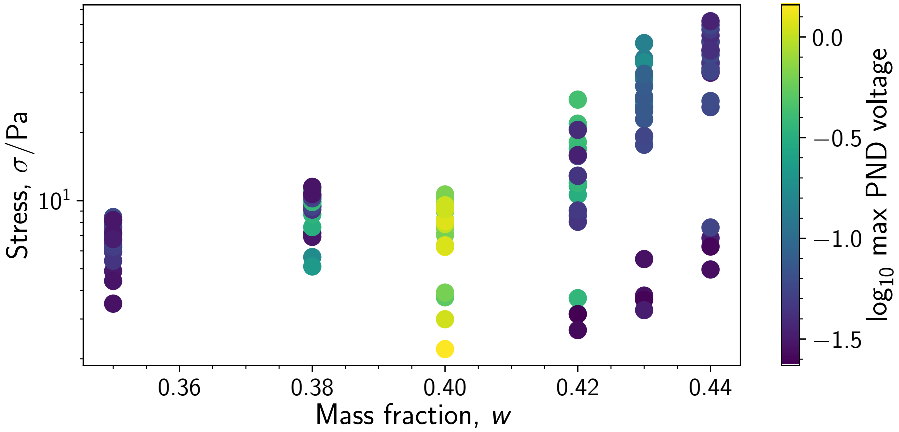

Figure 7.10: *Phase diagram showing areas with high PND activity. Scatter plot of stress against mass fraction for all runs in this Chapter, points are coloured by the* $\log_{10}$ *of the maximum PND voltage measured, value indicated by colour bar.*

On Figure 7.10, the brighter (more yellow) spots indicate higher maximum PND voltage (i.e. more active PND measurement). There is a clear difference between the measurements of **CS40:(G85:W15)** for all stresses, and the other compositions. For the other compositions, the lowest stresses incur the lowest PND voltages, other than for **CS38:(G85:W15)**, which is missing the lowest stress run measurement. Higher

PND voltage tends to occur at higher stress. For **CS40:(G85:W15)**, the PND voltage is uniformly high. This unusually high measurement of voltage on the PND disc sustained during measurements of this composition indicates the presence of a more dynamic or unstable aspect to the flow. A consistent high or low flow would result in a low voltage (as the voltage in the piezo decays) — however a high voltage indicates a *changing* load on the needle probe: unstable flow. This effect was consistent across several runs.

7.7 Anomalous Measurements

Left out of the data presented so far are some anomalous materials: **CS30:(G85:W15)** and **CS41:(G85:W15)**. These materials have been left until now as they fit less nicely in to the picture developed so far. The runs for **CS30:(G85:W15)** shows higher-than-expected noise in the PND measurements. The runs for **CS41:(G85:W15)**, on the other hand, show lower-than-expected PND measurements.

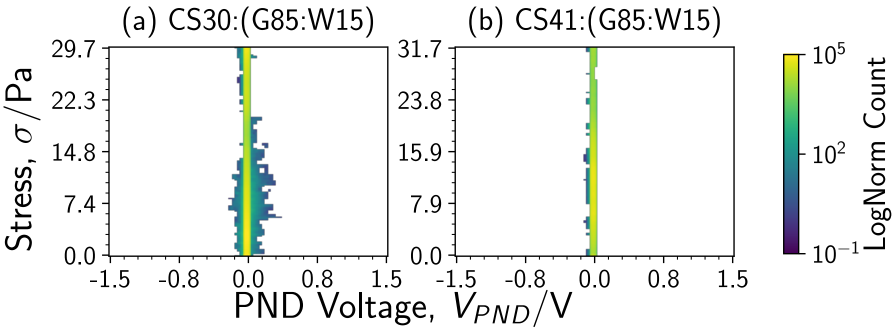

Figure 7.11: *2D Histogram of stress and PND voltage by composition. Colour indicates normalised histogram count as noted by the colour bar. White indicates no value.*

This can be seen best on the stress correlation heatmaps for these materials, shown on Figure 7.11 when compared to those shown previously on Figure 7.7.

It is possible that there were some issues in measuring out the suspensions , this is explored in the uncertainty estimate sections in Chapter 3 on in Section 3.4.4 and Section 3.5.5. The conclusion was that, across repeated runs, measurement inconsistencies is negligible indicating that inconsistencies between runs is not likely to be a cause of error. There seems to be a great sensitivity of the behaviour to even slight changes in concentration — owing to the large changes in observed behaviour even with a 1 % change in mass fraction.

Another possibility would be the sedimentation of particles over time. This is the danger of using a non-density matched solvent. Sedimentation has not been seen to occur over the course of a run; the bottom of the cylinder post-run was not seen to accumulate cornstarch appreciably. However after preparation the suspension is allowed to rest in order to ensure a consistent rheology without swelling. In this time the suspension does settle and needs to be re-suspended by vigorous stirring. If the re-suspension misses a part of the sediment, then the composition of the tested material will be different than expected. To avoid this, salt can be added to increase the density of the solvent (however this can introduce problems with the rheology and stability of the suspension — as discussed in Section 4.2.2). Again, the random error analysis in Section 3.4.4 and Section 3.5.5 does not indicate measurement inconsistency to be a likely cause of the anomalous results.

7.8 Conclusions

In this chapter, runs involving cornstarch suspensions at or near the **dst** regime on the WC phase diagram have been investigated. However, as pointed out in Section 4.2.2, cornstarch systems deviate from the assumptions made for the WC framework: cornstarch is not a hard particle, nor a sphere, nor monodisperse. This results in significant uncertainty about the position of the **dst** area on the phase diagram. Estimates for cornstarch show a transition to jamming behaviour around a *volume* fraction of 0.439 [4] or 0.55 [6]. Here, there is seen a marked increase in local pseudo-stress measurement by the PND (determined by a voltage) for a *mass* fraction of 0.4, the corresponding volume fraction is estimated (method discussed in Section 4.2.2) to be 0.404. This puts the estimated beginning of the transition to shear-jamming suspensions to a concentration significantly lower than previously estimated.

Correlation of stress and PND shows there is a link between high values of (global) stress, and high values of PND — a high value of PND indicates, potentially, a high local stress measurement, which sometimes coincides with a high global stress measurement and explaining the correlation.

Fourier analysis of measured PND shows the presence of a growing (with respect to duty-cycle) high time-frequency mode due perhaps to increasing sound interference from the motor. There are no clear frequencies corresponding to the increased activity in **CS40:(G85:W15)** — instead there is an across-the-board high value in the transformed measurement heatmap.

Finally, there are some seemingly anomalous materials (**CS30:(G85:W15)** and **CS41:(G85:W15)**) measurements of which don't quite match expectation. These runs are could be outliers due to the potentially significant error in the measurement process — errors to which the system which the system seems quite sensitive (even a 0.5 wt% change in suspension composition could provide a significant change in observed behaviour). This would ideally be repeated, and including intermediate concentrations ($w = 0.31, 0.32, 0.33 \ldots$).

References

[1] E. Han, N. Van Ha, and H. M. Jaeger, "Measuring the porosity and compressibility of liquid-suspended porous particles using ultrasound," *Soft Matter*, vol. 13, no. 19, pp. 3506–3513, 2017.

[2] V. Baranau and U. Tallarek, "Random-close packing limits for monodisperse and polydisperse hard spheres," *Soft Matter*, vol. 10, no. 21, pp. 3826–3841, 2014.

[3] G. Batchelor, "The stress generated in a non-dilute suspension of elongated particles by pure straining motion," *Journal of Fluid Mechanics*, vol. 46, no. 4, pp. 813–829, 1971.

[4] R. E. ONeill, J. R. Royer, and W. C. Poon, "Liquid migration in shear thickening suspensions flowing through constrictions," *Physical Review Letters*, vol. 123, no. 12, p. 128 002, 2019.

[5] A. Fall, A. Lematre, and G. Ovarlez, "Discontinuous shear thickening in cornstarch suspensions," in *EPJ Web of Conferences*, EDP Sciences, vol. 140, 2017, p. 09 001.

[6] B. M. Guy, C. Ness, M. Hermes, L. J. Sawiak, J. Sun, and W. C. K. Poon, "Testing the Wyart-Cates model for non-Brownian shear thickening using bidisperse suspensions," *Soft Matter*, vol. 16, no. 1, pp. 229–237, 2020.

8. Conclusions and Future Work

8.1 Overview

In this final chapter, the project is reflected upon with respect to the goals as set out in Chapter 1: to design a desktop rheometer alternative suitable to the lab environment and to investigate the flow of dense suspensions in the unstable regime — as predicted by Wyart-Cates theory. These goals are assessed in turn, then followed by a discussion about areas in which the work could be continued.

8.2 Rheometer Design

At the beginning of this project, it was decided to construct a custom rheometer to fit our needs. The rheometer was to be able to conduct rheometric measurements of a fluid system in shear flow. These measurements were to be reported instantaneously (*i.e.* with no time-averaging). This system would be open-source, with both software source code and hardware designs open. In this way, future similar efforts can better learn from the findings of this project.

This undertaking required research and investigation into the operation of commercially available rheometers, as well as study of apparatus constructed by other research groups (particularly that of Dalton *et al* [1]). This culminated in the design presented in this work: a concentric cylinder flow cell driven by a geared DC motor. Sensors including a novel in-line stress measurement device, an optical encoder for rate measurement, and an analogue-to-digital converter (ADC) for measurements from any additional sensor desired, such as the PND used in this work. This system packs in a fair amount of power (flexibility and extensibility) into a relatively simple and elegant design. Now the design has been completed and documented in this thesis, this project could be re-posed as a project for undergraduate study — bringing together many different areas of chemical engineering (control, fluid flow) and other areas of science and technology (electronics and programming) [2].

The custom rheometer was validated for use in suspension rheology and in general rheology of thick fluids. The stress sensor sensitivity limits low-viscosity fluid investigation — the rheometer is instead well suited to investigation of thick fluids. The open design and use of 3D printed components make the rheometer very flexible. While it was not investigated in this work, different flow geometries could be investigated with a little modification (parallel plate or cone-and-plate geometries would only require a replacement of the cylinder). Using the techniques developed in the process of this design, a similar rheometer device centred around a syringe pump was created (Appendix F) showing the versatility in the design approach.

8.3 Flow Instability

Experiments on cornstarch suspensions were conducted in a flow space predicted, by the Wyart-Cates framework [3], to exhibit complex, unsteady, flows. This regime of unsteady flow and local fluctuation was found, for this system, to start at a volume fraction of $\phi_{dst} = 0.433$ — not too dissimilar to that found for a system in literature (data of O'Neill *et al.* [4]) which gave $\phi_{dst} = 0.429$, and for a suspension sheared in a commercial rheometer (TA Discovery HR-3) which gave $\phi_{dst} = 0.392$. The regime of shear jamming was found to start at a volume fraction (estimated from mass fraction) around $\phi_m \approx 0.509$ — higher than other estimates for similar systems of $\phi_m = 0.43$ [4] and $\phi_m = 0.444$*. The three estimates use similar cornstarch-glycerol-water systems, but in different geometries. This could account for the difference in fit results. However, as noted in Section 4.2.2, the WC model fitting procedure is not simple. Fit results, even to measurements recorded by a commercial rheometer, can have significant uncertainty. In addition, cornstarch is porous and estimating its volume fraction (required for the WC model) is difficult and relies on accurate humidity measurements and porosity estimates.

The cornstarch system has many difficulties (polydisperse, anisometric, porous, soft) to go along with its positives (cheap, readily suspendable in water, safe). These difficulties make predictions based on the Wyart-Cates framework tough, albeit suitable for ballpark estimates of behaviour.

Despite predictions of unsteady flow at the compositions and stresses investigated,

---

*In the same system, but in a parallel plate rheometer (TA Discovery HR-3). See Section 4.2.2

no global unsteady flow was seen — only noise attributed to mechanical and/or electrical interference. Global unsteady flow is characterised by a chaotic variation in the non-fixed flow parameter [5]. In the experiments conducted here, rate is the fixed rheological parameter while stress is allowed to vary. It might have been expected to see a variation in the stress timeseries' then, in the predicted unsteady flow regime. However, this was not seen. This is in part due to a limitation of the developed hardware: stresses from orders of magnitude below to orders of magnitude above the Wyart-Cates onset stress would need to be examined, but the lowest stresses recordable are only an order of magnitude below the Wyart-Cates onset stress, which itself could vary over an order of magnitude due to the difficultly of performing WC model fits and the variety of fit parameters (see Table 4.3). In addition, there was a difficulty in reaching the low stresses due to the rate of rotation of the available DC motors and gearboxes. No global unsteady flow was seen — but there was some activity measured by the local stress sensor: the Piezoelectric Needle Device (PND).

The PND disc picks up deflection in an immersed probe and thus provides an indication of *local* changes in stress. Measurements recorded by the PND in the region at 40 wt% concentration show a marked increase in activity very suddenly. This increase in activity was shown to coincide often with large measurements of (global) stress and to have an unsteady pattern — phasing in and out of sync with the rotation rate. This indicates some local phenomena, worthy of further investigation. These local phenomena are supported by explanations of shear banding emergence are concentrations near the jamming volume fraction.

8.4 Future Work

The findings highlighted above have hinted at areas which are ripe for future investigations. The rheometer design has limitations which can be improved. The work on unsteady flow has areas raises questions for which further investigation could provide answers. In this section proposals to continue the work will be discussed.

8.4.1 Rheometer Design

A primary drawback of the custom rheometer was a limitation of sensitivity in the stress measurement. The bespoke design of linkage between cylinder and loadcell proved fit for purpose; main drawbacks being the sensor range of loadcell. It would perhaps be useful to employ a gear system to reduce or increase the torques involved — bringing the force to a level suitable to a sensor with a wider sensing range.

Another drawback in the design was an inability to create a large, controllable, range of strain rates in the material. This was mitigated in the design by allowing the changing of gear boxes, but this approach was cumbersome and increased the likelihood of unintentional pre-loading of the stress sensor (see Section 3.5). A better approach might be to use a variable speed gear box. There exist continuous speed range gearboxes [6] which would be well suited as a control mechanism.

8.4.2 More PND

The PND sensor has been shown to uncover information inaccessible to traditionally available stress sensors. The local information gathered by the device is important in finding out more information about the phenomenon of shear jamming in dense suspensions such as the cornstarch suspensions presented here.

In this work, only a single PND sensor was employed. However, it would be interesting to add more sensors (distributed around the cylinder's circumference) so that multiple measures of local stress could be recorded simultaneously. In this way, a time evolution of any changes in local stress could be approximated. In a similar vein, it would be interesting to have sensors distributed axially up the inside wall of the cylinder: providing context for the height of the differently-stressed region. This could be used to investigate the possibility of shear banding or the wave phenomena noted in Chapter 7. In the same vein, placing PND sensors at different radial positions would also provide valuable insight for the study of shear banding (especially with regards to confirming the band-size and composition analysis discussed in Appendix H). This would also pose a practical issue to be overcome: fitting multiple sensors in the gap at the same circumferential location. This could be ameliorated by using a larger gap scaling up the whole Couette cell, or by inserting sensors at different radial and circumferential positions. In addition, repetitions of the anomalous runs highlighted in that chapter would give better context to the effects seen — especially a more fine grained series of concentrations which were unfortunately not possible in the time for this project.

Outside of the context of research, the PND device is proposed as a very simple manner of indicating flow conditions that might otherwise be difficult to measure e.g. in a pipe — similar in action, differing in purpose, to wall-stress measurement devices such as [7]. The simplicity and cheap construction of the sensor would make it suitable in applications where funds are limited, the only downside being a larger flow disruption due to the larger probe than with more sophisticated sensors — a problem which could be ameliorated with some further design tweaking: the sewing needle in this design could be replace with any rigid probe, or even a taut thread or fishing line (a sensor similar to fish lateral line sensors [8], on a larger scale).

8.4.3 Simulations

There have been modifications to the friction-driven transition model proposed by Wyart and Cates, particularly that of Baumgarten and Kamrin [9], extending model to apply to dynamic systems, while preserving the mean-field nature of the model by taking the granular and fluid phases separately. The modified (BK) model has not (yet) been applied to unsteady flow problems (*i.e.* the development of unsteady stress by the fluid by application of steady strain rate or *vice-versa*). The model could uncover some interesting dynamics of friction-driven model — especially due to the addition of growth/death of friction allowing for friction “waves” to grow and die over time, in such a manner unsteady flow might be modelled.

References

[1] F. Dalton and D. Corcoran, “Self-organized criticality in a sheared granular stick-slip system,” *Physical Review E*, vol. 63, p. 061 312, 2001.

[2] C. Boyle, M. D. Haw, and L. Lue, “3D printed rheometer for investigation of dense suspension flow instability,” *American Journal of Physics*, 2021, In preparation.

[3] M. Wyart and M. E. Cates, “Discontinuous shear thickening without inertia in dense non-Brownian suspensions,” *Physical Review Letters*, vol. 112, no. 9, pp. 1–5, 2014.

[4] R. E. ONeill, J. R. Royer, and W. C. Poon, “Liquid migration in shear thickening suspensions flowing through constrictions,” *Physical Review Letters*, vol. 123, no. 12, p. 128 002, 2019.

[5] M. Hermes, B. M. Guy, G. Poy, M. E. Cates, M. Wyart, and W. C. K. Poon, “Unsteady flow and particle migration in dense non-brownian suspensions,” *Journal of Rheology*, vol. 60, p. 905, 2016.

[6] K. Atallah, J. Wang, S. D. Calverley, and S. Duggan, “Design and operation of a magnetic continuously variable transmission,” *IEEE Transactions on Industry Applications*, vol. 48, no. 4, pp. 1288–1295, 2012.

[7] S. GroSSe and W. Schröder, “Dynamic wall-shear stress measurements in turbulent pipe flow using the micro-pillar sensor MPS3,” *International Journal of Heat and Fluid Flow*, vol. 29, no. 3, pp. 830–840, 2008.

[8] Y. Zhai, X. Zheng, and G. Xie, “Fish lateral line inspired flow sensors and flow-aided control: A review,” *Journal of Bionic Engineering*, vol. 18, no. 2, pp. 264–291, 2021.

[9] A. S. Baumgarten and K. Kamrin, “A general constitutive model for dense, fine-particle suspensions validated in many geometries,” *Proceedings of the National Academy of Sciences*, vol. 116, no. 42, pp. 20 828–20 836, 2019.

A. Piezoelectricity

A piezoelectric disk is commonly used in microphony due to its ability to convert the tiniest movement to an electrical signal. This ability is called the piezoelectric effect. This is a property of ceramic materials which have an asymmetry in their structure [1]. When these materials are strained, a charge is created across the structure. When the strain is reversed, the charge is removed. This is, in theory, perfectly reversible. However in practice it is not the case. Given an impulse of strain, the piezoelectric signal shows a spike as expected, but upon returning to baseline it overshoots — shown on Figure A.1.

The overshoot is due to charge leaking from the crystal [2]. If a strain on the crystal charges it to 10 coulomb, while strained 2 C leaks (leaving a charge of 8 coulombs), the removal of the strain will result in a -10 coulomb charge. This takes the charge on the crystal to $8\,\mathrm{C} - 10\,\mathrm{C} = -2\,\mathrm{C}$ and is seen as an overshoot (ΔV on Figure A.1).

The crystal structure consists of polarising elements. At rest, the polarising elements are not aligned, and the overall structure has no polarity. When the structure is strained, the polarising elements are pulled into alignment and the structure is polarised [3]. If the strain is maintained, the charge decays to zero exponentially. Because of this, a piezoelectric sensor is suited for studying dynamic responses (varying faster than the decay) and not static response (where the decay will be noticeable).

The piezoelectric effect is described by a matrix of coefficients giving the relationship between a strain (change in length per length, γ in $^{m}/_{\mathrm{m}}$) in a direction (along or about any of x, y, z axes) and the charge developed (q in Coulombs). The structure of the piezoelectric crystal will have a great impact on the ability of the crystal to transform a deformation in a direction into a charge, described by the many coefficients in the matrix. The system of equations governing the direct piezoelectric effect [4]:

$$\boldsymbol{D} = \boldsymbol{d}\boldsymbol{\sigma} + \boldsymbol{\varepsilon}\boldsymbol{E} \tag{A.1}$$

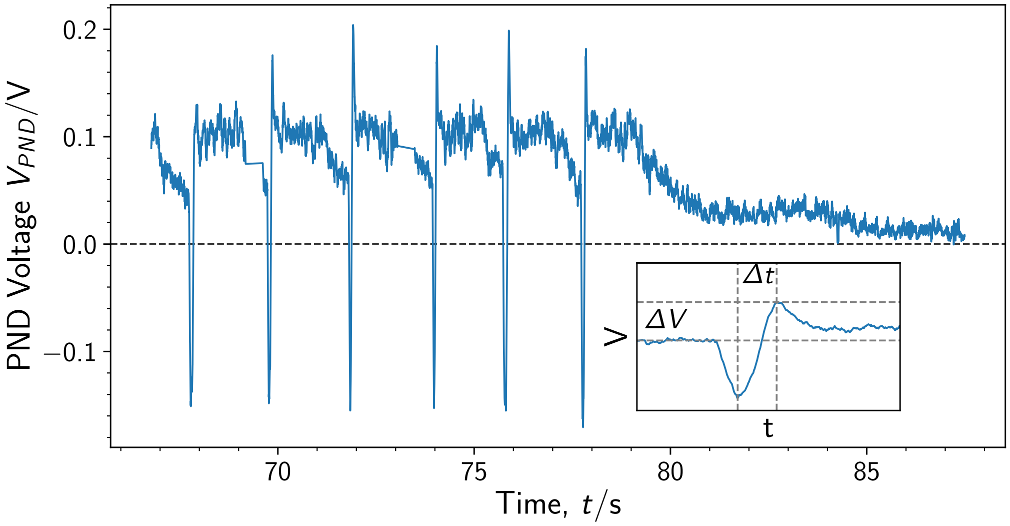

Figure A.1: *Plot showing piezoelectric event: the PND's probe was manually tapped with a finger to obtain the response shown. Inset shows a magnified single event with labelled change in voltage and time.*

where $\boldsymbol{D}$ is the electric displacement (a vector size 3), $\boldsymbol{d}$ are the coefficients for the direct piezoelectric effect (a 3 × 6 matrix), $\boldsymbol{\sigma}$ is the stress applied to the piezoelectric crystal (a vector size 6), $\boldsymbol{\varepsilon}$ is the dielectric constant for crystal (a 3 × 3 matrix), and $\boldsymbol{E}$ is the applied electric field (a vector size 3).

These equations can be simplified in this situation as the piezoelectric disk is only undergoing deflection in the y direction, about the x axis ($\boldsymbol{\sigma} \rightarrow \sigma_{xy} \equiv \sigma_{yx}$); there is no applied field ($\boldsymbol{E} = 0$); the resulting charge density movement is only measured between the sides on the xz plane, so $\boldsymbol{D} \rightarrow D_y$. In addition to the xy stresses there will be compressive and tensile stresses in the x-direction [5]. These x-direction stresses are present but do not create charge across the crystal in y, as $d_{y,x}$ turns out to be negligible [1] for the piezoelectric ceramic material used in the transducer.

$$\begin{aligned} D_y &= d_{y,yx}\sigma_{yx} + d_{y,x}\sigma_x \\ &= d_{y,yx}\sigma_{yx} \end{aligned} \tag{A.2}$$

The electric displacement is a change in charge (area) density[4]. Spread over the area of the disk, this results in a change in charge:

$$\Delta Q = D_y A \tag{A.3}$$

(A.4)

The piezoelectric disk operates as a capacitor: as charges move within itself, a voltage is produced around itself:

$$V = \frac{\Delta Q}{C} \tag{A.5}$$

Therefore the voltage produced by the piezoelectric disk is modulated by the direct piezoelectric coefficient matrix $\boldsymbol{d}$, the direction of strain, and the capacitance of the sensor C.

References

[1] J. Tichý, J. Erhart, E. Kittinger, and J. Prívratská, *Fundamentals of piezoelectric sensorics: mechanical, dielectric, and thermodynamical properties of piezoelectric materials*. Springer Science & Business Media, 2010.

[2] "Introduction to piezoelectric force sensors." (2020), [Online]. Available: `https://www.pcb.com/resources/technical-information/introduction-to-force-sensors` (visited on 01/10/2020).

[3] S. R. Moheimani and A. J. Fleming, *Piezoelectric transducers for vibration control and damping*. Springer Science & Business Media, 2006.

[4] D. Damjanovic, "Ferroelectric, dielectric and piezoelectric properties of ferroelectric thin films and ceramics," *Reports on Progress in Physics*, vol. 61, no. 9, p. 1267, 1998.

[5] L. D. Landau, E. M. Lifshitz, R. Atkin, and N. Fox, "The theory of elasticity," in *Physics of Continuous Media*, CRC Press, 2020, pp. 167–178.

B. 3D Printing Procedure

B.1 Overview

3D printing was used to create parts for the custom rheometer in this work. In this Appendix, the process involved in designing a part to be 3D printed is discussed. First, the design step is discussed, where an idea is converted into a 3D model. Second, the 3D model needs to be cut into layers, using a “slicer” software. Finally, the part is 3D printed.

B.2 Design

The first step in creating a 3D printed object, is to create a model of the desired object. This is achieved using CAD software. Two software packages were used: FreeCAD [1], and OpenSCAD [2]. FreeCAD software is a free, open source, traditional design suite. It features drafting and design tools, as well as finite element analysis, and animation. Each is available through its “workbenches”. OpenSCAD is a programming language and IDE which can be used to describe a 3D object using its scripting language. Both softwares emphasise the paradigm of *parametric* design; where a part is designed in a functional manner, so it is the output of a function on some data (measurements, for example). If the measurements should change then the function alters the output accordingly, without need to redesign.

B.3 Slicing

There are a variety of 3D printer types: fused deposition modelling (FDM) and stereolithography (SLA) are two common types [3]. The print method discussed here is FDM printing. This technology works by melting a filament of plastic and “drawing”

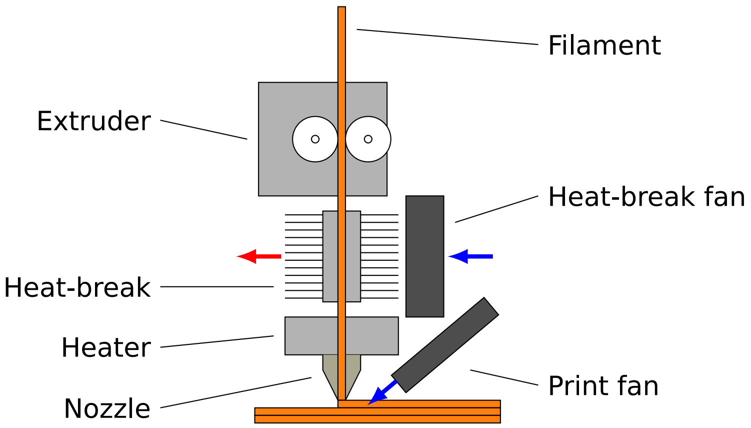

Figure B.1: *Schematic of an FDM 3D printer's print-head. Coloured arrows show direction and temperature of blown air. Plastic filament is pushed into a heated nozzle by an extruder, through a heat break. The break minimises the heat that can travel up the head, preventing premature melting of the filament. The print fan ensure the filament cools quickly after deposition, so that it stays in shape.*

out the layers of the desired model. Figure B.1 shows a diagram of an FDM printer's print head. This is the part of the printer than actually does the printing. Other important parts not shown on the diagram are the (heated) print-bed upon which a model is built, and the mechanism for moving the print head and print bed, allowing filament to be drawn anywhere within the print volume.

This step in the printing process converts the model from a 3D object into a set of layers than the printer can draw out. More correctly, it produces some GCODE instructions for the printer. GCODE is a family of languages based on a specification for traditional Computer Aided Manufacturing (CAM) use [4] and subsequently extended for use in 3D printing [5]. GCODE is essentially a series of "move here", "extrude a little", "move there" type instructions, along with temperature control instructions.

During slicing, the print settings are decided. Thickness of layer, fill percentage, extrusion, speed, all these factor into the end result. The best parameters are often a balance between quality and speed of the print. Smaller layers will result in longer print times, but a finer result. More infill will (slightly) increase the strength of the part, but again cost in time. Speed (velocity of the print head) affects the quality as high speed creates a more "jittery" print.

In addition, there are settings related to the temperature of the hot-end, which affect filament melting and print adhesion respectively. These settings are changed on a per-material basis. Even for the same material (e.g. polylactic acid, PLA) there can be differences between manufacturers.

For big, structural parts used in the custom rheometer, a layer height of 0.3 mm was used as the finish was not a concern. For more intricate parts (threaded parts, bearings) where finish quality did matter, 0.1 mm layer height was used along with post processing (filing, sanding) to ensure a smooth surface. Print speed was left at the default values given by the manufacturer, Prusa.

References

[1] The FreeCAD Team, *FreeCAD*. [Online]. Available: `https://www.freecadweb.org/`.

[2] Marius Kintel, *OpenSCAD*, version 2019.05. [Online]. Available: `https://openscad.org/index.html`.

[3] “Types of 3D printing,” PROTOLABS. (2021), [Online]. Available: `https://www.protolabs.com/resources/blog/types-of-3d-printing/` (visited on 09/22/2021).

[4] ISO 6983-1:2009, “Automation systems and integration — Numerical control of machines — Program format and definitions of address words — Part 1: Data format for positioning, line motion and contouring control systems,” International Organization for Standardization, Geneva, Switzerland, Standard, Dec. 2009.

[5] Marlin. “G-code Index.” (2021), [Online]. Available: `https://marlinfw.org/meta/gcode/` (visited on 06/26/2021).

C. Proportional-Integral (PI) Control

Strain rate and stress control

Using a control algorithm [1], a control loop can be implemented by measuring the speed from the optical encoder, comparing this with a desired rotation rate set point ω_{SP}, or a desired strain rate $\dot{\gamma}_{SP}$, and altering the supply voltage to achieve it. Similarly, stress could be measured and compared to set point σ_{SP} and controlled via supply voltage. The PI (Proportional-Integral) control algorithm is used here as it has effective disturbance rejection while being tolerant of noise, although it is vulnerable to overshoot if there exists a time delay in the measurement process.

The PI velocity (discrete-time) algorithm [1] gives the control action ca ($\equiv V_{ms}$, the desired supply voltage):

$$ca = K_P\left(\epsilon_n - \epsilon_{n-1}\right) + K_I \epsilon_n dt \tag{C.1}$$

where ca is the control action: the change in motor supply voltage or PWM duty cycle. ϵ_i is the measured error between the controlled variable y (*e.g.* stress or strain rate) and the set point y_{sp}: $\epsilon = y - y_{sp}$, with sample number i. K_P and K_I are coefficients defining the relative behaviours of the proportional and integral parts of the controller. dt is the time between samples in s.

The values of the coefficients K_P, K_I are found via a tuning process, for which there are different methods. One method is to manually alter the tuning parameters K_P and K_I until the desired response is achieved — trial-and-error tuning. Other methods require modelling the response of the process and using the model parameters to decide on the best tuning parameters based upon empirical relations such as Ziegler-Nichols (Equation (C.4)). A simple dynamic model often used in process control is the

First Order Plus Dead-Time (FOPDT) model [2]:

$$\tau \frac{dy}{dt} + y = Ku\left(t - t_d\right) \tag{C.2}$$

where y is the process output (process input) and u is the process input (controller output), τ is the time constant defining the “speed” of the response, K is the process gain converting input to output at steady-state, t is time, and t_d is dead-time, the time taken for changes to propagate into the process. The model can be fit to experimental data by performing a step-change experiment: a step change is made to the controller output u, the process response (y) is monitored. The same change is made to the model Equation (C.2) and the two responses are compared; the model parameters altered to achieve best fit. The step (size $= a$) response from a FOPDT model is given by:

$$y = aK\left(1 - e^{-t/\tau}\right) \tag{C.3}$$

The Ziegler-Nichols relations [3] give the control parameters in terms of the time constant τ, dead-time t_d, and process gain K:

$$K_P = 0.9 \frac{K\tau}{t_d} \tag{C.4a}$$

$$K_I = 3 \frac{K\tau}{t_d^2} \tag{C.4b}$$

Tuning by any method will normally end with a trial-and-error step to allow final tweaking of the controller response. The tuning procedure for the motor control system is as follows:

1. Turn off the control system (open-loop mode),
2. Turn on the motor with voltage so that the controlled variable (stress or strain rate) is around the intended value (desired control output),
3. Monitor the stress/strain rate for a period of time ($\sim 60\,\mathrm{s}$),
4. Step up the voltage by some known amount (e.g. 2 V),
5. Continue to monitor the changes in stress/strain rate,
6. Compare response to the same step change response in the FOPDT model Equation (C.3) to obtain the best fit and thus the model parameters K, t_d, and τ,
7. Calculate the control parameters using Equation (C.4)

8. Run the motor and monitor the controlled variable;
    - Is the fit satisfactory?
    - Does the control system reject small disturbances?
    - Does the controlled variable follow the set point?
9. Tweak the controller tuning parameters (iteratively making small changes to each control parameter) until the above criteria are satisfied.

The tuning can be evaluated in several ways; for example, assessing the system's ability to perform a unit-step test. Start with setpoint at one value and allow the system to come to steady state. Increase setpoint by a unit. The system is now in error (measured value does not match set point). The controller will now attempt to bring the measured value up to the set point. The time-weighted mean square error (MSE), measured over the course of the adjustment, can be used to judge how well the system recovers from this unit-step and assess the efficacy of the tuning.

References

[1] A. Visioli, *Practical PID control*. Springer Science & Business Media, 2006.

[2] C. I. Muresan and C. M. Ionescu, “Generalization of the FOPDT model for identification and control purposes,” *Processes*, vol. 8, no. 6, p. 682, 2020.

[3] H. Wu, W. Su, and Z. Liu, “PID controllers: Design and tuning methods,” in *2014 9th IEEE Conference on Industrial Electronics and Applications*, IEEE, 2014, pp. 808–813.

D. Electronics Summary

D.1 Overview

In this Appendix, the electronics in the custom rheometer are described in detail. Presented on Figure D.1 is the complete circuitry used for the custom rheometer. This is split into six sub-systems: Light Gates, motor voltage control, cylinder thermometer, ambient thermometer, loadcell interface, and PND interface. Each sub system will be discussed in turn, followed by a summary of the components used.

D.2 Light Gate Circuit

This circuit forms the basis of the optical encoder. Each gate, marked on Figure D.1, consists of a single IR LED used in combination with an NPN phototransistor. When light (of the correct wavelength) hits the phototransistor, current between its collector and emitter pins is allowed to pass: in this way, it acts like an IR-sensitive switch. Light emitted LED is not sufficient for full saturation of the phototransistor, leading to an amount of voltage loss in the transistor and resulting in low output voltage — insufficient to trip a GPIO on the Raspberry Pi (RPi). To overcome this, a complementary NPN transistor is used to boost the switching voltage, and allow a greater voltage to be sent to the GPIO. The IR LEDs are connected to system voltage supply through a 330Ω resistor for protection.

This circuit is doubled up, to allow averaging between the two sensors and obtaining a more accurate speed measurement, without resorting to time averaging.

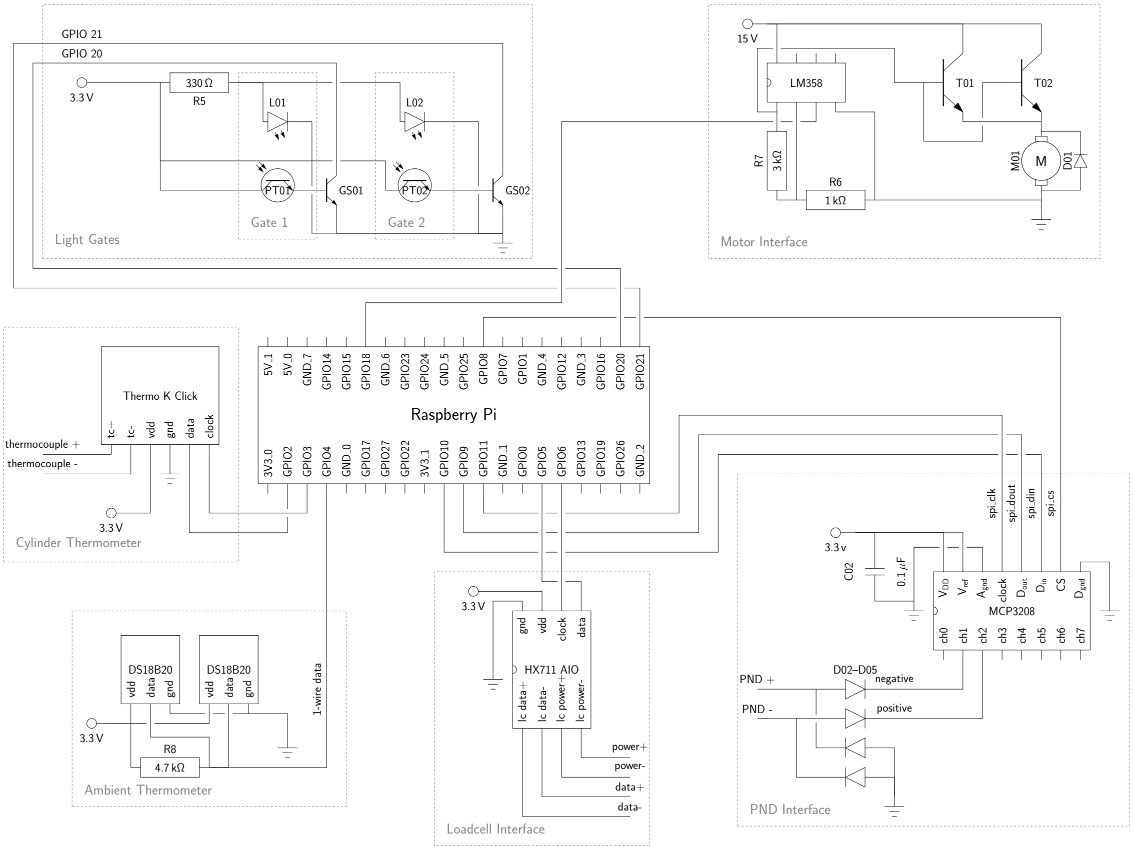

Figure D.1: *Complete circuit diagram for the peripherals of the custom device.*

D.3 Motor Interface Circuit

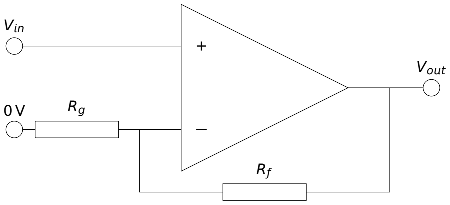

Figure D.2: *Operational Amplifier configured as a non-Inverting amplifier.*

The motor is controlled by a Pulse Width Modulation (PWM) signal generated by the RPi. The signal is a square wave, the proportion of “on-time” to “off-time” will affect the rotation rate of the motor, without sacrificing torque [1], thereby allowing slow rotation rates without stalling. This PWM signal is generated by the hardware Digital-Analogue Converter (DAC). This has 1024 (10-bit) “levels” of duty cycle adjustment.

This square wave of voltage, in the range 0–3.3 V, is passed into the motor interface subsystem from GPIO18. The PWM signal feeds first into an LM358 operational amplifier, configured as a non-inverting amplifier (as shown on Figure D.2). This is used to increase the voltage of the signal by a multiplier. The amplification goes according to

$$V_{out} = \frac{R_f + R_g}{R_g} V_{in} \tag{D.1}$$

where V_{out} is the voltage output from the amplifier and V_{in} is the input voltage, both in V. R_f is the resistance in Ω of the feedback resistor, connected between the amplifier's output and inverting input (see Figure D.2). R_g is the resistance in Ω of the ground resistor, connected between the amplifier's inverting input and ground. R_f and R_g correspond to R6 and R7 on Figure D.1 respectively.

The voltage output from the LM358 is then passed into a pair of current amplifying transistors (T01 and T02). This boosts the ≈ 100 mA of current that can be supplied by the operational amplifier up to the ≈ 2 A required to drive the motor. Each transistor has a gain of $h_{FE} = 200$ which would be sufficient for the amplification. However there is a great deal of heat released, and does not leave room for spikes in current consumption above the expected max of 2 A. Therefore two were used in parallel to split the load.

Finally, the voltage output from the bases of the power transistors is fed into the motor. A flyback diode D01 is included to protect the circuitry from any back EMF* by providing a low-resistance route for the EMF to traverse.

D.4 Cylinder Thermometer Circuit

The cylinder thermometer interface is handled by a specialised board (THERMO K click — based on the MCP9600 thermocouple driver IC) which converts the thermocouple signal into a temperature. This is interfaced with the RPi by use of the I2C serial protocol.

D.5 Ambient Thermometer Circuit

Ambient temperature is measured by two DS18B20 1-wire sensor modules. These only require power and one sensor wire. The sensor wire requires a pull-up resistor

---

[*] Back EMF is a phenomenon where a large negative voltage is produced by electro-magnetic devices (utilising coils and magnetic fields) as the magnetic field collapses [2].

(R8 on diagram) to interface.

D.6 Loadcell Interface

Similar to the cylinder thermometer, the loadcell is interfaced via a commercially available circuit (an example [3]) built around the HX711 24-bit ADC. This interfaces with the Raspberry Pi via a custom serial interface. The interface is based on a two wire set up: one clock and one data. The clock wire syncs the software on the RPi with the chip, while data is transmitted one bit at a time via the data line.

D.7 Piezoelectric Needle Device (PND) Interface

The PND produces a voltage when it is strained or stressed. The voltage produced ranges from $\approx 5\,\mathrm{V}$ up to $\approx 5\,\mathrm{V}$. If this was directly passed into an analogue to digital converter (ADC), then the negative part of the signal would be lost. To split the voltage into two channels of positive voltage, a diode rectifier circuit is used. This circuit consists of four diodes, which force current to flow in one direction.

After the rectifier, there are two channels of signal which are sent to the ADC (MCP3008, 12-bit ADC) where the analogue signal is converted to a digital signal which can be read by the RPi via SPI serial communication interface.

D.8 Components List

Main components on Figure D.1 are summarised on Table D.1.

Table D.1: *Summary of main electronic components labels and descriptions.*

Component	**Description**
Raspberry Pi	Single Board Computer; controller
HX711 AIO	HX711 ADC all-in-one board; loadcell interface
DS18B20	1-Wire interfacing temperature probe
Thermo K Click	Thermocouple interface board
GL01, GL02	IR LEDs; light gate sources
GT01, GT02	IR Phototransistors; light gate sensors
GS01, GS02	NPN transistors; light gate switching transistors
PT01, PT02	NPN power transistors; current amplifiers for motor supply
LM358	Operational amplifier; voltage amplifier for motor supply

References

[1] R. D. Christ and R. L. Wernli, “Chapter 7 — power and telemetry,” in *The ROV Manual (Second Edition)*, R. D. Christ and R. L. Wernli, Eds., Second Edition, Oxford: Butterworth-Heinemann, 2014, pp. 141–161.

[2] J. Chiasson, *Modeling and high performance control of electric machines*. John Wiley & Sons, 2005, vol. 26.

[3] “Diy load cell weight sensor 20kg portable scale+hx711 weighing sensor.” (2021), [Online]. Available: `https://www.ebay.co.uk/itm/DIY-Load-Cell-Weight-Sensor-20KG-Portable-Scale-HX711-Weighing-Sensor-Ad-Modl-UK/392955442217?hash=item5b7df83429:g:XlQAAOSwIaFZNTFf` (visited on 04/03/2021).

E. Estimating Viscous Heating Effect

The temperature dependence of viscosity was mentioned in Section 5.4 as an explanation for a slow drop in measured viscosity over time. Over the course of a run, the dissipation of rotational energy by the fluid can increase the temperature, causing a decrease in viscosity. This shear heating effect can be estimated by balancing the mechanical energy input to the fluid with the heat gained by the fluid.

Mechanical power is given by the product of angular velocity and torque:

$$W_{mech} = M\omega_r \tag{E.1}$$

where W_{mech} is the mechanical work input. Assuming no or negligible heat escapes from the cylinder, then the work input is equal to the heat gained. This is a fairly strong assumption given the low temperature differences (small heat transfer driving force) involved, and small surface area of the *xy*-table in contact with the cylinder (small area for conductive heat transfer) — therefore the heat transfer between fluid and the atmosphere is assumed negligible.

If M is replaced by the torque imposed on the shaft by the fluid alone (M_{visc}), then we get an equation giving the power dissipated by the fluid (W_{visc}):

$$W_{visc} = M_{visc}\omega_r \tag{E.2}$$

Energy input to the fluid is dissipated. It can be assumed that most of the energy is dissipated as heat. Temperature change can be found from:

$$W_{visc} \approx W_{heat} = m\, c_p(T_{pred})\, \dot{T} \tag{E.3}$$

where W_{heat} (W) is the rate of heat gained by the fluid (mass m in kg), specific heat capacity c_p in $\mathrm{J\,kg^{-1}\,K^{-1}}$), and $\dot{T}$ is the rate of temperature change in $\mathrm{K\,s^{-1}}$. Mass of fluid is found from the volume:

$$V = A_{ann} H \tag{E.4}$$

where A_{ann} is the annular area between the inner and outer cylinders in m^2 and H is the fill depth of the fluid within the Couette in m. Glycerol and water densities are found using the relations [1]:

$$\rho_g = 1.277 - 6.54 \times 10^{-4} (T - 273.15) \tag{E.5}$$

$$\rho_w = 1 - \left| \frac{T - 277.15}{622} \right|^{1.7} \tag{E.6}$$

where ρ is the density of the material in $\mathrm{g\,cm^{-3}}$, T is temperature in K, and subscripts g and w refers to glycerol and water respectively.

The fluids are mixed together, with glycerol mass fraction C_m. The combined properties of the fluid can be approximated [1]:

$$\rho_{gw} = \rho_g C_m + \rho_w (1 - C_m) \tag{E.7}$$

$$c_{p,gw}(T) = c_{p,g}(T) C_m + c_{p,w}(T) (1 - C_m) \tag{E.8}$$

Equation E.3 is rearranged to give the differential equation:

$$\frac{dT_{pred}}{dt} = \frac{M_{visc}\omega}{m\, c_p} \tag{E.9}$$

which can be solved numerically to give temperature versus time. This process calculates an estimated temperature rise for a sheared volume of a glycerol-water mixture. An example: shearing a mixture of 85 wt% glycerol and 15 wt% water for 100 seconds at an angular velocity of $10\,\mathrm{rad\,s^{-1}}$, initially at a temperature of 288.15 K, results in a temperature change of 4.10×10^{-4} K according to Equation E.9. Following through, using Equation 4.3, the viscosity drops by 4.78×10^{-5} Pa s.

In combination with Equation (4.3), the change in viscosity with temperature can also be estimated, as discussed in Chapter 5, Section 5.4.

References

[1] N.-S. Cheng, “Formula for the viscosity of a glycerol-water mixture,” *Industrial & Engineering Chemistry Research*, vol. 47, 2008.

F. Syringe Pump Rheometer

F.1 Overview

During the project, a second rheometer was constructed: in the form of a syringe pump, modified to take rheological measurements. This rheometer was applied throughout several undergraduate projects [1], [2], as well as a related PhD project [3].

Similar to the custom concentric-cylinder rheometer (CCR) described in this project, the syringe pump rheometer (SPR) was designed for use in the investigation of dense suspensions of cornstarch. In this set up however, the flow takes place within a syringe and attached tube — more complex than the simple shear flow in the Couette cell. However, the SPR results in pipe flow with a constriction (due to the nozzle) similar to the experimental set up of [4], but on a much smaller scale.

Differing from the CCR, the SPR was not designed with open access or repeatability in mind. It was constructed purely for use as a rheological investigative tool, leveraging the flexibility of an open hardware and software platform for flexible research on control methodology and rheology.

The repurposing of the syringe driver as a syringe-pump based rheometer was originally carried out by a Master's student [1], however the resulting design was unfortunately lost and the development was re-started. Presented here is the final version of the syringe pump rheometer.

F.2 Design

The SPR has the same four core components as the CCR: a rate measurement component, a force measurement component, a flow driving component, and a known geometry through which flow occurs. On top of this, the SPR incorporates a PI controller in order to drive flow at a specified rate or force. The physical basis for the SPR is a syringe pump (of the type used in hospital), upon which the controlling electronics were built to create a rheological measurement device, from a disused drug-delivery device.

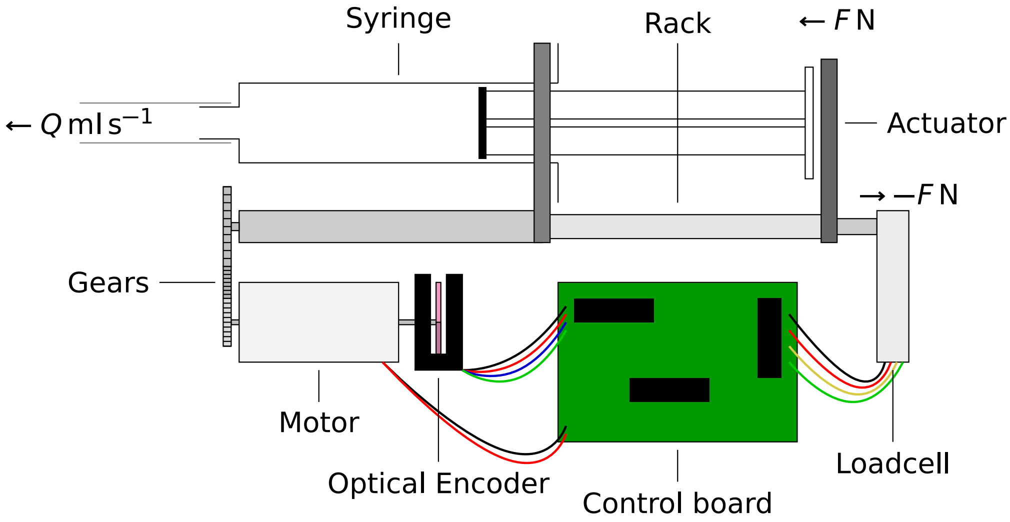

Figure F.1: *Schematic of syringe pump rheometer.*

A schematic of the SPR is shown on Figure F.1, showing the layout of the component systems. The "rack" is a worm gear driven by the motor, via a reduction gear chain (reducing the rotation rate from the motor). As the motor turns, the actuator plunges the syringe. The force applied by the actuator is measured by a loadcell balanced against the end of the rack. Rate is measured by an optical encoder attached directly to the driving shaft of the motor. The whole system is controlled by at Arduino microcontroller board, from which data are logged by interfacing with a GUI application run on a computer.

Each of the component systems will be described in turn in the following subsections.

F.2.1 Syringe pump

The core of the syringe pump rheometer is a syringe pump. This component was obtained from ebay*. The syringe pump already contains all of the components necessary for rheological measurement — the issues lie in extracting that information. The control and interface software it runs on is not designed to extract rheological

---

*The exact listing is no longer available. Many similar syringe pump drivers are available: an example is [5].

information, merely push a plunger at a tightly controlled rate and to shutdown if too high a pressure is applied.

During attempts to adapt the original control systems, some of the original electronic components were damaged (optical encoder, loadcell) which had to be replaced. The original loadcell was custom designed to fit in to the pump housing. This design was unable to be replicated. (Due to the fragility of the loadcells obtained, they broke when attempted to be machined to size in the workshop.) Instead the housing was adapted, using 3D printed components, to house the new loadcell (unknown brand, 5 kg rated, obtained from eBay[†]). After use for a while, the loadcell was found to be insufficient, being under rated for the forces involved. It was replaced with a loadcell rated to 20 kg[‡].

F.2.2 Rate Measurement

Rate is measured by use of an optical encoder on the motor output shaft. An optical encoder (similar to the one described Section 3.4) is a light source and sensor (forming a light gate), between which sits a slotted disc attached to a rotating shaft. This notes down a “tick” every time the light gate circuit “makes” (light is unblocked) or “breaks” (light is blocked). To convert a tick-rate (ticks per time) to an actuator velocity the gear ratio needs to be taken into account. After the velocity is known, the flow rate is calculated simply from the cross-sectional area of the syringe.

In this encoder, there are two slots. There is a tick for each “make” and a tick for each “break”; therefore 4 ticks per rotation and 1 tick per quarter-rotation.

$$\omega_m = \frac{1}{4}TR$$

where TR is tick rate in s^{-1}, and ω_m is the rotation rate of the motor shaft in $\mathrm{rot\,s}^{-1}$. This driving shaft is immediately passed into a gearbox (of unknown ratio) attached to the motor, and the output of this is passed to the gear train, as detailed on Figure F.2. To get the conversion ratio of the gearbox, a tooth on gear 2 was marked against a background sheet of paper. The motor shaft was rotated. When the tooth had rotated over to the position of the next tooth (compared against the markings made on paper), the motor shaft had rotated 3 times. There are 30 teeth on gear 2 — in one 30th of a rotation on 2, the motor rotated 3 times. This gives the conversion ratio from the motor shaft to gear 2 of $R_{0,2} = {}^1\!/_{90}$ and introduces a shortcut for getting the rotation

---

[†] Exact listing no longer available. An example of similar component is [6].

[‡] Exact listing no longer available. An example of similar component is [7]

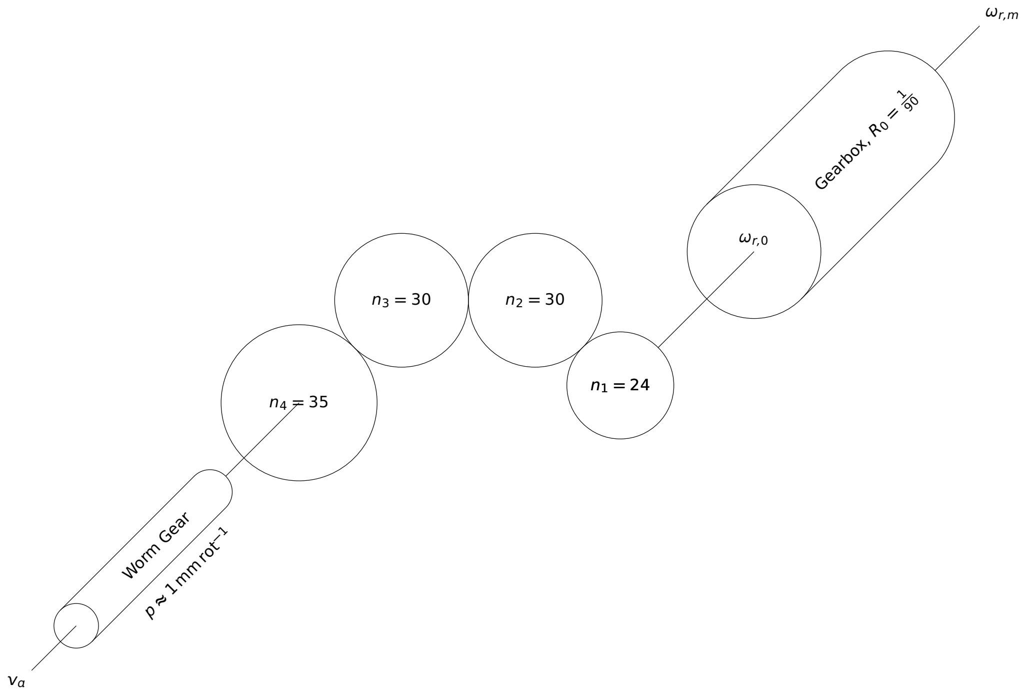

Figure F.2: *Gear train diagram between motor and worm gear.*

rate of gear 2 from motor rotation rate:

$$\omega_2 = \frac{1}{90}\omega_m$$

The overall gear ratio of a gear chain is the product of the ratios of the gear ratios in the chain. (Where the gear ratio is the ratio of number of teeth on the input divided by the number of teeth on the output.)

$$\omega_w = \frac{n_3}{n_4}\omega_3$$
$$\omega_3 = \frac{n_2}{n_3}\omega_2$$
$$\omega_w = \frac{n_3}{n_4}\frac{n_2}{n_3}\omega_2 = \frac{1}{105}\omega_m$$

where n_x is the number of teeth (see Figure F.2), ω_x is the rotation rate in $\mathrm{rot\,s^{-1}}$ on gear x, and ω_w is the rotation rate of the worm gear.

Finally, the pitch p ($\mathrm{mm\,rot^{-1}}$) of the worm gear converts the rotational rate of its input shaft to the linear velocity of the actuator v_a and hence, the plunger. By counting the number of teeth in a 1 cm section of the worm gear, the pitch was found to be 1 mm rot^{-1}. Therefore the conversion between ticks and linear position is

$$k_{tick\rightarrow dist,calc} = \frac{1}{105}\frac{1}{4} \approx 0.00238\text{mm tick}^{-1}$$

An alternative measurement was taken: by measuring the number of ticks over the course of the entire length of the rack and dividing through, an analogous conversion factor was obtained:

$$k_{tick\rightarrow dist,est} \approx 0.00272\text{mm tick}^{-1}$$

This latter was obtained early in the design process and persists in latest software for consistency. This value is not far off that calculated from the ratios, approximately 12.5% difference. There is potentially greater confidence in the estimated value of 0.00272mm tick^{-1}, being taken over a larger range while the worm pitch measurement was taken over only a 1 cm length.

F.2.3 Force Measurement

The rack pushes down on the syringe plunger and back on the loadcell. Any obstacle in its way (plunger friction, fluid resistance) requires force to overcome, this force is measured on the loadcell.

Calibration of the loadcell is performed by applying a known force to the cell, and recording the output. This is done by two methods: one method uses a build-up of air pressure to impose a pressure on the loadcell and the other piled on standard weights to impose known weight. The first method was used to calibrate for the first loadcell (rated to 5 kg) and the second method used for the final loadcell (rated to 20 kg).

Air Pressure Calibration

Two syringes are linked together by a tube with one syringe's plunger fully depressed and the other's plunger fully extended. The depressed syringe is mounted into the syringe pump. A pressure can be applied on the actuator of the syringe pump by depressing the extended plunger. By applying Boyle's law [8, p. 7] (assuming isothermal — syringe is not insulated), the pressure exerted can be calculated from the volume, (which can be read from the graduations on the syringe):

$$P_2 = \frac{V_1}{V_2}P_1 \tag{F.1}$$

$$\Delta P = P_1\left(\frac{V_1}{V_2} - 1\right) \tag{F.2}$$

where ΔP is the pressure (above atmospheric) imposed on the loadcell in Pa, P_1 and P_2 are the pressures before and after the plunger is depressed, in Pa. V_1 and V_2 are the volumes before and after the plunger is depressed, in ml.

The force is then calculated from the cross sectional area of the plunger,

$$F = \Delta P A \tag{F.3}$$

where F is the force applied to the loadcell in N, and P is the syringe pressure in Pa, and A is the cross sectional area in m^2. The diameter of the plunger is 21.5mm and therefore $A = 3.631 \times 10^{-4}\mathrm{m}^2$.

The calibration was conducted by holding the depression level of the plunger to different volumes while recording loadcell values. The results of two such calibration procedures is shown on Figure F.3b.

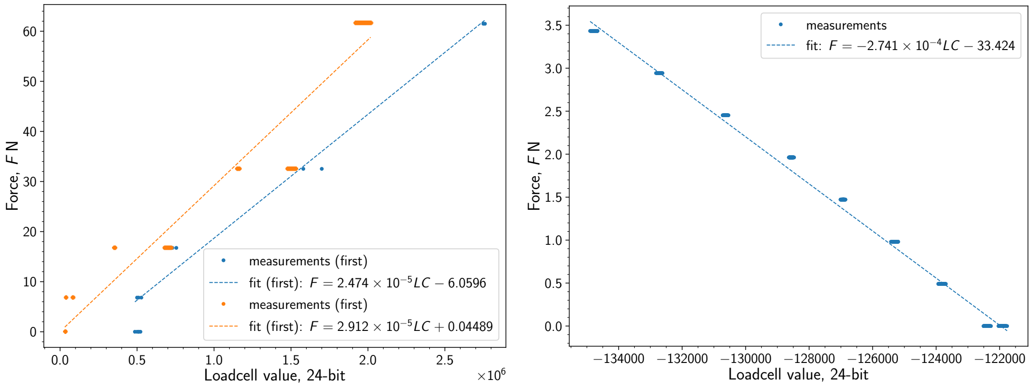

(a) (b)

Figure F.3: *Syringe pump calibration results achieved (a) by air-compression method for the initial* 5 kg *loadcell, and (b) by standard weights method for the latter* 20 kg *loadcell.*

The two results presented on Figure F.3b (performed approximately 7 months apart) have similar trends but are slightly offset. This can be due to differences over time, or with use. The loadcell is rated only to ≈ 50 N, but in use the loadcell is subject to forces in excess of 100 N. Due to this exceeding of the force rating, a new (larger) loadcell was sought and calibrated using the next method.

Standard Weights Calibration

Force is calibrated in this method by placing standard weights (brass masses) on the actuator and recording the loadcell value. Unlike the previous method, this method does not require any calculating nor any complex linkage, only relying on the mass and acceleration due to gravity,

$$F = mg \tag{F.4}$$

where F is the applied force in N, m is the mass of the brass set on the actuator in kg, and $g = 9.81\,\mathrm{m\,s^{-2}}$ is acceleration due to gravity.

The simplicity of the procedure is thought to reduce any error in calibration due to mis-loading of equipment during the calibration procedure. However, a downside lies in the small range of values available (masses were only available up to 250 g).

F.2.4 Motor

As for the CCR, motor supply voltage sets the extrusion rate through the cylinder and is set by by Pulse-Width Modulation (PWM) — the technique of controlling the ratio of time when voltage is applied to when it is not in order to control the rotation rate. The digital PWM signal is created by the Arduino control board, but needs to be current amplified as the motor's operation current is far higher than can be safely supplied by the Arduino. This is done through the use of a half-bridge circuit — a set of transistors used to amplify current.

F.2.5 PI Control

Flow rate measured by the optical encoder and force measured by the loadcell can both be controlled by applying the well-known PI algorithm [9] (described in Appendix C). However, tuning of the algorithm proved difficult and the bare PI algorithm was modified. The issue lay in oscillatory responses appearing in the controlled variables. Tuning was difficult as the fluids run in the SPR are widely varied and so one set of tuning parameters for one suspension composition did not apply well to another composition.

One solution proposed was to have different sets of control parameters varying with composition. This investigation formed the basis for a project for a Master's student [2], but the results have yet to be merged into the software.

To remove this oscillation from the response, a scheme termed "momentary" control was developed[§]. In this scheme, the controller applied the PI algorithm to the system (attempting to maintain a setpoint of either flow rate or force) for a period of

---

[§] To the best of the author's knowledge this scheme is not described in literature.

20 seconds at the start of the run. After this period ends, the controller applies whatever value it last calculated for the motor DC, and holds it until the end of the run. In this way, any oscillation due to controller action is limited to the active control period, while the passive period has no active control and therefore no controller oscillatory response is possible. In addition, the active period allows the system to come to (near) the setpoint, allowing for a semi-controlled rheological experiment.

F.3 Summary

In this chapter, a design for a syringe pump rheometer was presented. This SPR employed many of the same design principles as the CCR, showing the versatility of the techniques.

References

[1] I. Panesar, “Automation and controller of laboratory experiments using a raspberry pi — for use in analysing phenomena in non-Newtonian fluids by creating a time dependant rheometer,” M.S. thesis, University of Strathclyde, 2019.

[2] C. Laing, “Controlling the flow of shear-thickening non-Newtonian fluid in a pipe using PI control,” M.S. thesis, University of Strathclyde, 2020.

[3] A. Mukhopadhyay, “Jamming and flow in dense suspensions,” In preparation., Ph.D. dissertation, University of Strathclyde, 2021.

[4] R. E. ONeill, J. R. Royer, and W. C. Poon, “Liquid migration in shear thickening suspensions flowing through constrictions,” *Physical Review Letters*, vol. 123, no. 12, p. 128 002, 2019.

[5] “Syringe pump graseby omnifuse syringe driver pump infusion + brand new battery.” (2021), [Online]. Available: `https://www.ebay.co.uk/itm/Syringe-Pump-Graseby-Omnifuse-Syringe-Driver-Pump-Infusion-BRAND-NEW-BATTERY/174619160183?hash=item28a81cee77:g:VLgAAOSwtllf5eSU` (visited on 04/03/2021).

[6] “Electronic balance weighing load cell sensor 5kg with hx711 module.” (2021), [Online]. Available: `https://www.ebay.co.uk/itm/Electronic-Balance-Weighing-Load-Cell-Sensor-5Kg-with-HX711-Module/162241279056?hash=item25c6557450:g:l7gAAOSwh2xYAwSK` (visited on 04/03/2021).

[7] “Diy load cell weight sensor 20kg portable scale+hx711 weighing sensor.” (2021), [Online]. Available: `https://www.ebay.co.uk/itm/DIY-Load-Cell-Weight-Sensor-20KG-Portable-Scale-HX711-Weighing-Sensor-Ad-Modl-UK/392955442217?hash=item5b7df83429:g:XlQAAOSwIaFZNTFf` (visited on 04/03/2021).

[8] P. Peter Atkins and J. De Paula, *Atkins physical chemistry*. OUP Oxford, 2014.

[9] A. Visioli, *Practical PID control*. Springer Science & Business Media, 2006.

G. Cylinder Wall Heat Transfer

G.1 Overview

In the Concentric Cylinder Rheometer (CCR) described in this thesis, temperature is monitored by thermocouple placed on the outside of the outer cylinder. This is an indirect measure of the temperature of the fluid in-between the outer and inner cylinders. This design was opted for as it eliminated intrusion into the flow cell, while still allowing measurement of the temperature. However, the temperature measured will be at a slight delay due to the heat needing to travel through the glass before it can affect the thermocouple. The thermocouple on the glass might also be at a lower temperature than the fluid itself (if *e.g.* the fluid is subject to viscous heating). In this chapter, the heat transfer calculation is performed in two cases: unsteady heat transfer (before steady state is achieved) in Section G.2 and steady state temperature difference across the Couette cylinder in Section G.3.

G.2 Unsteady Heat Transfer Calculation

Heat is transferred from the fluid, through the glass cylinder, and to the thermocouple. The temperature on the outside surface of the glass is assumed to be the same temperature as measured by the thermocouple. For this analysis, the fluid and air are taken to have a constant temperature. This is to gauge how long it would take, if the fluid heated up, for the fluid temperature to propagate through to the thermocouple.

Start by taking an energy balance over the glass wall:

$$\mathrm{accumulation} = \mathrm{generation} - \mathrm{consumption} + \mathrm{in} - \mathrm{out}$$

No reaction taking place, so no generation or consumption. Assume early time — steady state has not been achieved and heat has not yet exited the system: outlet

Table G.1: *Heat transfer coefficients and thermal conductivities for Couette cell.*

Parameter	**Value**	**Notes**
h_{fw}	$500\,\mathrm{W\,m^{-2}\,K^{-1}}$	Approximated as lower bound of values given in [1] for low temperature free convection for water.
k_w	$0.78\,\mathrm{W\,m^{-1}\,K^{-1}}$	Glass thermal conductivity from [1].
h_{wa}	$28\,\mathrm{W\,m^{-2}\,K^{-1}}$	From [2]

can be neglected. Accumulation is the enthalpy change in the thermocouple, and inlet is the heat transferred through the wall of the cylinder, Q_{in}.

$$\frac{dE}{dt} = Q_{in}$$

$$\frac{d}{dt}\left[m\,c_p\,(T_T(t) - T_{T,0})\right] = U A_c\,\Delta T_F(t)$$

where m is mass of the glass cylinder in kg, c_p is the specific heat capacity of the glass in $\mathrm{kJ\,kg^{-1}\,K^{-1}}$, $T_T(t)$ is the temperature of the thermocouple over time in K, $T_{T,0}$ is the initial thermocouple temperature in K, U is the overall heat transfer coefficient for the fluid-glass system in $\mathrm{kW\,m^{-2}\,K^{-1}}$, A_c is surface area of the cylinder in $\mathrm{m^2}$, and $\Delta T_F(t) = T_F - T_T(t)$ is the temperature difference between the fluid and thermocouple.

The glass has mass of 119 g and heat capacity $0.75\,\mathrm{kJ\,kg^{-1}\,K^{-1}}$. The cylinder wall has heat transfer area $A = 1.14 \times 10^{-2}\,\mathrm{m^2}$. The overall heat transfer coefficient can be calculated from:

$$\frac{1}{U} = \frac{1}{h_{fw}} + \frac{t_w}{k_w} + \frac{1}{h_{wt}} \tag{G.1}$$

where h_{fw} and h_{wt} are the heat transfer coefficients for between the fluid and wall, and wall and thermocouple in $\mathrm{W\,m^{-2}\,K^{-1}}$, k_w is the thermal conductivity of the glass wall in $\mathrm{W\,m^{-1}\,K^{-1}}$, and $t_w = 2\,\mathrm{mm}$ is the wall thickness. Assuming the solid-solid heat transfer coefficient h_{wt} is large, then $\frac{1}{h_{wt}}$ can be neglected. The heat transfer coefficients for the Couette cell used in the Custom Couette Rheometer (CCR) are presented on Table G.1

Take $\frac{m\,c_p}{UA} = \tau$ as the time constant for the transfer. This differential equation can be easily solved to give a formula for thermocouple temperature at a time t:

$$\Delta T_T(t) = T_F(1 - e^{-t/\tau}) \tag{G.2}$$

For a first order process like this, we can expect a disturbance to transmit through the process completely after approximately 5τ. For this process, τ has a value of $0.12\,\mathrm{s}$ and the temperature disturbance is fully propagated after $\sim 0.6\,\mathrm{s}$. This can be seen graphically on a plot of $T_T(t)$ against time, Figure G.1. This plot shows different fluid temperatures and how long they take to propagate.

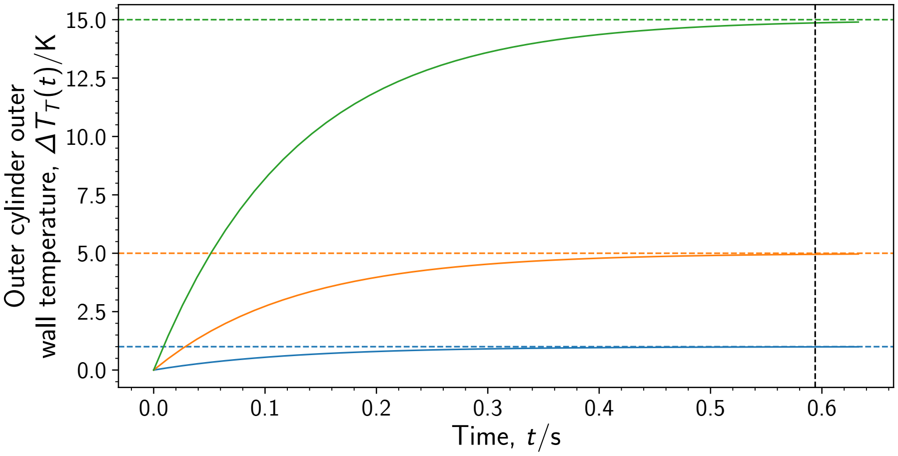

Figure G.1: *Outer cylinder wall temperature (solid lines) plotted against time. Calculated using Equation* (G.2)*. Dashed lines indicate final value, and time taken to reach* 99% *of the final value.*

G.3 Steady state temperature difference

At steady state the work input by the motor does not accumulate and transfers through the cylinder wall. Heat convects through the suspension in the Couette cylinder, the conducts through the glass cylinder wall, then convects away through the air. The heat transfer rate can be calculated using:

$$W_{heat} = UA(T_f - T_a) \tag{G.3}$$

where W_{heat} is the heat flowing through the system (equal to the work done by the motor in the fluid, W_{visc}) in W, $A = 1.14 \times 10^{-2}\,\mathrm{m}^2$ is the heat transfer area, T_f is the temperature of the fluid at steady state, T_a is the temperature of the air, and U is the overall heat transfer coefficient in $\mathrm{W\,m^{-2}\,K^{-1}}$ which can be calculated using:

$$\frac{1}{U} = \frac{1}{h_{fw}} + \frac{t_w}{k_w} + \frac{1}{h_{wa}} \tag{G.4}$$

If the heat transfer rate, heat transfer coefficients, thermal conductivity, and ambient temperature are known, then the fluid temperature can be calculated using Equation G.3. Then, the temperatures of the inside wall T_{iw}, and outside wall T_{ow} can be calculated using:

$$W_{heat} = h_{fw} A \left(T_f - T_{iw}\right) \tag{G.5a}$$

$$W_{heat} = \frac{k_w A}{t_w} \left(T_{iw} - T_{ow}\right) \tag{G.5b}$$

The steady state temperature difference between the fluid and the outside of the cylinder can then be found.

The heat transfer coefficients for the Couette cell used in the Custom Couette Rheometer (CCR) are presented on Table G.1. The calculation outlined above is performed for runs in the CCR to uncover the difference between the fluid temperature (the temperature of interest) and the temperature of the outside of the cylinder (temperature measured by the thermocouple). For a suspension of **CS45:(G85:W15)** sheared at $1.825\,\mathrm{rad\,s^{-1}}$, the heat input to the fluid is $16.49\,\mathrm{mW}$. The resulting temperature difference between the outside wall and fluid is $T_f - T_{ow} = 4.018\,\mathrm{mK}$.

G.4 Summary

Heat is transferred through the glass wall of the cylinder at a slight delay of $\sim 0.6\,\mathrm{s}$. This is a short time in comparison to the longer 3–5 min experimental runs in the CCR. In addition, the temperature does not change much during a run, at most by a few degrees over the course of five minutes. This slight change should be noted, but its dynamics are not important to this thesis. Therefore, this $\sim 0.6\,\mathrm{s}$ delay is acceptable. In addition, the steady state temperature difference between the fluid and outside the cylinder wall is negligibly small.

References

[1] R. Karwa, *Heat and mass transfer*. Springer Nature, 2020.

[2] R. Conti, A. A. Gallitto, and E. Fiordilino, “Measurement of the convective heat-transfer coefficient,” *The Physics Teacher*, vol. 52, no. 2, pp. 109–111, 2014.

H. Shear Banding

H.1 Overview

In this appendix, the calculation of shear band width within the Couette cell of the Custom Couette Rheometer (CCR) will be discussed. First, the calculation is described, then the results of performing the calculation for the runs of cornstarch suspension discussed in Chapter 6 are presented and discussed.

H.2 Calculation

A suspension is sheared in a Couette cell of inner radius $r_i$mm and outer $r_o$mm. The outer cylinder is held stationary and the inner cylinder is rotated such that the (apparent) shear rate in the fluid is $\dot{\gamma}$. The suspension may be jammed in whole or in part or not at all depending on the solute, its concentration, and the rate of shear. If the fluid is jammed completely, it can no longer be sheared. If the fluid is shear thickened enough, then the dilation effect causes particles in suspension to move apart. This may not occur homogeneously throughout the gap, and the result is fluid is pulled from a slowly-shearing part (band) into a high shear part.

Wyart-Cates theory [1] allows the prediction of the shear properties of a fluid by determining the strain rate corresponding to an applied stress given the composition of the fluid and some model parameters (empirically determined for the system). The composition of the jammed region is a parameter of the Wyart-Cates model and is therefore known. The composition of the high-rate (dilated) region can be determined by mass balance:

$$m_r = \rho_p \phi_{rest} V_t$$
$$m_s = \rho_p \left(\phi_{hr} V_{hr} + \phi_{lr} V_{lr}\right)$$

where m_r and m_s are the masses of particles at rest and when sheared respectively in kg. ρ_p is the particle density in $\mathrm{kg\,m^{-3}}$. V_t, V_{hr} and V_{lr} are the total, high-rate band (dilated) and low-rate band (un-dilated) volumes of suspension within the Couette cell. ϕ_{hr} and ϕ_{lr} are the volume fractions of solids in the high- and low-rate bands, and ϕ_{rest} is the volume fraction of solids at rest. This simplified slightly. The volume fraction in the low-rate region must be volume fraction of jamming in Wyart-Cates theory, $\phi_{lr} = \phi_j$. The high rate volume fraction is renamed $\phi_{hr} \to \phi_B$ to indicate (dilated) band volume fraction. Similarly, band radial position r_{hr} is renamed r_B. Starting with a mass balance and knowing the solids are incompressible, the mass balance reduces to a volume balance:

$$\begin{aligned} m_r &= m_s \\ \rho_p \phi_{rest} V_t &= \rho_p \left(\phi_{hr} V_{hr} + \phi_j V_{lr}\right) \\ \phi_{rest} V_t &= \phi_B V_{hr} + \phi_j V_{lr} \end{aligned} \tag{H.1}$$

Total Couette shear cell volume is volume of an annular cylinder, as are the low-rate and high-rate band volumes. The low rate band is assumed to be next to the immobile outer cylinder, while the high rate band is assumed to be next to the rotated inner cylinder. Total volume and band volumes given approximately by (invoking a narrow gap assumption:

$$V_t \approx \pi H (r_{out} - r_{in})(r_{out} + r_{in}) \tag{H.2}$$

$$V_{hr} \approx \pi H (r_B - r_{in})(r_{out} + r_{in}) \tag{H.3}$$

$$V_{lr} \approx \pi H (r_{out} - r_B)(r_{out} + r_{in}) \tag{H.4}$$

where H is the height of the Couette cell and r_B is the radial position of the band. Substituting Equations (H.2) to (H.4) into Equation (H.1) yields:

$$\begin{aligned} \phi_{rest} \pi H (r_{out} - r_{in})(r_{out} + r_{in}) &= \phi_B \pi H (r_B - r_{in})(r_{out} + r_{in}) + \phi_j \pi H (r_{out} - r_B)(r_{out} + r_{in}) \\ \phi_{rest} (r_{out} - r_{in}) &= \phi_B (r_B - r_{in}) + \phi_j (r_{out} - r_B) \end{aligned}$$

which can be rearranged to give the radial size of the high-rate band:

$$r_B = \frac{\phi_{rest}(r_{out} - r_{in}) + \phi_j r_{out} - \phi_B r_{in}}{\left(\phi_B - \phi_j\right)} \tag{H.5}$$

Equation H.5 gives the size of the shear band, knowing the volume fraction of the high rate region, ϕ_B. ϕ_B is calculable, knowing the stress, by finding the volume fraction where the rate of change of strain rate with respect to stress ($\frac{d\dot{\gamma}}{d\sigma}$) is zero — See Equation 2.9.

H.2.1 Calculating band width for cornstarch suspensions

The methodology described above is applied to the cornstarch suspensions used in this thesis. Runs of cornstarch are selected based on whether they are predicted by Wyart-Cates theory to have unstable flow (*i.e.* are in the **dst** region of the phase diagram — see Figure 7.1). For each run of cornstarch in the rheometer — a suspension of particular volume fraction ϕ sheared at a particular stress σ – r_B is calculated using Equation H.5. ϕ_j is calculated using Equation 2.5. The results of this calculation for a selection of runs of cornstarch suspension are presented and discussed in Section 6.4.

References

[1] M. Wyart and M. E. Cates, “Discontinuous shear thickening without inertia in dense non-Brownian suspensions,” *Physical Review Letters*, vol. 112, no. 9, pp. 1–5, 2014.

I. Paper in Preparation

I.1 Overview

Included on the following pages is the paper in preparation detailing the design of the custom rheometer, and its application to investigation of cornstarch suspension. Following on from the design, experiments on Newtonian mixtures of glycerol and water, and on suspensions of cornstarch are detailed. These experiments are proposed to be used in the custom rheometer as part of a laboratory demonstration or undergraduate project piece. The custom rheometer incorporates many aspects of engineering and science from electronics through fluid flow to computer programming, and therefore would make an effective tool for building these skills, in an undergraduate cohort.

3D Printed Rheometer for Investigation of Dense Suspension Flow Instability

Christopher Boyle,* Mark Haw, and Leo Lue
Department of Chemical and Process Engineering, University of Strathclyde, Glasgow

(Dated: January 29, 2022)

Rheometry is an important technique in pharmaceutical, cement, and paint Industries for appraisal of fluid characteristics. However, conventional lab rheometers can be prohibitively expensive, limiting their use. In addition, desired time-varying measurements are not always available, being locked by the vendor. In this work, a custom rheometer is designed, constructed, and validated for investigation of high-viscosity Newtonian and non-Newtonian rheologies. The design offers several advantages over commercially available devices; cost-effective (under $500), extensible/flexible hardware, and unlimited access to measurements. The design makes heavy use of 3D printing technologies to create the bulk of the instrument, giving it flexibility and keeping costs low. The construction process is proposed as a project and subsequent lab demonstration piece. Example experiments are performed with the device, showing its utility both as a research instrument and educational/project piece.

I. INTRODUCTION

Suspension rheology presents with interesting phenomena such as a rise in viscosity with increase in strain rate, (shear thickening), time-dependent (thixotropy), or visco-elasticity: the effect depends on the nature of the suspended particle and solvent. Hard-sphere suspensions exhibit shear thickening, and a more dramatic form, shear jamming [1–4]. Shear jamming is a transition to a solid-like state of a suspension under flow. This is perhaps most well-known through the ability to run on a pool of cornstarch suspended in water. Perhaps due to the complex dynamic rheology, such suspensions are of importance to many industries including cement [5, 6], paints [7] and cosmetics [8] production, advanced material development [9], and battery technologies [10].

The main instrument of rheological investigation is the rheometer, an instrument which produces a flow in a test fluid and measures stress and strain rate. A commercial rheometer can be quite costly: starting prices are on the order of tens of thousands of dollars [11–13]. This large cost can be prohibitive to a small business, researcher, or educator. In addition, the commercial device is unlikely to succeed in every situation; instead favouring a particular operating mode and requiring significant modification (whether by trained technicians, or by purchasing of extension modules from the manufacturer). A commercial device, may have special requirements further increasing its cost, such as a compressed air supply, or a water supply. The commercial device is, by nature, a sensitive piece of equipment liable to any number of operational failures. This requires the maintenance often only supplied by the manufacturer. Finally, the software required to run the device is not free or open, so that the operator may not be able to get the information desired from the device due to imposed limitations. If the researcher desires to investigate the effect of control action on rheology, they are limited by the software. The device may be limited to reporting only time-averaged data limiting the study of dynamic response. This inhibits the utility of the commercial device; whether in a research lab or an educational environment.

Typically, custom rheometers are built in order to facilitate non-conventional investigation [14–16] as commercial rheometers are not able to report the desired information, are too big to enter into (or too small to admit) the scope of another instrument, do not report the desired information, or are not sufficiently adaptable to do what the investigator desires. The DIY instrument can be made to accommodate any specification allowing the researcher great freedom.

However there is a trade off: custom devices lack the accuracy and ease of use of a commercial device. Traditionally, custom devices have had a lengthy design/production phase due to the time cost of organising parts to be built, or time to acquire the relevant materials. Enter: rapid prototyping. 3D printing has come a long way in the last 20 years to the point that consumer 3D printing units are widely available with consumer desktop units costing $400–$4000 [17–19]. This opens up not only the “maker” community (the hobbyists and enthusiasts that enjoy creating) but also opens up new avenues for instrumentation design for the laboratory.

In research, this drastically shortens the development time and, with only a little training, allows the researcher to build their own bespoke equipment. This can range from simple mechanical supports to create consistent positioning of apparatus, to fully fledged instrumentation.

3D printing not only shortens the development cycle, it allows flexibility impossible with other production methods. The speed of production means new parts can be re-printed in a matter of hours. If something breaks, it is repaired that same day. If a design of part is required, it is fitted by the afternoon. A redesign that might have been avoided due to lengthy construction times is now possible.

In this paper we will present a design for a 3D printed rheometer, discussing its abilities and limitations. We

---

* christopher.boyle.101@strath.ac.uk

will then present experiments showcasing the use of the custom rheometer: calibration of the device using model fluids, then rheological testing of Newtonian fluids, followed by a more niche investigation into the dynamic response of non-Newtonian fluids.

II. DESIGN

The core of all rheometers are the same: a mechanism for controlling and driving flow, and sensors for recording the forces/torques, and the strain rates. This is summarised through Newton's viscosity law [20]:

$$\mu = \frac{\sigma}{\dot{\gamma}}. \tag{1}$$

The viscosity μ (Pa s) given by the ratio of stress σ (Pa) to strain rate $\dot{\gamma}$ (s^{-1}). To allow calculation of rheological properties, flow is created through a well-known geometry. We have chosen to use a Couette cell geometry (Fig. 2a) (also known as a concentric cylinder geometry). An inner cylinder sits within an outer cylinder with fluid in-between. One of the cylinders is rotated, causing a shear flow in the fluid. In this work, the inner cylinder is rotated.

In addition to the Couette cell [21], the rheometer designed here (Fig. 1) consists of the following components; a strain rate sensor, a stress sensor, flow driving component, a temperature sensor, and a controller. We use a Raspberry Pi (RPi) single board computer [22] to control the apparatus and handle data acquisition.

Both the optical encoder disk, and the stress measurement apparatus were modelled in FreeCAD and OpenSCAD softwares and 3D printed in PLA filament on a Prusa i3 Mk3 3D printer. A list of purchased and printed components are given in Appendix A. A full set of prints took approximately 28 hours, details of the print procedure are given in Appendix B. 3D printer aside, no specialty equipment was used. The electronic components are those available to the public from online retailers. Circuit diagrams are given in Appendix C. Electronics are interfaced though the Raspberry Pi with software written for the purpose described in Appendix D.

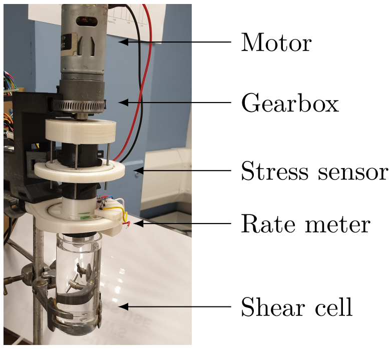

FIG. 1: Photograph of the custom rheometer with labelled components.

The components assembled together are held on a clamp stand by 3D printed supports. The outer cylinder is held via an X-Y table, to allow fine control of the cylinder position, ensuring the cylinders are concentric before a run is commenced.

A. Strain Rate Measurement

Rotation rate measurement is achieved in this work by use of an optical encoder: a slotted disk paired up with light gates so that rotational position is encoded as peaks and troughs in a square-wave signal (Fig. 2b). The rotation rate ω is inversely proportional to the square-wave period t_{opt}: $\omega = \theta_{slot}/t_{opt}$, where θ_{slot} is the angular size of the slot in rad, t_{opt} is in seconds, and ω in $\mathrm{rad\,s^{-1}}$. Two light gates are employed, giving two measures of rate that can be averaged across to reduce error. The gates consists of a light source and sensor: an IR LED and IR-sensitive phototransistor respectively. When the slotted disk blocks light from shining on the transistor, its output voltage changes which is measured by the controlling Raspberry Pi computer.

In a Couette cell strain rate is then calculated from the rate of rotation:

$$\dot{\gamma}(r) = -\frac{2\omega_r}{r^2} \cdot \frac{{r_{in}}^2 {r_{out}}^2}{{r_{out}}^2 - {r_{in}}^2} \tag{2}$$

where $r' = r_{in}/l_{gap}$ is the normalised inner radius, $l_{gap} = r_{out} - r_{in}$ is the gap width, and r_{in} and r_{out} are the radii of the inner and outer cylinder respectively and have values given in Table. I. If the gap is small enough, the strain rate can be taken to be $\dot{\gamma} \approx \frac{r_{in}\omega}{l_{gap}}$ (narrow gap approximation).

This method achieves accurate rate measurement (standard error of the mean less than 1%). However, due to the nature of the encoder, the time resolution of measurement varies directly with rate of rotation (fewer rotations in a given time gives fewer full waves and so fewer periods with which to calculate rate): time granularity is given by $\Delta t_{opt} = \theta_{slot}/\omega$.

B. Stress Measurement

The stress developed by driving a fluid to flow exerts a load torque on the inner cylinder. Measuring this torque can be achieved by splitting the cylinder drive shaft into driving and driven parts, with a torque sensor in between.

The torque sensor used in this work (Fig. 2c) is designed as follows; the driven shaft is coarsely threaded with a very wide pitch, and has a compatibly-threaded annular runner so that if the runner is not allowed to rotate, rotation of the driven shaft causes axial movement in the runner. The driving shaft has steel rods protruding

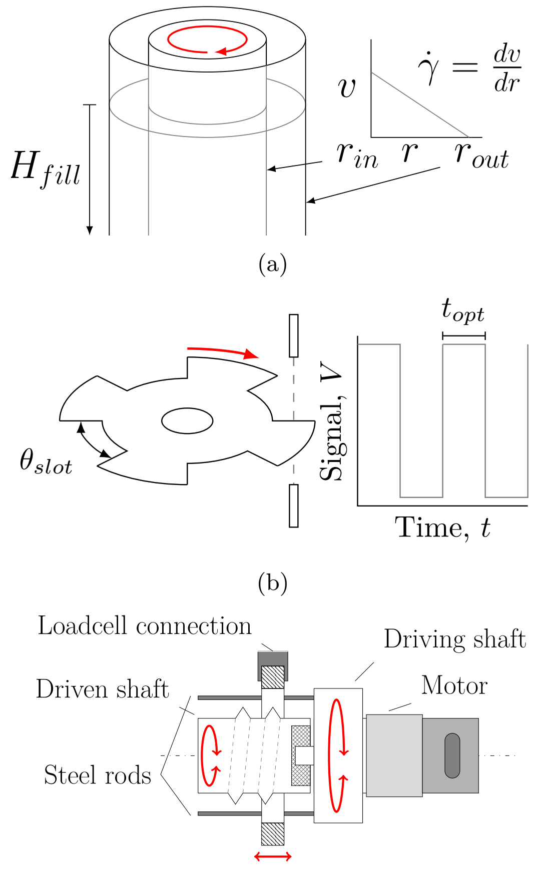

(c)

FIG. 2: Schematic diagrams of (a) Couette shear cell, (b) optical encoder, and (c) stress sensor. Red arrows indicate directions of movement.

TABLE I: Summary of geometry

Parameter	Symbol	Value
Fill depth	H_{fill}	Variable; 50–75 mm ± 2%
Inner cylinder radius	r_{in}	15.05 mm ± 0.17%
Outer cylinder radius	r_{out}	19.75 mm ± 0.13%
Gap width	l_{gap}	4.7 mm ± 0.11%

into the runner, through lubricated holes: vertical/axial movement of the runner relative to the motor is allowed, but rotational (relative to the driving shaft) is not. This results in a connection that converts a difference in rotation between driven and driving shafts into an axial position of the runner, or difference in torque between the driver and driven shafts to a linear force on the runner.

The runner is connected to a loadcell via a bearing, so that rotational force of the driven shaft relative to the driving shaft (i.e. a load torque) presents as a force measurement on the loadcell. Loadcell value is read by analogue-to-digital converter (ADC). Total torque M_{total} can be calculated from loadcell value using the relation:

$$M_{total} = k_{LC\to M}\left(LC - LC_z\right), \tag{3}$$

where LC is the 24-bit reading from the loadcell ADC, and LC_z is the ADC value at zero load, and $k_{LC\to M}$ is the term converting a loadcell value to a torque. The latter two are fitting parameters. This total torque is split between the load due to the fluid and loading due to bearing friction:

$$M_{total} = M_{load} + M_{friction}. \tag{4}$$

Friction torque is related to the rate of rotation,

$$M_{friction} = k_{\omega\to M}\,\omega, \tag{5}$$

giving the third and final fitting parameter of the calibration. The stress can be calculated from torque on the inner cylinder:

$$\sigma = \frac{M}{2\pi r_{in}^2 H_{fill}}. \tag{6}$$

The loadcell is the main deciding factor in the range of stresses that can be measured. A loadcell rated for 1kg will be able to measure up to ∼ 9.8N, however small forces may become lost in noise (less than one-third of a percent of the range seems to be the limit for this hardware, according to our tests). It is important therefore to suit the loadcell to the intended measurement.

Force on the loadcell can be estimated from the stress, assuming negligible friction, using $F_{lc} \approx \sigma\, H_{fill}\, r_i$, informing the choice of loadcell.

A loadcell of differing rating may not have the same form factor or size as another. 3D printing enables quick creation of a suitable “jig” or fitting for the new loadcell.

Time resolution of the loadcell is limited by the ADC. For a high-resolution ADC there is a significant time devoted to converting the analogue signal into digital. For the HX711 used here, the conversion time is $\Delta t_{lc} = 0.0125\,\mathrm{s}$.

C. Driving Shear

A DC motor (Fig. 2c) drives the rotation of the inner cylinder. This motor is connected to the driving shaft by a gearbox, which reduces the rate of rotation by its gear ratio. DC motors tend to rotated quickly or stall, so the gearbox allows access to a lower range of rotation rates. This gearbox/motor combination can be swapped out to achieve different range of rates if so desired.

The motor’s rotation is controlled by means of Pulse Width Modulation (PWM): the motor is powered by a square wave signal, where the ratio of peaks to troughs (the duty cycle, DC) changes the rotation rate. PWM is a feature built in to the Raspberry Pi where it is set as a 10-bit number, allowing changes of the total motor supply voltage, which feeds on to set the motor rotation rate.

D. Controller

Control of the equipment is managed via discrete electronic circuits and a Raspberry Pi. The controller's purpose is to ensure the desired flow is achieved in the rheometer (i. e. at the desired rate or with the desired stress). It is also responsible for data acquisition from attached sensors and outputting it in a logical manner.

Control is possible of both stress and strain rate using the Proportional-Integral-Derivative (PID) [23] algorithm.

An alternative "control" method is to control neither stress nor strain rate, but instead, instead only to control the motor PWM DC (corresponding roughly to rotation rate). This eliminates dynamics effects of the controller itself and is useful when investigating dynamic rheology and is the control method employed here. The rotation rate of a given DC set point will vary depending on the viscosity of the material, and the gearbox in use.

E. Limitations

There are limits on the measurement abilities of the custom rheometer. Uncertainties in the measurements were estimated (summarised in Table II). Uncertainties were estimated for the different parts of the custom rheometer. Geometry was measured using a set of digital calipers — uncertainty estimated as half the smallest increment of $\frac{1}{2} \times 0.01\,\mathrm{mm}$. Strain rate measurement has uncertainty estimated by taking the percentage relative standard deviation (PRSD) over many runs, resulting in a percentage uncertainty of 4.03%. Stress measurement is similarly estimated from PRSD measurements giving an uncertainty of 25.67%.

The stress measurement uncertainty is fairly significant, at 25.67%. This is likely due to the coupling between loadcell and Couette cylinder. The design has a fair few moving parts and while care has been taken to reduce friction between this parts as much as possible, perhaps more could be done to improve this. At present no grease or other lubrication is employed in the stress coupling — addition of friction-reducing grease could give smoother operation that without. In addition, alternative materials could be investigated for the runner, threaded shaft, and bearing components (see Figure 7) as these components see the most friction and could benefit from harder materials than PLA (which is relatively soft [24]) such as Acetylonitrile-butadiene-styrene (ABS) [25].

TABLE II: Summary of Measurement Uncertainties

Property	Symbol	Uncertainty
Fill depth	H_{fill}	less than ±2%
Inner cylinder radius	r_{in}	±0.17%
Outer cylinder radius	r_{out}	±0.13%
Gap width	l_{gap}	±0.11%
Strain rate	$\dot{\gamma}$	±4.03%
Stress	σ	±25.67%

III. EXPERIMENTS

A. Calibration

The loadcell needs to be calibrated by shearing glycerol-water solutions of known mass composition $\phi^w = m_{solute}/m_{solvent}$ in the rheometer; the fitting parameters LC_Z, $k_{LC\to M}$, and $k_{\omega\to M}$ can be obtained by least-squares fit of Eqs 3–6 to the measured loadcell and strain rate values, and viscosity found from composition and temperature for aqueous glycerol solutions using an expression fit to tabulated data [26].

1. Method

Aqueous solutions of glycerol (99.9%, Sigma-Aldrich) were prepared by weighing out the relevant amounts of glycerol and water and mixing together in a large jar. The lid was then sealed, and the solution shaken and allowed to rest for at least an hour before use to allow bubbles to rise out of the solution.

The rheometer is loaded by filling the cylinder with approximately 50 ml of test fluid and the fill depth H_{fill} measured and recorded using a ruler or pair of calipers. The cylinders are centred by adjustment of the X-Y table while the inner cylinder is running. If the inner cylinder is off centre, then the fluid can be seen to rise up the side of the outer cylinder. This effect is used to perform the centering; the outer cylinder's position is varied until the rising effect is minimised.

Runs of 3 minutes at a set motor supply voltage are performed, corresponding approximately to constant rotation rate. Voltage is increased and decreased in an up-down-up sweep to highlight any possible hysteresis in measurement (although hysteresis was found not to occur). This set of runs is repeated for another sample of the same fluid. Then, the whole process is repeated for another test fluid.

Pure glycerol, and both 85 wt% and 95 wt% aqueous solutions of glycerol are used.

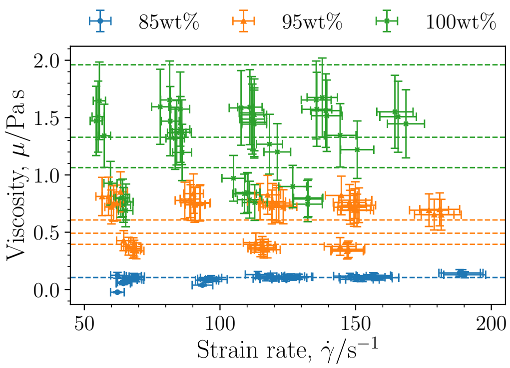

FIG. 3: Viscosity plotted against strain rate for Newtonian fluids glycerol and glycerol-water 95 wt%. The dashed lines show the maximum, mean, and minimum expected viscosity (as this varies with temperature). There is only a single dashed line for glycerol-water 85 wt% as there is no significant heating effect and all three lines collapse together.

2. Results and discussion

The rheometer measures loadcell, strain rate, and temperature, while the expected viscosity is known from the temperature and tabulated data. The stress is obtained using Eq. 1 and torque from Eq. 6. The calibration parameters for Eq. 3 and Eq. 5 are found by least-squares fitting the load torque to the loadcell value.

The fitting procedure is performed using a `Python` script, using the `lmfit` module [27]. `lmfit` provides a consistent interface to a number of fitting algorithms provided by other modules, most from the well-known `scipy` library [28], simplifying the fitting process.

Figure 3 shows shear experiment data obtained for the calibration materials (filled circles — each represents the average of a single 3 minute run), and compares this to the expectation from tabulated data (dashed lines). There is appreciable scatter in the measurements at low strain rate, which reduces at high rate. This rate dependence is in part due to the configured range of the stress sensor, and (for the glycerol) in part due to an off-centring of the inner cylinder exacerbated by the longer timescale for the glycerol to flow back. As the rotation timescale reduces (rate increases), this effect reduces. This scatter is used to estimate measurement error.

Standard error of the mean (SEM) for the Newtonian timeseries is used to quantify the measurement error. The timeseries are split into segments. Standard deviation in the means of those segments gives the SEM — an indication in how "stable" the signal is in time. Encoder (strain rate) measurement was calculated to have a worst-case SEM of 0.04 % at $\dot{\gamma} < 25\,\mathrm{s}^{-1}$. At best, an SEM of 0.01 % at $\dot{\gamma} > 175\,\mathrm{s}^{-1}$. Both errors are acceptably low. It is therefore concluded that the limits of measurement for the encoder are outside the working range achieved here. Slower and faster rates would need to be investigated to find the lower and upper bounds.

To check goodness of fit to viscosity expressions of Cheng [26], standard error is calculated for the parameters by `lmfit` (by inverting the matrix of second-derivatives for the fit function), resulting in errors of 5% or less, average error $\bar{\epsilon}_{fit} = 2.81\%$. The expression of Cheng used to obtain the viscosities of glycerol-water solutions has a reported [26] average error of $\bar{\epsilon}_{cheng} = 1.43\%$ which must be included in the stress conversion error: $\bar{\epsilon}_{stress} = \bar{\epsilon}_{fit} + \bar{\epsilon}_{cheng} = 4.24\%$.

The stress sensor was found to perform worst (SEM $> 2\%$) for stresses below 20 Pa, with error falling to $\sim 0.2\,\%$ as stress increases above 100 Pa. As stress increases the error falls. The upper measurement limit is then outwith the practically achievable stress range. For the strain rates and materials used in this work, stresses below 20 Pa cannot be achieved with this hardware and so the error in stress measurement is acceptable. To measure accurately smaller stresses, a loadcell rated for smaller forces can be used, along with a high reduction ratio gearbox to shear the fluids at a lower rate.

Together, these measurements are used to calculate fluid viscosity. Due to the much smaller error in strain rate measurement the viscosity result has an error resembling that of the stress measurement; higher error of $> 2\,\%$ below 0.15 Pa s, stepping down to 0.25 % above 0.2 Pa s.

B. Newtonian Fluid Rheology

Newtonian fluids are those that abide by Newton's viscosity law Eqn. 1: when sheared, the stress they develop is in direct proportion to the rate of shearing. The constant of proportionality is the viscosity. The rheology of a Newtonian suspension can be used as a test for the custom rheometer: measured stress and strain rate plotted against one another — a flowcurve plot — is expected to yeild a straight line for Newtonian fluids, with viscosity given by the gradient.

The custom device is used to investigate these Newtonian fluids. Shear experiments are performed, and flowcurves constructed and compared to tabulated data.

1. Method

Newtonian solutions of glycerol and water 85 wt%, 95 wt% are made up using the same method as the calibration experiment, and are run in the same manner. Solutions are made up on a mass basis according to their desired composition, the fluids are run sequentially in the rheometer for periods of constant voltage for 3 minutes at a time. Each material is repeated at least once to confirm measurements.

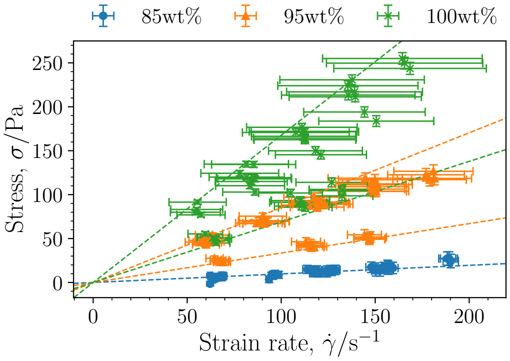

FIG. 4: Newtonian Flow-curve: plot of stress against strain rate for Newtonian glycerol-water mixtures. Each point is the average of a 3 minute run, error bars show measurement uncertainty. Dashed lines show gradient (viscosity) expected by the empirical formulae of [26].

2. *Results and Discussion*

Stress evolved during each run of the materials is calculated using the fit parameters found in calibration and Eqs. 3–6 to first calculate total torque, then friction torque and from that the load torque. Stress can then be calculated from the load torque, the geometry, and the fill height noted at the start of the experiment.

Figure 4a shows the flow curve recorded for the Newtonian fluids. The measurements fall on the same straight line for the same material, bar the 85 wt%, which split into two lines, emphasised by the dashed lines. This is perhaps due to differences in pre-loading on the loadcell, or insufficient lubrication in the threaded shaft (which dries up over time). Despite this, the average readings (Fig. 4b) of viscosity match closely the expected value.

This experiment showcases the ability of the custom rheometer to perform simple rheological testing. This set up could therefore be used to test the viscosity of various materials, or mixtures of materials. For example, household materials like honey, dish-soap, or ketchup could be tested to discover their viscosities or whether they are Newtonian or not. Other experiments include testing a blood-analogue for sickle cell syndrome [29], or using the rheometer as part of a material development project [30].

C. Shear Thickening Rheology

The custom rheometer is designed not only for Newtonian testing, but to be used to investigate more complex non-Newtonian rheologies such as dense suspensions which exhibit shear jamming. The prevailing Wyart-Cates (WC) model attributes shear jamming to a transition from lubricated to frictional flow [2, 3]: resulting in an S-shaped flowcurve (Fig. 6a). At high stress, there is an unstable region resulting in a jump in stress termed discontinuous shear thickening (**dst**). Where this jump results in a jam, the effect is called Shear Jamming. There is some evidence however that jamming is not always the case [14]: instead there is a separation into a thinned (flowing) region and a jammed region within the suspension: showing that more investigation is required, especially into local behaviours of the suspension.

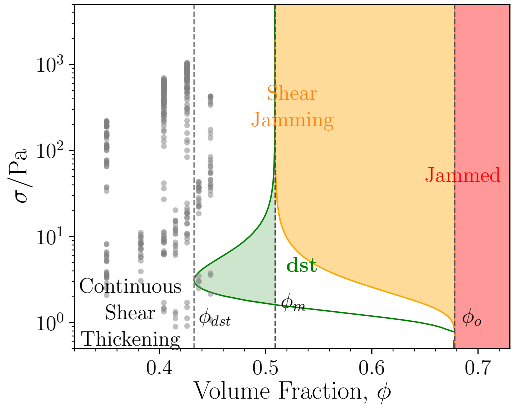

FIG. 5: WC phase diagram [16] showing whether a suspension of cornstarch in an 85 wt% glycerol-water solvent will be jammed, shear jammed, discontinuously thickened, or not. Grey circles show the predicted phase for the shear experiments in this work. The phase diagram is constructed by fitting measurements of sheared cornstarch suspensions (in the CCR) to the Wyart-Cates model.

The WC phase diagram (Fig. 5 [31]) predicts the behaviour for a suspension given the volume fraction ϕ and the stress with which the suspension is sheared. There are two key volume fractions for the model demarcating the regions above which shear jamming occurs (ϕ_m) and above which the suspension is fully jammed (ϕ_o) even without the application of shear. Additionally, there is a limit above which **dst** is observed, ϕ_{dst}.

At high stress, near the jamming point, dense suspensions have been seen to exhibit fluctuating or unstable flow [32, 33]. There is evidence pointing towards particle-migration between bands of specified shear stress which results in these bands growing and shrinking as the average stress changes. A phenomenological model has been proposed which uses competing rates of structure growth and decay within the suspension [4]. Further investigation of the fluctuation or instability is needed to unveil its origin, perhaps along with it key information about the nature of shear jamming.

The custom rheometer is used to investigate the rheology of dense suspensions. To gauge its effectiveness at this task, the result of rheological testing of cornstarch suspensions in the rheometer is compared to those obtained from a commercially available rheometer (TA Discovery HR 3).

1. *Method*

Suspensions of cornstarch in 85 wt% glycerol-water solvent were prepared on a mass basis of concentrations 30 wt%, 35 wt%, 40 wt%, 42 wt%, and 44 wt%.

The solvent is made up in advance using the method discussed previously. To make the suspension, cornstarch was weighed into a large beaker, then the solvent was weighed into the same beaker careful to avoid over filling. With the desired amounts of solvent and solute, the suspension was slowly mixed to get the solids up off the base of the beaker then mixed vigorously to break any clumps that may have formed. The result was a homogeneous suspension, milky in appearance with a viscosity ranging from thin syrup to honey, depending on the concentration of cornstarch.

The suspensions were allowed to rest to account for the swelling/wicking effect described by Han et. al. [34] which causes the solids volume fraction of the resulting suspension to increase over time as solvent enters into pores on the particles. For the average relative humidity in our laboratory of 44%, the solids volume fraction of cornstarch turns out to be similar to the weight fraction: $\phi \approx \phi^w \pm 1\%$ calculated using the estimation and particle porosity of Han et. al. [34].

The suspensions were then run as described previously in the custom rheometer: 3 minute constant motor supply voltage runs, with voltage changing between runs in an up-down-up pattern. Stress, strain rate, and temperature timeseries are recorded (although temperature is not reported here).

2. *Results and Discussion*

Figure 6 shows the two flow curves for the custom and commercial rheometers. There is a stark difference in the accessible ranges of measurement. The stresses developed in the commercial rheometer are magnitudes lower than the lowest reachable by the custom apparatus. There is overlap in the strain rate, but only for the lowest density suspension. Following the dashed guide lines, it can be seen that the custom rheometer measurements do not match the commercial device for the high concentration (43 wt%), but match fairly well for the lower concentration shown (30 wt%). However, there is a lot of noise in the measurement, even in the commercial machine. This is the nature of investigation into jamming fluids due to the dynamic response under high stress [32, 33, 35, 36]. In addition, there are many factors which contribute to the viscosity of a cornstarch suspension: solvent viscosity, temperature, storage temperature and humidity, suspension age. These differences could account for the offset in measurement.

The ranges of measurement are limited by the gearing on the motor, which decides the range of available strain rates. Slow strain rate will develop a low stress in the fluid, however this low stress could be lost in the measurement noise if the loadcell is better suited to larger stresses.

The two timeseries Fig. 6b–c show low-frequency oscillations in the rheology, not present on Fig. 6e. Stress in particular oscillates, for high viscosity fluids, with a frequency substantially lower than the frequency of rotation (oscillation frequency ~ 0.1 Hz cf. rotation frequency ~ 10 Hz). This oscillation is present for dense suspensions > 35 wt%, absent in suspensions of lower density. Looking at the crossover from slow oscillation to nothing apparent, from 40 wt% to 30 wt% it would place some critical weight fraction for onset of **dst** between those two volume fractions. This fits with the WC model value obtained for this system of $\phi_{dst} \approx 0.41$. This suggests that fluctuation is brought into the system as suspension density increases above ϕ_{dst} somewhat consistent with the results of [32], however they predict *chaotic* fluctuation in place of the steady oscillation seen here.

The investigation of the fluctuations is hampered by the strain rates achievable by the device, and the stresses measurable by the loadcell. This is ameliorated by the flexible nature of the device; the motor gearbox and loadcell can both be swapped out to change the limits of operation. The stresses readily achieved are a factor of 100 higher than minimum estimated onset stress (thus would miss the **dst** region on Fig. 5), and so a larger reduction gearbox of 264:1 from 27:1 along with a loadcell of lower rating of 100 g from 1 kg will allow the device to investigate the fluctuating **dst** regime on Fig. 5.

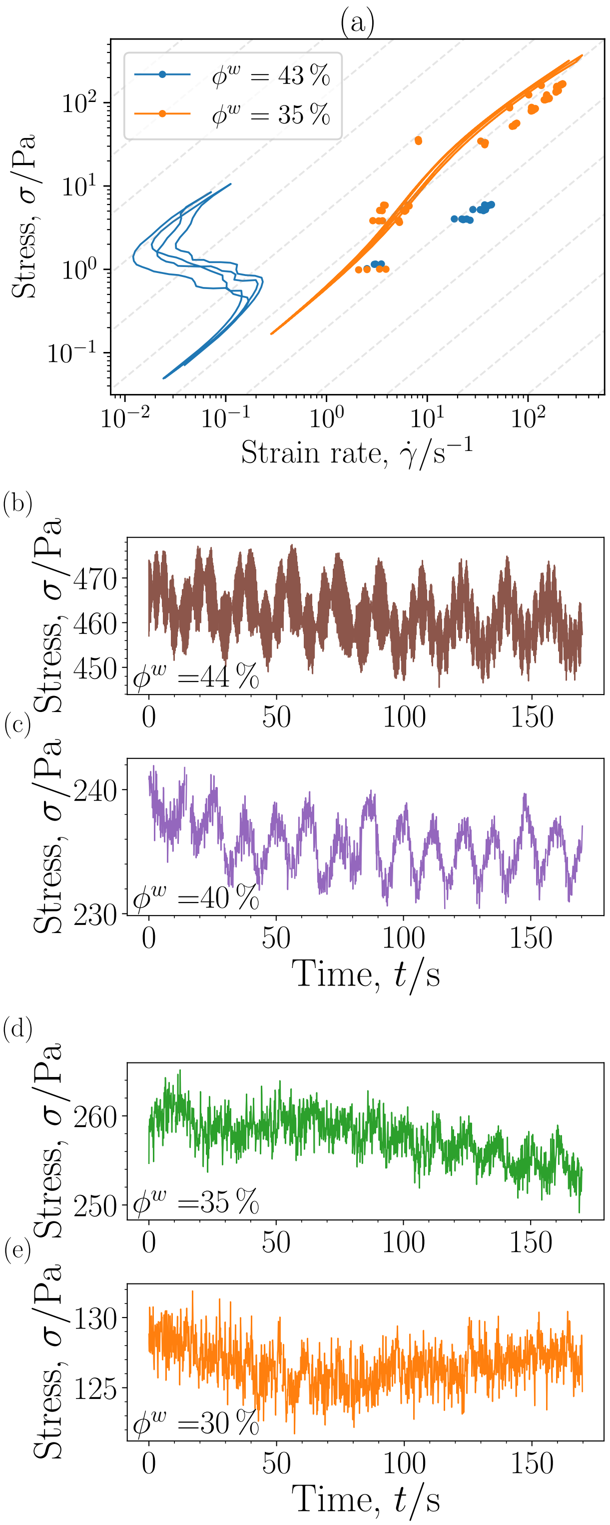

FIG. 6: (a) Plot of stress against strain rate for cornstarch suspensions in glycerol-water (85 wt%) of varying composition. Lines are results from a commercially available shear rheometer (TA Discovery HR-2). Circles are results from the equipment designed in this work. Dashed lines are Newtonian guide lines, to emphasise non-Newtonian behaviour. Only two concentrations of suspension (35 wt% in orange and 43 wt% in blue) are shown to maintain clarity. (b)–(e) plots of stress against time for select runs of suspension at max strain rate, showing the time-varying signal fluctuation recorded by the custom rheometer.

IV. CONCLUSIONS

In this paper we have presented a 3D printed rheometer, constructable for under \$500 and designed for the investigation of dense suspension rheology. We have validated the custom rheometer for use in measurement of viscosity for viscous Newtonian fluids and for dynamic measurement of suspension rheology. Newtonian rheology measured by the custom rheometer matches closely that expected from previous works. Non-Newtonian rheology is not as close, but with more factors at play there is a larger margin of error. There is also qualitative agreement with the dynamic results obtained as compared to those previously reported.

We have presented showcase experiments that the custom rheometer can be used for, as a researcher or as an educator looking for student projects for Physics or Engineering.

The design of the rheometer is relatively simple and requires only a few components readily available to the public in addition to the printed structure, making basic rheometry accessible to more people. Moreover, the custom rheometer has advantages over a commercially available instrument as it has unparalleled flexibility of use and design due to the 3D printed nature of the bulk of the design. The custom rheometer is open about its methods and technology, so the instrument is not a “black box” performing the analysis in the dark. However, this comes at a cost of loss of accuracy and ease-of-use.

The open nature of the device makes it rather easy to modify and able to implement niche investigative techniques such as inserting probes [37], basing the rheometer cell within an MRI [14], investigating granular flow [15], or performing dynamic light scattering experiments during shear [38].

The potential of 3D printing as a means of quickly, cheaply, developing laboratory instrumentation is great. Once a design has been created, it takes little time to gather the components and construct another from scratch. This empowers the researcher to perform modifications and necessary repairs *themselves*, not beholden to a manufacturer.

Appendix A: Components

Table III gives details of the non-printed components used in the construction of the rheometer. Suppliers are listed for the components along with part numbers where available. If a part was not purchased but already owned for this work, a similar part number/supplier is listed.

Table IV gives details of the printed components, the settings used (if different from default), and the approximate time required to print the part. The default settings are 0.3 mm layers, 3 perimeters, 20% infill, and no support structures. **3D models for the printed parts will be available, along with the datasets used in**

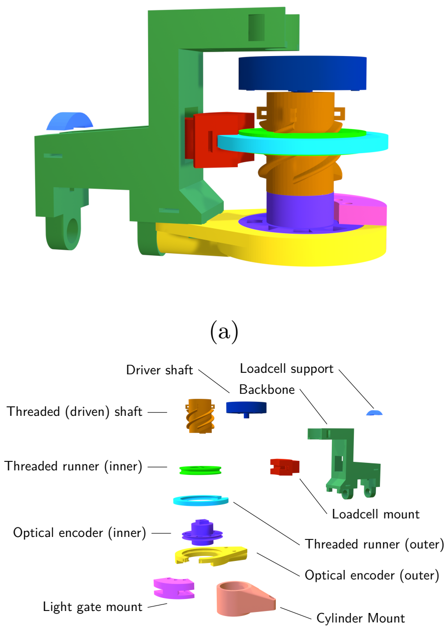

(a)

(b)

FIG. 7: Render of 3D printed parts (a) and labelled exploded-view diagram (b)

this work, via doi link. 3D rendered versions of the printed parts are shown on Fig. 7.

TABLE III: Summary of non-printed components

Name	**No.**	**Cost**[a]	**Part No./Supplier**
DC Motor, gearbox	1	\$70.75	RS Pro 942D271, RS Components
IR LED	2	[b]\$5.50	Vishay TSHF5210, RS Components
Phototransistor	2	[b]\$4.90	Osram Opto SFH 309, RS Components
NPN Switching Transistor	2	[e]\$6.60	Taiwan Semiconductor TSC961CT, RS Components
NPN Power Transistor	2	\$10.26	Texas Instruments LM395T, RS Components
100 μF Capacitors	5	[b]\$5.58	711-1731, RS Components
Loadcell (1 kg), HX711 ADC	1	\$8.23	HALJIA via Amazon
Operational Amplifier	1	[b]\$15.48	Texas Instruments LM358AN, RS Components
10 × 1 mm steel RC axels	10	\$7.48	Sourcingmap via Amazon
Clip-on ferrite core	10	\$8.84	YARADECRO via Amazon
2 mm Steel ball bearings	100[f]	\$6.79	Sourcingmap via Amazon
5 mm Steel ball bearings	100[f]	\$10.88	QLING via Amazon
Burette stand (1m)	1	\$30.62	e.g. MissZM via Amazon
Clamp stand	1	\$10.88	e.g. quieting via Amazon
G-clamp	1	\$6.24	e.g. Blue Spot 10031 via Amazon
Jubilee clips (~ 10 mm diameter)	2	\$9.40	Jubilee via Amazon
M8 × 70 mm bolt	1	[d]\$16.26	917-2886, RS Components
M2 × 8 mm bolt	2	[c]\$7.15	e.g. Singularity Supplies via Amazon
X-Y table (microscope stage)	1	\$236.50	e.g. Jectse via Amazon
Alt. X-Y table (drill press)	1	\$44.92	e.g. KATSU Tools via Amazon
	Total cost:	\$478.29	(\$286.71 with alternative table)

[a] Costs converted from GBP to USD.
[b] Pack of 10.
[c] Pack of 20.
[d] Pack of 25.
[e] Pack of 50.
[f] Approximate count.

TABLE IV: Summary of printed components.

Name	**Print Settings**	**Printing Time**
Threaded (driven) shaft	0.2 mm layers; 8 perimeters; 10% infill; with supports	3h
Threaded runner (inner)	0.2 mm layers; 10% infill.	1h
Threaded runner (outer)	0.2 mm layers; 10% infill.	45m
Driver shaft	—	85m
Loadcell-bearing linkage	0.2 mm layers; 10% infill; with supports.	1h
Loadcell cap	—	10m
Optical encoder (inner)	0.2 mm layers; 10% infill; with supports.	2h 15m
Optical encoder (outer)	0.2 mm layers; 10% infill.	2h
Light gate mount	0.2 mm layers; 10% infill; with supports.	1h 15m
Inner cylinder guide	—	30m
Backbone	With supports.	6h
PCB and RPi mount	—	2h
Outer cylinder base	—	4h
X-Y table mount	—	2h 45m

Appendix B: Printing Procedure

3D printing a part can be broken into three stages: design, slicing, and printing [39]. Design is the creation of the model for 3D printing. This is done using CAD tools such as Autodesk Inventor, FreeCAD, or OpenSCAD. Once the model is created, it needs to be converted into a format understandable by the printer in a process called “slicing”. Once the model is sliced into layers, the part can be printed.

The design step very much depends on the software used and will not be discussed here. In general, the design must take into account the practicalities of the model: tiny details and thin walls may not translate well into the final product.

The slicing step is where the print settings are put into action. This step decides the level of detail with which the model will be printed, the physical strength of the part, and how long it may take. These options will vary with material and printer.

Slicing is done using a piece of software called a “Slicer”, for example Ultimaker Cura, or Prusa Slic3r. This software converts the 3D model into layers, which can be exported into a GCODE file containings printer-understandable instructions on how to print the model.

Polylactic acid (PLA) is used in this work as it is very easy to work with, is widely available, and is cost effective. PLA printer filaments are best used with a printhead temperature around 200°C, a rough estimate of the temperature will be given on the packaging. Testing, and trial-and-error will help find the best temperature for each machine/filament combination.

Layer height sets the level of detail of the print at the cost of time consumed. Layer height is normally on the order of a tenth of a millimeter, around the nozzle diameter. 0.1 mm or less is fine detail, while 0.3 mm or greater is rough, better suited to situations where a good finish is not essential. For this rheometer, for the most part there is no need for a fine finish and so a large layer height can be used to expedite printing.

Once the desired settings are set, the model can be sliced and the GCODE can be generated, ready for printing.

Appendix C: Circuit diagrams

Presented on Fig. 8 is the schematic of electronic circuits used in this work. For clarity power lines 3.3 V, 5 V and ground from the Raspberry Pi to the sub-circuits have been omitted. 15 V DC is supplied by a benchtop power supply, the ground of which is connected to the Raspberry Pi ground. Ferrite cores are attached to both the Raspberry Pi microusb power supply, and to the benchtop power supply to reduce possible interference.

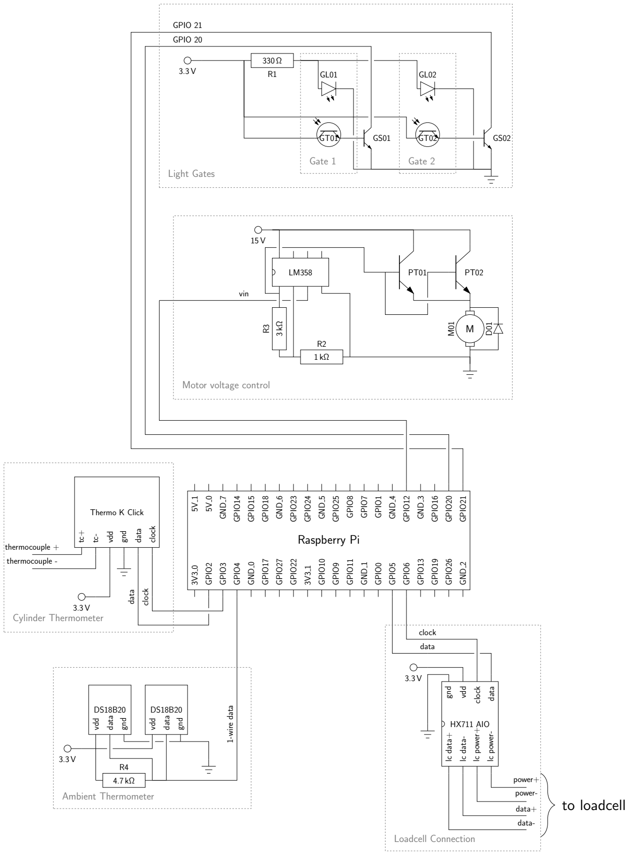

FIG. 8: Circuit Diagram

TABLE V: Summary of electronic components labels and descriptions.

Component	Description
Raspberry Pi	Single Board Computer; controller
HX711 AIO	HX711 ADC all-in-one board; loadcell interface
DS18B20	1-Wire interfacing temperature probe
Thermo K Click	Thermocouple interface board
GL01, GL02	IR LEDs; light gate sources
GT01, GT02	IR Phototransistors; light gate sensors
GS01, GS02	NPN transistors; light gate switching transistors
PT01, PT02	NPN power transistors; current amplifiers for motor supply
LM358	Operational amplifier; voltage amplifier for motor supply

Appendix D: Software

Software was written for controlling the custom rheometer, with a dual-focus on computational efficiency (making use of the limited power of the Raspberry Pi), and flexibility. The software manages a single shear experiment; controlling motor PWM, and monitoring stress, strain rate, and temperature.

The software has a mode to facilitate the running of a sample multiple times (e.g. for performing a strain rate sweep). This system is flexible to allow the user to design any pattern of runs they may wish.

Control of run parameters is defined in simple text files dubbed “control schemes”. These files specify the controlled variable, what control method to use, and what value the variable should have over the course of a run. The controller and controlled variable setpoint (“setter”) functions are defined in plug-in modules. Included modules support some common control methods (PID control, constant or sinusoidal setpoint). New modules can be easily written by the user in a few lines of `c` code. Guides on installing, using, and extending the software are included with the source code. This modular approach opens up the platform for investigation of anything from control techniques for the inhibition of thickening behaviour or performing oscillatory or reversal tests.

The software is freely available under the permissive MIT license [40], obtainable from `github`: github.com/cbosoft/rheometer.

ACKNOWLEDGMENTS

We would like to thank Aditi Mukhopadhyay and Jose Ruiz-Lopez for discussions and help with experiments. This work was supported by the John Anderson Research Award.

[1] Eric Brown and Heinrich M. Jaeger. Shear thickening in concentrated suspensions: phenomenology, mechanisms and relations to jamming. *Reports on Progress in Physics*, 77, 2014.

[2] Matthieu Wyart and Michael E. Cates. Discontinuous shear thickening without inertia in dense non-Brownian suspensions. *Physical Review Letters*, 112(9):1–5, 2014.

[3] Ben M. Guy, Christopher Ness, Michiel Hermes, Laura J. Sawiak, Jin Sun, and Wilson C. K. Poon. Testing the Wyart-Cates model for non-Brownian shear thickening using bidisperse suspensions. *Soft Matter*, 16(1):229–237, 2020.

[4] Aaron S. Baumgarten and Ken Kamrin. A general constitutive model for dense, fine-particle suspensions validated in many geometries. *Proceedings of the National Academy of Sciences*, 116(42):20828–20836, 2019.

[5] Phillip Frank Gower Banfill. The rheology of fresh cement and concrete-a review. In *Proceedings of the 11th international cement chemistry congress*, volume 1, pages 50–62, 2003.

[6] O Boukendakdji, S Kenai, EH Kadri, and F Rouis. Effect of slag on the rheology of fresh self-compacted concrete. *Construction and Building Materials*, 23(7):2593–2598, 2009.

[7] Richard R Eley. Applied rheology and architectural coating performance. *Journal of Coatings Technology and Research*, 16(2):263–305, 2019.

[8] C Gallegos and JM Franco. Rheology of food, cosmetics and pharmaceuticals. *Current opinion in colloid & interface science*, 4(4):288–293, 1999.

[9] Neelanchali Asija, Hemant Chouhan, Shishay Amare Gebremeskel, and Naresh Bhatnagar. Impact response of shear thickening fluid (stf) treated high strength polymer composites — effect of stf intercalation method. *Procedia engineering*, 173:655–662, 2017.

[10] Hiroshi Nakamura and Masahiko Ishii. Rheological behavior of concentrated monodispersed colloidal suspensions. *Nihon Reoroji Gakkaishi*, 47(1):1–7, 2019.

[11] TA Instruments. Received quote for Discovery HR-20, 2020.

[12] Thermo Fisher. Received quote for Haake MARS iQ, 2020.

[13] Thermo Fisher. Received quote for Haake VT iQ, 2020.

[14] Abdoulaye Fall, Anaël Lemaître, and Guillaume Ovarlez. Discontinuous shear thickening in cornstarch suspensions. In *EPJ Web of Conferences*, volume 140, page 09001. EDP Sciences, 2017.

[15] Fergal Dalton, Francis Farrelly, Alberto Petri, Luciano Pietronero, Luca Pitolli, and Giorgio Pontuale. Shear stress fluctuations in the granular liquid and solid phases. *Physical review letters*, 95(13):138001, 2005.

[16] Rory E O'Neill, John R Royer, and Wilson CK Poon. Liquid migration in shear thickening suspensions flowing through constrictions. *Physical Review Letters*, 123(12):128002, 2019.

[17] Creality 3D. Creality 3d. [Online] `https://www.creality3d.shop/products/creality3d-ender-3-pro-high-precision-3d-printer`, 2020. Accessed: 15 May 2020.

[18] Josef Prusa. Prusa research. [Online] `https://www.prusa3d.com/`, 2020. Accessed: 15 May 2020.

[19] RS Components. Ultimaker 3d printer. [Online] `https://uk.rs-online.com/web/p/3d-printers/1249474/`, 2020. Accessed: 15 May 2020.

[20] Isaac S. Newton. *Philosophiae naturalis principia mathematica*, volume 2. 1687.

[21] Russell J Donnelly. Taylor–couette flow: the early days. *Phys. Today*, 44(11):32–39, 1991.

[22] Raspberry Pi 3 Model B+. [Online] `https://www.raspberrypi.org/products/raspberry-pi-3-model-b-plus/`, 2021. Accessed: 13 June 2021.

[23] Antonio Visioli. *Practical PID control*. Springer Science & Business Media, 2006.

[24] Shady Farah, Daniel G Anderson, and Robert Langer. Physical and mechanical properties of PLA, and their functions in widespread applications—a comprehensive review. *Advanced drug delivery reviews*, 107:367–392, 2016.

[25] P Sukwisute, R Sakdanuphab, and A Sakulkalavek. Hardness and wear resistance improvement of ABS surface by crn thin film. *Materials Today: Proceedings*, 4(5):6553–6561, 2017.

[26] Nian-Sheng Cheng. Formula for the viscosity of a

glycerol-water mixture. *Industrial & Engineering Chemistry Research*, 47, 2008.

[27] Matt Newville, Renee Otten, Andrew Nelson, Antonino Ingargiola, Till Stensitzki, Dan Allan, Austin Fox, Faustin Carter, Michał, Dima Pustakhod, Yoav Ram, Glenn, Christoph Deil, Stuermer, Alexandre Beelen, Oliver Frost, Nicholas Zobrist, Mark, Gustavo Pasquevich, Allan L. R. Hansen, Tim Spillane, Shane Caldwell, Anthony Polloreno, andrewhannum, Jonathan Fraine, deep 42-thought, Benjamin F. Maier, Ben Gamari, Arun Persaud, and Anthony Almarza. lmfit/lmfit-py 1.0.1, May 2020.

[28] Pauli Virtanen, Ralf Gommers, Travis E. Oliphant, Matt Haberland, Tyler Reddy, David Cournapeau, Evgeni Burovski, Pearu Peterson, Warren Weckesser, Jonathan Bright, Stéfan J. van der Walt, Matthew Brett, Joshua Wilson, K. Jarrod Millman, Nikolay Mayorov, Andrew R. J. Nelson, Eric Jones, Robert Kern, Eric Larson, CJ Carey, İlhan Polat, Yu Feng, Eric W. Moore, Jake Vand erPlas, Denis Laxalde, Josef Perktold, Robert Cimrman, Ian Henriksen, E. A. Quintero, Charles R Harris, Anne M. Archibald, Antônio H. Ribeiro, Fabian Pedregosa, Paul van Mulbregt, and SciPy 1. 0 Contributors. SciPy 1.0: Fundamental Algorithms for Scientific Computing in Python. *Nature Methods*, 2020.

[29] Jennifer Vernengo, Caitlin Purdy, and Stephanie Farrell. An experiment for the undergraduate laboratory that teaches fundamental concepts of rheology within the context of sickle cell anemia. 2014.

[30] Robb M Winter and Victoria Olson. Integrated undergraduate polymer technology laboratory. In *30th Annual Frontiers in Education Conference. Building on A Century of Progress in Engineering Education. Conference Proceedings (IEEE Cat. No. 00CH37135)*, volume 1, pages F1D–14. IEEE, 2000.

[31] Endao Han, Nicole M James, and Heinrich M Jaeger. Stress controlled rheology of dense suspensions using transient flows. *Physical Review Letters*, 123(24):248002, 2019.

[32] Michiel Hermes, Ben M. Guy, Guilhem Poy, Michael E. Cates, Matthieu Wyart, and Wilcon C. K. Poon. Unsteady flow and particle migration in dense non-brownian suspensions. *Journal of Rheology*, 60:905, 2016.

[33] Matthias Grob, Annette Zippelius, and Claus Heussinger. Rheological chaos of frictional grains. *Physical Review E*, 93:030901, 2016.

[34] Endao Han, Nigel Van Ha, and Heinrich M Jaeger. Measuring the porosity and compressibility of liquid-suspended porous particles using ultrasound. *Soft Matter*, 13(19):3506–3513, 2017.

[35] S. M. Fielding and P. D. Olmstead. Spatiotemporal oscillations and rheochaos in a simple model of shear banding. *Physical Review Letters*, 92(8), 2004.

[36] Brice Saint-Michel, Thomas Gibaud, and Sébastien Manneville. Uncovering instabilities in the spatiotemporal dynamics of a shear-thickening cornstarch suspension. *Physical Review X*, 8(3):031006, 2018.

[37] Claire Forsyth. *Complex flow of concentrated suspensions*. PhD thesis, University of Strathclyde, 2015.

[38] Stefano Aime, Luca Cipelletti, and Laurence Ramos. Power law viscoelasticity of a fractal colloidal gel. *Journal of Rheology*, 62(6):1429–1441, 2018.

[39] Original prusa i3 MK3S user manual. [Online] `https://help.prusa3d.com/en/tag/mk3s-2/`, 2021. Accessed: 27 November 2020.

[40] Source code is hosted on github: `https://github.com/cbosoft/rheometer`.